



Doctor of Philosophy degree in Environmental and Energy  
Engineering Science

Cycle XXXII

Title

“Structural and Thermodynamic Properties  
of Transition Metal Ions in Room  
Temperature Ionic Liquids”

Ph. D. candidate  
Matteo Busato

Supervisor  
Prof. Andrea Melchior

Co-supervisor  
Prof. Marilena Tolazzi

2020



Humankind cannot gain anything without first giving something in return.  
To obtain, something of equal value must be lost.  
That is alchemy's first law of Equivalent Exchange.  
In those days, we really believed that to be the world's one, and only Truth.

*Fullmetal Alchemist*



# Abstract

Room temperature ionic liquids (RTILs) are salts made by an organic cation and an organic or inorganic anion, which are at the liquid state at 25 °C. RTILs have attracted much attention as new sustainable solvents owing to some unique properties they usually possess, such as a practically negligible vapor pressure, non-flammability, high thermal stability, wide electrochemical windows, good solvation ability and supposed low toxicity. These features make RTILs good candidates for the substitution of classical organic solvents in many technological applications. For these reasons, they are currently studied as new media for chemical separations, electrodepositions, electrolytes for batteries and supercapacitors, catalysis and pharmaceutical research.

Several of these applications also involve the presence of metal ions as solvated species in RTILs. In this field, structural and thermodynamic data about single-ion solvation are fundamental quantities that need to be known to improve new technologies. However, this fundamental knowledge still lacks for many metal species in several ionic liquids. The aim of this thesis is to obtain a complete description of metal ions solvation in RTILs both from a structural and thermodynamic point of view. Molecular dynamics (MD) simulations and X-ray absorption spectroscopy (XAS) experiments have been performed to study solutions of metal ions of industrial, environmental and economic interest such as  $\text{Zn}^{2+}$ ,  $\text{Co}^{2+}$ ,  $\text{Ag}^+$  in widely used RTILs like those based on the  $[\text{Tf}_2\text{N}]^-$  (bis(trifluoromethylsulfonyl)imide) and  $[\text{BF}_4]^-$  (tetrafluoroborate) anions within the  $[\text{C}_n\text{mim}]^+$  (1-alkyl-3-methylimidazolium) cation.

MD simulations have been carried out on  $\text{Zn}^{2+}$  in  $[\text{C}_n\text{mim}][\text{Tf}_2\text{N}]$  ( $n = 2, 4$ ) and  $[\text{C}_4\text{mim}][\text{BF}_4]$ . The obtained thermodynamic data are in good agreement with literature experimental values and indicate the goodness of the employed protocol. The calculated Gibbs free energies of transfer ( $\Delta G_{\text{trans}}$ ) from water to the  $[\text{C}_n\text{mim}][\text{Tf}_2\text{N}]$  RTILs suggest that  $\text{Zn}^{2+}$  is more favorably solvated in aqueous solution than in this class of ionic liquids, while the opposite is found for  $[\text{C}_4\text{mim}][\text{BF}_4]$ . The obtained single-ion solvation enthalpies and entropies provided an interpretation of the different contributions to the calculated free energies. In addition, XAS experimental results allowed to understand the coordination of  $\text{Zn}^{2+}$  in water-saturated  $[\text{C}_4\text{mim}][\text{Tf}_2\text{N}]$ , representing the real-operating condition in a liquid-liquid extraction.

A similar picture has been obtained for  $\text{Co}^{2+}$  in  $[\text{C}_4\text{mim}][\text{Tf}_2\text{N}]$ . MD calculated  $\Delta G_{\text{trans}}$  showed that the metal ion is still more favorably solvated in water than in the RTIL because of an unfavorable entropic contribution. XAS experiments and data-fitting allowed to obtain  $\text{Co}^{2+}$  coordination in dry

[C<sub>4</sub>mim][Tf<sub>2</sub>N]. The metal resulted to be bound by six monodentate anions forming the [Co(Tf<sub>2</sub>N)<sub>6</sub>]<sup>4-</sup> octahedral species, differently to what was observed for the solid state. In addition, water is found to preferentially coordinate the metal when present at high concentrations in the RTIL, as provided by UV-Vis data. The electronic spectra also showed a blue-shift by passing from [Tf<sub>2</sub>N]<sup>-</sup> to water coordination, confirming the bis(trifluoromethylsulfonyl)imide anion as a weak ligand. The obtained negative enthalpy of transfer from water to [C<sub>4</sub>mim][Tf<sub>2</sub>N] must therefore be attributed to outer-sphere effects induced by the reorganization of the solvent around the first coordination sphere of the metal ion.

As regards the study about Ag<sup>+</sup> in RTILs, a totally different picture with respect to Zn<sup>2+</sup> and Co<sup>2+</sup> has been obtained. MD results showed that this ion is more favorably solvated both in [C<sub>4</sub>mim][Tf<sub>2</sub>N] and [C<sub>4</sub>mim][BF<sub>4</sub>] with respect to water, and this encourages the employment of these RTILs as extracting phase for this metal. Ag<sup>+</sup> resulted coordinated by four or five RTILs anions, depending on the employed interaction potential. However, when considering the transfer of Ag<sup>+</sup> from water to the RTILs, great care must be taken because of a possible change in the coordination number. Indeed, preliminary XAS data suggest a linear coordination for this metal ion in aqueous solution, differently from the tetrahedral model that is usually accepted and reproduced by the current classical potentials. *Ab initio* MD simulations with the Car-Parrinello method seemed to confirm this observation.



# Contents

Abstract.....	I
Contents.....	IV
List of Figures.....	VIII
List of Tables.....	XIII
List of abbreviations.....	XVI
<b>1. Introduction</b> .....	<b>1</b>
1.1 Ionic liquids: historical remarks.....	1
1.2 Ionic liquids: some chemical-physical properties.....	2
1.3 Metal ions and ionic liquids.....	5
1.3.1 Applications.....	6
1.3.1.1 <i>Electrochemical and energy applications</i> .....	6
1.3.1.2 <i>Catalysis</i> .....	7
1.3.1.3 <i>Chemical separations</i> .....	8
1.3.2 Structural properties of metal ions in ILs.....	10
1.3.2.1 <i>Alkali and alkali-earth metal ions</i> .....	11
1.3.2.2 <i>Transition metal ions</i> .....	13
1.3.2.3 <i>Rare-earth metal ions</i> .....	16
1.3.3 Solvation thermodynamics of metal ions in ILs.....	17
1.3.4 Complex formation thermodynamics of metal ions in ILs.....	20
1.3.4.1 <i>Alkali and alkali-earth metal ions</i> .....	20
1.3.4.2 <i>Transition metal-ions</i> .....	21
1.3.4.3 <i>Rare-earth metal ions</i> .....	22
Bibliography.....	24
<b>2. Focus of the work</b> .....	<b>40</b>
Bibliography.....	42

<b>3. Methods</b>	<b>44</b>
3.1 Simulation techniques.....	44
3.1.1 Classical Molecular Dynamics.....	45
3.1.1.1 Long-range interactions.....	49
3.1.1.2 Constraint algorithms.....	50
3.1.1.3 Box definition and periodic boundary conditions.....	50
3.1.1.4 Integrators.....	51
3.1.1.5 Statistical ensembles, thermostats and barostats.....	52
3.1.1.6 Free energy calculations.....	55
3.1.1.7 Umbrella sampling.....	59
3.1.2 Ab initio Molecular Dynamics.....	59
3.2 X-ray absorption spectroscopy.....	61
3.2.1 EXAFS analysis.....	66
3.2.1.1 Liquid systems.....	70
3.2.2 XANES analysis.....	71
Bibliography.....	73
<b>4. Zn<sup>2+</sup> ion in Tf<sub>2</sub>N- and BF<sub>4</sub>-based imidazolium RTILs</b>	<b>78</b>
4.1 Introduction.....	78
4.2 Methods.....	80
4.2.1 Zn <sup>2+</sup> in [C <sub>n</sub> mim][Tf <sub>2</sub> N] (n = 2, 4).....	80
4.2.1.1 MD simulations details.....	80
4.2.1.2 Umbrella sampling simulations.....	82
4.2.1.3 X-ray absorption measurements.....	83
4.2.1.4 EXAFS data analysis.....	83
4.2.2 Zn <sup>2+</sup> in [C <sub>4</sub> mim][BF <sub>4</sub> ].....	84
4.2.2.1 MD simulations details.....	84
4.3 Results.....	86
4.3.1 Zn <sup>2+</sup> in [C <sub>n</sub> mim][Tf <sub>2</sub> N] (n = 2, 4).....	86
4.3.1.1 Zn <sup>2+</sup> coordination.....	86
4.3.1.2 Zn <sup>2+</sup> Solvation thermodynamics.....	92
4.3.1.3 Zn <sup>2+</sup> coordination in wet [C <sub>4</sub> mim][Tf <sub>2</sub> N]: XAS results.....	98
4.3.2 Zn <sup>2+</sup> in [C <sub>4</sub> mim][BF <sub>4</sub> ].....	101

4.4 Conclusions.....	104
Bibliography.....	106
<b>5. Co<sup>2+</sup> ion in [C<sub>4</sub>mim][Tf<sub>2</sub>N]</b>	<b>112</b>
5.1 Introduction.....	112
5.2 Methods.....	113
5.2.1 MD simulations details.....	113
5.2.2 X-ray absorption measurements.....	114
5.2.3 EXAFS data analysis.....	115
5.2.4 UV-Vis absorption spectra.....	116
5.3 Results.....	116
5.3.1 Co <sup>2+</sup> coordination.....	116
5.3.2 Co <sup>2+</sup> solvation thermodynamics.....	123
5.3.3 Co <sup>2+</sup> in wet [C <sub>4</sub> mim][Tf <sub>2</sub> N]: UV-Vis titration.....	125
5.4 Conclusions.....	127
Bibliography.....	129
<b>6. Ag<sup>+</sup> ion between water and RTILs</b>	<b>134</b>
6.1 Introduction.....	134
6.2 Methods.....	137
6.2.1 Ag <sup>+</sup> in water.....	137
6.2.1.1 X-Ray absorption measurements.....	137
6.2.1.2 EXAFS data analysis.....	137
6.2.1.3 XANES data analysis.....	137
6.2.1.4 Car-Parrinello Molecular Dynamics.....	138
6.2.1.5 Lennard-Jones parameters for the Ag <sup>+</sup> ion.....	139
6.2.2 Ag <sup>+</sup> in RTILs.....	139
6.3 Results.....	140
6.3.1 Ag <sup>+</sup> in water.....	140
6.3.1.1 XAS results.....	140
6.3.1.2 CPMD simulation results.....	143
6.3.1.3 Reproduction of Ag <sup>+</sup> coordination in water with classical MD.....	147
6.3.2 Ag <sup>+</sup> in RTILs.....	150

6.3.2.1 Solvation thermodynamics.....	154
6.4 Conclusions.....	156
Bibliography.....	158
<b>Appendix A: <i>Ab initio</i> generation of Ag<sup>+</sup>-H<sub>2</sub>O interaction potential</b>	<b>163</b>
A.1 Method.....	163
A.2 Results.....	165
A.3 Conclusions.....	168
Bibliography.....	169
<b>Appendix B: Zn<sup>2+</sup> ion in [C<sub>2</sub>mim][Tf<sub>2</sub>N]: adding explicit polarizability</b>	<b>171</b>
B.1 Introduction.....	171
B.2 Methods and Results.....	173
B.3 Conclusions.....	178
Bibliography.....	179
<b>Appendix C</b>	<b>183</b>
<b>General conclusions and perspectives</b>	<b>191</b>
<b>Acknowledgements</b>	<b>196</b>
<b>List of publications and communications</b>	<b>197</b>

# List of Figures

## 1. Introduction

<b>Figure 1.1.</b> Number of publications per year as found in Scopus by typing “ionic liquids” as keyword	2
<b>Figure 1.2.</b> Schematic representation of some common ILs anions and cations with the relative nomenclature employed in this work.....	3
<b>Figure 1.3.</b> Possible coordinations of the [Tf <sub>2</sub> N] <sup>-</sup> anion in a tetrahedral ligand field towards a generic M <sup>n+</sup> metal ion.....	12
<b>Figure 1.4.</b> Possible coordinations of the [Tf <sub>2</sub> N] <sup>-</sup> anion in an octahedral ligand field towards a generic M <sup>n+</sup> metal ion.....	15
<b>Scheme 1.1.</b> Schematic representation of the thermodynamic cycle employed in this work for the calculation of the Gibbs free energy of solvation in the RTILs ( $\Delta G_{\text{solv}}$ ) and free energy of transfer from water to the RTILs ( $\Delta G_{\text{trans}}(\text{water} \rightarrow \text{RTIL})$ ) from literature experimental data.....	18

## 3. Methods

<b>Figure 3.1.</b> Pictorial representation of the two-, three- and four-body bonded interactions described by a force field.....	47
<b>Figure 3.2.</b> Schematic representation of the Lennard-Jones potential between two <i>i</i> and <i>j</i> particles in function of their reciprocal distance.....	48
<b>Figure 3.3.</b> Pictorial representation of the transitions that can take place at the various absorption edges.....	62
<b>Figure 3.4.</b> Division of a XAS spectrum into the XANES and EXAFS energy regions.....	64
<b>Figure 3.5.</b> Pictorial view of the possible photoelectron paths included in the $\chi_2$ , $\chi_3$ and $\chi_4$ terms.....	67
<b>Figure 3.6.</b> Pictorial view of the MS expansion for the $\gamma^{(2)}$ and $\gamma^{(3)}$ signals including terms up to $\chi_6$ and $\chi_4$ , respectively.....	69

## 4. Zn<sup>2+</sup> ion in Tf<sub>2</sub>N- and BF<sub>4</sub>-based imidazolium RTILs

<b>Figure 4.1.</b> Zn-O(Tf <sub>2</sub> N) and Zn-N(Tf <sub>2</sub> N) pairs <i>g</i> ( <i>r</i> )’s radial distribution functions calculated for Zn <sup>2+</sup> in [C <sub>2</sub> mim]Tf <sub>2</sub> N] employing different Zn <sup>2+</sup> LJ parameters and RTILs force fields.....	88
---	----

<b>Figure 4.2.</b> Zn-O(Tf <sub>2</sub> N) and Zn-N(Tf <sub>2</sub> N) pairs radial distribution functions calculated for Zn <sup>2+</sup> in [C <sub>4</sub> mim]Tf <sub>2</sub> N] employing different Zn <sup>2+</sup> LJ parameters and RTILs force fields.....	89
<b>Figure 4.3.</b> MD snapshots of Zn <sup>2+</sup> in [C <sub>4</sub> mim][Tf <sub>2</sub> N] giving A) [Zn(Tf <sub>2</sub> N) <sub>6</sub> ] <sup>4+</sup> (Zn <sup>2+</sup> LJ parameters: Merz; RTIL force field: CL&P) and B) [Zn(Tf <sub>2</sub> N) <sub>5</sub> ] <sup>3-</sup> (Zn <sup>2+</sup> LJ parameters: AMBER; RTIL force field: MP).....	90
<b>Figure 4.4.</b> Selected MD snapshots from the umbrella sampling simulation showing A) the [Zn(Tf <sub>2</sub> N) <sub>5</sub> ] <sup>3-</sup> unit and the [Tf <sub>2</sub> N] <sup>-</sup> anion set in the second solvation shell, B) the approach of the [Tf <sub>2</sub> N] <sup>-</sup> anion leading to the aperture of the bidentate [Tf <sub>2</sub> N] <sup>-</sup> ligand and C) the resulting [Zn(Tf <sub>2</sub> N) <sub>6</sub> ] <sup>4+</sup> species.....	91
<b>Figure 4.5.</b> Calculated PMF profile for the addition of a [Tf <sub>2</sub> N] <sup>-</sup> anion to a [Zn(Tf <sub>2</sub> N) <sub>5</sub> ] <sup>3-</sup> unit to give [Zn(Tf <sub>2</sub> N) <sub>6</sub> ] <sup>4+</sup> .....	92
<b>Figure 4.6.</b> Initial configuration of the simulated system for the pulling of Zn <sup>2+</sup> through a water/[C <sub>4</sub> mim][Tf <sub>2</sub> N] interphase.....	95
<b>Figure 4.7.</b> Calculated PMF profile for the umbrella sampling simulation of one Zn <sup>2+</sup> ion pulled through a water/[C <sub>4</sub> mim][Tf <sub>2</sub> N] biphasic system.....	96
<b>Figure 4.8.</b> ΔG/T vs. 1/T plots obtained from calculated Zn <sup>2+</sup> Gibbs free energies A) in water and B) in [C <sub>4</sub> mim][Tf <sub>2</sub> N] at different temperatures (R <sup>2</sup> = 0.99).....	97
<b>Figure 4.10.</b> Upper panel: EXAFS analysis of the Zn K-edge EXAFS spectrum of the 0.1 Zn(Tf <sub>2</sub> N) <sub>2</sub> solution in [C <sub>4</sub> mim][Tf <sub>2</sub> N] with 1 M water content. From the top the following curves are reported: best fit theoretical Zn-O and Zn-H SS contributions, O-Zn-O MS signals, total theoretical signal (blue line) together with the experimental spectrum (red line) and the correspondent residuals (green line). Lower panel: non-phase shift corrected Fourier Transforms of the best-fit EXAFS theoretical signal (blue line) of the experimental data (red line) and of the residual curve (green line).....	100
<b>Figure 4.11.</b> MD calculated A) Zn-F and B) Zn-B pairs <i>g(r)</i> 's radial distribution functions (black lines, left scale) and corresponding integration numbers (red lines, right scales) for Zn <sup>2+</sup> in [C <sub>4</sub> mim][BF <sub>4</sub> ] (RTIL force field: CL&P).....	102
<b>Figure 4.12.</b> MD snapshot of Zn <sup>2+</sup> in [C <sub>4</sub> mim][BF <sub>4</sub> ] forming the [Zn(BF <sub>4</sub> ) <sub>6</sub> ] <sup>4+</sup> species (RTIL force field: CL&P).....	102
<b>Figure 4.13.</b> ΔG/T vs. 1/T plot obtained from calculated Zn <sup>2+</sup> Gibbs free energies in [C <sub>4</sub> mim][BF <sub>4</sub> ] at different temperatures (R <sup>2</sup> = 0.99).....	104

## 5. Co<sup>2+</sup> ion in [C<sub>4</sub>mim][Tf<sub>2</sub>N]

<b>Figure 5.1.</b> Structural arrangement of the [Tf <sub>2</sub> N] <sup>-</sup> anions around Co <sup>2+</sup> A) in the Co(Tf <sub>2</sub> N) <sub>2</sub> crystal as determined starting from the crystallographic structure of Ref. <sup>13</sup> and B) in the [C <sub>4</sub> mim][Tf <sub>2</sub> N] ionic liquid as showed by a snapshot from the MD simulation.....	117
---	-----

<b>Figure 5.2.</b> Radial distribution functions $g(r)$ 's (black lines, left scale) and corresponding integration number (red lines, right scale) for the A) Co-O, B) Co-S and C) Co-N pairs calculated from the MD simulation of the $\text{Co}(\text{Tf}_2\text{N})_2$ solution in $[\text{C}_4\text{mim}][\text{Tf}_2\text{N}]$ for the structural part.....	118
<b>Figure 5.3.</b> Co K-edge XANES experimental spectra of solid $\text{Co}(\text{Tf}_2\text{N})_2$ as compared to the 0.1 M solution of $\text{Co}(\text{Tf}_2\text{N})_2$ in $[\text{C}_4\text{mim}][\text{Tf}_2\text{N}]$ .....	120
<b>Figure 5.4.</b> Upper panels: fit of Co K-edge EXAFS spectra of $\text{Co}(\text{Tf}_2\text{N})_2$ crystal (left panel) and of the 0.1 M solution of $\text{Co}(\text{Tf}_2\text{N})_2$ in $[\text{C}_4\text{mim}][\text{Tf}_2\text{N}]$ (right panel). From the top to the bottom: Co-O, Co-S and Co-N SS theoretical signals, O-Co-O and Co-O-S MS three-body theoretical signals, total theoretical signal (blue line) compared with the experimental spectrum (red dotted line) and resulting residual. Lower panels: non-phase shift corrected Fourier transforms of the experimental data (red dotted line), of the total theoretical signals (blue line) and of the residuals (blue dashed line).....	121
<b>Figure 5.5.</b> $\Delta G/T$ vs. $1/T$ plots obtained from MD calculated $\text{Co}^{2+}$ Gibbs free energies A) in water and B) in $[\text{C}_4\text{mim}][\text{Tf}_2\text{N}]$ at different temperatures ( $R^2 = 0.99$ ).....	124
<b>Figure 5.6.</b> From the top to the bottom: absorption spectra of $\text{Co}(\text{Tf}_2\text{N})_2$ 0.05 M solutions in dry $[\text{C}_4\text{mim}][\text{Tf}_2\text{N}]$ and with increasing content of water. The spectrum in pure water is also reported. The molar absorbance corresponds to the experimental absorbance divided by the total $\text{Co}^{2+}$ concentration.....	127

## 6. $\text{Ag}^+$ ion between water and RTILs

<b>Figure 6.1.</b> Values of the A) $R_{sq}$ residual function and of the B) $\sigma^2$ Debye-Waller factor obtained from the EXAFS fitting procedure for all the tested $\text{Ag}^+$ coordination numbers (CN).....	141
<b>Figure 6.2.</b> Upper panel: analysis of the Ag K-edge EXAFS spectrum of the 2 M $\text{AgClO}_4$ in water. From the top the theoretical Ag-O and Ag-H SS signals are shown, as well as the total theoretical signal (blue line) together with the experimental spectrum (red dots) and the correspondent residuals (green line). Lower panel: non-phase shift corrected Fourier Transforms of the best-fit EXAFS theoretical signal (blue line) of the experimental data (red dots) and of the residual curve (green line)	142
<b>Figure 6.3.</b> From left to the right: comparison of the XANES experimental spectrum (red dots) with the theoretical ones (black lines) optimized by starting from clusters with $\text{Ag}^+$ CN of 2 (linear), “2+2” (linearly-distorted tetrahedral), 4 (tetrahedral) and 6 (octahedral).....	143
<b>Figure 6.4.</b> A) Ag-O pairs radial distribution function $g(r)$ (black line, left scale) and corresponding integration number (red line, right scale) and B) trajectory snapshot as obtained by the CPMD simulation.....	144
<b>Figure 6.5.</b> Combined distributions functions (CDFs) between the $\text{O}_{1\text{st}}\text{-Ag-O}_{2\text{nd}}/\text{H}_{2\text{nd}}$ angles and $\text{Ag-O}_{2\text{nd}}/\text{H}_{2\text{nd}}$ distances calculated from the CPMD simulation.....	146

<b>Figure 6.6.</b> Spatial distribution function (SDF) between the $O_{1st}-Ag-O_{1st}$ vector and outer-sphere oxygen atoms.....	147
<b>Figure 6.7.</b> MD calculated $Ag^+$ coordination number CN (black dots, left scales) and average distance with coordinating water oxygen atoms (red dots, right scales) against $Ag^+$ LJ parameters A) $\sigma$ and B) $\epsilon$ .....	148
<b>Figure 6.8.</b> A) $Ag-O(H_2O)$ pair $g(r)$ radial distribution function (black line, left scale) and corresponding integration number (red line, right scale) within B) MD snapshot obtained from the simulation of $Ag^+$ in water with the LJ parameters found in this work.....	149
<b>Figure 6.9.</b> $\Delta G/T$ vs. $1/T$ plots obtained from calculated $Ag^+$ Gibbs free energies in water at different temperatures ( $R^2 = 0.99$ ). $Ag^+$ represented with LJ parameters obtained in this work.....	150
<b>Figure 6.10.</b> MD calculated $Ag-O(Tf_2N)$ and $Ag-N(Tf_2N)$ pairs radial distribution functions $g(r)$ 's obtained from simulations in $[C_4mim][Tf_2N]$ with LJ parameters for $Ag^+$ obtained in this work (A and C) and from Merz <i>et al.</i> "HFE" set (B and D) (black lines, left scales). The correspondent integration numbers (red lines, right scales) are also reported.....	152
<b>Figure 6.11.</b> MD snapshots of $Ag^+$ in $[C_4mim][Tf_2N]$ obtained by representing the metal ion A) with the LJ parameters obtained in this work and B) from Merz <i>et al.</i> .....	153
<b>Figure 6.12.</b> MD calculated $Ag-F(BF_4)$ and $Ag-B(BF_4)$ pairs radial distribution functions $g(r)$ 's obtained from simulations in $[C_4mim][BF_4]$ with LJ parameters for $Ag^+$ obtained in this work (A and C) and from Merz <i>et al.</i> "HFE" set (B and D) (black lines, left scales). The correspondent integration numbers (red lines, right scales) are also reported.....	153
<b>Figure 6.13.</b> MD snapshots of $Ag^+$ in $[C_4mim][BF_4]$ obtained by representing the metal ion A) with the LJ parameters obtained in this work and B) from Merz <i>et al.</i> .....	154
<b>Figure 6.14.</b> $\Delta G/T$ vs. $1/T$ plots obtained from calculated $Ag^+$ Gibbs free energies A) in $[C_4mim][Tf_2N]$ and B) in $[C_4mim][BF_4]$ at different temperatures ( $R^2 = 0.99$ ).....	156

## Appendix A: *Ab initio* generation of $Ag^+-H_2O$ interaction potential

<b>Figure A.1.</b> Geometrical parameters definition for the $Ag-H_2O$ cluster employed to generate the interaction potential.....	165
<b>Figure A.2.</b> CPCM cavity radius optimization curves for the $Ag^+$ ion.....	166
<b>Figure A.3.</b> A) $Ag^+-H_2O$ interaction energy curves vs. the ion-oxygen ( $r_{AgO}$ ) distance.....	166
<b>Figure A.4.</b> A) $Ag-O(H_2O)$ pair $g(r)$ radial distribution function (black line, left scale) and corresponding integration number (red line, right scale) within B) MD snapshot obtained from the simulation of $Ag^+$ in water with the fitted <i>ab initio</i> potential.....	167

## Appendix B: Zn<sup>2+</sup> ion in [C<sub>2</sub>mim][Tf<sub>2</sub>N]: adding explicit polarizability

<b>Figure B.1.</b> Mean-square relative error $\chi^2$ calculated between the atomic forces acting on Zn <sup>2+</sup> at DFT level and in the polarizable MD simulation at dependence of Zn <sup>2+</sup> LJ parameters.....	175
<b>Figure B.2.</b> Zn-O(Tf <sub>2</sub> N) and Zn-N(Tf <sub>2</sub> N) pairs $g(r)$ 's obtained for Zn <sup>2+</sup> in [C <sub>2</sub> mim][Tf <sub>2</sub> N] by representing the RTIL with CL&P polarizable force field and the metal ion with LJ parameters from the <i>ab initio</i> fitting procedure.....	176
<b>Figure B.3.</b> Zn-O(Tf <sub>2</sub> N) and Zn-N(Tf <sub>2</sub> N) pairs $g(r)$ 's obtained for Zn <sup>2+</sup> in [C <sub>2</sub> mim][Tf <sub>2</sub> N] by representing the RTIL with CL&P polarizable force field <sup>5</sup> and the metal ion with parameters adapted from Borodin <i>et al.</i> <sup>28</sup> .....	178

## Appendix C

<b>Figure C.1.</b> Histograms of the configurations within the umbrella sampling windows for the addition of a [Tf <sub>2</sub> N] <sup>-</sup> anion to the [Zn(Tf <sub>2</sub> N) <sub>5</sub> ] <sup>3+</sup> unit.....	183
<b>Figure C.2.</b> Gromacs BAR module output showing the relative free energy differences calculated between neighboring $\lambda$ windows for Zn <sup>2+</sup> represented with Merz LJ parameters in [C <sub>4</sub> mim][Tf <sub>2</sub> N] with A) CL&P; B) KLP and C) MP force fields.....	184
<b>Figure C.3.</b> Histograms of the configurations within the umbrella sampling windows for the transfer of Zn <sup>2+</sup> from water to [C <sub>4</sub> mim][Tf <sub>2</sub> N] in the biphasic system.....	185
<b>Figure C.4.</b> A) Zn-O(H <sub>2</sub> O) and B) Zn-O(Tf <sub>2</sub> N) pairs $g(r)$ along the reaction coordinate between the interphase (from top) to the ionic liquid bulk (to bottom).....	185
<b>Figure C.5.</b> A) Co-O, B) Co-S and C) Co-N $g(r)$ 's obtained from the MD simulations of Co(Tf <sub>2</sub> N) <sub>2</sub> in [C <sub>4</sub> mim][Tf <sub>2</sub> N] for the structural part (red dotted lines) as compared with the $\Gamma$ -like functions obtained from the fitting procedure (solid black lines).....	186
<b>Figure C.6.</b> Radial distribution functions $g(r)$ 's for the A) Co-O, B) Co-S and C) Co-N pairs calculated from the MD simulation of the Co(Tf <sub>2</sub> N) <sub>2</sub> solution in [C <sub>4</sub> mim][Tf <sub>2</sub> N] for the thermodynamic part.....	187
<b>Figure C.7.</b> Comparison between A) Ag-O and B) Ag-H $g(r)$ 's obtained from the CPMD simulation of Ag <sup>+</sup> in water (red dots) and from the fitting of the Ag K-edge EXAFS spectrum in aqueous solution (blue lines).....	188
<b>Figure C.8.</b> Representative snapshot from the CPMD simulations of Ag <sup>+</sup> in water showing the two coordinating water molecules in addition to selected outer-sphere waters.....	189

# List of Tables

## 1. Introduction

<b>Table 1.1.</b> Melting points (K), densities ( $\rho$ , g cm <sup>-3</sup> , 298.15 K) and viscosities ( $\eta$ , cP, 298.15 K) of ILs carrying the 1-alkyl-3-methylimidazolium cation [C <sub>n</sub> mim] <sup>+</sup> (n = 1 – 18) within the [Tf <sub>2</sub> N] <sup>-</sup> and [BF <sub>4</sub> ] <sup>-</sup> anions.....	4
<b>Table 1.2.</b> Gibbs free energies of solvation in several RTILs within free energies of transfer from DMSO and water for the Cu <sup>2+</sup> , Zn <sup>2+</sup> and Ag <sup>+</sup> ions at 298 K. Data in kcal mol <sup>-1</sup> .....	19
<b>Table 1.3.</b> Stability constants for Ag <sup>+</sup> complexation with cryptand 222 at 298 K in various RTILs...	22

## 2. Methods

<b>Table 3.1.</b> Parameters for cubic, rhombic dodecahedron and truncated dodecahedron boxes.....	51
--	----

## 3. Zn<sup>2+</sup> ion in Tf<sub>2</sub>N- and BF<sub>4</sub>-based imidazolium RTILs

<b>Table 4.1.</b> Zn <sup>2+</sup> experimental Gibbs free energies of solvation ( $\Delta G_{\text{solv}}$ ) and transfer from water ( $\Delta G_{\text{trans}}$ ) for the RTILs studied in this work obtained as reported in <b>Sec. 1.3.3 of Chapter 1</b> at 298.15 K. Values in kcal mol <sup>-1</sup> .....	79
<b>Table 4.2.</b> Non-bonded parameters for Zn <sup>2+</sup> and the oxygen atom of the [Tf <sub>2</sub> N] <sup>-</sup> anion taken from the force fields employed in this work.....	82
<b>Table 4.3.</b> Non-bonded parameters for the [BF <sub>4</sub> ] <sup>-</sup> anion taken from the force fields employed in this work.....	85
<b>Table 4.4.</b> MD results of Zn <sup>2+</sup> first solvation shell structure in [C <sub>2</sub> mim][Tf <sub>2</sub> N] and [C <sub>4</sub> mim][Tf <sub>2</sub> N] employing all the tested Zn <sup>2+</sup> LJ parameters <sup>23-25</sup> and RTILs force fields. <sup>18-22</sup> .....	87
<b>Table 4.5.</b> Calculated Zn <sup>2+</sup> Gibbs free energies of solvation $\Delta G_{\text{solv}}$ (kcal mol <sup>-1</sup> ) in [C <sub>2</sub> mim][Tf <sub>2</sub> N] and [C <sub>4</sub> mim][Tf <sub>2</sub> N] and free energies of transfer from water to the RTILs employing all the tested Zn <sup>2+</sup> LJ parameters <sup>23-25</sup> and RTIL force fields. <sup>18-22</sup> T = 298.15 K, P = 1 atm. Errors given by BAR module.	94
<b>Table 4.6.</b> MD calculated Zn <sup>2+</sup> Gibbs free energy of hydration ( $\Delta G_{\text{hyd}}$ , kcal mol <sup>-1</sup> ) with the LJ parameters <sup>23-25</sup> tested in this work at T = 298.15 K and P = 1 atm. Errors given by BAR module.....	95
<b>Table 4.7.</b> Hydration enthalpies (kcal mol <sup>-1</sup> ) and entropies (kcal mol <sup>-1</sup> K <sup>-1</sup> ) for Zn <sup>2+</sup> calculated from MD simulations (obtained from plot in <b>Fig. 4.8 A</b> ) and from experimental data.....	97

<b>Table 4.8.</b> MD calculated enthalpy (kcal mol <sup>-1</sup> ) and entropy (kcal mol <sup>-1</sup> K <sup>-1</sup> ) of solvation for Zn <sup>2+</sup> in [C <sub>4</sub> mim][Tf <sub>2</sub> N] and transfer from water to the RTIL obtained from the plot in <b>Fig. 4.8 B</b> .....	98
<b>Table 4.9.</b> Coordination number CN, average distance R, Debye-Waller factor $\sigma^2$ and asymmetry index $\beta$ optimized during the EXAFS fitting procedure for 0.1 M Zn(Tf <sub>2</sub> N) <sub>2</sub> in [C <sub>4</sub> mim][Tf <sub>2</sub> N] with 1 M water content. Standard deviation in parenthesis.....	101
<b>Table 4.10.</b> MD results of Zn <sup>2+</sup> first solvation shell structure in [C <sub>4</sub> mim][BF <sub>4</sub> ] employing the tested RTIL force fields. <sup>18,43</sup> .....	101
<b>Table 4.11.</b> MD calculated Gibbs free energies of solvation in [C <sub>4</sub> mim][BF <sub>4</sub> ] ( $\Delta G_{\text{solv}}$ ) and transfer from water ( $\Delta G_{\text{trans}}$ ) obtained at T = 298.15 K and P = 1 atm for Zn <sup>2+</sup> with the tested RTIL force fields. <sup>18,43</sup> Errors given by the BAR module. Values in kcal mol <sup>-1</sup> .....	103
<b>Table 4.12.</b> MD calculated enthalpy (kcal mol <sup>-1</sup> ) and entropy (kcal mol <sup>-1</sup> K <sup>-1</sup> ) of solvation for Zn <sup>2+</sup> in [C <sub>4</sub> mim][BF <sub>4</sub> ] and transfer from water to the RTIL obtained from the plot in <b>Fig. 4.13</b> .....	104

## 6. Ag<sup>+</sup> ion between water and RTILs

<b>Table 6.1.</b> Ag <sup>+</sup> literature experimental Gibbs free energies of solvation ( $\Delta G_{\text{solv}}$ ) and transfer from water ( $\Delta G_{\text{trans}}$ ) for the RTILs studied in this work obtained as reported in <b>Sec. 1.3.3 of Chapter 1</b> at 298.15 K. Data in kcal mol <sup>-1</sup> .....	136
<b>Table 6.2.</b> MD boxes details for the simulation of Ag <sup>+</sup> in the [C <sub>4</sub> mim][Tf <sub>2</sub> N] and [C <sub>4</sub> mim][BF <sub>4</sub> ] RTILs.....	140
<b>Table 6.3.</b> Best-fit coordination number CN, average distance R, Debye-Waller factor $\sigma^2$ and asymmetry index $\beta$ of the Ag-O and Ag-H distributions as obtained during the EXAFS fitting procedure for the 2 M AgClO <sub>4</sub> solution in water.....	142
<b>Table 6.4.</b> MD calculated Ag <sup>+</sup> coordination in water and Gibbs free energy of hydration ( $\Delta G_{\text{hyd}}$ , kcal mol <sup>-1</sup> ) with the LJ parameters obtained in this work and from Merz <i>et al.</i> <sup>18</sup> .....	149
<b>Table 6.5.</b> Hydration enthalpies (kcal mol <sup>-1</sup> ) and entropies (kcal mol <sup>-1</sup> K <sup>-1</sup> ) for Ag <sup>+</sup> calculated from MD simulations (obtained from plot in <b>Fig. 6.9</b> ) and from experimental data.....	150
<b>Table 6.6.</b> MD results of Ag <sup>+</sup> first solvation shell structure in [C <sub>4</sub> mim][Tf <sub>2</sub> N] and [C <sub>4</sub> mim][BF <sub>4</sub> ] with both the tested LJ sets for the metal ion.....	151
<b>Table 6.7.</b> MD calculated Gibbs free energies of solvation in [C <sub>4</sub> mim][Tf <sub>2</sub> N] and [C <sub>4</sub> mim][BF <sub>4</sub> ] ( $\Delta G_{\text{solv}}$ ) as well as transfer from water to the RTILs ( $\Delta G_{\text{trans}}$ ) obtained at T = 298.15 K and P = 1 atm for the Ag <sup>+</sup> ion. Values in kcal mol <sup>-1</sup> .....	155
<b>Table 6.8.</b> MD calculated enthalpy (kcal mol <sup>-1</sup> ) and entropy (kcal mol <sup>-1</sup> K <sup>-1</sup> ) of solvation for Ag <sup>+</sup> in [C <sub>4</sub> mim][Tf <sub>2</sub> N] and [C <sub>4</sub> mim][BF <sub>4</sub> ] transfer from water to the RTILs obtained from the plots in <b>Fig. 6.14</b> .....	156

## Appendix A: *Ab initio* generation of Ag<sup>+</sup>-H<sub>2</sub>O interaction potential

<b>Table A.1.</b> Calculated CHelpG charges for water oxygen and hydrogen atoms obtained at different levels of theory compared with charges from the SPC/E water model.....	165
<b>Table A.2.</b> Fitted parameters for the Ag-H <sub>2</sub> O 4-6-8-12 interaction potential.....	167

## Appendix B: Zn<sup>2+</sup> ion in [C<sub>2</sub>mim][Tf<sub>2</sub>N]: adding explicit polarizability

<b>Table B.1.</b> MD results of first solvation sphere structure for Zn <sup>2+</sup> in [C <sub>2</sub> mim][Tf <sub>2</sub> N] obtained by representing the RTIL with CL&P polarizable force field <sup>5</sup> and the Zn-RTIL interaction with parameters from the <i>ab initio</i> fitting procedure (LJ potential) and from those adapted from Borodin <i>et al.</i> <sup>28</sup> (Buckingham potential).....	177
--	-----

# List of abbreviations

(Alphabetical order)

<b>AIMD</b>	<i>Ab initio</i> molecular dynamics
<b>AN</b>	Acetonitrile
<b>BAR</b>	Bennett Acceptance Ratio
<b>BASIL</b>	Biphasic Acid Scavenging utilizing Ionic Liquids
<b>BOMD</b>	Born-Oppenheimer molecular dynamics
<b>CDF(s)</b>	Combined distribution function(s)
<b>CL&amp;P</b>	Canongia Lopes and Padua force field
<b>CMPO</b>	Diisobutylcarbamoylmethyl phosphine oxide
<b>CN(s)</b>	Coordination number(s)
<b>COM</b>	Center of mass
<b>CPMD</b>	Car-Parrinello molecular dynamics
<b>DFT</b>	Density functional theory
<b>DMSO</b>	Dimethyl sulfoxide
<b>EAN</b>	Ethylammonium nitrate
<b>EXAFS</b>	Extended X-ray absorption fine structure
<b>FEP</b>	Free energy perturbation
<b>FSA</b>	Bis(fluorosulfonyl)imide
<b>GGA</b>	Generalized gradient approximation
<b>HL</b>	Hedin-Lundqvist
<b>Htta</b>	Thenoyltrifluoroacetone
<b>IL(s)</b>	Ionic liquid(s)
<b>KPL</b>	Ludwig <i>et al.</i> force field
<b>LJ</b>	Lennard-Jones
<b>MC</b>	Monte Carlo
<b>MD</b>	Molecular dynamics
<b>MP</b>	Müller-Plathe <i>et al.</i> force field
<b>MS</b>	Multiple-scattering
<b>MSRD</b>	Mean square relative displacement

<b>NPT</b>	Isothermal–isobaric ensemble
<b>NVE</b>	Microcanonical ensemble
<b>NVT</b>	Canonical ensemble
<b>pbc</b>	Periodic boundary conditions
<b>PES</b>	Potential energy surface
<b>PIM</b>	Polarizable ion model
<b>PME</b>	Particle Mesh Ewald
<b>PMF</b>	Potential of mean force
<b>QM/MM</b>	Quantum Mechanical/Molecular Mechanics
<b>RTIL(s)</b>	Room temperature ionic liquid(s)
<b>sd</b>	Stochastic dynamics
<b>SDF(s)</b>	Spatial distribution function(s)
<b>SK</b>	Stote and Karplus Lennard-Jones parameters
<b>SLM(s)</b>	Supported liquid membrane(s)
<b>SS</b>	Single-scattering
<b>TBP</b>	Tri-n-butylphosphate
<b>TI</b>	Thermodynamic integration
<b>TODGA</b>	N,N,N',N'-tetraoctylglycolamide
<b>TRES</b>	Time-Resolved Emission Spectroscopy
<b>TSIL(s)</b>	Task specific ionic liquid(s)
<b>vdW</b>	van der Waals
<b>VOC(s)</b>	Volatile organic compound(s)
<b>WHAM</b>	Weighted Histogram Analysis Method
<b>XANES</b>	X-ray absorption near edge structure
<b>XAS</b>	X-ray absorption spectroscopy

**Notes for the reader:** in mathematical notation, vectors are indicated in **bold**. For sake of clarity, differentiation is sometimes expressed with Leibniz's notation (*i.e.*  $\frac{df}{dx}$ ), Lagrange's notation (*i.e.*  $f'(x) = \frac{df}{dx}$ ) or Newton's notation (*i.e.*  $\dot{f} = \frac{df}{dt}$ ), where indicated explicitly. For partial derivatives, the  $d$  operator is replaced with  $\partial$ .



# Chapter 1

## Introduction

### 1.1 Ionic liquids: historical remarks

Ionic liquids (ILs) are salts made by an organic cation and an organic or inorganic anion, which are liquid below 100 °C.<sup>1-3</sup> Among them, room temperature ionic liquids (RTILs) are melt at 25 °C. Even though they are often referred as a new class of solvents, their origin goes back to 1914, when ethylammonium nitrate (EAN) was reported as a molten salt at room temperature.<sup>4</sup> Strangely, this discover did not brought to much interest about these compounds, at least until more recent times, as at the end of the 90s when new attention was provoked owing to the synthesis of new air- and water-stable ILs.<sup>5,6</sup> This led to a growth in the number of publications that lasts since nowadays (**Fig. 1.1**). ILs have attracted much attention owing to some unique properties they usually display, such as negligible volatility, non-flammability, high thermal and electrochemical stabilities and a supposed low toxicity.<sup>7</sup> These characteristics make ILs much safer and environmentally sustainable than conventional solvents that are usually employed in numerous applications. In particular, the substitution of organic solvents (VOC, volatile organic compounds) which are often toxic, flammable and highly volatile, is highly desirable. In addition, being composed by ions, ILs display high conductivity and a good solvation ability for both neutral and charged species. Specific cations and anions can also be synthetized to achieve desired physical-chemical properties and task specific ionic liquids (TSILs) can be designed for particular applications,<sup>8</sup> making the number of potentially available ILs almost infinite.

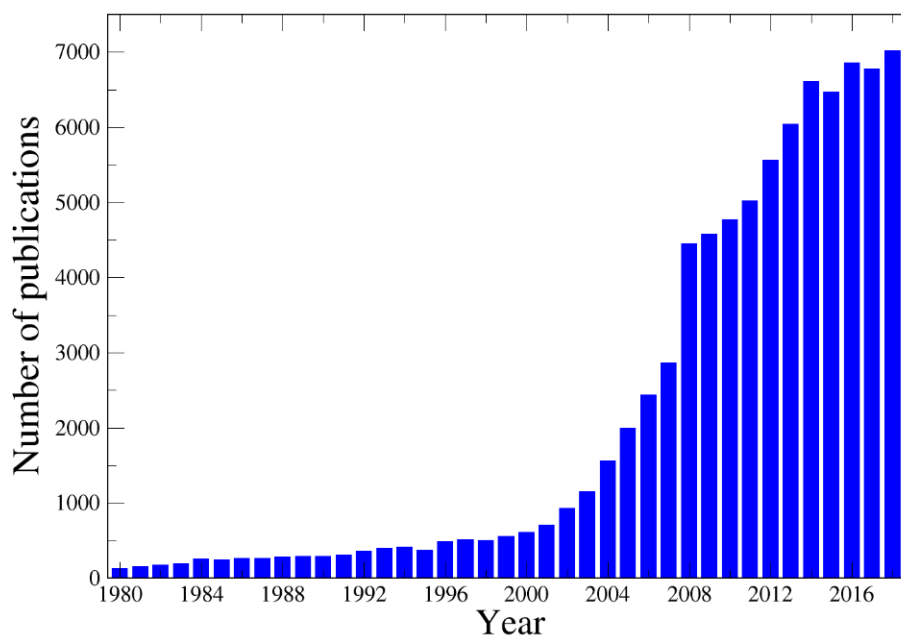


**Figure 1.1.** Number of publications per year as found in Scopus by typing “ionic liquids” as keyword.

## 1.2 Ionic liquids: some chemical-physical properties

The low melting points of these salts seem to be caused by the high molecular weights and delocalized charges of the relative cations and anions, the first consisting usually in large organic species such as imidazolium, pyridinium, pyrrolidinium, quaternary ammonium or phosphonium among the most common ones (**Fig. 1.2**).<sup>9–12</sup> Their melting point is governed by the cation-cation, cation-anion, anion-anion van der Waals (vdW) and electrostatic interactions, therefore depending strictly on their structural features. For example, taking into account the 1-alkyl-3-methylimidazolium ( $[C_n\text{mim}]^+$ ) series, we can observe that small and high symmetric cations like 1-methyl-3-methylimidazolium ( $[C_1\text{mim}]^+$ ) provide ILs with high melting points, which are lowered with increasing the alkyl chain length.<sup>13</sup> This is true only up to a certain extent, while starting from  $n = 9, 10$  the melting point tends to increase with increasing the alkyl chain length due to the attractive forces between these substituents (**Tab. 1.1**). As regards the anionic counterpart, it can consist in inorganic species like  $\text{Cl}^-$ ,  $\text{Br}^-$ ,  $\text{NO}_3^-$  or bigger anions such as tetrafluoroborate ( $[\text{BF}_4]^-$ ), hexafluorophosphate ( $[\text{PF}_6]^-$ ) and bis(trifluoromethylsulfonyl)imide ( $[\text{Tf}_2\text{N}]^-$ ) among the most employed (**Fig. 1.2**). The general trend is that the smaller is the anion, the higher the melting point, since larger anions should display weaker electrostatic interactions with the IL cation. Interestingly,  $[\text{PF}_6]^-$  represents an exception to this series, which has been attributed to the formation of strong hydrogen bonds between fluorine atoms and the cation hydrogen atoms.<sup>13</sup>

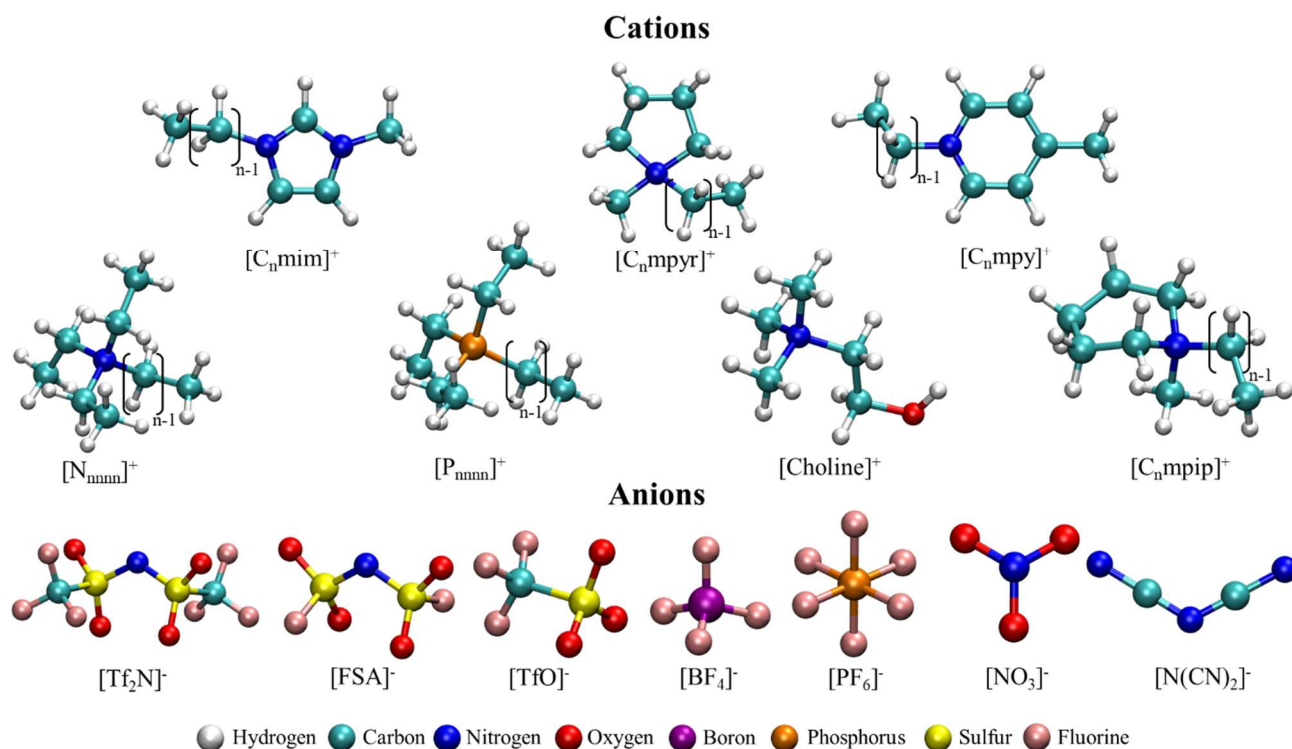


**Figure 1.2.** Schematic representation of some common ILs anions and cations with the relative nomenclature employed in this work. Cations:  $[C_n\text{mim}]^+$  = 1-alkyl-3-methylimidazolium,  $[C_n\text{mpyr}]^+$  = 1-alkyl-1-methylpyrrolidinium,  $[C_n\text{mpy}]^+$  = 1-alkyl-4-methylpyridinium,  $[N_{nnnn}]^+$  = tetraalkylammonium,  $[P_{nnnn}]^+$  = tetraalkylphosphonium,  $[\text{Choline}]^+$  = (2-hydroxyethyl)trimethylammonium,  $[C_n\text{mpip}]^+$  = 1-alkyl-1-methylpiperidinium. Anions:  $[\text{Tf}_2\text{N}]^-$  = bis(trifluoromethylsulfonyl)imide,  $[\text{FSA}]^-$  = bis(fluorosulfonyl)imide,  $[\text{TfO}]^-$  = trifluoromethanesulfonate or triflate,  $[\text{BF}_4]^-$  = tetrafluoroborate,  $[\text{PF}_6]^-$  = hexafluorophosphate,  $[\text{NO}_3]^-$  = nitrate,  $[\text{N}(\text{CN})_2]^-$  = dicyanamide. For  $[N_{nnnn}]^+$  and  $[P_{nnnn}]^+$ , the four  $n$  values may be different among each other.

Another characteristic that strictly depends on the nature of the ions is the usually high density of ILs, which is higher than water for almost all of them.<sup>13</sup> An exception is given by tetraalkylammonium ILs with inorganic anions such as chloride or nitrate, which show densities smaller than  $1 \text{ g cm}^{-3}$ . In particular, small cations and anions exhibit lower steric hindrance and higher “packing” abilities, bringing to higher densities. For the same reason, the smaller is the substituent on the cation (*e.g.* the shorter the alkyl chain), the higher is the density (**Tab. 1.1**).

The viscosities are generally higher than those of organic solvents of 1 – 3 orders of magnitude (**Tab. 1.1**).<sup>14</sup> Usually, viscosity displays the opposite trend of density, due to the increase in vdW interactions causing a higher friction between the alkyl chains following their increase in length.

Hydrogen bonding is another factor influencing viscosity, thus fluorination of the ions usually provides more viscous ILs.

**Table 1.1.** Melting points (K), densities ( $\rho$ , g cm<sup>-3</sup>, 298.15 K) and viscosities ( $\eta$ , cP, 298.15 K) of ILs carrying the 1-alkyl-3-methylimidazolium cation [C<sub>n</sub>mim]<sup>+</sup> (n = 1 – 18) within the [Tf<sub>2</sub>N]<sup>-</sup> and [BF<sub>4</sub>]<sup>-</sup> anions. Data from ref.<sup>13</sup> and references therein except when indicated differently.

Cation	[Tf <sub>2</sub> N] <sup>-</sup>			[BF <sub>4</sub> ] <sup>-</sup>		
	MP	$\rho$	$\eta$	MP	$\rho$	$\eta$
[C <sub>1</sub> mim] <sup>+</sup>	295.15	1.559	100	376.55		67
[C <sub>2</sub> mim] <sup>+</sup>	258.15	1.52	28	288.15	1.26	48.8
[C <sub>3</sub> mim] <sup>+</sup>		1.475	42.8 <sup>15</sup>	256.15	1.24	103
[C <sub>4</sub> mim] <sup>+</sup>	269.15	1.43	69	190.65	1.12 – 1.26	180
[C <sub>5</sub> mim] <sup>+</sup>	264.15	1.403	59.1 <sup>15</sup>			158.1 <sup>15</sup>
[C <sub>6</sub> mim] <sup>+</sup>		1.372	87.3*			314
[C <sub>7</sub> mim] <sup>+</sup>	280.15	1.344				
[C <sub>8</sub> mim] <sup>+</sup>	310.15	1.32	119.3*	193.15	1.08	294.3 <sup>16</sup>
[C <sub>9</sub> mim] <sup>+</sup>		1.299				
[C <sub>10</sub> mim] <sup>+</sup>	244.15	1.271	152.8*	268.95	1.04	416*
[C <sub>11</sub> mim] <sup>+</sup>				294.55		
[C <sub>12</sub> mim] <sup>+</sup>	289.85			312.15		
[C <sub>13</sub> mim] <sup>+</sup>				322.25		
[C <sub>14</sub> mim] <sup>+</sup>	307.45			315.55		
[C <sub>16</sub> mim] <sup>+</sup>	315.25			322.75		
[C <sub>18</sub> mim] <sup>+</sup>	317.95			339.95		

\*Data referred to 293.15 K.

The mutual solubility of ILs with water is one of the most important features of these solvents and an easy way to classify them is between *hydrophobic* and *hydrophilic*, depending on their attitude to form two separate phases with an aqueous solution. Differently from the properties discussed above, ILs solubility with water is primarily dependent on the nature of the anion, while a smaller effect is provided by the cation and its substituents. In particular, hydrophobicity is found to increase according to the NO<sub>3</sub><sup>-</sup> < Cl<sup>-</sup> < Br<sup>-</sup> < [BF<sub>4</sub>]<sup>-</sup> < [PF<sub>6</sub>]<sup>-</sup> < [TfO]<sup>-</sup> < [Tf<sub>2</sub>N]<sup>-</sup> trend. As regards the cation, the longer is the alkyl chain length, the higher the hydrophobicity of the IL, as expected.<sup>17-19</sup> It is interesting to note that even the most hydrophobic ILs, such as those from the [C<sub>n</sub>mim][Tf<sub>2</sub>N] family,

present a water solubility ranging from 0.17 to 0.36 in mole fraction for  $n = 2 - 8$ , while ILs solubility in water is much lower, going from  $3.2 \times 10^{-5}$  to  $1.1 \times 10^{-3}$ .<sup>20</sup> It has to be pointed out that, although hydrophobic, these ILs are often *hygroscopic*, and that they tend to accumulate water very easily if left in contact with the moisture of the air.

Thermal decomposition is another fundamental property, which strongly depends on the structure of the ions. The high decomposition temperatures of ILs make them interesting for applications because, differently from many organic solvents, they can be kept at the liquid state above 400 °C. This usually allows reaching high dynamic properties or catalytic activity, as well as to lower their high viscosity. In general, imidazolium cations provide the most stable ILs, while the trend of relative stabilities for the most common anions is  $[\text{PF}_6]^- > [\text{Tf}_2\text{N}]^- > [\text{TfO}]^- > [\text{BF}_4]^- \gg \text{I}^-, \text{Br}^-, \text{Cl}^-$ .<sup>13</sup>

A general comment about the safety of ILs has to be carried out. All the characteristics reported here do not mean that ionic liquids are inherently sustainable and safe solvents. For example, some works have reported that ILs with fluorinated anions such as  $[\text{BF}_4]^-$  and  $[\text{PF}_6]^-$  can undergo hydrolysis and consequent production of hydrofluoric acid if put in contact with high molar fractions of water.<sup>21-24</sup> Differently, the “greenness” of a solvent, if not of a chemical compound, should be always considered in a relative way, *i.e.* with respect to the species which are currently employed in an application and that could be potentially substituted. Another limit that has to be faced to improve the applications is ILs cost, which is usually higher than traditional solvents, as well as the difficulty in obtaining them with high purity levels.<sup>25</sup> However, this should not prevent the continuous research to develop cations and anions that allow to obtain desired ILs characteristics with less and less effort.

### 1.3 Metal ions and ionic liquids

Owing to their unique properties, ILs have been proposed for a variety of applications such as chemical extractions and analysis, electrodepositions, batteries, solar cells, corrosion protection, catalysis and pharmaceutical research.<sup>25-29</sup> Several of these applications involve the presence of dissolved metal ions and/or metal complexes. Usually, to have an efficient application, the metal ion should be completely solvated by the IL, *e.g.* the metal salt needs to be solubilized by the solvent. Sufficient solubility for a wide range of metal salts is an obvious but not trivial prerequisite for applications involving metals in ILs. In addition, depending on the specific case, also high concentrations of the metal could be required.

A typical strategy is that of solubilizing metal salts having the anion in common with the IL. However, some salts have been found to possess very low solubility in several ionic liquids.<sup>30,31</sup> This seems to

be caused by the poor coordinating ability of many common anions like  $[\text{Tf}_2\text{N}]^-$  or  $[\text{PF}_6]^-$ , but also to be very dependent on the considered metal. For example, it has been found that concentrated solutions up to 1 M can be obtained for  $\text{Co}(\text{Tf}_2\text{N})_2$  and  $\text{Ni}(\text{Tf}_2\text{N})_2$  in respectively  $[\text{C}_2\text{mim}][\text{Tf}_2\text{N}]$  and  $[\text{C}_4\text{mim}][\text{Tf}_2\text{N}]$ , while the maximum concentration is 0.4 M for  $\text{AgTf}_2\text{N}$  in  $[\text{C}_4\text{mim}][\text{Tf}_2\text{N}]$  and only 0.06 M for  $\text{AgPF}_6$  in  $[\text{C}_4\text{mim}][\text{PF}_6]$ .<sup>30</sup>

## 1.3.1 Applications

### *1.3.1.1 Electrochemical and energy applications*

Many of the main characteristics of ILs make them suitable candidates for a huge number of energy-related applications. In particular, their wide electrochemical windows coupled with high electrochemical and thermal stabilities can provide ILs that could be considered as ideal electrolytes for batteries, supercapacitors or solar cells. As a counterpart, their high viscosity is what usually limits their employment in this field. For these reasons, many studies have been devoted to the structural, thermodynamic and transport properties of alkali metal ions in ILs to replace the current Li-ion batteries.<sup>32-34</sup> This research topic has been extended also to divalent and trivalent cations which, carrying more than one elementary charge per atom, should be potentially more efficient as energy-storage systems.<sup>35,36</sup> In addition, species like  $\text{Mg}^{2+}$ ,  $\text{Zn}^{2+}$  or  $\text{Al}^{3+}$  are way more abundant and economic, safer and environmental sustainable than lithium,<sup>25</sup> therefore some studies have been devoted to the development of batteries also involving these metal ions.<sup>36-42</sup> In this field, the knowledge of the speciation of the complex formed by the metal ion in the IL solution is somewhat mandatory to understand its influence on ion transport.

In general, a metal ion is coordinated by the IL anions in the “neat and dry” IL. As a consequence, a negative charged complex is usually formed, bringing to a loss in the metal self-diffusion coefficients and a lowering in conductivity. Taking into account that forming these anionic species is detrimental for electrochemical applications, the complexation of alkali-metal ions with ligands of different nature in order to form whether neutral or cationic species has been widely studied. One of the first attempts was the addition of water in the IL electrolyte. In this case, water is expected to coordinate the metal and provoke the release of ILs anions from the first solvation shell, increasing the overall charge of the metal complex.<sup>43</sup> The disadvantage is that the addition of water to the IL is destined to reduce the electrochemical window of the solution. Another effort has been the introduction of neutral ligands with coordinating ability. For example, the complexation of metal ions by crown ethers of

various nature has been widely studied in several ILs both from a structural and thermodynamic point of view.<sup>44–49</sup>

A further attempt to influence the electrolyte properties in this direction has been the introduction of potentially coordinating substituents in the IL cation, *e.g.* alkoxy or cyano functionalities. Also in this case, the cation should be able to coordinate the metal and provide species with an overall positive charge.<sup>50,51</sup> Furthermore, the dilution of the IL with additives such as  $G_n$  glymes of general formula  $\text{CH}_3(\text{OCH}_2\text{CH}_2)_n\text{OCH}_3$  or co-solvents like vinylene or ethylene carbonate has been studied.<sup>52,53</sup>

As regards supercapacitors, here ILs can play a role in particular owing to their electrochemical stability. In fact, significant improvement in the energy density of a capacitor can be obtained by increasing the cell voltage, which is limited by the electrochemical stability of the employed electrolyte.<sup>54</sup> If water is used, the potential cannot go beyond 1 V in the majority of the cases, while with organic solvents like acetonitrile (AN) or propylene carbonate cell voltages of almost 3 V have been reached. With ILs, this limit may be pushed even to higher voltages.<sup>25</sup>

High electrochemical windows make ILs also suitable solvents for metals electrodeposition. For example, it seems possible to obtain metals that cannot be deposited from aqueous solutions due to the limited electrochemical window of water or by organic solvents.<sup>28,55–64</sup> In addition, the low vapor pressure of ILs allows to carry out these deposition processes at high temperature. This should allow direct deposition of water-sensitive metals such as aluminum, as well as many other metals having deposition potentials conflicting with water decomposition. For example, metallic zinc and cobalt have been successfully electrodeposited from  $\text{Zn}^{2+}$  and  $\text{Co}^{2+}$  solutions in RTILs carrying the  $[\text{Tf}_2\text{N}]^-$ ,  $[\text{TfO}]^-$  and  $[\text{BF}_4]^-$  anions,<sup>65–68</sup> while electrodeposition of copper thin films have been obtained from  $[\text{C}_2\text{mim}][\text{Tf}_2\text{N}]$  and  $[\text{C}_2\text{mim}][\text{EtSO}_4]$  (1-ethyl-3-methylimidazolium ethyl sulfate).<sup>58,59</sup>

### 1.3.1.2 Catalysis

ILs have been also turned out to be a unique medium for several organic reactions promoted by transition metal catalysts.<sup>69–72</sup> The general idea is that of having a catalytic reaction followed by spontaneous separation of the products, which should allow their recovery as well as the recycle of the catalyst. This mechanism is often guaranteed by multiphase systems involving both heterogeneous and homogeneous catalysis. In both cases, the IL forms the catalyst-philic phase, while an organic phase should confine most of the reagents and products. Occasionally, an aqueous phase can also be present. In addition, we can distinguish between situations in which the catalyst confined in the IL is catalytically active as itself and those in which a chemical reaction between the IL and the metal complex is required to provide the catalyst. The first case is certainly the most interesting, as the

catalytic species consists in the solvated metal ion, the regeneration of the spent catalyst being simply the dissolution of a new amount of metallic salt in the ionic liquid phase.<sup>72</sup> To this purpose, ILs with inert and weakly coordinating anions that do not compete with the substrate for the coordination to the metal are preferred. A further advantage is that recovery of the metal can be performed by means of electrodeposition at the end of the catalytic process. As an example, the dissolution of  $\text{Zn}(\text{Tf}_2\text{N})_2$  and  $\text{Co}(\text{Tf}_2\text{N})_2$  in  $[\text{C}_4\text{mim}][\text{Tf}_2\text{N}]$  has turned out to provide a solution with a high catalytic activity for the acylation of chloro- and fluorobenzene.<sup>72</sup> Cobalt(II) phthalocyanine in  $[\text{C}_4\text{mim}][\text{Br}]$  also showed excellent yields and high recycling capabilities for the aerobic oxidation of alkyl arenes and alcohols.<sup>73</sup>

Currently, the most important industrial application employing catalysis with ILs is probably the BASIL<sup>TM</sup> (Biphasic Acid Scavenging utilizing Ionic Liquids) process by BASF for the synthesis of alkoxyphenyl phosphines.<sup>74</sup>

### 1.3.1.3 Chemical separations

One of the applications that promoted the largest number of works about ILs is certainly their employment as receiving phase for the separation of metal ions from aqueous solutions (*e.g.* wastewaters), allowing the recovery of critical metals of economic or environmental interest.<sup>17,75–84</sup> In this case, the employment of non-toxic, non-volatile and non-flammable ILs is particularly desirable since traditional extractions are usually performed by means of toxic, highly volatile and flammable organic solvents. In addition, the recovery of the metal confined in the IL phase by electrodeposition at the end of the extraction procedure is a key advantage.

Many methods can be applied, depending on the nature of the IL. For example, hydrophobic ionic liquids allow the formation of biphasic systems with water. In these liquid-liquid extractions, the ideal line-up should imply the initial presence of the metal in the aqueous solution, distributing in the IL phase either in presence of auxiliary extracting agents or not. In the first case, the actual species that goes in the hydrophobic phase is the complex formed between the metal ion and the extracting ligands, the IL anions and/or water. In the latter, the extracted metal can be coordinated only by the molecules of the two solvents and/or by the counterions. Differently, in case the IL is soluble with water, different systems have to be employed to confine the extracting phase. For example, “supported liquid membranes” (SLMs) can be interposed by the two liquids, these membranes often consisting in porous polymeric materials impregnated with the extracting agent.<sup>82</sup>

As regards the extraction mechanism, it can be classified according to the charge of the transferred metal complex: if positive, we are in front of a cation-exchange mechanism; if negative, anion-

exchange has occurred. The neutral mechanism is actually identical to that of extractions with traditional molecular solvents.

The first application of an IL in metal extraction dates back to 1999, when Dai *et al.* presented the results for the separation of  $\text{Sr}^{2+}$  by means of the dicyclohexyl-18-crown-6 (DCH18C6) crown ether in ILs carrying  $[\text{Tf}_2\text{N}]^-$  and  $[\text{PF}_6]^-$  anions within various  $[\text{C}_n\text{mim}]^+$  cations.<sup>85</sup> In general, the efficiency of an extraction procedure seems to be strictly related to the considered system, depending on the metal ion, the nature of the IL and of the extracting agents, if present. For example, some authors have found that  $\text{Zn}^{2+}$  and  $\text{Cd}^{2+}$  are selectively extracted from  $\text{Zn}^{2+}/\text{Fe}^{2+}$  and  $\text{Cd}^{2+}/\text{Fe}^{2+}$  mixtures, respectively, by the  $[\text{C}_4\text{mim}][\text{BF}_4]$  and  $[\text{C}_8\text{mim}][\text{BF}_4]$  RTILs.<sup>84,86</sup> By changing the anion and employing  $[\text{C}_4\text{mim}][\text{Tf}_2\text{N}]$  and  $[\text{C}_8\text{mim}][\text{Tf}_2\text{N}]$ , the same authors found that  $\text{Cd}^{2+}$  and  $\text{Fe}^{2+}$  are selectively extracted from respectively  $\text{Cd}^{2+}/\text{Zn}^{2+}$  and  $\text{Fe}^{2+}/\text{Zn}^{2+}$  mixtures. In addition, the separation of  $\text{Cu}^{2+}$  and  $\text{Zn}^{2+}$  by means of  $[\text{C}_8\text{mim}][\text{BF}_4]$  and  $[\text{C}_{10}\text{mim}][\text{BF}_4]$  gave poor results according to other authors, but the efficiency of extraction for  $\text{Zn}^{2+}$  seemed to increase with addition of chlorides, indicating that the transfer of an anionic complex was somewhat more favored.<sup>87</sup> The addition of auxiliary ligands seems therefore to increase the extraction, in particular if the IL possess weakly-coordinating anions, as was found for the addition of thenoyltrifluoroacetone (Htta) to  $[\text{C}_n\text{mim}][\text{Tf}_2\text{N}]$  ( $n = 4, 6, 8$ ), resulting in high extraction rates for  $\text{Cu}^{2+}$ ,  $\text{Co}^{2+}$ ,  $\text{Ni}^{2+}$ ,  $\text{Zn}^{2+}$  and  $\text{Cd}^{2+}$ .<sup>88</sup>  $[\text{C}_8\text{mim}][\text{BF}_4]$  has been found to efficiently extract  $\text{Hg}^{2+}$ , while in the same conditions the separation of  $\text{Ni}^{2+}$ ,  $\text{Zn}^{2+}$  and  $\text{Pb}^{2+}$  was found to be poor.<sup>89</sup> The extraction of  $\text{Ag}^+$  and  $\text{Pb}^{2+}$  was way more efficient with  $[\text{C}_n\text{eim}][\text{Tf}_2\text{N}]$  ( $n = 2, 4, 6$ , 1-alkyl-3-ethylimidazolium bis(trifluoromethylsulfonyl)imide) than the traditional process with chloroform, on the contrary of the correspondent RTILs carrying the  $[\text{PF}_6]^-$  anion.<sup>76</sup> Differently,  $\text{Ag}^+$  was found to be the only species extracted by  $[\text{C}_n\text{mim}][\text{PF}_6]$  ( $n = 2, 4, 6$ ) with the addition of a pyridinocalix-[4]arene in a mixture containing also  $\text{Cu}^{2+}$ ,  $\text{Co}^{2+}$ ,  $\text{Ni}^{2+}$  and  $\text{Zn}^{2+}$ .<sup>90</sup> The suitability of RTILs as receiving phase for the separation of rare-earth metals from aqueous solutions has also been demonstrated in many works.<sup>75,77,91,92</sup> The most employed extractants for lanthanides are  $\beta$ -diketones, dialkylphosphoric and dialkylphosphinic acids, diisobutylcarbamoylmethyl phosphine oxide (CMPO), tri-*n*-butylphosphate (TBP) and N,N,N',N'-tetraoctylglycolamide (TODGA).<sup>91,93,94</sup> Nakashima *et al.* found that many lanthanides nitrates were extracted to  $[\text{C}_4\text{mim}][\text{PF}_6]$  in presence of CMPO without the addition of further anionic species, differently from other molecular solvents where high concentration of nitric acid is required.<sup>75</sup> Lanthanide ions resulted to be efficiently extracted also by means of  $[\text{C}_4\text{mim}][\text{Tf}_2\text{N}]$  with the addition of Htta.<sup>95</sup> In this case, metals were extracted as the  $[\text{Ln}(\text{tta})_4]^-$  anionic species with no presence of coordinating water molecules, differently to what was found for the extraction with traditional organic solvents. On the other hand, extraction of the uranyl cation  $[\text{UO}_2]^{2+}$ ,  $\text{Am}^{3+}$ ,  $\text{Nd}^{3+}$  and  $\text{Eu}^{3+}$  from water

to hydrophobic  $[\text{C}_{12}\text{mim}][\text{Tf}_2\text{N}]$  showed that metals were transferred as the same species as found in the traditional extraction with dodecane.<sup>96</sup> The same observation has been pointed out for uranyl extraction to  $[\text{C}_4\text{mim}][\text{PF}_6]$  by means of TBP.<sup>93</sup> However, the situation is different for  $[\text{C}_4\text{mim}][\text{Tf}_2\text{N}]$  and  $[\text{C}_8\text{mim}][\text{Tf}_2\text{N}]$  with CMPO, where the cationic species  $[\text{UO}_2(\text{NO}_3)(\text{CMPO})]^+$  is extracted, differently from extraction to dodecane where the neutral  $[\text{UO}_2(\text{NO}_3)_2(\text{CMPO})_2]$  complex was found.<sup>97</sup> This situation is probably due to the shorter alkyl chain length in the last two cases with respect to  $[\text{C}_{12}\text{mim}][\text{Tf}_2\text{N}]$ , which gives to the RTIL an hydrophobicity similar to dodecane.

The structure of the IL cation and anion seems therefore to have a crucial influence on the extraction efficiency. This should derive from the level of hydrophobicity of the IL and from its effect on the extraction mechanism. In fact, it has been found that an hydrophobic IL cation tends to suppress a cationic-exchange mechanism, while increase in the hydrophobicity of the anion suppresses the anionic-exchange.<sup>98</sup> For example, studies on  $\text{Sr}^{2+}$  extraction with a series of  $[\text{C}_n\text{mim}][\text{Tf}_2\text{N}]$  RTILs demonstrated that the mechanism is fully cation-exchange for  $n = 5 - 6$ , but neutral extraction starts increasing for  $n = 9$  and becomes dominant for  $n = 10$ .<sup>99,100</sup> In addition, the decrease of the cation-exchange mechanism seems to be followed by a general decrease in the extraction efficiency.<sup>98</sup> For example, extraction of  $\text{Ag}^+$  and  $\text{Pb}^{2+}$  to  $[\text{C}_n\text{mim}][\text{Tf}_2\text{N}]$  and  $[\text{C}_n\text{mim}][\text{PF}_6]$  ( $n = 2 - 6$ ) showed that the increase in the alkyl chain length of the imidazolium cation from ethyl- to hexyl- decreased the efficiency of the extraction.<sup>76</sup> The same tendency, *i.e.* neutral-exchange and low extraction for longer alkyl chains of the imidazolium cation, has been observed for the extraction of several alkali metal ions and uranium.<sup>101–103</sup>

### 1.3.2 Structural properties of metal ions in ILs

The knowledge of a metal ion coordination in solution is a fundamental quantity that needs to be known to design an efficient application. If we consider the case of a “neat and dry” IL where only the IL anions and occasionally cations (depending on their functionalization) can coordinate the metal, this turns into knowing the number of ligands set in the first solvation shell as well as their binding mode (mono-, bi-, tridentate etc.). The whole of these data gives access to the total coordination number (CN), *i.e.* the number of atoms coordinating the metal. The former information is somewhat more important for the applications, as was already underlined that the nature of the negatively charged species formed by a metal ion in an IL is directly related to its transference number and has a crucial influence on the working of electrochemical devices. In addition, the nature of the formed species is also important to understand the efficiency of an extraction mechanism as well as for catalytic processes.

### 1.3.2.1 Alkali and alkali-earth metal ions

As previously reported, a huge number of publications has been devoted to the solvation of alkali and alkali-earth metal ions in ILs owing to their extended number of applications in electrochemical devices. Among them,  $\text{Li}^+$  is certainly the ion that inspired the largest number of works.<sup>25,28</sup> A particular effort has been dedicated to the study of  $\text{Li}^+$  in RTILs carrying the  $[\text{Tf}_2\text{N}]^-$  anion, giving the potential advantages of this class of ionic liquids as electrolytes.<sup>28</sup> The largest part of these works agrees in depicting  $\text{Li}^+$  as tetrahedrally coordinated in these ILs. However, taking into account that  $[\text{Tf}_2\text{N}]^-$  can act both as mono- and bidentate ligand, this does not give access to the full knowledge of the species formed in solution, nor to its total charge, which is even more important for the applications. In case of a tetrahedral coordination, the problem to address is to understand whether the existence of the  $[\text{M}(\text{Tf}_2\text{N})_2]^-$ ,  $[\text{M}(\text{Tf}_2\text{N})_3]^{2-}$  or  $[\text{M}(\text{Tf}_2\text{N})_4]^{3-}$  ( $\text{M} = \text{metal}$ ) complex (**Fig. 1.3**) occurs in solution, the first involving two bidentate, the second one bidentate and two monodentate, and the latter four monodentate  $[\text{Tf}_2\text{N}]^-$ . Given its small atomic number and the impossibility to employ useful methods such as X-ray absorption spectroscopy (XAS) or neutron diffraction to study its local environment in solution, a large amount of works studying  $\text{Li}^+$  in ILs by means of IR and Raman spectroscopies have been published so far.<sup>34</sup> The diagnostic vibration to understand  $[\text{Tf}_2\text{N}]^-$  coordination has been identified with the band arising from the overlapping of the  $\delta_3(\text{CF}_3)$  bending and the  $\nu_s(\text{SNS})$  stretching, corresponding to a whole expansion and contraction of the anion which has often been referred as  $[\text{Tf}_2\text{N}]^-$  “breathing mode”.<sup>34</sup> When present at  $\sim 740 \text{ cm}^{-1}$ , this band is related to the “free” uncoordinated  $[\text{Tf}_2\text{N}]^-$ , while it is shifted to higher wavenumbers when contact ion-pairs are formed. The ratio of these relative peaks areas could therefore provide the number of anions coordinating the metal. No general agreement seems to be present in literature about the number of anions coordinating  $\text{Li}^+$ , some pointing out the presence of two, three or four  $[\text{Tf}_2\text{N}]^-$  anions binding the metal. However, the majority of these authors seems to support the formation of the  $[\text{Li}(\text{Tf}_2\text{N})_2]^-$  species where the metal is coordinated by two bidentate  $[\text{Tf}_2\text{N}]^-$ .<sup>52,53,104–106</sup>

Another issue that has been faced in different works is the conformational isomerism of coordinating  $[\text{Tf}_2\text{N}]^-$ , *i.e.* the presence in the first solvation shell of anions displaying *cis* or *trans*  $-\text{CF}_3$  groups with respect to the S-N-S plane.<sup>52,104</sup> Considering the  $[\text{M}(\text{Tf}_2\text{N})_2]^-$  cluster, three species are possible, namely  $[\text{M}(\textit{cis}\text{-Tf}_2\text{N})_2]^-$  (**Fig. 1.3 A**),  $[\text{M}(\textit{cis}\text{-Tf}_2\text{N})(\textit{trans}\text{-Tf}_2\text{N})]^-$  (**Fig. 1.3 B**), and  $[\text{M}(\textit{trans}\text{-Tf}_2\text{N})_2]^-$  (**Fig. 1.3 C**). According to different authors, the  $250 - 500 \text{ cm}^{-1}$  frequency range of the Raman spectrum can provide information about this conformational distribution.<sup>107–109</sup> Taking into account that the *trans* isomer is largely preferred in neat  $\text{Tf}_2\text{N}$ -based ILs,<sup>107,109–111</sup> changes in this region of

the spectrum upon dissolution of the metal salt should suggest coordination of this anion in the *cis* form.

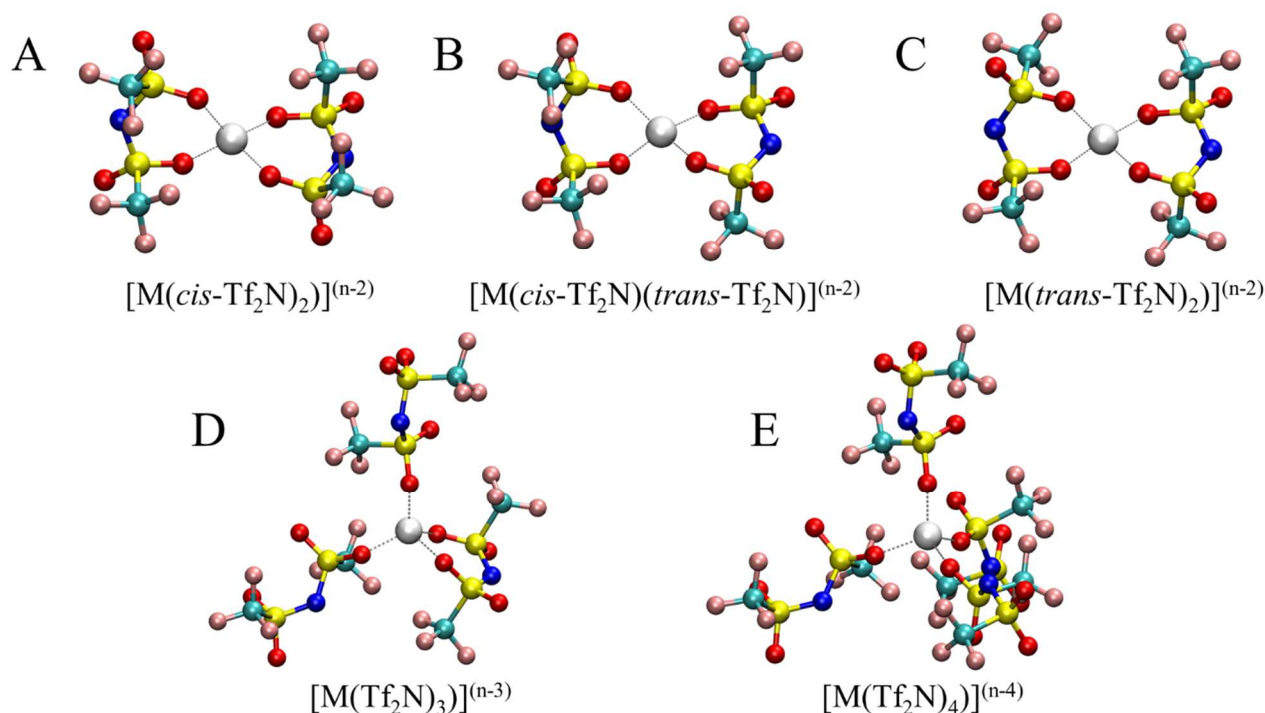


**Figure 1.3.** Possible coordinations of the  $[\text{Tf}_2\text{N}]^-$  anion in a tetrahedral ligand field towards a generic  $\text{M}^{n+}$  metal ion. The case of a two-fold coordination involving two *cis* (A), one *cis* and one *trans* (B) and two *trans* isomers (C) of  $[\text{Tf}_2\text{N}]^-$  are showed. In case of three- (D) and four-fold (E) coordinations, only species with *trans* isomers are reported.

Besides  $[\text{Tf}_2\text{N}]^-$ , other anions have been studied to overcome some technical problems in batteries and reach better performances as electrolytes for  $\text{Li}^+$ .<sup>112,113</sup> Given its smaller size and lower anion-cation binding energies that should favor the metal transport number,<sup>114</sup> a good candidate seems to be the  $[\text{FSA}]^-$  anion, where  $-\text{CF}_3$  groups of  $[\text{Tf}_2\text{N}]^-$  are substituted by fluorine atoms. In this case, IR and Raman spectroscopies works seem to agree in assigning a higher number of anions in the metal first solvation shell with respect to  $[\text{Tf}_2\text{N}]^-$  coordination and thus a preference for the  $[\text{Li}(\text{FSA})_3]^{2-}$  species, at least in equilibrium with  $[\text{Li}(\text{FSA})_2]^-$ .<sup>115–117</sup> As regards fluorine-donor anions, experimental data on  $\text{Li}^+$  coordination are quite scarce. However, according to classical and *ab initio* molecular dynamics (MD and AIMD) simulations,  $\text{Li}^+$  results to be coordinated by four  $[\text{BF}_4]^-$  anions in a tetrahedral geometry in  $[\text{C}_2\text{mim}][\text{BF}_4]$ ,<sup>116</sup> while MD simulations performed by other authors<sup>118</sup> pointed out that 3.3  $[\text{BF}_4]^-$  and three  $[\text{PF}_6]^-$  anions surround  $\text{Li}^+$  respectively in  $[\text{C}_4\text{mim}][\text{BF}_4]$  and  $[\text{C}_4\text{mim}][\text{PF}_6]$ . A  $^1\text{H-NMR}$  study suggested the formation of the tetrahedral  $[\text{Li}(\text{NO}_3)_4]^{3-}$  species<sup>119</sup>

when  $\text{Li}^+$  is solubilized in EAN and a similar picture has been confirmed by X-ray diffraction measures and MD simulations.<sup>120-122</sup>

Higher CNs are usually displayed by the other alkali metal ions, as it is expectable from the higher ionic radii. For example,  $\text{Na}^+$  seems to be preferentially coordinated as  $[\text{Na}(\text{Tf}_2\text{N})_3]^{2-}$  by  $\text{Tf}_2\text{N}$ -based RTILs, but it is not clear if its CN is five or six and thus how many anions act as mono- or bidentate.<sup>123-125</sup> These experimental findings have been reproduced also by classical MD simulations both with polarizable and non-polarizable models.<sup>126,127</sup> Raman spectroscopy measures on  $\text{KTF}_2\text{N}$  solutions in  $[\text{C}_4\text{mim}][\text{Tf}_2\text{N}]$  suggested that  $\text{K}^+$  is coordinated in an octahedral environment by three  $[\text{Tf}_2\text{N}]^-$  bidentate anions similarly to the structure proposed for  $\text{Na}^+$ , while even a higher number of anions (3.9) surrounding the metal resulted for  $\text{Cs}^+$  in the same RTIL.<sup>123</sup>

As regards alkali-earth metals,  $\text{Mg}^{2+}$  has almost the same ionic radius of  $\text{Li}^+$  ( $0.65 \text{ \AA}$  vs.  $0.60 \text{ \AA}$ ),<sup>128</sup> but being a divalent cation it possesses a higher charge-to-size ratio and a different coordination should be expected.<sup>129</sup> In fact, according to Raman spectroscopy measures, the number of  $[\text{Tf}_2\text{N}]^-$  coordinating  $\text{Mg}^{2+}$  in solution stands between three and four and is therefore greater than that generally observed for  $\text{Li}^+$ .<sup>129-131</sup> These structural features have been well reproduced also by means of MD simulations employing a polarizable model.<sup>127</sup> Data about  $\text{Mg}^{2+}$  coordination in RTILs with other anions are quite scarce. In a MD work about  $[\text{C}_4\text{mim}][\text{PF}_6]$  and EAN,  $\text{Mg}^{2+}$  resulted coordinated still in an octahedral fashion and the average number of anions in the first solvation shell is comprised between three and four for  $[\text{PF}_6]^-$  (one bidentate and the remaining monodentate) and between four and five for  $\text{NO}_3^-$ , which showed no bidentate coordination.<sup>35</sup> In the same work, it has been found that the number of  $[\text{PF}_6]^-$  anions in  $\text{Ca}^{2+}$  first solvation shell still stands between three and four. In addition,  $\text{Ca}^{2+}$  in EAN resulted coordinated by 4 - 5  $\text{NO}_3^-$  anions, but bidentate coordination is dominant in this case, probably because of the higher dimensions of this metal ion with respect to  $\text{Mg}^{2+}$ . As expected, even higher CNs have been obtained for  $\text{Sr}^{2+}$ . MD simulations of the  $\text{Sr}^{2+}$  ion in  $[\text{C}_4\text{mim}][\text{PF}_6]$  and  $[\text{C}_2\text{mim}][\text{AlCl}_4]$  reproduced this metal as coordinated by 10.1 fluorine atoms in the first case and 7.4 chlorides in the latter.<sup>132</sup> The number of anions in the metal first solvation sphere resulted to be 5.0 for  $[\text{PF}_6]^-$  and 7.0 for  $[\text{AlCl}_4]^-$ , being the first mostly bidentate and the latter monodentate.

### 1.3.2.2 Transition metal ions

IR and Raman spectroscopies have been employed by many authors also to understand the coordination of transition metal ions in ILs.<sup>34</sup> In particular, a number of  $\sim 3$  coordinating anions in  $\text{Tf}_2\text{N}$ -based RTILs, therefore the octahedral  $[\text{M}(\text{Tf}_2\text{N})_3]^-$  species (**Fig. 1.4**), has been found for  $\text{M} =$

Mn<sup>2+</sup>, Fe<sup>2+</sup>, Co<sup>2+</sup> and Ni<sup>2+</sup> and Zn<sup>2+</sup>.<sup>133,134</sup> In this case, three [Tf<sub>2</sub>N]<sup>-</sup> are supposed to act as bidentate. This coordination has been confirmed also by Bortolini *et al.*,<sup>30,135</sup> who detected [M(Tf<sub>2</sub>N)<sub>3</sub>]<sup>-</sup> (M = Cu<sup>2+</sup>, Co<sup>2+</sup>, Zn<sup>2+</sup>, Ni<sup>2+</sup>) as the only species in [C<sub>4</sub>mim][Tf<sub>2</sub>N] by the analysis of ESI-MS peaks. However, it has to be underlined that in this work<sup>135</sup> the RTIL solutions have been diluted with organic solvents like methanol, acetonitrile and dichloromethane in order to perform the ESI-MS analysis. A slight different approach has been employed by other authors for the Ag<sup>+</sup> ion in [C<sub>2</sub>mim][Tf<sub>2</sub>N].<sup>136</sup> Here IR and Raman spectra were collected on AgTf<sub>2</sub>N solutions for different concentrations of the metal, up to a molar fraction of  $x_{\text{Ag}} = 0.2$ . The dissolution of the metal salt led to spectral modifications that the authors were able to reproduce by means of density functional theory (DFT) simulated spectra. To this purpose, an optimization was performed for an Ag<sup>+</sup> cluster including three [Tf<sub>2</sub>N]<sup>-</sup> anions coordinating in a tetrahedral field, *i.e.* one bidentate and two monodentate, thus for the [Ag(Tf<sub>2</sub>N)<sub>3</sub>]<sup>2-</sup> species. However, it has to be pointed out that theoretical spectra have not been generated for other possible [Tf<sub>2</sub>N]<sup>-</sup> coordination mode in a tetrahedral arrangement (**Fig. 1.3**), that is for the [Ag(Tf<sub>2</sub>N)<sub>2</sub>]<sup>-</sup> (two bidentate) and [Ag(Tf<sub>2</sub>N)<sub>4</sub>]<sup>3-</sup> (four monodentate anions) species. A similar approach has been used also by Pendleton *et al.* for Zn<sup>2+</sup>,<sup>137</sup> finding that the DFT simulated IR spectrum for the [C<sub>2</sub>mim][Zn(Tf<sub>2</sub>N)<sub>3</sub>] cluster well agreed with the experimental collected on a Zn(Tf<sub>2</sub>N)<sub>2</sub> solution in [C<sub>2</sub>mim][Tf<sub>2</sub>N]. Also in this case, the existence of the other possible coordinations involving the [Tf<sub>2</sub>N]<sup>-</sup> anion in an octahedral field (**Fig. 1.4**), *i.e.* [Zn(Tf<sub>2</sub>N)<sub>4</sub>]<sup>2-</sup> (two mono- and two bidentate [Tf<sub>2</sub>N]<sup>-</sup>), [Zn(Tf<sub>2</sub>N)<sub>5</sub>]<sup>3-</sup> (four monodentate and one bidentate) and [Zn(Tf<sub>2</sub>N)<sub>6</sub>]<sup>4-</sup> (six monodentate) has not been verified.

A recent work<sup>138</sup> reported the analysis of EXAFS (extended X-ray absorption fine structure) spectra of 0.03 M Ni(Tf<sub>2</sub>N)<sub>2</sub> solutions in [C<sub>4</sub>mim][Tf<sub>2</sub>N]. In that case, the [Ni(Tf<sub>2</sub>N)<sub>5</sub>]<sup>3-</sup> species with one bidentate and four monodentate anions was supposed, also on the basis of MD simulations. In particular, a first coordination shell made by six oxygen atoms has been found at 2.03 Å from the metal, while a sulfur shell is present at 3.23 Å. This coordination mode was in agreement with solid state data obtained from the crystal of a Co(Tf<sub>2</sub>N)<sub>2</sub> solution in [C<sub>4</sub>mpyr][Tf<sub>2</sub>N], where the octahedral [Co(Tf<sub>2</sub>N)<sub>4</sub>]<sup>2-</sup> unit (with two apical monodentate and two equatorial bidentate anions) was found.<sup>139</sup> Here the Co-S distance for monodentate coordination is 3.19 Å, while for bidentate it is comprised between 3.27 and 3.31 Å. Considering that Co<sup>2+</sup> has a similar ionic radius with respect to Ni<sup>2+</sup> (79 vs. 83 pm)<sup>128</sup> and that a Ni-S(Tf<sub>2</sub>N) average distance of 3.23 Å was obtained, it has been argued that a mixed coordination of [Tf<sub>2</sub>N]<sup>-</sup> towards Ni<sup>2+</sup> should be present in solution. This picture has been reproduced by MD simulations also by other authors, finding that Ni<sup>2+</sup> in [C<sub>4</sub>mim][Tf<sub>2</sub>N] is for the 59.5% surrounded by five [Tf<sub>2</sub>N]<sup>-</sup> anions and for 40.5% by six anions.<sup>140</sup>

An even more synergic approach between EXAFS and MD has been employed by D'Angelo *et al.*<sup>141</sup> for the study of  $Zn^{2+}$  in  $Tf_2N$ -based RTILs carrying different cations, namely  $[C_4mim]^+$ ,  $[N_{1114}]^+$ ,  $[Choline]^+$  and  $[C_8(mim)_2]^{2+}$  (1,8-bis(3-methylimidazolium-1-yl)octane). In this work, a different strategy has been employed to differentiate between mono- and bidentate  $[Tf_2N]^-$  coordination. In particular, the authors observed that the Zn-O-S three-body distribution giving rise to a strong multiple-scattering (MS) signal is characterized by a  $\sim 132^\circ$  angle in case of bidentate coordination, as also showed by the solid state structure of the  $Zn(Tf_2N)_2$  salt.<sup>72</sup> Differently, it assumes a quasi-linear geometry with a  $\sim 180^\circ$  angle in the monodentate case. MD simulations performed by the authors provided the  $[Zn(Tf_2N)_6]^{4-}$  species with monodentate-only coordination and a  $\sim 180^\circ$  Zn-O-S angle. EXAFS theoretical spectra were then calculated for this coordination and resulted to be in excellent agreement with the experimental.

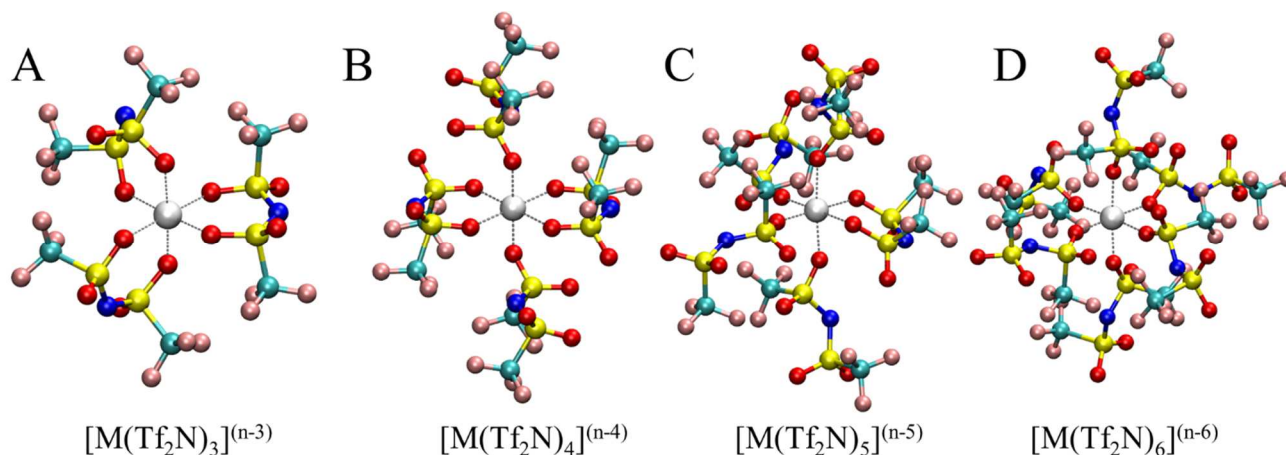


**Figure 1.4.** Possible coordinations of the  $[Tf_2N]^-$  anion in an octahedral ligand field towards a generic  $M^{n+}$  metal ion. *Cis* and *trans*  $[Tf_2N]^-$  isomers are randomly shown.

Different CNs seem to be provided by chloride coordination in RTILs. For example, EXAFS and X-ray photoelectron spectroscopy (XPS) measures on  $Co^{2+}$ ,  $Mn^{2+}$ ,  $Ni^{2+}$ , and  $Zn^{2+}$  solutions in RTILs carrying the  $Cl^-$  anion showed the formation of the  $[MCl_4]^{2-}$  species.<sup>142,143</sup> EXAFS data analysis of  $Cu^{2+}$  solutions in  $[C_6mim][Cl]$  suggested also the formation of  $[CuCl_3]^-$ ,<sup>144</sup> even if according to other authors  $[CuCl_4]^{2-}$  is found to dominate in  $[C_2mim][Cl]$  and  $[Choline][Cl]$ .<sup>145,146</sup> As a consequence, the presence of  $[CuCl_3]^-$  in  $[C_6mim][Cl]$  seems to be caused by the effect of the RTIL cation, suggesting that longer alkyl chains could promote the formation of complexes with a lower charge. A three-fold coordination of  $Cu^{2+}$  has been found also in  $[C_2mim][SCN]$  (1-ethyl-3-methylimidazolium thiocyanate), where two anions bind the metal *via* nitrogen and one *via* sulfur atoms forming the  $[Cu(NCS)_2(SCN)]^-$  species. Interestingly, the  $Cr^{3+}$  ion resulted coordinated by five

thiocyanate anions binding through nitrogen atoms in the same RTIL.<sup>144</sup>  $\text{Cu}^{2+}$  is certainly the metal ion showing the highest multiplicity of CNs in RTILs, due to the well-known Jahn-Teller effect that provokes the elongation of two apical ligands in the ideal octahedron providing CNs ranging from four to six even in water.<sup>147–150</sup> For example, UV-Vis spectra and DFT calculations on  $\text{Cu}(\text{TfO})_2$  solutions in  $[\text{C}_4\text{mim}][\text{TfO}]$  suggested  $\text{Cu}^{2+}$  as four-fold coordinated, forming the square-planar  $[\text{Cu}(\text{TfO})_4]^{2-}$  species.<sup>151</sup>

The coordination of  $[\text{TfO}]^-$  has been studied also for  $\text{Zn}^{2+}$  by means of IR and Raman spectra collected on  $\text{Zn}(\text{TfO})_2$  solutions in  $[\text{C}_2\text{mim}][\text{TfO}]$  and  $[\text{C}_4\text{mpyr}][\text{TfO}]$ .<sup>152</sup> The average number of  $[\text{TfO}]^-$  anions in the first solvation shell of the metal was calculated according to peak areas related to “free” and coordinating  $[\text{TfO}]^-$  and resulted to be 3.8 for  $[\text{C}_2\text{mim}][\text{TfO}]$ , indicating the presence of the  $[\text{Zn}(\text{TfO})_4]^{2-}$  species. Supposing  $\text{Zn}^{2+}$  as octahedrally coordinated, two  $[\text{TfO}]^-$  should bind the metal in a bidentate fashion and two as monodentate. Differently, 4.5 anions coordinating  $\text{Zn}^{2+}$  were found in  $[\text{C}_4\text{mpyr}][\text{TfO}]$ , thus suggesting the presence of an equilibrium between  $[\text{Zn}(\text{TfO})_4]^{2-}$  and  $[\text{Zn}(\text{TfO})_5]^{3-}$ . According to the authors, this is probably due to a weaker interaction between  $[\text{TfO}]^-$  and the  $[\text{C}_4\text{mpyr}]^+$  cation in comparison with  $[\text{C}_2\text{mim}]^+$ . Further insights into the influence of the RTIL cation-anion interaction on the coordination tendencies of the metal have been obtained in a work of the same group, analyzing  $\text{Zn}(\text{TfO})_2$  0.2 M solutions in  $[\text{Hmim}][\text{TfO}]$  ( $\text{Hmim}$  = 1-methylimidazolium),  $[\text{C}_2\text{mim}][\text{TfO}]$  and  $[\text{C}_2\text{C}_1\text{mim}][\text{TfO}]$  ( $[\text{C}_2\text{C}_1\text{mim}]$  = 1-ethyl-2,3-dimethylimidazolium).<sup>153</sup> The Far-IR part of the spectra below  $200\text{ cm}^{-1}$ , revealing the RTILs cation-anion interaction, is shifted to lower wavenumbers by changing the RTIL cation and suggests a  $[\text{Hmim}]^+ > [\text{C}_2\text{mim}]^+ > [\text{C}_2\text{C}_1\text{mim}]^+$  trend for the interaction strength with the RTIL anion. Interestingly, the average number of  $[\text{TfO}]^-$  anions coordinating  $\text{Zn}^{2+}$  has been found to be 3.0 in  $[\text{Hmim}][\text{TfO}]$ , 3.8 in  $[\text{C}_2\text{mim}][\text{TfO}]$  and 5.1 in  $[\text{C}_2\text{C}_1\text{mim}][\text{TfO}]$ , suggesting respectively the presence of the  $[\text{Zn}(\text{TfO})_3]^-$ ,  $[\text{Zn}(\text{TfO})_4]^{2-}$  and  $[\text{Zn}(\text{TfO})_5]^{3-}$  species. This confirms that the stronger is the interaction between the RTIL cation and the anion, the smaller is the “availability” of the anion to coordinate the metal.

### 1.3.2.3 Rare-earth metal ions

Data about solvated lanthanides and actinides metal ions coordination in RTILs are quite scarce in comparison with the studies about the complexation of these metals,<sup>91</sup> the latter having been inspired by the great interest towards the separation processes of these ions by means of auxiliary ligands.

The first solvation sphere structure of  $\text{Eu}^{3+}$  in RTILs carrying the  $[\text{C}_4\text{mim}]^+$  cation within several anions ( $[\text{PF}_6]^-$ ,  $[\text{BF}_4]^-$ ,  $[\text{TfO}]^-$  and  $[\text{Tf}_2\text{N}]^-$ ) has been studied by means of TRES (Time-Resolved Emission Spectroscopy) and EXAFS.<sup>154</sup> The results showed that  $\text{Eu}^{3+}$  is surrounded by ~9 fluorine

atoms at an average distance of  $\sim 2.35$  Å in [C<sub>4</sub>mim][PF<sub>6</sub>] and [C<sub>4</sub>mim][BF<sub>4</sub>], while in [C<sub>4</sub>mim][Tf<sub>2</sub>N] and [C<sub>4</sub>mim][TfO] it resulted coordinated by 9.8 and 11.5 oxygen atoms, respectively, at an average distance of  $\sim 2.42$  Å. Classical MD simulations on the same systems provided results in good agreement with the experimental data.<sup>155</sup> Similar CNs have been found by means of MD simulations for La<sup>3+</sup>, Eu<sup>3+</sup> and Yb<sup>3+</sup> in [C<sub>4</sub>mim][SCN] and [N<sub>4441</sub>][SCN], where the metals resulted to be bound by 6 – 8 N-coordinating ligands.<sup>156</sup> This is in agreement with X-ray structures collected on a crystallized solution of La<sup>3+</sup> from [C<sub>4</sub>mim][SCN] in presence of water, showing the [La(SCN)<sub>7</sub>H<sub>2</sub>O]<sup>4-</sup> unit where thiocyanate coordinates only *via* nitrogen atoms.<sup>157</sup> In addition, absorption spectra for these systems did not show differences between the solid and the liquid states, thus it can be supposed that this coordination is retained even in solution.<sup>156</sup>

As regards the Nd<sup>3+</sup> ion, Raman spectroscopy data for Nd(Tf<sub>2</sub>N)<sub>3</sub> solutions in [P<sub>2225</sub>][Tf<sub>2</sub>N] indicated that the number of anions in the metal first solvation sphere was  $\sim 5$ , compatible with the [Nd(Tf<sub>2</sub>N)<sub>5</sub>]<sup>2-</sup> species.<sup>158</sup>

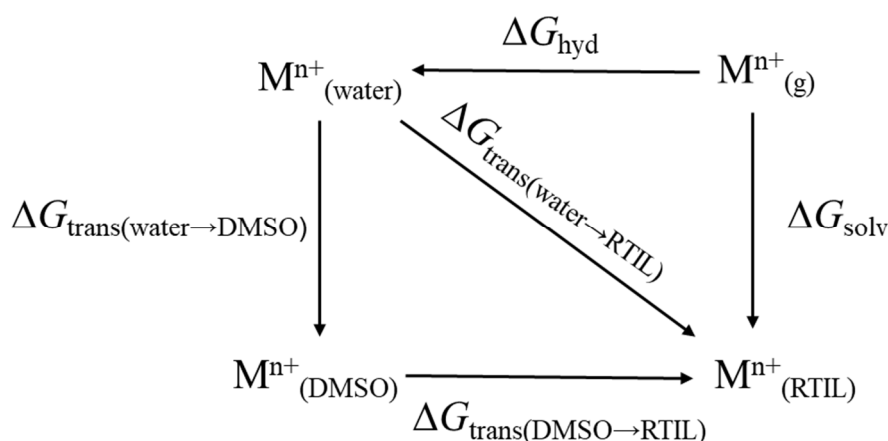
La<sup>3+</sup> and Lu<sup>3+</sup> coordination in EAN has been studied by means of *ab initio* MD simulations.<sup>159</sup> La<sup>3+</sup> resulted to be coordinated by five bidentate NO<sub>3</sub><sup>-</sup> anions, while Lu<sup>3+</sup> by six anions with half of them acting as bidentate and half as monodentate. This is traduced in CNs of 10 for the former metal and 8 for the latter, in agreement with the trend of their ionic radii.

Coordination in EAN has been explored also for Ce<sup>3+</sup> by means of EXAFS data analysis performed on Ce(NO<sub>3</sub>)<sub>3</sub> solutions in combination with MD simulations carried out with both polarizable and non-polarizable methods.<sup>160</sup> The results unambiguously showed that Ce<sup>3+</sup> is coordinated in an icosahedral geometry by three bidentate and six monodentate NO<sub>3</sub><sup>-</sup>, differently from the solid state where six bidentate nitrates are found.<sup>161</sup>

### 1.3.3 Solvation thermodynamics of metal ions in ILs

Free energies, enthalpies and entropies of solvation can provide useful data about single-ion interaction with a given solvent, while transfer parameters can give insights about the relative solvation capability of two different media. Gibbs free energies of transfer from dimethyl sulfoxide (DMSO) to several RTILs ( $\Delta G_{\text{trans}}(\text{DMSO} \rightarrow \text{RTIL})$ ) have been obtained by electrode potentials for Cu<sup>2+</sup>, Zn<sup>2+</sup>, Ag<sup>+</sup> and Cd<sup>2+</sup> by Lewandowski *et al.*<sup>162,163</sup> By employing the experimental hydration free energies<sup>164,165</sup> ( $\Delta G_{\text{hyd}}$ ) and free energies of transfer between water and DMSO ( $\Delta G_{\text{trans}}(\text{water} \rightarrow \text{DMSO})$ ) for these metal ions,<sup>165</sup> it is possible to calculate the free energies of solvation in the RTILs ( $\Delta G_{\text{solv}}$ ) as well as free energies of transfer from water to the RTILs ( $\Delta G_{\text{trans}}(\text{water} \rightarrow \text{RTIL})$ ) according to the thermodynamic cycle showed in **Scheme 1.1**. In particular,

$\Delta G_{\text{trans}}(\text{water} \rightarrow \text{RTIL})$  reflects the spontaneity related to the transfer process of the metal ion from an aqueous solution to the ionic liquid, thus giving useful insights into the capabilities of RTILs as receiving phase for a chemical separation.



**Scheme 1.1.** Schematic representation of the thermodynamic cycle employed in this work for the calculation of the Gibbs free energy of solvation in the RTILs ( $\Delta G_{\text{solv}}$ ) and free energy of transfer from water to the RTILs ( $\Delta G_{\text{trans}}(\text{water} \rightarrow \text{RTIL})$ ) from literature experimental data.<sup>162–165</sup>

The values obtained according to **Scheme 1.1** are reported in **Tab. 1.2** and depict a very different situation depending on the considered metal and ionic liquid. The first observation is that positive  $\Delta G_{\text{trans}}(\text{water} \rightarrow \text{RTIL})$  values are obtained for  $\text{Cu}^{2+}$  and  $\text{Zn}^{2+}$  in  $\text{Tf}_2\text{N}$ -based RTILs, suggesting that these metal ions are more favorably solvated in water than in this class of ionic liquids. A different picture is obtained for  $\text{Ag}^+$ , whose transfer from water to these RTILs is only little unfavorable or even favorable, and the same happens for  $[\text{C}_2\text{mim}][\text{TfO}]$ . Indeed, transfer values towards  $\text{BF}_4$ -based RTILs are always negative, reporting that  $\text{Cu}^{2+}$ ,  $\text{Zn}^{2+}$  and  $\text{Ag}^+$  are much favorably solvated in these solvents than in water and suggesting a higher solvation capability of the  $[\text{BF}_4]^-$  anion in comparison with  $[\text{Tf}_2\text{N}]^-$ . In addition, the transfer of  $\text{Zn}^{2+}$  from water to  $[\text{C}_2\text{mim}][\text{PF}_6]$  results to be unfavorable, even if of a less extent with respect to  $\text{Tf}_2\text{N}$ -based RTILs. Furthermore, the transfer to  $[\text{C}_4\text{mim}][\text{Br}]$  is always largely favorable for all the considered metal ions.

**Table 1.2.** Gibbs free energies of solvation in several RTILs within free energies of transfer from DMSO and water for the Cu<sup>2+</sup>, Zn<sup>2+</sup> and Ag<sup>+</sup> ions at 298 K. Data in kcal mol<sup>-1</sup>.

RTIL	$\Delta G_{\text{trans}}(\text{DMSO} \rightarrow \text{RTIL})$			$\Delta G_{\text{solv}}(\text{g} \rightarrow \text{RTIL})^{\text{a}}$			$\Delta G_{\text{trans}}(\text{water} \rightarrow \text{RTIL})^{\text{b}}$		
	Cu <sup>2+</sup>	Zn <sup>2+</sup>	Ag <sup>+</sup>	Cu <sup>2+</sup>	Zn <sup>2+</sup>	Ag <sup>+</sup>	Cu <sup>2+</sup>	Zn <sup>2+</sup>	Ag <sup>+</sup>
[C <sub>2</sub> mim][Tf <sub>2</sub> N] <sup>162</sup>	18.8	21.4	8.6	-473.6 <sup>§</sup>	-457.1 <sup>§</sup>	-102.2 <sup>§</sup>	6.8	10.2	0.5
				-491.0 <sup>†</sup>	-473.6 <sup>†</sup>	-113.5 <sup>†</sup>			
[C <sub>4</sub> mim][Tf <sub>2</sub> N] <sup>162</sup>	27.8	21.2	3.97	-464.6 <sup>§</sup>	-457.2 <sup>§</sup>	-107.1 <sup>§</sup>	15.8	10.0	-4.4
				-482.0 <sup>†</sup>	-473.7 <sup>†</sup>	-118.4 <sup>†</sup>			
[C <sub>3</sub> mpyr][Tf <sub>2</sub> N]	27.4 <sup>162</sup>	24.8 <sup>162</sup>	12.8 <sup>162</sup>	-464.9 <sup>§</sup>	-453.7 <sup>§</sup>	-109.3 <sup>†</sup>	15.5	13.6	4.7
			11.6 <sup>163</sup>	-482.4 <sup>†</sup>	-470.1 <sup>†</sup>	-99.2 <sup>§</sup>			3.5
						-110.5 <sup>†</sup>			
[C <sub>4</sub> mpyr][Tf <sub>2</sub> N]	25.3 <sup>162</sup>	27.2 <sup>162</sup>	13.1 <sup>162</sup>	-467.0 <sup>§</sup>	-451.3 <sup>§</sup>	-109.0 <sup>†</sup>	13.4	16.0	5.0
			13.5 <sup>163</sup>	-484.5 <sup>†</sup>	-467.8 <sup>†</sup>	-97.3 <sup>§</sup>			5.4
						-108.6 <sup>†</sup>			
[C <sub>2</sub> mim][TfO] <sup>162</sup>			5.9			-105.0 <sup>§</sup>			-2.2
[C <sub>2</sub> mim][BF <sub>4</sub> ]	-12.5 <sup>162</sup>	-7.0 <sup>162</sup>	-8.8 <sup>162</sup>	-504.8 <sup>§</sup>	-485.5 <sup>§</sup>	-119.6 <sup>§</sup>	-24.4	-18.2	-16.8
			1.5 <sup>163</sup>	-522.3 <sup>†</sup>	-502.0 <sup>†</sup>	-130.8 <sup>†</sup>			-16.8
						-109.3 <sup>§</sup>			-6.5
						-120.5 <sup>†</sup>			
[C <sub>4</sub> mim][BF <sub>4</sub> ]	-18.2 <sup>162</sup>	-0.7 <sup>162</sup>	-4.3 <sup>162</sup>	-510.5 <sup>§</sup>	-479.2 <sup>§</sup>	-115.2 <sup>§</sup>	-30.1	-12.0	-12.4
			4.1 <sup>163</sup>	-528.0 <sup>†</sup>	-495.7 <sup>†</sup>	-126.4 <sup>†</sup>			-12.4
						-106.7 <sup>§</sup>			-4.0
						-118.0 <sup>†</sup>			
[C <sub>2</sub> mim][PF <sub>6</sub> ] <sup>162</sup>		14.1			-464.4 <sup>§</sup>			2.9	
									-480.9 <sup>†</sup>
[C <sub>4</sub> mim][Br] <sup>162</sup>	-30.3	-20.3	-17.9	-522.7 <sup>§</sup>	-498.8 <sup>§</sup>	-128.8 <sup>§</sup>	-42.3	-31.5	-26.0
				-540.1 <sup>†</sup>	-515.3 <sup>†</sup>	-140.0 <sup>†</sup>			

<sup>a</sup>Gibbs free energies of solvation calculated according to the thermodynamic cycle reported in **Scheme 1**.

<sup>§</sup> $\Delta G_{\text{solv}}$  calculated by employing  $\Delta G_{\text{hyd}}$  from Marcus<sup>164</sup> or <sup>†</sup>from Ahrlund.<sup>165</sup> In all cases,  $\Delta G_{\text{trans}}(\text{water} \rightarrow \text{DMSO})$  from Ahrlund<sup>165</sup> has been used. <sup>b</sup>Gibbs free energies of transfer from water to the RTILs calculated as  $\Delta G_{\text{trans}}(\text{water} \rightarrow \text{RTIL}) = \Delta G_{\text{solv}}(\text{g} \rightarrow \text{RTIL}) - \Delta G_{\text{hyd}}$ . Note that the choice of the employed  $\Delta G_{\text{hyd}}$  is irrelevant in this case.

### 1.3.4 Complex formation thermodynamics of metal ions in ILs

The coordination of a metal ion by a ligand in solution occurs in competition with the solvent molecules.<sup>166</sup> As a consequence, thermodynamic data about metal ions complexation in ILs can provide useful insights also about the interaction between the metal and the ionic liquid. Several works studying the complexation of various metal in ILs with ligands of different nature have been carried out as inspired by different potential applications. As underlined previously, metal ions complexation with organic ligands is often desirable in electrochemical devices. Alternatively, the wastewaters from which a metal has to be separated can be particularly rich in some anions, often inorganic species such as nitrates or chlorides.<sup>138</sup> Otherwise, ligands can be added to the IL solution as extracting agents to increase the separation rate.

#### 1.3.4.1 Alkali and alkali-earth metal ions

A large amount of works about the formation of  $\text{Li}^+$  complexes in ionic liquids has been certainly inspired by the potential electrochemical applications.<sup>167</sup> For example,  $\text{Li}^+$  complexation with crown ethers was studied by  $^7\text{Li}$ -NMR and it was found that only 1:1 species were formed with 15C5 (1,4,7,10,13-pentaoxacyclopentadecane) and 18C6 (1,4,7,10,13,16-hexaoxacyclooctadecane) in  $[\text{C}_4\text{mim}][\text{Tf}_2\text{N}]$ .<sup>44</sup> Interestingly, complexation with both 15C5 and 18C6 does not occur in water and with 18C6 not even in methanol,<sup>168</sup> indicating that solvation of  $\text{Li}^+$  in these media is strong enough to prevent the coordination of the crown ethers, while 15C5 and 18C6 are able to displace  $[\text{Tf}_2\text{N}]^-$  from  $\text{Li}^+$  first solvation sphere in the RTIL. Complexation with 15C5 in  $[\text{C}_4\text{mim}][\text{Tf}_2\text{N}]$  resulted to be entropy stabilized and showed small negligible enthalpy, on the contrary of what is found in the other molecular solvents.<sup>168</sup> This result was related to the increase in entropy following the release of a flexible ligand such as the  $[\text{Tf}_2\text{N}]^-$  anion from the metal first solvation sphere. Regardless of the anion, the ionic liquid determines a general increase of metal complexes stability relative to the aqueous solution and a unique reaction environment. Also complexation of  $\text{Na}^+$ ,  $\text{K}^+$  and  $\text{Rb}^+$  with DB18C6 (2,3,11,12-dibenzo-1,4,7,10,13,16-hexaoxacyclooctadeca-2,11-diene) and 18C6 in different RTILs showed formation constants higher than in water.<sup>45,46,49</sup>

Many works have been devoted to the complexation of  $\text{Cs}^+$  in ILs, due to the interest in designing new extraction procedures for this metal ion.<sup>167,169-174</sup> For 1:1 complexation with 18C6, formation constants in RTILs carrying the  $[\text{Tf}_2\text{N}]^-$  anion are higher than those with the  $[\text{BF}_4]^-$  or  $[\text{PF}_6]^-$  anions, this picture confirming the poor solvation ability of  $[\text{Tf}_2\text{N}]^-$ . In addition,  $\text{Cs}^+$  1:2 species are formed only in  $\text{Tf}_2\text{N}$ -based RTILs, while they have not been observed in RTILs with other anions. An

interesting fact is that if we assume that  $[\text{Tf}_2\text{N}]^-$  bond with alkali metals is weaker than that of the other RTILs anions, we should expect more negative values for the reaction enthalpy and a more exothermic complexation. However, enthalpy is the most negative in RTILs carrying  $[\text{BF}_4]^-$ ,  $[\text{PF}_6]^-$  and  $[\text{N}(\text{CN}_2)]^-$  anions, while it is only slight negative or even positive for  $\text{Tf}_2\text{N}$ -based RTILs. On the other side, the determining contribution to complexation in  $\text{Tf}_2\text{N}$ -RTILs derives from the entropic term, which results to be positive for complexation in this class of ionic liquids, while it is negative for the other RTILs. As in the case of  $\text{Li}^+$  complexation with 15C5 in  $[\text{C}_4\text{mim}][\text{Tf}_2\text{N}]$ ,<sup>44</sup> this could be reasonably explained by the gain in entropy following the release of the flexible  $[\text{Tf}_2\text{N}]^-$  with respect to  $[\text{BF}_4]^-$ ,  $[\text{PF}_6]^-$  and  $[\text{N}(\text{CN}_2)]^-$ , possessing more rigid structures, overwhelming the enthalpic factor and determining the global favorable free energies.

#### 1.3.4.2 Transition metal-ions

A more intricate picture is obtained when complexation goes beyond the 1:1 or 1:2 steps, as in the case of transition and rare-earth metals. For example,  $\text{Ni}^{2+}$  complexation with nitrate in  $[\text{C}_4\text{mim}][\text{Tf}_2\text{N}]$  has been studied by means of spectroscopic and microcalorimetric titrations.<sup>138</sup> The formation of  $[\text{Ni}(\text{NO}_3)_n]^{2-n}$  species up to  $n = 3$  was found to occur, where the first two complexation steps resulted to be enthalpy driven, while for  $[\text{Ni}(\text{NO}_3)_3]^{2-}$  unfavorable enthalpy together with large and positive entropy were observed.

Chloride complexation with  $\text{Cu}^{2+}$  in  $[\text{C}_4\text{mim}][\text{TfO}]$  has been studied by means of UV-Vis and calorimetric titrations with the support of DFT calculations by Kanzaki *et al.*<sup>151</sup> The results pointed out that a 1:1 ligand exchange occurs between  $\text{Cl}^-$  and  $[\text{TfO}]^-$  until the formation of the final  $[\text{CuCl}_4]^{2-}$  tetrahedral species. The overall process is almost athermal and the driving force of chloro-complexation seems to be once again the desolvation entropy provided by the release of  $[\text{TfO}]^-$  anions from the metal first solvation sphere. In particular, the  $[\text{CuCl}]^+ + \text{Cl}^- \rightarrow [\text{CuCl}_2]$  process was promoted by a large and positive entropic contribution. This trend was reversed in the next step, *i.e.* for the  $[\text{CuCl}_2] + \text{Cl}^- \rightarrow [\text{CuCl}_3]^-$  reaction, where complexation resulted to be enthalpically-driven. This opposite picture suggests that a different coordination structure occurs between these two steps. To this extent, the authors supposed that a lowering of  $\text{Cu}^{2+}$  coordination number may occur in the  $[\text{CuCl}]^+ + \text{Cl}^- \rightarrow [\text{CuCl}_2]$  process, passing from  $[\text{CuCl}(\text{TfO})_3]^+$  to  $[\text{CuCl}_2(\text{TfO})]^-$ . When the species with three chloride anions is formed, the coordination number becomes four again, with the formation of  $[\text{CuCl}_3(\text{TfO})]^{2-}$ . In this complexation step,  $\text{Cl}^-$  anion can enter the first solvation sphere without an enthalpic cost and without entropic gain, since no  $[\text{TfO}]^-$  release occurs, and this should explain the negative enthalpy and very low complexation entropy associated with the formation of  $[\text{CuCl}_3]^-$ .

Stability constants for the complexation of  $\text{Ag}^+$  with cryptand 222 in several RTILs have been also obtained by Lewandowski *et al.*<sup>163,175</sup> and the values are reported in **Tab. 1.3**. Firstly, it has to be noted that complexation in RTILs is in general more favorable than in classical organic solvents such as DMSO and AN.<sup>176</sup> In addition, the obtained trend of  $\log K$  values is in agreement with data reported in **Tab. 1.2** for  $\text{Ag}^+$  solvation. In fact, since both the RTIL anions and cryptand 222 compete to coordinate the metal, the more  $\text{Ag}^+$  is solvated, the less its complexation with the ligand should be favorable. In particular,  $\log K$  values obtained in  $\text{Tf}_2\text{N}$ -based RTILs are more favorable than those in ionic liquids carrying the  $[\text{TfO}]^-$  and  $[\text{BF}_4]^-$  anions and this is in agreement with  $\text{Ag}^+$  more favorable solvation in the latter classes of RTILs than in the former one, as showed by the comparison between  $\Delta G_{\text{solv}}(\text{g} \rightarrow \text{RTIL})$  and  $\Delta G_{\text{trans}}(\text{water} \rightarrow \text{RTIL})$  values (**Tab. 1.2**).

**Table 1.3.** Stability constants for  $\text{Ag}^+$  complexation with cryptand 222 at 298 K in various RTILs.

Solvent	$\log K$	Solvent	$\log K$
$[\text{C}_2\text{mim}][\text{Tf}_2\text{N}]^{163}$	13.6	$[\text{C}_2\text{mim}][\text{TfO}]^{163}$	11.6
$[\text{C}_4\text{mim}][\text{Tf}_2\text{N}]^{163}$	10.0	$[\text{C}_4\text{mim}][\text{TfO}]^{175}$	13.4
$[\text{C}_3\text{mpyr}][\text{Tf}_2\text{N}]^{163}$	15.8	$[\text{C}_2\text{mim}][\text{BF}_4]^{163}$	8.4
$[\text{C}_4\text{mpyr}][\text{Tf}_2\text{N}]^{163}$	17.2	$[\text{C}_4\text{mim}][\text{BF}_4]^{163}$	10.3
$[\text{C}_3\text{mpy}][\text{Tf}_2\text{N}]^{175}$	16.7	$[\text{C}_4\text{mim}][\text{PF}_6]^{175}$	8.9
$[\text{N}_{8881}][\text{Tf}_2\text{N}]^{175}$	15.5	DMSO <sup>176</sup>	7.3
$[\text{S}_{221}][\text{Tf}_2\text{N}]^{*175}$	16.6	AN <sup>176</sup>	8.9

\*Diethylmethyl-sulfonium bis(trifluoromethylsulfonyl)imide.

#### 1.3.4.3 Rare-earth metal ions

The unique environment provided by RTILs solutions was also confirmed for complexation of rare-earth metal ions. For example, a study about nitrate complexation of  $\text{Nd}^{3+}$  in  $[\text{C}_4\text{mim}][\text{Tf}_2\text{N}]$  showed that the limiting complex in this environment is  $[\text{Nd}(\text{NO}_3)_6]^{3-}$ ,<sup>177</sup> in contrast with the aqueous solution where up to the  $[\text{Nd}(\text{NO}_3)_2]^+$  species is formed.<sup>178</sup> In addition, stability constants of several orders of magnitude with respect to water have been obtained and complexation resulted highly exothermic, differently from the slight positive enthalpy values obtained in water. The difference in enthalpy was explained by taking into account that water solvates more strongly than  $[\text{Tf}_2\text{N}]^-$  both  $\text{Nd}^{3+}$  and  $\text{NO}_3^-$ . Furthermore, negative entropy values were obtained, reporting that the overall degree of disorder was reduced upon complexation. This was interpreted as due to the decrease in the number of species that can break the RTIL internal order and also with a lowering of the charges of the solubilized species

by passing from  $\text{Nd}^{3+}$  to  $[\text{Nd}(\text{NO}_3)_n]^{3-n}$ . The competitive effect of water on such systems has been inspected by studying  $\text{Nd}^{3+}$  and  $\text{Eu}^{3+}$  complexation by nitrate also in water-saturated  $[\text{C}_4\text{mim}][\text{Tf}_2\text{N}]$ .<sup>179,180</sup> In this solution, the metal ions were found to form nitrate species up to  $[\text{Ln}(\text{NO}_3)_4]^-$  ( $\text{Ln} = \text{Nd}, \text{Eu}$ ) with overall formation constants greater of several orders of magnitude with respect to complexation in water, but lower than in dry RTIL. Each step resulted to be endothermic and with larger and positive entropy change, on the contrary of complexation in dry  $[\text{C}_4\text{mim}][\text{Tf}_2\text{N}]$ .<sup>177</sup> The positive enthalpy obtained in the water-saturated RTIL was explained with the higher energy required to remove water molecules from the first coordination sphere in comparison with the  $[\text{Tf}_2\text{N}]^-$  anions.

Also  $\text{Eu}^{3+}$  complexation by  $\text{Cl}^-$  in RTILs carrying the  $[\text{PF}_6]^-$ ,  $[\text{BF}_4]^-$ ,  $[\text{Tf}_2\text{N}]^-$  and  $[\text{TfO}]^-$  anions has been studied by means of TRES and EXAFS. The results showed that chloride anions are able to partially replace the  $[\text{BF}_4]^-$  and  $[\text{TfO}]^-$  anions, while all the coordinating  $[\text{Tf}_2\text{N}]^-$  are displaced from the first solvation shell.<sup>154</sup>  $[\text{Tf}_2\text{N}]^-$  is therefore confirmed to be a weaker ligand in comparison with other RTILs anions.

As far as the complexation of  $\text{La}^{3+}$ ,  $\text{Nd}^{3+}$  and  $\text{Eu}^{3+}$  with CMPO in  $[\text{C}_4\text{mim}][\text{Tf}_2\text{N}]$ <sup>181</sup> was considered, it came out that  $[\text{Ln}(\text{CMPO})_n]^{3+}$  complexes up to  $n = 4$  were formed both in dry and wet conditions. In the first case complexation is stronger and enthalpy-driven, while in the latter it is less favorable and mainly driven by high positive entropies. This is still in agreement with the picture suggesting that less energy is required to desolvate the metal ion and the complexing ligand when they are coordinated by  $[\text{Tf}_2\text{N}]^-$  rather than by water. Similar results have been obtained for uranyl complexation with CMPO in  $[\text{C}_4\text{mim}][\text{PF}_6]$  and  $[\text{C}_8\text{mim}][\text{Tf}_2\text{N}]$ .<sup>97,182</sup>

## Bibliography

- 1 T. Welton, Room-Temperature Ionic Liquids. Solvents for Synthesis and Catalysis, *Chem. Rev.*, 1999, **99**, 2071–2084.
- 2 M. Earle, Ionic liquids. Green solvents for the future, *Pure Appl. Chem.*, 2000, **72**, 1391–1398.
- 3 P. Wasserscheid and W. Keim, Ionic Liquids—New “Solutions” for Transition Metal Catalysis, *Angew. Chemie Int. Ed.*, 2000, **39**, 3772–3789.
- 4 P. Walden, Molecular weights and electrical conductivity of several fused salts, *Bull. Acad. Imper. Sci. (St. Petersburg)*, 1914, 405–422.
- 5 K. R. Seddon, in *Molten Salt Forum: Proceedings of 5th International Conference on Molten Salt Chemistry and Technology*, ed. H. Wendt, 1998, vol. 5–6, pp. 53–62.
- 6 R. D. Rogers and K. R. Seddon, in *Ionic Liquids, Industrial Applications for Green Chemistry*, ACS Symposium Series 818, Washington, DC, 2002, p. 214.
- 7 K. M. Docherty and C. F. Kulpa, Jr., Toxicity and antimicrobial activity of imidazolium and pyridinium ionic liquids, *Green Chem.*, 2005, **7**, 185–189.
- 8 R. Giernoth, Task-Specific Ionic Liquids, *Angew. Chemie Int. Ed.*, 2010, **49**, 2834–2839.
- 9 D. R. MacFarlane, P. Meakin, J. Sun, N. Amini and M. Forsyth, Pyrrolidinium Imides: A New Family of Molten Salts and Conductive Plastic Crystal Phases, *J. Phys. Chem. B*, 1999, **103**, 4164–4170.
- 10 J. Sun, M. Forsyth and D. R. MacFarlane, Room-Temperature Molten Salts Based on the Quaternary Ammonium Ion, *J. Phys. Chem. B*, 1998, **102**, 8858–8864.
- 11 H. Chen, D. C. Kwait, Z. S. Gönen, B. T. Weslowski, D. J. Abdallah and R. G. Weiss, Phase Characterization and Properties of Completely Saturated Quaternary Phosphonium Salts. Ordered, Room-Temperature Ionic Liquids, *Chem. Mater.*, 2002, **14**, 4063–4072.
- 12 C. J. Bradaric, A. Downard, C. Kennedy, A. J. Robertson and Y. Zhou, Industrial preparation of phosphonium ionic liquids, *Green Chem.*, 2003, **5**, 143–152.
- 13 S. Zhang, N. Sun, X. He, X. Lu and X. Zhang, Physical properties of ionic liquids: Database and evaluation, *J. Phys. Chem. Ref. Data*, 2006, **35**, 1475–1517.
- 14 J. D. Holbrey, R. D. Rogers, R. A. Mantz, P. C. Trulove, V. A. Cocalia, A. E. Visser, J. L. Anderson, J. L. Anthony, J. F. Brennecke, E. J. Maginn, T. Welton and R. A. Mantz, in *Ionic Liquids in Synthesis*, John Wiley & Sons, Ltd, 2008, pp. 57–174.
- 15 H. Shirota, T. Mandai, H. Fukazawa and T. Kato, Comparison between dicationic and

- monocationic ionic liquids: Liquid density, thermal properties, surface tension, and shear viscosity, *J. Chem. Eng. Data*, 2011, **56**, 2453–2459.
- 16 L. C. Branco, J. N. Rosa, J. J. Moura Ramos and C. A. M. Afonso, Preparation and Characterization of New Room Temperature Ionic Liquids, *Chem. – A Eur. J.*, 2002, **8**, 3671–3677.
- 17 M. Regel-Rosocka and M. Wisniewski, in *Applications of Ionic Liquids in Science and Technology*, ed. S. Handy, 2011, pp. 375–398.
- 18 M. G. Freire, L. M. N. B. F. Santos, A. M. Fernandes, J. A. P. Coutinho and I. M. Marrucho, An overview of the mutual solubilities of water–imidazolium-based ionic liquids systems, *Fluid Phase Equilib.*, 2007, **261**, 449–454.
- 19 P. Verdía, M. Hernaiz, E. J. González, E. A. Macedo, J. Salgado and E. Tojo, Effect of the number, position and length of alkyl chains on the physical properties of polysubstituted pyridinium ionic liquids, *J. Chem. Thermodyn.*, 2014, **69**, 19–26.
- 20 M. G. Freire, P. J. Carvalho, R. L. Gardas, I. M. Marrucho, L. M. N. B. F. Santos and J. A. P. Coutinho, Mutual solubilities of water and the [Cnmim][Tf2N] hydrophobic ionic liquids, *J. Phys. Chem. B*, 2008, **112**, 1604–1610.
- 21 M. G. Freire, C. M. S. S. Neves, I. M. Marrucho, J. A. P. Coutinho and A. M. Fernandes, Hydrolysis of tetrafluoroborate and hexafluorophosphate counter ions in imidazolium-based ionic liquids, *J. Phys. Chem. A*, 2010, **114**, 3744–3749.
- 22 B. Wang, L. Qin, T. Mu, Z. Xue and G. Gao, Are Ionic Liquids Chemically Stable?, *Chem. Rev.*, 2017, **117**, 7113–7131.
- 23 K. S. Aihara, A. S. Himizu, H. A. Be and Y. Y. Oshimura, Hydrolysis of the Room Temperature Ionic Liquid, N, N-Diethyl-N-methyl-N-(2-methoxyethyl)ammonium Tetrafluoroborate, *J. Japan Inst. Energy*, 2014, **93**, 328–332.
- 24 K. Saihara, Y. Yoshimura, H. Fujimoto and A. Shimizu, Detrimental effect of glass sample tubes on investigations of BF<sub>4</sub><sup>-</sup>-based room temperature ionic liquid-water mixtures, *J. Mol. Liq.*, 2016, **219**, 493–496.
- 25 D. R. MacFarlane, N. Tachikawa, M. Forsyth, J. M. Pringle, P. C. Howlett, G. D. Elliott, J. H. Davis, M. Watanabe, P. Simon and C. A. Angell, Energy applications of ionic liquids, *Energy Environ. Sci.*, 2014, **7**, 232–250.
- 26 N. V. Plechkova and K. R. Seddon, Applications of ionic liquids in the chemical industry, *Chem. Soc. Rev.*, 2008, **37**, 123–150.
- 27 K. S. Egorova, E. G. Gordeev and V. P. Ananikov, Biological Activity of Ionic Liquids and Their Application in Pharmaceuticals and Medicine, *Chem. Rev.*, 2017, **117**, 7132–7189.

- 28 M. Armand, F. Endres, D. R. MacFarlane, H. Ohno and B. Scrosati, Ionic-liquid materials for the electrochemical challenges of the future, *Nat. Mater.*, 2009, **8**, 621–629.
- 29 M. Koel, Ionic Liquids in Chemical Analysis, *Crit. Rev. Anal. Chem.*, 2005, **35**, 177–192.
- 30 C. Chiappe, M. Malvaldi, B. Melai, S. Fantini, U. Bardi and S. Caporali, An unusual common ion effect promotes dissolution of metal salts in room-temperature ionic liquids: a strategy to obtain ionic liquids having organic–inorganic mixed cations, *Green Chem.*, 2010, **12**, 77–80.
- 31 C. Chiappe and M. Malvaldi, Highly concentrated “solutions” of metal cations in ionic liquids: current status and future challenges, *Phys. Chem. Chem. Phys.*, 2010, **12**, 11191.
- 32 M. Galiński, A. Lewandowski and I. Stepniak, Ionic liquids as electrolytes, *Electrochim. Acta*, 2006, **51**, 5567–5580.
- 33 A. Mauger, C. M. Julien, A. Paoletta, M. Armand and K. Zaghib, A comprehensive review of lithium salts and beyond for rechargeable batteries: Progress and perspectives, *Mater. Sci. Eng. R Reports*, 2018, **134**, 1–21.
- 34 V. H. Paschoal, L. F. O. Faria and M. C. C. Ribeiro, Vibrational Spectroscopy of Ionic Liquids, *Chem. Rev.*, 2017, **117**, 7053–7112.
- 35 V. Gómez-González, B. Docampo-Álvarez, O. Cabeza, M. Fedorov, R. M. Lynden-Bell, L. J. Gallego and L. M. Varela, Molecular dynamics simulations of the structure and single-particle dynamics of mixtures of divalent salts and ionic liquids, *J. Chem. Phys.*, 2015, **143**, 124507.
- 36 Y. Zhang, S. Liu, Y. Ji, J. Ma and H. Yu, Emerging Nonaqueous Aluminum-Ion Batteries: Challenges, Status, and Perspectives, *Adv. Mater.*, 2018, **30**, 1706310.
- 37 T. J. Simons, P. M. Bayley, Z. Zhang, P. C. Howlett, D. R. Macfarlane, L. A. Madsen and M. Forsyth, Influence of Zn<sup>2+</sup> and water on the transport properties of a pyrrolidinium dicyanamide ionic liquid, *J. Phys. Chem. B*, 2014, **118**, 4895–4905.
- 38 M. Xu, D. G. Ivey, W. Qu and Z. Xie, Improved Zn/Zn(II) redox kinetics, reversibility and cyclability in 1-ethyl-3-methylimidazolium dicyanamide with water and dimethyl sulfoxide added, *J. Power Sources*, 2014, **252**, 327–332.
- 39 M. Xu, D. G. Ivey, Z. Xie, W. Qu and E. Dy, The state of water in 1-butyl-1-methylpyrrolidinium bis(trifluoromethanesulfonyl)imide and its effect on Zn/Zn(II) redox behavior, *Electrochim. Acta*, 2013, **97**, 289–295.
- 40 T. J. Simons, P. C. Howlett, A. A. J. Torriero, D. R. MacFarlane and M. Forsyth, Electrochemical, transport, and spectroscopic properties of 1-ethyl-3-methylimidazolium ionic liquid electrolytes containing zinc dicyanamide, *J. Phys. Chem. C*, 2013, **117**, 2662–2669.
- 41 T. J. Simons, A. A. J. Torriero, P. C. Howlett, D. R. MacFarlane and M. Forsyth, High current density, efficient cycling of Zn<sup>2+</sup> in 1-ethyl-3-methylimidazolium dicyanamide ionic liquid:

- The effect of Zn<sup>2+</sup> salt and water concentration, *Electrochem. commun.*, 2012, **18**, 119–122.
- 42 T. Khoo, P. C. Howlett, M. Tsagouria, D. R. MacFarlane and M. Forsyth, The potential for ionic liquid electrolytes to stabilise the magnesium interface for magnesium/air batteries, *Electrochim. Acta*, 2011, **58**, 583–588.
- 43 V. L. Martins, B. G. Nicolau, S. M. Urahata, M. C. C. Ribeiro and R. M. Torresi, Influence of the water content on the structure and physicochemical properties of an ionic liquid and its Li<sup>+</sup> mixture, *J. Phys. Chem. B*, 2013, **117**, 8782–8792.
- 44 K. I. Popov, A. G. Vendilo, V. Chistov, H. Rönkkömäki, M. Lajunen, V. Privalov and J. Dikareva, Stability constants of lithium complexes with 15-crown-5 and 18-crown-6 in a hydrophobic ionic liquid 1-butyl-3-methylimidazolium bis[(trifluoromethyl)sulphonyl]imide, *Polyhedron*, 2013, **63**, 50–54.
- 45 T. Umecky and T. Takamuku, Role of water in complexation of 1,4,7,10,13,16-hexaoxacyclooctadecane (18-crown-6) with Li<sup>+</sup> and K<sup>+</sup> in hydrophobic 1-ethyl-3-methylimidazolium bis(trifluoromethanesulfonyl)amide ionic liquid, *J. Incl. Phenom. Macrocycl. Chem*, 2014, **80**, 401–407.
- 46 N. Nishi, H. Murakami, S. Imakura and T. Kakiuchi, Facilitated transfer of alkali-metal cations by dibenzo-18-crown-6 across the electrochemically polarized interface between an aqueous solution and a hydrophobic room-temperature ionic liquid, *Anal. Chem.*, 2006, **78**, 5805–5812.
- 47 A. Gerhard, D. P. Cobranchi, B. A. Garland, A. M. Highley, Y.-H. Huang, G. Konya, A. Zahl, R. van Eldik, S. Petrucci and E. M. Eyring, <sup>7</sup>Li-NMR Determination of Stability Constants as a Function of Temperature for Lithium-Crown Ether Complexes in a Molten Salt Mixture, *J. Phys. Chem.*, 1994, **98**, 7923–7928.
- 48 M. Shamsipur and M. Irandoust, Li-NMR study of the stoichiometry, stability and exchange kinetics of Li<sup>+</sup> ion ionic liquid – acetonitrile mixtures, *Polyhedron*, 2012, **31**, 395–401.
- 49 K. Popov, H. Rönkkömäki, M. Hannu-Kuure, T. Kuokkanen, M. Lajunen, A. Vendilo, P. Oksman and L. H. J. Lajunen, Stability of crown-ether complexes with alkali-metal ions in ionic liquid-water mixed solvents, *J. Incl. Phenom. Macrocycl. Chem.*, 2007, **59**, 377–381.
- 50 J. von Zamory, G. A. Giffin, S. Jeremias, F. Castiglione, A. Mele, E. Paillard and S. Passerini, Influence of oligo(ethylene oxide) substituents on pyrrolidinium-based ionic liquid properties, Li<sup>+</sup> solvation and transport, *Phys. Chem. Chem. Phys.*, 2016, **18**, 21539–21547.
- 51 M. Kar, B. Winther-Jensen, M. Forsyth and D. R. MacFarlane, Chelating ionic liquids for reversible zinc electrochemistry, *Phys. Chem. Chem. Phys.*, 2013, **15**, 7191–7197.
- 52 J. C. Lassègues, J. Grondin and D. Talaga, Lithium solvation in bis(trifluoromethanesulfonyl)imide-based ionic liquids, *Phys. Chem. Chem. Phys.*, 2006, **8**,

5629–5632.

- 53 L. J. Hardwick, M. Holzapfel, A. Wokaun and P. Novák, Raman study of lithium coordination in EMI-TFSI additive systems as lithium-ion battery ionic liquid electrolytes, *J. Raman Spectrosc.*, 2007, **38**, 110–112.
- 54 P. Simon and Y. Gogotsi, Materials for electrochemical capacitors, *Nat. Mater.*, 2008, **7**, 845–854.
- 55 F. Endres, Ionic liquids: Solvents for the electrodeposition of metals and semiconductors, *ChemPhysChem*, 2002, **3**, 144–154.
- 56 O. Shimamura, N. Yoshimoto, M. Matsumoto, M. Egashia and M. Morita, Electrochemical co-deposition of magnesium with lithium from quaternary ammonium-based ionic liquid, *J. Power Sources*, 2011, **196**, 1586–1588.
- 57 S. Zein El Abedin and F. Endres, Electrodeposition of metals and semiconductors in air- and water-stable ionic liquids, *ChemPhysChem*, 2006, **7**, 58–61.
- 58 T. Liu, R. Vilar, S. Eugénio, J. Grondin and Y. Danten, Electrodeposition of nanocrystalline copper thin films from 1-ethyl-3-methylimidazolium ethylsulphate ionic liquid, *J. Appl. Electrochem.*, 2014, **44**, 189–198.
- 59 T. Liu, R. Vilar, S. Eugénio, J. Grondin and Y. Danten, Electrodeposition of copper thin films from 1-ethyl-3-methylimidazolium bis(trifluoromethylsulfonyl)imide, *J. Appl. Electrochem.*, 2015, **45**, 87–93.
- 60 P. Y. Chen and C. L. Hussey, Electrodeposition of cesium at mercury electrodes in the tri-1-butylmethylammonium bis((trifluoromethyl)sulfonyl)imide room-temperature ionic liquid, *Electrochim. Acta*, 2004, **49**, 5125–5138.
- 61 G. T. Cheek, W. E. O. Grady, S. Z. El Abedin, E. M. Moustafa and F. Endres, Studies on the Electrodeposition of Magnesium in Ionic Liquids, *J. Electrochem. Soc.*, 2008, **155**, 91–95.
- 62 Y. Nuli, J. Yang and R. Wu, Reversible deposition and dissolution of magnesium from BMIMBF<sub>4</sub> ionic liquid, *Electrochem. commun.*, 2005, **7**, 1105–1110.
- 63 Y. Nuli, J. Yang and P. Wang, Electrodeposition of magnesium film from BMIMBF<sub>4</sub> ionic liquid, *Appl. Surf. Sci.*, 2006, **252**, 8086–8090.
- 64 P. Wang, Y. Nuli, J. Yang and Z. Feng, Mixed ionic liquids as electrolyte for reversible deposition and dissolution of magnesium, *Surf. Coatings Technol.*, 2006, **201**, 3783–3787.
- 65 Z. Liu, S. Z. El Abedin and F. Endres, Electrodeposition of zinc films from ionic liquids and ionic liquid/water mixtures, *Electrochim. Acta*, 2013, **89**, 635–643.
- 66 Y. Katayama, R. Fukui and T. Miura, Electrodeposition of Cobalt from an Imide-Type Room-Temperature Ionic Liquid, *J. Electrochem. Soc.*, 2007, **154**, D534.

- 67 C. Su, M. An, P. Yang, H. Gu and X. Guo, Electrochemical behavior of cobalt from 1-butyl-3-methylimidazolium tetrafluoroborate ionic liquid, *Appl. Surf. Sci.*, 2010, **256**, 4888–4893.
- 68 M. Li, Z. Shi, Z. Wang and R. G. Reddy, in *EPD Congress 2015*, John Wiley & Sons, Ltd, 2015, pp. 21–30.
- 69 P. Mastrorilli, A. Monopoli, M. M. Dell’Anna, M. Latronico, P. Cotugno and A. Nacci, in *Ionic Liquids (ILs) in Organometallic Catalysis*, eds. J. Dupont and L. Kollár, Springer Berlin Heidelberg, Berlin, Heidelberg, 2015, pp. 237–285.
- 70 N. A. Hamill, C. Hardacre and S. E. J. McMath, In situ XAFS investigation of palladium species present during the Heck reaction in room temperature ionic liquids, *Green Chem.*, 2002, **4**, 139–142.
- 71 P. Wasserscheid, in *Handbook of Green Chemistry*, American Cancer Society, 2010, pp. 65–91.
- 72 M. J. Earle, U. Hakala, B. J. Mcauley and M. Nieuwenhuyzen, Metal bis{(trifluoromethyl)sulfonyl}amide complexes: highly efficient Friedel – Crafts acylation catalysts, *Chem. Commun.*, 2004, 1368–1369.
- 73 A. Shaabani, E. Farhangi and A. Rahmati, Aerobic oxidation of alkyl arenes and alcohols using cobalt(II) phthalocyanine as a catalyst in 1-butyl-3-methyl-imidazolium bromide, *Appl. Catal. A Gen.*, 2008, **338**, 14–19.
- 74 S. BASF, Method for Isolating Acids from Chemical Reaction Mixtures by Using 1-Alkylimidazoles, *World Pat. WO2005/061416*.
- 75 K. Nakashima, F. Kubota, T. Maruyama and M. Goto, Ionic liquids as a novel solvent for lanthanide extraction, *Anal. Sci.*, 2003, **19**, 1097–1098.
- 76 U. Domańska and A. Rejzawek, Extraction of metal ions from aqueous solutions using imidazolium based ionic liquids, *J. Solution Chem.*, 2009, **38**, 739–751.
- 77 I. Billard, in *Handbook on the Physics and Chemistry of Rare Earths*, eds. J.-C. G. Bünzli and V. K. Pecharsky, Elsevier, 2013, vol. 43, pp. 213–273.
- 78 K. Nakashima, F. Kubota, T. Maruyama and M. Goto, Feasibility of ionic liquids as alternative separation media for industrial solvent extraction processes, *Ind. Eng. Chem. Res.*, 2005, **44**, 4368–4372.
- 79 M. Gras, N. Papaiconomou, N. Schaeffer, E. Chainet, F. Tedjar, J. A. P. Coutinho and I. Billard, Ionic-Liquid-Based Acidic Aqueous Biphasic Systems for Simultaneous Leaching and Extraction of Metallic Ions, *Angew. Chemie Int. Ed.*, 2018, **57**, 1–5.
- 80 B. K. Kim, E. J. Lee, Y. Kang and J. J. Lee, Application of ionic liquids for metal dissolution and extraction, *J. Ind. Eng. Chem.*, 2018, **61**, 388–397.

- 81 T. Makanyire, S. Sanchez-Segado and A. Jha, Separation and recovery of critical metal ions using ionic liquids, *Adv. Manuf.*, 2016, **4**, 33–46.
- 82 A. Stojanovic and B. K. Keppler, Ionic Liquids as Extracting Agents for Heavy Metals, *Sep. Sci. Technol.*, 2012, **47**, 189–203.
- 83 M. Fuerhacker, T. M. Haile, D. Kogelnig, A. Stojanovic and B. Keppler, Application of ionic liquids for the removal of heavy metals from wastewater and activated sludge, *Water Sci. Technol.*, 2012, **65**, 1765–1773.
- 84 A. P. De Los Ríos, F. J. Hernández-Fernández, L. J. Lozano, S. Sánchez, J. I. Moreno, C. Godínez, F. J. Herna and C. Godínez, Removal of Metal Ions from Aqueous Solutions by Extraction with Ionic Liquids, *J. Chem. Eng. Data*, 2010, **55**, 605–608.
- 85 S. Dai, Y. H. Ju and C. E. Barnes, Solvent extraction of strontium nitrate by a crown ether using room-temperature ionic liquids, *J. Chem. Soc., Dalt. Trans.*, 1999, 1201–1202.
- 86 P. A. De Los Rios, F. J. Hernandez-Fernandez, S. Sanchez-Segado, L. J. Lozano, J. I. Moreno and C. Godinez, Selective Separation of Zn(II) and Fe(III) from Acidic Media Using Ionic Liquids as Sole Extraction Agents, *Chem. Eng. Trans.*, 2010, **21**, 625–630.
- 87 S. T. M. Vidal, M. J. N. Correia, M. M. Marques, M. R. Ismael and M. T. A. Reis, Studies on the Use of Ionic Liquids as Potential Extractants of Phenolic Compounds and Metal Ions, *Sep. Sci. Technol.*, 2004, **39**, 2155–2169.
- 88 K. Kidani, N. Hirayama and H. Imura, Extraction behavior of divalent metal cations in ionic liquid chelate extraction systems using 1-alkyl-3-methylimidazolium bis(trifluoromethanesulfonyl)imides and thenoyltrifluoroacetone, *Anal. Sci.*, 2008, **24**, 1251–4.
- 89 N. Papaiconomou, J.-M. Lee, J. Salminen, M. von Stosch and J. M. Prausnitz, Selective Extraction of Copper, Mercury, Silver, and Palladium Ions from Water Using Hydrophobic Ionic Liquids, *Ind. Eng. Chem. Res.*, 2007, **47**, 5080–5086.
- 90 K. Shimojo and M. Goto, Solvent extraction and stripping of silver ions in room-temperature ionic liquids containing calixarenes, *Anal. Chem.*, 2004, **76**, 5039–5044.
- 91 K. Binnemans, Lanthanides and Actinides in Ionic Liquids, *Chem Rev.*, 2007, **107**, 2592–2614.
- 92 I. Billard, A. Ouadi and C. Gaillard, Liquid-liquid extraction of actinides, lanthanides, and fission products by use of ionic liquids: From discovery to understanding, *Anal. Bioanal. Chem.*, 2011, **400**, 1555–1566.
- 93 P. Giridhar, K. A. Venkatesan, T. G. Srinivasan and P. R. Vasudeva Rao, Extraction of uranium(VI) from nitric acid medium by 1.1M tri-n-butylphosphate in ionic liquid diluent, *J. Radioanal. Nucl. Chem.*, 2005, **265**, 31–38.

- 94 K. Shimojo, K. Kurahashi and H. Naganawa, Extraction behavior of lanthanides using a diglycolamide derivative TODGA in ionic liquids, *Dalt. Trans.*, 2008, 5083–5088.
- 95 M. P. Jensen, J. Neuefeind, J. V. Beitz, S. Skanthakumar and L. Soderholm, Mechanisms of Metal Ion Transfer into Room-Temperature Ionic Liquids: The Role of Anion Exchange, *J. Am. Chem. Soc.*, 2003, **125**, 15466–15473.
- 96 V. A. Cocalia, M. P. Jensen, J. D. Holbrey, S. K. Spear, D. C. Stepinski and R. D. Rogers, Identical extraction behavior and coordination of trivalent or hexavalent f-element cations using ionic liquid and molecular solvents, *Dalt. Trans.*, 2005, 1966–1971.
- 97 G. R. Choppin, R. D. Rogers, M. P. Jensen, A. E. Visser, K. L. Nash and I. Laszak, Uranyl Coordination Environment in Hydrophobic Ionic Liquids: An in Situ Investigation, *Inorg. Chem.*, 2003, **42**, 2197–2199.
- 98 C. H. C. Janssen, N. A. Macías-Ruvalcaba, M. Aguilar-Martínez and M. N. KobraK, Metal extraction to ionic liquids: the relationship between structure, mechanism and application, *Int. Rev. Phys. Chem.*, 2015, **34**, 591–622.
- 99 M. L. Dietz and J. A. Dzielawa, Ion-exchange as a mode of cation transfer into room-temperature ionic liquids containing crown ethers: implications for the ‘greenness’ of ionic liquids as diluents in liquid–liquid extraction, *Chem. Commun.*, 2001, 2124–2125.
- 100 M. L. Dietz, J. A. Dzielawa, I. Laszak, B. A. Young and M. P. Jensen, Influence of solvent structural variations on the mechanism of facilitated ion transfer into room-temperature ionic liquids, *Green Chem.*, 2003, **5**, 682–685.
- 101 M. L. Dietz and D. C. Stepinski, Anion concentration-dependent partitioning mechanism in the extraction of uranium into room-temperature ionic liquids, *Talanta*, 2008, **75**, 598–603.
- 102 M. L. Dietz and D. C. Stepinski, A ternary mechanism for the facilitated transfer of metal ions into room-temperature ionic liquids (RTILs): implications for the “greenness” of RTILs as extraction solvents, *Green Chem.*, 2005, **7**, 747–750.
- 103 S. L. Garvey, C. A. Hawkins and M. L. Dietz, Effect of aqueous phase anion on the mode of facilitated ion transfer into room-temperature ionic liquids, *Talanta*, 2012, **95**, 25–30.
- 104 Y. Umebayashi, T. Mitsugi, S. Fukuda, T. Fujimori, K. Fujii, R. Kanzaki, M. Takeuchi and S. I. Ishiguro, Lithium ion solvation in room-temperature ionic liquids involving bis(trifluoromethanesulfonyl)imide anion studied by Raman spectroscopy and DFT calculations, *J. Phys. Chem. B*, 2007, **111**, 13028–13032.
- 105 J. C. Lassègues, J. Grondin, C. Aupetit and P. Johansson, Spectroscopic identification of the lithium ion transporting species in LiTFSI-doped ionic liquids, *J. Phys. Chem. A*, 2009, **113**, 305–314.

- 106 Y. Umebayashi, S. Mori, K. Fujii, S. Tsuzuki, S. Seki, K. Hayamizu and S. I. Ishiguro, Raman spectroscopic studies and ab initio calculations on conformational isomerism of 1-Butyl-3-methylimidazolium Bis-(trifluoromethanesulfonyl)amide solvated to a lithium ion in ionic liquids: Effects of the second solvation sphere of the lithium ion, *J. Phys. Chem. B*, 2010, **114**, 6513–6521.
- 107 M. Herstedt, W. A. Henderson, M. Smirnov, L. Ducasse, L. Servant, D. Talaga and J. C. Lassègues, Conformational isomerism and phase transitions in tetraethylammonium bis(trifluoromethanesulfonyl)imide Et4NTFSI, *J. Mol. Struct.*, 2006, **783**, 145–156.
- 108 J.-C. Lassègues, J. Grondin, R. Holomb and P. Johansson, Raman and ab initio study of the conformational isomerism in the 1-ethyl-3-methyl-imidazolium bis(trifluoromethanesulfonyl)imide ionic liquid, *J. Raman Spectrosc.*, 2007, **38**, 551–558.
- 109 M. Herstedt, M. Smirnov, P. Johansson, M. Chami, J. Grondin, L. Servant and J. C. Lassègues, Spectroscopic characterization of the conformational states of the bis(trifluoromethanesulfonyl)imide anion (TFSI<sup>-</sup>), *J. Raman Spectrosc.*, 2005, **36**, 762–770.
- 110 O. Palumbo, F. Trequattrini, F. M. Vitucci, M. A. Navarra, S. Panero and A. Paolone, An infrared spectroscopy study of the conformational evolution of the Bis(trifluoromethanesulfonyl)imide ion in the liquid and in the glass state, *Adv. Condens. Matter Phys.*, 2015, 1–11.
- 111 K. Fujii, T. Fujimori, T. Takamuku, R. Kanzaki, Y. Umebayashi and S. I. Ishiguro, Conformational equilibrium of bis(trifluoromethanesulfonyl)imide anion of a room-temperature ionic liquid: Raman spectroscopic study and DFT calculations, *J. Phys. Chem. B*, 2006, **110**, 8179–8183.
- 112 H. Matsumoto, H. Sakaebe, K. Tatsumi, M. Kikuta, E. Ishiko and M. Kono, Fast cycling of Li/LiCoO<sub>2</sub> cell with low-viscosity ionic liquids based on bis(fluorosulfonyl)imide [FSI]<sup>-</sup>, *J. Power Sources*, 2006, **160**, 1308–1313.
- 113 A. Guerfi, S. Duchesne, Y. Kobayashi, A. Vijn and K. Zaghbi, LiFePO<sub>4</sub> and graphite electrodes with ionic liquids based on bis(fluorosulfonyl)imide (FSI)<sup>-</sup> for Li-ion batteries, *J. Power Sources*, 2008, **175**, 866–873.
- 114 O. Borodin, W. Gorecki, G. D. Smith and M. Armand, Molecular Dynamics Simulation and Pulsed-Field Gradient NMR Studies of Bis(fluorosulfonyl)imide (FSI) and Bis[(trifluoromethyl)sulfonyl]imide (TFSI)-Based Ionic Liquids, *J. Phys. Chem. B*, 2010, **114**, 6786–6798.
- 115 K. Fujii, H. Hamano, H. Doi, X. Song, S. Tsuzuki, K. Hayamizu, S. Seki, Y. Kameda, K. Dokko, M. Watanabe and Y. Umebayashi, Unusual Li<sup>+</sup> ion solvation structure in

- bis(fluorosulfonyl)amide based ionic liquid, *J. Phys. Chem. C*, 2013, **117**, 19314–19324.
- 116 J. B. Haskins, C. W. Bauschlicher and J. W. Lawson, Ab Initio Simulations and Electronic Structure of Lithium-Doped Ionic Liquids: Structure, Transport, and Electrochemical Stability, *J. Phys. Chem. B*, 2015, **119**, 14705–14719.
- 117 C. J. F. Solano, S. Jeremias, E. Paillard, D. Beljonne and R. Lazzaroni, A joint theoretical/experimental study of the structure, dynamics, and Li<sup>+</sup> transport in bis([tri]fluoro[methane]sulfonyl)imide [T]FSI-based ionic liquids, *J. Chem. Phys.*, 2013, **139**, 034502.
- 118 T. Méndez-Morales, J. Carrete, S. Bouzón-Capelo, M. Pérez-Rodríguez, Ó. Cabeza, L. J. Gallego and L. M. Varela, MD Simulations of the Formation of Stable Clusters in Mixtures of Alkaline Salts and Imidazolium-Based Ionic Liquids, *J. Phys. Chem. B*, 2013, **117**, 3207–3220.
- 119 V. V Matveev, A. V Ievlev, M. A. Vovk, O. Cabeza, J. Salgado-carballo, J. J. Parajó, J. R. Rodríguez, R. De, E. Lähderanta and L. M. Varela, NMR investigation of the structure and single-particle dynamics of inorganic salt solutions in a protic ionic liquid, *J. Mol. Liq.*, 2019, **278**, 239–246.
- 120 T. Méndez-Morales, J. Carrete, Ó. Cabeza, O. Russina, A. Triolo, L. J. Gallego and L. M. Varela, Solvation of Lithium Salts in Protic Ionic Liquids: A Molecular Dynamics Study, *J. Phys. Chem. B*, 2014, **118**, 761–770.
- 121 R. Hayes, S. A. Bernard, S. Imberti, G. G. Warr and R. Atkin, Solvation of Inorganic Nitrate Salts in Protic Ionic Liquids, *J. Phys. Chem. C*, 2014, **118**, 21215–21225.
- 122 O. Russina, R. Caminiti, T. Méndez-Morales, J. Carrete, O. Cabeza, L. J. Gallego, L. M. Varela and A. Triolo, How does lithium nitrate dissolve in a protic ionic liquid?, *J. Mol. Liq.*, 2015, **205**, 16–21.
- 123 Y. Umebayashi, T. Yamaguchi, S. Fukuda, T. Mitsugi, M. Takeuchi, K. Fujii and S. Ishiguro, Raman Spectroscopic Study on Alkaline Metal Ion Solvation in 1-Butyl-3-methylimidazolium Bis(trifluoromethanesulfonyl)amide Ionic Liquid, *Anal. Sci.*, 2008, **24**, 1297–1304.
- 124 D. Monti, E. Jónsson, M. R. Palacín and P. Johansson, Ionic liquid based electrolytes for sodium-ion batteries: Na<sup>+</sup> solvation and ionic conductivity, *J. Power Sources*, 2014, **245**, 630–636.
- 125 S. Tsuzuki, K. Kubota and H. Matsumoto, Cation and Anion Dependence of Stable Geometries and Stabilization Energies of Alkali Metal Cation Complexes with FSA<sup>-</sup>, FTA<sup>-</sup>, and TFSA<sup>-</sup> Anions: Relationship with Physicochemical Properties of Molten Salts, *J. Phys. Chem. B*, 2013, **117**, 16212–16218.
- 126 P. Kubisiak and A. Eilmes, Molecular Dynamics Simulations of Ionic Liquid Based

- Electrolytes for Na-Ion Batteries: Effects of Force Field, *J. Phys. Chem. B*, 2017, **121**, 9957–9968.
- 127 O. Borodin, G. A. Giffin, A. Moretti, J. B. Haskins, J. W. Lawson, W. A. Henderson and S. Passerini, Insights into the Structure and Transport of the Lithium, Sodium, Magnesium, and Zinc Bis(trifluoromethanesulfonyl)imide Salts in Ionic Liquids, *J. Phys. Chem. C*, 2018, **122**, 20108–20121.
- 128 R. D. Shannon, Revised effective ionic radii and systematic studies of interatomic distances in halides and chalcogenides, *Acta Crystallogr. Sect. A*, 1976, **32**, 751–767.
- 129 S. Jeremias, G. A. Giffin, A. Moretti, S. Jeong and S. Passerini, Mechanisms of Magnesium Ion Transport in Pyrrolidinium Bis(trifluoromethanesulfonyl)imide-Based Ionic Liquid Electrolytes, *J. Phys. Chem. C*, 2014, **118**, 28361–28368.
- 130 G. A. Giffin, A. Moretti, S. Jeong and S. Passerini, Complex Nature of Ionic Coordination in Magnesium Ionic Liquid-Based Electrolytes: Solvates with Mobile Mg<sup>2+</sup> Cations, *J. Phys. Chem. C*, 2014, **118**, 9966–9973.
- 131 T. Watkins and D. A. Buttry, Determination of Mg<sup>2+</sup> Speciation in a TFSI–Based Ionic Liquid With and Without Chelating Ethers Using Raman Spectroscopy, *J. Phys. Chem. B*, 2015, **119**, 7003–7014.
- 132 A. Chaumont, E. Engler and G. Wipff, Uranyl and strontium salt solvation in room-temperature ionic liquids. A molecular dynamics investigation, *Inorg. Chem.*, 2003, **42**, 5348–5356.
- 133 K. Fujii, T. Nonaka, Y. Akimoto, Y. Umebayashi and S. Ishiguro, Solvation Structures of Some Transition Metal(II) Ions in a Room-Temperature Ionic Liquid, 1-Ethyl-3-methylimidazolium Bis(trifluoromethanesulfonyl)amide, *Anal. Sci.*, 2008, **24**, 1377–1380.
- 134 M. Matsumiya, Y. Kamo, K. Hata and K. Tsunashima, Solvation structure of iron group metal ion in TFSA-based ionic liquids investigated by Raman spectroscopy and DFT calculations, *J. Mol. Struct.*, 2013, **1048**, 59–63.
- 135 O. Bortolini, C. Chiappe, T. Ghilardi, A. Massi and C. S. Pomelli, Dissolution of Metal Salts in Bis(trifluoromethylsulfonyl)imide-Based Ionic Liquids: Studying the Affinity of Metal Cations Toward a “Weakly Coordinating” Anion, *J. Phys. Chem. A*, 2015, **119**, 5078–5087.
- 136 T. Liu, Y. Danten, J. Grondin and R. Vilar, Solvation of AgTFSI in 1-ethyl-3-methylimidazolium bis(trifluoromethylsulfonyl)imide ionic liquid investigated by vibrational spectroscopy and DFT calculations, *J. Raman Spectrosc.*, 2016, **47**, 449–456.
- 137 I. H. Arellano, J. Huang and P. Pendleton, Computational insights into the molecular interaction and ion-pair structures of a novel zinc-functionalized ionic liquid,

- [Emim][Zn(TFSI)<sub>3</sub>], *Spectrochim. Acta - Part A Mol. Biomol. Spectrosc.*, 2016, **153**, 6–15.
- 138 A. Melchior, C. Gaillard, S. Gràcia Lanas, M. Tolazzi, I. Billard, S. Georg, L. Sarrasin and M. Boltoeva, Nickel(II) Complexation with Nitrate in Dry [C<sub>4</sub>mim][Tf<sub>2</sub>N] Ionic Liquid: A Spectroscopic, Microcalorimetric, and Molecular Dynamics Study, *Inorg. Chem.*, 2016, **55**, 3498–3507.
- 139 P. Nockemann, M. Pellens, K. Van Hecke, L. Van Meervelt, J. Wouters, B. Thijs, E. Vanecht, T. N. Parac-Vogt, H. Mehdi, S. Schaltin, J. Fransaer, S. Zahn, B. Kirchner and K. Binnemans, Cobalt(II) complexes of nitrile-functionalized ionic liquids, *Chem. - A Eur. J.*, 2010, **16**, 1849–1858.
- 140 J. M. Vicent-Luna, E. Azaceta, S. Hamad, J. M. Ortiz-Roldán, R. Tena-Zaera, S. Calero and J. A. Anta, Molecular Dynamics Analysis of Charge Transport in Ionic-Liquid Electrolytes Containing Added Salt with Mono, Di, and Trivalent Metal Cations, *ChemPhysChem*, 2018, **19**, 1665–1673.
- 141 F. Sessa, V. Migliorati, A. Serva, A. Lapi, G. Aquilanti, G. Mancini and P. D'Angelo, On the coordination of Zn<sup>2+</sup> ion in Tf<sub>2</sub>N<sup>-</sup> based ionic liquids: structural and dynamic properties depending on the nature of the organic cation, *Phys. Chem. Chem. Phys.*, 2018, **20**, 2662–2675.
- 142 A. J. Dent, K. R. Seddon and T. Welton, The Structure of Halogenometallate Complexes dissolved in both Basic and Acidic Room-temperature Halogenoaluminate(III) Ionic Liquids, as determined by EXAFS, *J. Chem. Soc., Chem. Commun.*, 1990, 315–316.
- 143 A. W. Taylor, S. Men, C. J. Clarke and P. Licence, Acidity and basicity of halometallate-based ionic liquids from X-ray photoelectron spectroscopy, *RSC Adv.*, 2013, **3**, 9436–9445.
- 144 J. M. Hartley, C. M. Ip, G. C. H. Forrest, K. Singh, S. J. Gurman, K. S. Ryder, A. P. Abbott and G. Frisch, EXAFS study into the speciation of metal salts dissolved in ionic liquids and deep eutectic solvents, *Inorg. Chem.*, 2014, **53**, 6280–6288.
- 145 G. Li, D. M. Camaioni, J. E. Amonette, Z. C. Zhang, T. J. Johnson and J. L. Fulton, [CuCl<sub>n</sub>]<sup>2-</sup> ion-pair species in 1-ethyl-3-methylimidazolium chloride ionic liquid-water mixtures: Ultraviolet-visible, X-ray absorption fine structure, and density functional theory characterization, *J. Phys. Chem. B*, 2010, **114**, 12614–12622.
- 146 P. De Vreese, N. R. Brooks, K. Van Hecke, L. Van Meervelt, E. Mattheijs, K. Binnemans and R. Van Deun, Speciation of copper(II) complexes in an ionic liquid based on choline chloride and in choline chloride/water mixtures, *Inorg. Chem.*, 2012, **51**, 4972–4981.
- 147 A. Pasquarello, I. Petri, P. S. Salmon, O. Parisel, R. Car, E. Toth, D. H. Powell, H. E. Fischer, L. Helm and A. Merbach, First solvation shell of the Cu(II) aqua ion: evidence for fivefold coordination., *Science*, 2001, **291**, 856–859.

- 148 J. Chaboy, A. Muñoz-Páez, P. J. Merklings and E. S. Marcos, The hydration of Cu<sup>2+</sup>: Can the Jahn-Teller effect be detected in liquid solution?, *J. Chem. Phys.*, 2006, **124**, 064509.
- 149 D. T. Bowron, M. Amboage, R. Boada, A. Freeman, S. Hayama and S. Díaz-Moreno, The hydration structure of Cu<sup>2+</sup>: more tetrahedral than octahedral?, *RSC Adv.*, 2013, **3**, 17803–17812.
- 150 G. Chillemi, E. Pace, M. D’Abramo and M. Benfatto, Equilibrium between 5- and 6-fold coordination in the first hydration shell of Cu(II), *J. Phys. Chem. A*, 2016, **120**, 3958–3965.
- 151 R. Kanzaki, S. Uchida, H. Kodamatani and T. Tomiyasu, Copper(II) Chloro Complex Formation Thermodynamics and Structure in Ionic Liquid, 1-Butyl-3-Methylimidazolium Trifluoromethanesulfonate, *J. Phys. Chem. B*, 2017, **121**, 9659–9665.
- 152 Z. Liu, S. Z. El Abedin and F. Endres, Raman and FTIR spectroscopic studies of 1-Ethyl-3-methylimidazolium trifluoromethylsulfonate, its mixtures with water and the solvation of Zinc ions, *ChemPhysChem*, 2015, **16**, 970–977.
- 153 Z. Liu, S. Z. El Abedin and F. Endres, Electrochemical and spectroscopic study of Zn(II) coordination and Zn electrodeposition in three ionic liquids with the trifluoromethylsulfonate anion, different imidazolium ions and their mixtures with water, *Phys. Chem. Chem. Phys.*, 2015, **17**, 15945–15952.
- 154 C. Gaillard, I. Billard, A. Chaumont, S. Mekki, A. Ouadi, M. A. Denecke, G. Moutiers and G. Wipff, Europium(III) and its halides in anhydrous room-temperature imidazolium-based ionic liquids: A combined TRES, EXAFS, and molecular dynamics study, *Inorg. Chem.*, 2005, **44**, 8355–8367.
- 155 A. Chaumont and G. Wipff, Solvation of M<sup>3+</sup> lanthanide cations in room-temperature ionic liquids. A molecular dynamics investigation, *Phys. Chem. Chem. Phys.*, 2003, **5**, 3481–3488.
- 156 A. Chaumont and G. Wipff, Solvation of Ln(III) Lanthanide Cations in the [BMI][SCN], [MeBu<sub>3</sub>N][SCN], and [BMI]<sub>5</sub>[Ln(NCS)<sub>8</sub>] Ionic Liquids: A Molecular Dynamics Study, *Inorg. Chem.*, 2009, **48**, 4277–4289.
- 157 K. Binnemans, L. Van Meervelt, P. Nockemann, B. Thijs, N. Postelmans and K. Van Hecke, Anionic Rare-Earth Thiocyanate Complexes as Building Blocks for Low-Melting Metal-Containing Ionic Liquids, *J. Am. Chem. Soc.*, 2006, **128**, 13658–13659.
- 158 N. Tsuda, M. Matsumiya, K. Tsunashima and S. Kodama, Electrochemical behavior and solvation analysis of rare earth complexes in ionic liquids media investigated by SECM and Raman spectroscopy Nanae Tsuda, *ECS Trans.*, 2012, **50**, 539–548.
- 159 E. Bodo, Lanthanum(III) and Lutetium(III) in Nitrate-Based Ionic Liquids: A Theoretical Study of Their Coordination Shell, *J. Phys. Chem. B*, 2015, **119**, 11833–11838.

- 160 A. Serva, V. Migliorati, R. Spezia and P. D'Angelo, How Does Ce(III) Nitrate Dissolve in a Protic Ionic Liquid? A Combined Molecular Dynamics and EXAFS Study, *Chem. – A Eur. J.*, 2017, **23**, 8424–8433.
- 161 D. Ramalakshmi and M. V. Rajasekharan, Crystallographic disorder in mixed-valent dioxo-bridged Mn<sup>III,IV</sup> complexes. [Mn<sub>2</sub>O<sub>2</sub>(bpy)<sub>4</sub>]-[Ce(NO<sub>3</sub>)<sub>6</sub>].5H<sub>2</sub>O, *Acta Crystallogr. Sect. B Struct. Sci.*, 1999, **55**, 186–191.
- 162 A. Lewandowski and I. Stępniać, Relative molar Gibbs energies of cation transfer from a molecular liquid to ionic liquids at 298.15 K, *Phys. Chem. Chem. Phys.*, 2003, **5**, 4215–4218.
- 163 A. Lewandowski, M. Osińska and I. Stępniać, Stability of Ag<sup>+</sup> complexes with cryptand 222 in ionic liquids, *J. Incl. Phenom.*, 2005, **52**, 237–240.
- 164 Y. Marcus, Thermodynamics of Solvation of Ions, *J. Chem. Soc., Faraday Trans.*, 1991, **87**, 2995–2999.
- 165 S. Ahrland, Solvation and Complex Formation-Competing and Cooperative Processes in Solution, *Pure Appl. Chem.*, 1982, **54**, 1451–1468.
- 166 P. Di Bernardo, A. Melchior, M. Tolazzi and P. L. Zanonato, Thermodynamics of lanthanide(III) complexation in non-aqueous solvents, *Coord. Chem. Rev.*, 2012, **256**, 328–351.
- 167 K. Popov, V. Chistov, E. Esipova, J. Dikareva and A. Vendilo, in *Application, Purification, and Recovery of Ionic Liquids*, eds. O. Kuzmina and J. P. Hallett, Elsevier, Amsterdam, 2016, pp. 161–204.
- 168 A. J. Smetana and A. I. Popov, Lithium-7 nuclear magnetic resonance and calorimetric study of lithium crown complexes in various solvents, *J. Solution Chem.*, 1980, **9**, 183–196.
- 169 F. Arnaud-Neu, R. Delgado and S. Chaves, Critical evaluation of stability constants and thermodynamic functions of metal complexes of crown ethers, *Pure Appl. Chem.*, 2003, **75**, 71–102.
- 170 A. Vendilo, K. Popov, M. Lajunen, V. Chistov, D. Djigailo, H. Rönkkömäki, V. Privalov and I. Pletnev, A cesium-133 nuclear magnetic resonance study of the cesium cation complexation by macrocyclic polyethers in hydrophobic RITLs, *Polyhedron*, 2014, **81**, 341–348.
- 171 A. G. Vendilo, D. I. Dzhigailo, I. V. Pletnev, K. I. Popov and I. I. Torocheshnikova, Thermodynamics of complexation of cesium ions with dibenzo-18-crown-6 in hydrophobic ionic liquids, *Russ. J. Inorg. Chem.*, 2011, **56**, 954–960.
- 172 S. Katsuta, H. Tachibana and Y. Takeda, Stabilities in Water of Alkali Metal Ion Complexes with Dibenzo-24-crown-8 and Dibenzo-18-crown-6 and Their Transfer Activity Coefficients from Water to Nonaqueous Solvents, *J. Solut.*, 2002, **31**, 499–510.

- 173 A. G. Vendilo, V. I. Chistov and V. I. Privalov, Thermodynamics of complexation of cesium with dibenzo-21-crown-7 and dibenzo-24-crown-8 in 1-butyl-3-methylimidazolium bis((trifluoromethyl)sulfonyl)imide, *Russ. J. Inorg. Chem.*, 2012, **57**, 629–633.
- 174 H.-J. Buschmann, E. Cleve, U. Denter and E. Schollmeyer, Determination of complex stabilities with nearly insoluble host molecules. Part II. Complexation of alkali and alkaline earth metal cations with dibenzo crown ethers in aqueous solution, *J. Phys. Org. Chem.*, 1997, **10**, 781–785.
- 175 A. Lewandowski, M. Osińska, A. Swiderska-Mocek and M. Galinski, A cryptate reference electrode for ionic liquids, *Electroanalysis*, 2008, **20**, 1903–1908.
- 176 C. A. Brooks and A. P. Doherty, Concentration-dependent diffusion in room temperature ionic liquids: A microelectrode study, *Electrochem. commun.*, 2004, **6**, 867–871.
- 177 L. Liu, G. Tian and L. Rao, Effect of Solvation? Complexation of Neodymium (III) with Nitrate in an Ionic Liquid (BumimTf2N) in Comparison with Water, *Solvent Extr. Ion Exch.*, 2013, **31**, 384–400.
- 178 L. Rao and G. Tian, Complexation of Lanthanides with Nitrate at Variable Temperatures: Thermodynamics and Coordination Modes, *Inorg. Chem.*, 2009, **48**, 964–970.
- 179 S. A. Ansari, L. Liu, P. D. Dau, J. K. Gibson and L. Rao, Unusual complexation of nitrate with lanthanides in a wet ionic liquid: a new approach for aqueous separation of trivalent f-elements using an ionic liquid as solvent, *RSC Adv.*, 2014, **4**, 37988–37991.
- 180 S. A. Ansari, L. Liu and L. Rao, Binary Lanthanide(III)/Nitrate and Ternary Lanthanide(III)/Nitrate/Chloride Complexes in an Ionic Liquid Containing Water: Optical Absorption and Luminescence Studies, *Dalt. Trans.*, 2015, **44**, 2907–2914.
- 181 W. Wu, T. Sun, N. Pu, D. Meng, Y. Li, J. Dang, Y. Yang, J. Chen and C. Xu, Thermodynamic and spectroscopic study on the solvation and complexation behavior of Ln(iii) in ionic liquids: Binding of Ln(iii) with CMPO in C4mimNTf2, *New J. Chem.*, 2018, **42**, 9098–9109.
- 182 Q. Wu, T. Sun, X. Meng, J. Chen and C. Xu, Thermodynamic Insight into the Solvation and Complexation Behavior of U(VI) in Ionic Liquid: Binding of CMPO with U(VI) Studied by Optical Spectroscopy and Calorimetry, *Inorg. Chem.*, 2017, **56**, 3014–3021.



# Chapter 2

## Focus of the work

The aim of this work is to obtain a detailed description at molecular level of structural and thermodynamic properties of transition metal ions in RTILs.

Several technological applications involve metal ions and their complexes in ionic liquids. To improve these applications, the achievement of a clear picture about their structural and thermodynamic solvation features in these media is essential. As regards the structural part, this means the knowledge of the metal first solvation sphere structure, *i.e.* of its coordination in solution. On the other hand, thermodynamic quantities such as Gibbs free energies, enthalpies and entropies of solvation in the RTIL, as well as for transfer from other solutions, are useful to describe the nature of the interaction between a metal ion and a solvent and to predict its behavior in a system. However, this fundamental knowledge still lacks for many metal ions in several RTILs.

The work developed in this thesis is focused on metal ions involved in numerous applications in RTILs:  $\text{Zn}^{2+}$ ,  $\text{Co}^{2+}$  and  $\text{Ag}^+$ . The studied RTILs belong to the family formed by the 1-alkyl-3-methylimidazolium cation  $[\text{C}_n\text{mim}]^+$  together with the bis(trifluoromethylsulfonyl)imide anion  $[\text{Tf}_2\text{N}]^-$ . It has been shown that this anion can produce RTILs with high thermal and electrochemical stabilities, low toxicity and with an ion conductivity comparable to the best organic solvents employed in electrochemical devices.<sup>1</sup> This is particularly true when this anion is combined with an imidazolium cation. Furthermore, being hydrophobic, these RTILs are among the most studied for extraction processes by means of liquid-liquid biphasic systems.<sup>2</sup> In addition, the family of RTILs carrying the  $[\text{BF}_4]^-$  anion within the  $[\text{C}_n\text{mim}]^+$  cation has been taken into account owing to the high solvation capabilities they seem to display towards some of the studied metal ions, as reported by experimental thermodynamic data (**Sec. 1.3.3 of Chapter 1**).

The employed methods combine computational techniques such as Molecular Dynamics (MD) simulations and DFT calculations with experimental methods like X-ray absorption spectroscopy (XAS).

The abundance of *force fields* for several RTILs within an accessible computational cost and the possibility of reproducing several properties in good agreement with experimental data have made MD one of the most useful techniques in the study of ionic liquids.<sup>3,4</sup> However, the choice of the

potential describing the interaction between the simulated species is not trivial and can have a crucial influence on the calculated structural and thermodynamic properties. A force field is usually parametrized to fit some target data, whether if they are empirical or provided by quantum-chemical calculations. In other words, it does not come from *ab initio* principles. Such issue does not mean that a force field cannot be *predictive*. For example, the parametrization of RTILs force fields is usually performed on bulk solvent properties like density, viscosity or vaporization enthalpy.<sup>5</sup> However, this does not prevent the possibility that such a force field could reproduce also other features like the diffusion coefficients of the ions or even properties related with metal ions solvation. In this sense, it can be said that a force field is *predictive*. As a consequence, one initial challenge of this project has been also to verify if reliable structural and thermodynamic data about metal ions solvation in RTILs could be obtained by MD simulations with the employment of interaction potentials that have not been parametrized specifically for the present case study. To this purpose, the impact of different force fields and the comparison of the results with available experimental data has been a constant effort.

In addition, it is known that the achievement of a definite picture reporting structural information on disordered liquid systems can be a difficult task.<sup>6</sup> In this respect, XAS is a very powerful tool for the study of the first shell structure surrounding a metal ion in solution, owing to its high sensitivity on the closest environment of the photoabsorbing atom. In particular, if used in combination with MD, it has turned out to be a useful technique in the study of RTILs both in dry and wet conditions and in the analysis of metal ions solvation structure in these media.<sup>7-10</sup> A source of inspiration for this work has been therefore also the validation of a combined approach between MD and XAS in the study of metal ions in RTILs, with the hope that a more standardized application of this methodology could help the improvement of new potential applications involving this class of solvents in the future.

This thesis is organized as follows. An overview about ILs general properties and of the available literature data on metal ions solvation in these solvents has been provided in **Chapter 1**. In the next Chapter, the theoretical background of the employed methods will be given. **Chapter 4** contains the results about a study on  $\text{Zn}^{2+}$  in  $[\text{C}_n\text{mim}][\text{Tf}_2\text{N}]$  ( $n = 2, 4$ ) and  $[\text{C}_4\text{mim}][\text{BF}_4]$ . In **Chapter 5**, results for  $\text{Co}^{2+}$  in  $[\text{C}_4\text{mim}][\text{Tf}_2\text{N}]$  are provided. **Chapter 6** reports a study about  $\text{Ag}^+$  both in aqueous solution and in the  $[\text{C}_4\text{mim}][\text{Tf}_2\text{N}]$  and  $[\text{C}_4\text{mim}][\text{BF}_4]$  RTILs. Successively, **Appendix A** contains details about the generation of a new  $\text{Ag-H}_2\text{O}$  interaction potential carried out starting from *ab initio* data. **Appendix B** is concerned with a preliminary MD study about  $\text{Zn}^{2+}$  in  $[\text{C}_2\text{mim}][\text{Tf}_2\text{N}]$  with the inclusion of many-body explicit polarizability. Finally, **Appendix C** is employed as Supporting Information.

## Bibliography

- 1 M. Armand, F. Endres, D. R. MacFarlane, H. Ohno and B. Scrosati, Ionic-liquid materials for the electrochemical challenges of the future, *Nat. Mater.*, 2009, **8**, 621–629.
- 2 T. Makanyire, S. Sanchez-Segado and A. Jha, Separation and recovery of critical metal ions using ionic liquids, *Adv. Manuf.*, 2016, **4**, 33–46.
- 3 M. Salanne, Simulations of room temperature ionic liquids: from polarizable to coarse-grained force fields, *Phys. Chem. Chem. Phys.*, 2015, **17**, 14270–14279.
- 4 F. Dommert, K. Wendler, R. Berger, L. Delle Site and C. Holm, Force fields for studying the structure and dynamics of ionic liquids: A critical review of recent developments, *ChemPhysChem*, 2012, **13**, 1625–1637.
- 5 J. N. Canongia Lopes and A. A. H. Pádua, CL&P: A generic and systematic force field for ionic liquids modeling, *Theor. Chem. Acc.*, 2012, **131**, 1–11.
- 6 A. Filipponi and P. D'Angelo, in *X-Ray Absorption and X-Ray Emission Spectroscopy*, John Wiley & Sons, Ltd, 2016, pp. 745–771.
- 7 V. Migliorati, A. Zitolo and P. D'Angelo, Using a Combined Theoretical and Experimental Approach to Understand the Structure and Dynamics of Imidazolium-Based Ionic Liquids/Water Mixtures. 1. MD Simulations, *J. Phys. Chem. B*, 2013, **117**, 12505–12515.
- 8 P. D'Angelo, A. Zitolo, G. Aquilanti and V. Migliorati, Using a Combined Theoretical and Experimental Approach to Understand the Structure and Dynamics of Imidazolium-Based Ionic Liquids/Water Mixtures. 2. EXAFS Spectroscopy, *J. Phys. Chem. B*, 2013, **117**, 12516–12524.
- 9 F. Sessa, V. Migliorati, A. Serva, A. Lapi, G. Aquilanti, G. Mancini and P. D'Angelo, On the coordination of Zn<sup>2+</sup> ion in Tf<sub>2</sub>N<sup>-</sup> based ionic liquids: structural and dynamic properties depending on the nature of the organic cation, *Phys. Chem. Chem. Phys.*, 2018, **20**, 2662–2675.
- 10 A. Melchior, C. Gaillard, S. Gràcia Lanas, M. Tolazzi, I. Billard, S. Georg, L. Sarrasin and M. Boltoeva, Nickel(II) Complexation with Nitrate in Dry [C<sub>4</sub>mim][Tf<sub>2</sub>N] Ionic Liquid: A Spectroscopic, Microcalorimetric, and Molecular Dynamics Study, *Inorg. Chem.*, 2016, **55**, 3498–3507.



# Chapter 3

## Methods

### 3.1 Simulation techniques

Molecular modelling techniques are based on the assumption that the description of a chemical system at atomistic level can provide knowledge also on macroscopic phenomena.<sup>1,2</sup> Furthermore, these methods can give access to properties that are difficult or impossible to measure experimentally. The obtained knowledge can have a two-fold employment: *i*) predictive, *i.e.* it can supply *a priori* understanding of a phenomenon and help to set up an experiment or a process; *ii*) it can provide an *a posteriori* explanation of a physical observable. In both cases, the intimate relationship and continuous comparison between theoretical and experimental data should never be forgotten.

Macroscopic physical properties are ensemble averages over a molecular system. As a consequence, the knowledge of a single state, even if the absolute energy minimum, is usually not sufficient to obtain the desired macroscopic description. Differently, it is necessary to generate a representative ensemble of states at a given temperature. The generation of equilibrium ensembles is faced by two methods: *i*) *Monte Carlo* (MC) and *ii*) *Molecular Dynamics* (MD) simulations. While MC methods compute the average of a function of the coordinates and momenta of the system by ensemble averaging, MD simulations do so by time averaging.

In principle, a full description of such a many-body molecular system could be provided by solving the relativistic time-dependent Schrödinger equation including the electronic and nuclear degrees of freedom. The expectation value of a physical observable could be then computed for all the quantum states with non-negligible statistical weight. However, only a system consisting in a few atoms can be treated at this level of theory, therefore approximations are necessary for bigger ensembles. These approximations become more and more rude as the complexity of the system and/or the required simulation time increase. A very first try is the *Born-Oppenheimer approximation*, *i.e.* admit that the electron cloud adjusts instantaneously with changes in the nuclear configuration. However, at a certain point also this *ab initio* description needs to be substituted by empirical parameterization. This means renouncing to the inclusion of the electronic motion and to describe particles interactions with a potential form that is a function of atomic (nuclear) positions only. If the system is treated only by

the laws of classical physics, we are in the realm of *classical molecular dynamics*. Here the system is considered as composed of point-like nuclei with forces acting on them derived from a previously determined empirical effective potential. Differently, in *ab initio molecular dynamics* (AIMD) the classical treatment of nuclei is maintained, but forces are considered as quantum-mechanical in nature and derived from calculations including also the electronic structure.<sup>3</sup> Other possible approaches are for example mixed Quantum Mechanical/Molecular Mechanics (QM/MM) methods, where one part of a system is classically treated and another, usually considered as the most relevant, is described from *ab initio* principles.

In the next sections, a brief description of the simulation methods employed in this work, *i.e.* classical and *ab initio* MD, will be given.

### 3.1.1 Classical Molecular Dynamics

In a MD simulation, the dynamics of a system in time is predicted by solving step-by-step the Newton's equations of motion for a system of  $N$  interacting particles:

$$m_i \frac{\partial^2 \mathbf{r}_i}{\partial t^2} = \mathbf{F}_i; \quad i = 1 \dots N \quad (3.1)$$

where the forces are the negative derivatives of the potential function  $V(\mathbf{r}_1, \mathbf{r}_2, \dots, \mathbf{r}_N)$ :

$$\mathbf{F}_i = - \frac{\partial V}{\partial \mathbf{r}_i} \quad (3.2)$$

The coordinates as a function of time constitute what is called the *trajectory* of the system. The potential energy function depends on the complete set of the  $3N$  coordinates and it is often referred to as *force field*. It can be useful to divide this function into a *bonded* and a *non-bonded* part:

$$V = V_{bonded} + V_{non-bonded} \quad (3.3)$$

Bonded interactions are again the sum of various terms:

$$V_{bonded} = V_{bonds} + V_{angles} + V_{dihedrals} + V_{improper} \quad (3.4)$$

being  $V_{bonds}$  related to two-body,  $V_{angles}$  to three-body,  $V_{dihedrals}$  and  $V_{improper}$  to four-body interactions (**Fig. 3.1**).

$V_{bonds}$  represents the bond stretching between two  $i$  and  $j$  atoms covalently bonded and in the simplest case it can be described by a harmonic potential:

$$V_{bonds} = \frac{1}{2} k_{ij}^b (r_{ij} - r_{ij}^0)^2 \quad (3.5)$$

where  $k_{ij}^b$  is a force constant,  $r_{ij}$  and  $r_{ij}^0$  the instantaneous and equilibrium distances, respectively.

The  $V_{angles}$  term is related to the bond-angle vibration for the  $\theta_{ijk}$  angle between three atoms  $i, j$  and  $k$ :

$$V_{angles} = \frac{1}{2} k_{ijk}^\theta (\theta_{ijk} - \theta_{ijk}^0)^2 \quad (3.6)$$

with harmonic constant  $k_{ij}^\theta$ , instantaneous and equilibrium angles  $\theta_{ijk}$  and  $\theta_{ijk}^0$ .

$V_{dihedrals}$  describes the potential related to the motion of a proper dihedral angle involving four  $i, j, k$  and  $l$  atoms. According to the IUPAC convention, it is defined as the  $\varphi$  angle between the  $ijk$  and  $jkl$  planes, a value of zero corresponding to a *cis* configuration of the  $i$  and  $l$  atoms.

$$V_{dihedrals} = k_{ijkl}^\varphi (1 - \cos(n\varphi - \gamma)) \quad (3.7)$$

where  $\gamma$  is the phase and  $n$  the number of peaks for a full rotation.

$V_{improper}$  is referred to improper dihedrals, which can be employed to keep certain groups planar (*e.g.* for aromatic rings), or to prevent transitions of molecules to their mirror images. In its harmonic form, it is given by:

$$V_{improper} = \frac{1}{2} k_{ijkl}^\xi (\xi_{ijkl} - \xi_{ijkl}^0)^2 \quad (3.8)$$

with  $k_{ijkl}^\xi$ ,  $\xi_{ijkl}$  and  $\xi_{ijkl}^0$  as respectively the force constant, instantaneous and equilibrium improper dihedral angles.

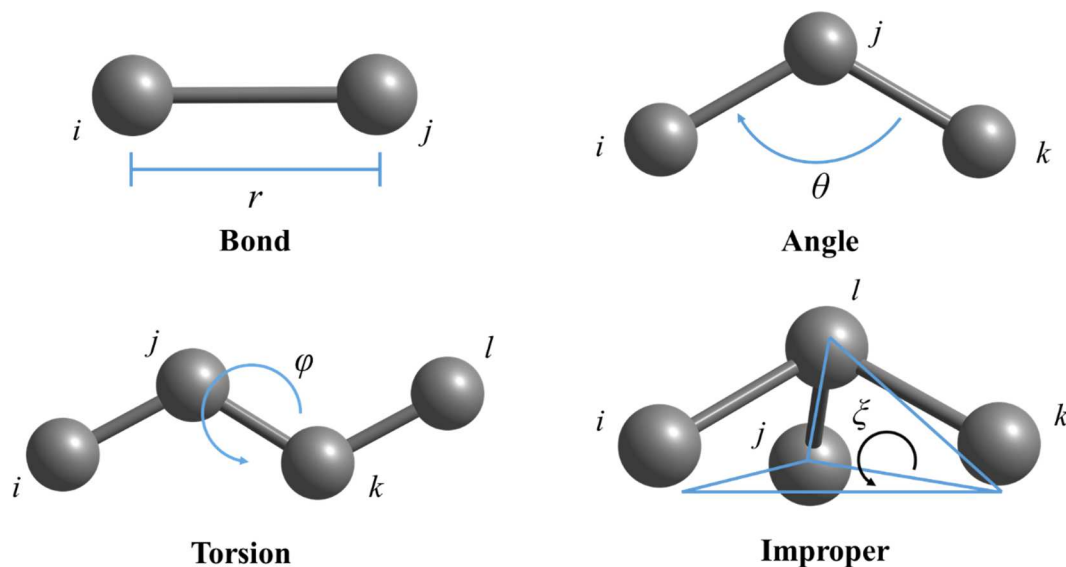


**Figure 3.1.** Pictorial representation of the two-, three- and four-body bonded interactions described by a force field.

As regards the non-bonded interaction included in the  $V_{non-bond}$  term, in the simplest case it is made by an electrostatic term plus another term representing van der Waals (vdW) interactions including repulsion and dispersion:

$$V_{non-bonded} = V_{elec} + V_{vdW} \quad (3.9)$$

The electrostatic part can be represented by a Coulomb potential between two point charges  $q_i$  and  $q_j$  at a given distance  $r_{ij}$ :

$$V_{Coulomb} = f \frac{q_i q_j}{\epsilon_r r_{ij}} \quad (3.10)$$

with  $f = \frac{1}{4\pi\epsilon_0} = 138.935 \text{ kJ mol}^{-1} \text{ nm e}^{-2}$  and  $\epsilon_r$  as the relative dielectric constant.

Different potentials can be employed for the vdW part. One of the simplest and most employed is certainly the *Lennard-Jones* (LJ) potential, described as:

$$V_{LJ} = 4\epsilon_{ij} \left( \left( \frac{\sigma_{ij}}{r_{ij}} \right)^{12} - \left( \frac{\sigma_{ij}}{r_{ij}} \right)^6 \right) \quad (3.11)$$

where  $\sigma_{ij}$  and  $\varepsilon_{ij}$  are the LJ parameters, whose physical meaning is showed in **Fig. 3.2**. These parameters are combined for each mixed pair interaction starting from the single  $\sigma_{ii}$ ,  $\sigma_{jj}$  and  $\varepsilon_{ii}$ ,  $\varepsilon_{jj}$  terms by means of appropriate combination rules. Among the most employed, the Lorentz-Berthelot rules are defined as:

$$\sigma_{ij} = \frac{1}{2}(\sigma_{ii} + \sigma_{jj})$$

$$\varepsilon_{ij} = (\varepsilon_{ii} + \varepsilon_{jj})^{1/2}$$

(3.12)

which imply an arithmetic average for  $\sigma_{ij}$  and a geometric average for  $\varepsilon_{ij}$ . Alternatively, a geometric average for both can be used, this last rule being the default in the OPLS force field.<sup>4</sup>

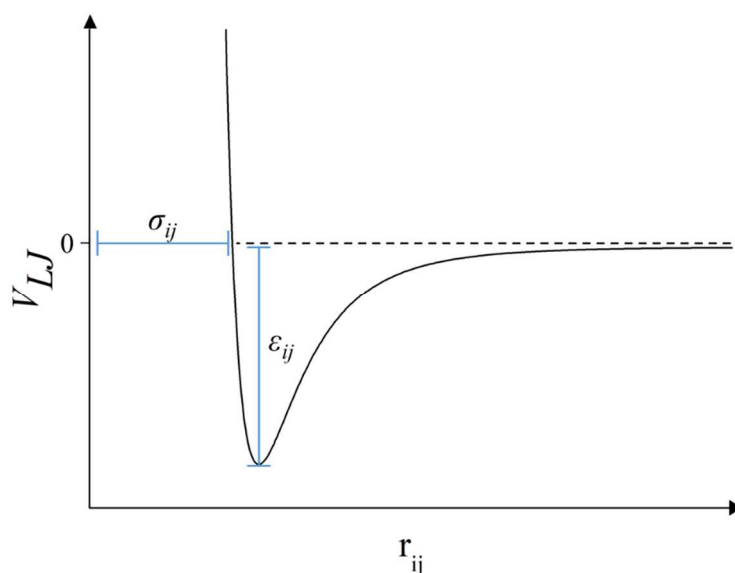


**Figure 3.2.** Schematic representation of the Lennard-Jones potential between two  $i$  and  $j$  particles in function of their reciprocal distance.

Interatomic potentials other than LJ can be employed for the vdW part. For example, the Buckingham potential includes a third term that allows a less approximated description of repulsion and dispersion:

$$V_{Buckingham} = A_{ij}e^{-B_{ij}r_{ij}} - \frac{C_{ij}}{r_{ij}^6}$$

(3.13)

where  $A_{ij}$ ,  $B_{ij}$  and  $C_{ij}$  are the Buckingham parameters. A more accurate representation of pair interactions usually implies the introduction of further terms in the potential form, at the expense of an increase in the computational cost.

### 3.1.1.1 Long-range interactions

In order to reduce the computational effort of certain simulations, non-bonded interactions are usually not calculated beyond a given cut-off distance. However, the introduction of a simple cut-off can introduce serious artifacts at least for Coulomb interactions. As a consequence, various methods have been developed for the handling of long-range electrostatics. One of the first to be introduced was the *Ewald summation*, which was initially thought for taking into account long-range electrostatic interactions of periodic images in crystals.<sup>5</sup> In this formalism, the considered system is infinite and each particle interacts also with the periodic images of the other particles. The potential is split into one term in the real space including short-range interactions, one in the reciprocal space including long-range ones, plus a constant term. For a system of  $N$  particles and their periodic images:

$$V_{Coulomb} = V_{dir} + V_{rec} + V_0 \quad (3.14)$$

with

$$V_{dir} = \frac{f}{2} \sum_{i,j}^N \sum_{n_x} \sum_{n_y} \sum_{n_z^*} q_i q_j \frac{\text{erfc}(\beta r_{ij,\mathbf{n}})}{r_{ij,\mathbf{n}}} \quad (3.15)$$

$$V_{rec} = \frac{f}{2\pi V} \sum_{i,j}^N q_i q_j \sum_{m_x} \sum_{m_y} \sum_{m_z^*} \frac{e^{-(\pi \mathbf{m}/\beta)^2 + 2\pi i \mathbf{m}(\mathbf{r}_i - \mathbf{r}_j)}}{m^2} \quad (3.16)$$

$$V_0 = -\frac{f\beta}{\sqrt{\pi}} \sum_i^N q_i^2 \quad (3.17)$$

where  $\mathbf{n} = (n_x, n_y, n_z)$  and  $\mathbf{m} = (m_x, m_y, m_z)$  are the box index vectors, the star indicating that terms with  $i = j$  are omitted for  $(0, 0, 0)$ .  $\beta$  is a parameter providing the relative weights of direct and reciprocal sums, while  $\text{erfc}(x)$  is the error function. The limit of Ewald summation is that the

computational cost of the reciprocal sum increases with  $N^2$ , making it unpractical for large systems. To improve the performance of Ewald summation, the *Particle Mesh Ewald* (PME) method was introduced.<sup>6</sup> In this case, charges are associated to a grid using interpolation and the algorithm scales as  $N \log N$ , being therefore much faster than classical Ewald.

### 3.1.1.2 Constraint algorithms

Constraints are often introduced in the interaction potential to fix bond distances and/or angles to constant values. This is particularly useful for bonds displaying very high vibration frequencies that should be treated at a quantum mechanical level of theory. This is the case of hydrogen atoms, which in some situations can show a quantum mechanical behavior like tunneling effects or vibrations with frequency  $\nu$  such that  $h\nu > k_B T$ .

Various algorithms have been developed to constraint bonds in MD simulations. One of the first to be introduced was the SHAKE algorithm, which operates by changing a set of unconstrained coordinates  $\mathbf{r}'$  to a set of  $\mathbf{r}''$  coordinates that satisfies a list of distance constraints by employing a set  $\mathbf{r}$  as reference.<sup>7</sup> This method is iterative and the computation continues until all the constraints are satisfied within a chosen tolerance. Differently, the probably more employed LINCS algorithm resets bonds to their imposed distances after an unconstrained update.<sup>8</sup> This method is non-iterative and is always made by two steps. In the first one, projections of the new obtained lengths on old ones are set to zero. In the second step, a correction is applied for the lengthening of the bonds caused by rotation. The LINCS algorithm is usually faster and more stable than SHAKE.

### 3.1.1.3 Box definition and periodic boundary conditions

*Periodic boundary conditions* (pbc) are usually employed to minimize edge effects that may arise from the simulation of a finite system. In this way, the MD system consists in the studied chemical species filling a box that is surrounded by translated copies of itself. This box is defined by three vectors  $\mathbf{a}$ ,  $\mathbf{b}$  and  $\mathbf{c}$ , which must satisfy the following relationships:

$$a_y = a_z = b_z = 0 \tag{3.18}$$

$$a_x > 0; b_y > 0; c_z > 0 \tag{3.19}$$

$$|b_x| \leq \frac{1}{2}a_x; |c_x| \leq \frac{1}{2}a_x; |c_y| \leq \frac{1}{2}b_y \quad (3.20)$$

The features of some very common box geometries are reported in **Tab. 3.1**.

**Table 3.1.** Parameters for cubic, rhombic dodecahedron and truncated dodecahedron boxes.

Box type	Image distance	Volume	Vectors			Vector angles		
			<b>a</b>	<b>b</b>	<b>c</b>	<b>&lt;bc</b>	<b>&lt;ac</b>	<b>&lt;ab</b>
Cubic	$d$	$d^3$	$d$	0	0	$90^\circ$	$90^\circ$	$90^\circ$
			0	$d$	0			
			0	0	$d$			
Rhombic dodecahedron (xy: square)	$d$	$\frac{1}{2}\sqrt{2}d^3$	$d$	0	$\frac{1}{2}d$	$60^\circ$	$60^\circ$	$90^\circ$
			0	$d$	$\frac{1}{2}d$			
			0	0	$\frac{1}{2}\sqrt{2}d$			
Rhombic dodecahedron (xy: hexagon)	$d$	$\frac{1}{2}\sqrt{2}d^3$	$d$	$\frac{1}{2}d$	$\frac{1}{2}d$	$60^\circ$	$60^\circ$	$60^\circ$
			0	$\frac{1}{2}\sqrt{3}d$	$\frac{1}{6}\sqrt{3}d$			
			0	0	$\frac{1}{3}\sqrt{6}d$			
Truncated octahedron	$d$	$\frac{4}{9}\sqrt{3}d^3$	$d$	$\frac{1}{3}d$	$-\frac{1}{3}d$	$71.53^\circ$	$109.47^\circ$	$71.53^\circ$
			0	$\frac{2}{3}\sqrt{2}d$	$\frac{1}{3}\sqrt{2}d$			
			0	0	$\frac{1}{3}\sqrt{6}d$			

### 3.1.1.4 Integrators

As an input to start a MD simulation, some information is needed. This includes the already described potential interaction  $V$  as a function of the positions  $\mathbf{r}$  of all the particles of the system, the positions themselves, and velocities  $\mathbf{v}$ . At this point, the force acting on each particle is calculated including forces coming from bonded and non-bonded interactions, in addition to those associated with constraints and/or external forces. Particles movement is then simulated by integrating Newton's

equations of motion. The last computations, starting from force calculation, are repeated for the new set of coordinates.

Many algorithms have been proposed to integrate the equations of motion step-by-step. One of the most employed is certainly the *leap-frog* algorithm,<sup>9</sup> which evaluates the velocities at half-integer time steps and employs these velocities to compute the new positions:

$$\mathbf{v}\left(t + \frac{1}{2}\Delta t\right) = \mathbf{v}\left(t - \frac{1}{2}\Delta t\right) + \frac{\Delta t}{m}\mathbf{F}(t) \quad (3.21)$$

$$\mathbf{r}(t + \Delta t) = \mathbf{r}(t) + \Delta t\mathbf{v}\left(t + \frac{1}{2}\Delta t\right) \quad (3.22)$$

The so-defined leap-frog algorithm is basically identical to the popular Verlet algorithm, *i.e.* it gives rise to identical trajectories. However, it has to be noted that velocities are not defined at the same time as positions in this scheme. Consequently, kinetic and potential energies are not defined at the same time. To solve this issue, an algorithm that uses positions and velocities computed at equal times can be defined, as for example the *Velocity Verlet* algorithm.<sup>10</sup> Here positions  $\mathbf{r}$  and velocities  $\mathbf{v}$  at time  $t$  to integrate the equations of motion and velocities of the previous half step are not required:

$$\mathbf{v}(t + \Delta t) = \mathbf{v}(t) + \frac{\Delta t}{2m}[\mathbf{F}(t) + \mathbf{F}(t + \Delta t)] \quad (3.23)$$

$$\mathbf{r}(t + \Delta t) = \mathbf{r}(t) + \Delta t\mathbf{v}(t) + \frac{\Delta t^2}{2m}\mathbf{F}(t) \quad (3.24)$$

### 3.1.1.5 Statistical ensembles, thermostats and barostats

When solving Newton's equations of motion in an MD simulation, the total energy becomes a constant of motion and the simulation is run in the microcanonical NVE ensemble (constant number of particles, volume and energy). However, to calculate some chemical-physical properties it is usually more useful to keep the system in the NVT canonical ensemble (constant number of particles, volume and temperature). To accomplish that, an algorithm for reaching the desired temperature and keeping it constant, *i.e.* a thermostat, is required. One of the first thermostats to be introduced was the

*Berendsen* algorithm, which mimics a weak coupling to an external heat bath with a given temperature  $T_0$ .<sup>11</sup> The deviation of the system from  $T_0$  is corrected according to:

$$\frac{dT}{dt} = \frac{T_0 - T}{\tau} \quad (3.25)$$

This means that temperature deviation decays exponentially with the time constant  $\tau$ , which can be chosen accordingly to the purpose of the MD run (*i.e.* for equilibrating the system or keep it equilibrated). The heat flow going into or out the system is affected by rescaling the velocities of each particle every  $n_{TC}$  steps by means of a  $\lambda$  factor expressed as:

$$\lambda = \left\{ 1 + \frac{n_{TC}\Delta t}{\tau_T} \left[ \frac{T_0}{T(t - \frac{1}{2}\Delta t)} - 1 \right] \right\}^{1/2} \quad (3.26)$$

where the parameter  $\tau_T$  is close to  $\tau$  but does not exactly match it:

$$\tau_T = \frac{N_{df}k_B\tau}{2C_V} \quad (3.27)$$

with  $C_V$  the heat capacity of the system,  $k_B$  Boltzmann's constant and  $N_{df}$  the total number of degrees of freedom. The origin of the difference between  $\tau$  and  $\tau_T$  is that the change in the kinetic energy caused by velocities rescaling is partially redistributed between kinetic and potential energies. The  $\tau/\tau_T$  ratio usually oscillates between 1 for a gas and 3 for water.

Although the *Berendsen* algorithm is very good to relax the system to a given temperature, its weak-coupling scheme is not recommended to keep the system oscillating around a constant temperature. In this case, the most appropriate method is probably the *Nosé-Hoover* thermostat which was first proposed by S. Nosé<sup>12</sup> and then modified by W. G. Hoover.<sup>13</sup> This algorithm implies a modification in the Hamiltonian of the system, since a thermal reservoir and a friction term are inserted in the equations of motion. The force related to friction is proportional to the product between the velocity of each particle and a friction parameter  $\zeta$ , which is a full-dynamic quantity with its own momentum  $p_\zeta$ . Equations of motion are therefore modified as:

$$\frac{d^2 \mathbf{r}_i}{dt^2} = \frac{\mathbf{F}_i}{m_i} - \frac{p_\xi}{Q} \frac{d\mathbf{r}_i}{dt} \quad (3.28)$$

and the equation of motion for  $\xi$  is:

$$\frac{dp_\xi}{dt} = (T - T_0) \quad (3.29)$$

The  $Q$  constant determines the strength of the coupling and is usually referred to as the “mass parameter” of the reservoir. It is connected to  $\tau_T$  by:

$$Q = \frac{\tau_T^2 T_0}{4\pi^2} \quad (3.30)$$

The total energy for a system of  $N$  particles therefore becomes:

$$\hat{H}(\mathbf{p}, \mathbf{r}) = \sum_{i=1}^N \frac{\mathbf{p}_i^2}{2m_i} + V(\mathbf{r}_1, \mathbf{r}_2, \dots, \mathbf{r}_N) + \frac{p_\xi^2}{2Q} + N_{df} k_B T \xi \quad (3.31)$$

Even though NVT conditions are often very useful to simulate a system, most of the chemical transformation in nature occur at constant pressure. Therefore, simulating the system in NPT conditions (constant number of particles, pressure and temperature) is often desirable. As a consequence, the introduction of a barostat is required and the volume becomes a dynamical variable that changes during simulation time. With the *Berendsen* algorithm,<sup>11</sup> the coordinates and box vectors are rescaled every  $n_{PC}$  steps by means of a kinetic relaxation of the pressure given a reference pressure  $P_0$  according to:

$$\frac{dP}{dt} = \frac{P_0 - P}{\tau_p} \quad (3.32)$$

where  $\tau_p$  is the pressure coupling parameter. Another popular algorithm is the *Parrinello-Rahman* barostat,<sup>14</sup> where the box vectors represented as the matrix  $\mathbf{b}$  obey the following equation of motion:

$$\frac{d\mathbf{b}^2}{dt^2} = V\mathbf{W}^{-1}\mathbf{b}'^{-1}(\mathbf{P} - \mathbf{P}_0) \quad (3.33)$$

with  $V$  as the volume of the box and  $\mathbf{W}$  as the matrix parameter determining the strength of the coupling and basically how much the box can be deformed. Its inverse is defined as:

$$\mathbf{W}_{ij}^{-1} = \frac{4\pi^2\beta_{ij}}{3\tau_p^2L} \quad (3.34)$$

where  $\beta$  is the isothermal compressibility and  $L$  the largest box matrix element. As for the Nosé-Hoover thermostat, the equations of motion of the particles are also changed with the introduction of the Parrinello-Rahman barostat:

$$\frac{d^2\mathbf{r}_i}{dt^2} = \frac{\mathbf{F}_i}{m_i} - \mathbf{M} \frac{d\mathbf{r}_i}{dt} \quad (3.35)$$

with

$$\mathbf{M} = \mathbf{b}^{-1} \left( \mathbf{b} \frac{d\mathbf{b}'}{dt} + \frac{d\mathbf{b}}{dt} \mathbf{b}' \right) \mathbf{b}'^{-1} \quad (3.36)$$

Also in this case, the weak-coupling Berendsen algorithm is suggested when the system is far from the desired pressure value, while Parrinello-Rahman is good for maintaining the system around the desired pressure and therefore particularly suggested for calculating thermodynamic properties in “true” NPT conditions.

### 3.1.1.6 Free energy calculations

One of the most useful physical observable that is possible to calculate with MD simulations is the estimated free energy for a given process. These quantities are often highly desirable to compute, as they indicate how much favorable a process is and the direction that the thermodynamic system will take spontaneously. Helmholtz free energy  $F$  of a system in the NVT ensemble is given by:

$$F = -\frac{1}{\beta} \ln Q \quad (3.37)$$

where  $\beta = 1/k_B T$  and  $Q$  is the canonical partition function. For a system of  $N$  particles at the thermodynamic equilibrium, it can be expressed as:

$$Q = \frac{1}{h^{3N} N!} \int \int e^{-\beta H(\mathbf{p}, \mathbf{r})} d\mathbf{p} d\mathbf{r} \quad (3.38)$$

with  $h$  as Planck's constant. It is straightforward to say that in NPT conditions Gibbs free energy (usually denoted as  $G$ ) is defined. In condensed phases like liquids, which are hardly compressible, Helmholtz and Gibbs free energies can be numerically very similar.

An absolute free energy can be calculated only in case an analytical expression for the partition function can be obtained, which is practically possible only for very small systems with simple Hamiltonians. If this is not possible, one has to limit to the difference in free energy between the system of interest and a given reference state. In case of an ideal gas or an ideal crystal, the free energy of the reference state is known, and the absolute free energy of the system can still be calculated. In these cases, an analytical expression for  $Q$  is indeed possible owing to lack of interactions between the particles (ideal gas) or symmetry simplifications (ideal crystal).<sup>15</sup> However, defining such a reference state for a liquid phase is usually not allowed. In this latter case, it is only possible to calculate relative free energy differences between two states A and B of the system:

$$\Delta F_{BA} = F_B - F_A = -\beta^{-1} \ln \frac{Q_B}{Q_A} \quad (3.39)$$

This is also usually more interesting from a chemical point of view, since A and B (*i.e.*  $H_A$  and  $H_B$ ) can differ for example in how particles interact among each other, allowing to associate free energies differences to chemical processes as the binding of a compound to a substrate or the interaction of a species with a solvent.

As regards free energy calculations performed in molecular simulations, they consist of three fundamental ingredients: *i*) the Hamiltonian employed to represent the system; *ii*) the sampling used to generate representative configurations of the system; *iii*) a method for calculating the free energy difference.<sup>15-18</sup> As regards point *i*), the Hamiltonian should be chosen such that all the configurations present the correct relative probability. Practically, it should be computationally affordable in order to allow sufficient sampling, but enough accurate to estimate a free energy in a reliable way.

Point *ii*) strictly depends on the nature of states A and B. In case they present an intersection region of their relative energies, it is sufficient to sample adequately representative configurations at the intersection region.<sup>15</sup> However, if they do not overlap, it is necessary to find an Hamiltonian connecting the two A and B states. This can be carried out by defining a combined Hamiltonian  $H_{comb}$  that will be in some way a function of the end-state Hamiltonians  $H_A$  and  $H_B$ . One of the most employed strategies is to make the Hamiltonian dependent on a coupling parameter  $\lambda$  such as for a certain value (*e.g.*  $\lambda = 0$ ),  $H_{comb} = H_A$  (or, equivalently,  $V_{comb} = V_A$ ) and for another value (*e.g.*  $\lambda = 1$ ),  $H_{comb} = H_B$  (or  $V_{comb} = V_B$ ). In this case, sampling of configurations can be done by windowing between different values of  $\lambda$ . For each value, an independent simulation has to be run with the system constrained to that particular  $\lambda$ . In case of the decoupling of non-bonded interactions, the Coulomb potential between two particles with charges varying with  $\lambda$  can be rewritten as:

$$V_{Coulomb} = \frac{f}{\epsilon_r r_{ij}} [(1 - \lambda)q_i^A q_j^A + \lambda q_i^B q_j^B] \quad (3.40)$$

while for a LJ interaction:

$$V_{LJ} = \frac{(1 - \lambda)4\epsilon_A\sigma_A^{12} + \lambda 4\epsilon_B\sigma_B^{12}}{r_{ij}^{12}} - \frac{(1 - \lambda)4\epsilon_A\sigma_A^6 + \lambda 4\epsilon_B\sigma_B^6}{r_{ij}^6} \quad (3.41)$$

However, this simple linear combination can lead to numerical problems in some cases. Among them, the calculation of free energies of solvation of a species in a solvent, performed by making the solute appearing/disappearing in the medium, can give problems if this species interacts *via* LJ due to some singularities connected with this form of potential.<sup>15</sup> In fact, if we think about a Coulomb and LJ interacting particle in a solvent, there will be one moment in which the particle is nearly disappearing ( $\lambda$  close to 0 or 1, depending on the chosen path). In this situation, the interaction energy and in particular the repulsion term will be weak enough to cause penetration effects. To circumvent this issue, the LJ and/or electrostatic potentials can be replaced by *soft core* potentials.<sup>19–23</sup> In their general form, they can be expressed as:

$$V_{sc}(r) = (1 - \lambda)V^A(r_A) + \lambda V^B(r_B) \quad (3.42)$$

with

$$r_A = (\alpha\sigma_A^6\lambda^p + r^6)^{\frac{1}{6}} \quad (3.43)$$

$$r_B = [\alpha\sigma_B^6(1 - \lambda)^p + r^6]^{\frac{1}{6}} \quad (3.44)$$

$V_A$  and  $V_B$  are the normal LJ and electrostatic potentials in states A ( $\lambda = 0$ ) and B ( $\lambda = 1$ ),  $\alpha$  can be referred to as the “soft-core parameter”,  $p$  as the “soft-core power” and  $\sigma$  is the radius of the interaction. The effect of the “soft-core” potential is that, for intermediate  $\lambda$  values,  $r_A$  and  $r_B$  alter the interaction only to a little extent for  $r > \alpha^{1/6}\sigma$ , while it turns from the soft-core interaction to a constant value for smaller distances, so that the singularity in the potential at  $r = 0$  is never reached.

Once the sampling of the various configurations has been carried out, there are several different ways to face point *iii*), since a huge number of available free energy estimators has been developed. In general, it is possible to divide them into two families: *thermodynamic integration* (TI) and *free energy perturbation* (FEP) methods. In the former case, the free energy along a thermodynamic path of  $K$  states is calculated as a weighted sum of ensemble averages of the potential energy derivative with respect to  $\lambda$  derivatives:

$$\Delta F = \sum_{i=1}^K W_i \left\langle \frac{\partial V}{\partial \lambda} \right\rangle_{\lambda} \quad (3.45)$$

where  $W_i$  are weighting factors. As regards FEP, different methods are available. For example, it is possible to employ an exponential averaging scheme related to the potential energies of two adjacent windows:<sup>22</sup>

$$\Delta F_{ij} = -\frac{1}{\beta} \ln \langle e^{-\beta \Delta V_{ij}} \rangle_i \quad (3.46)$$

In other popular methods like the *Bennett Acceptance Ratio* (BAR),<sup>24</sup> the free energy difference between the two adjacent states  $i$  and  $j$ , each constituted of  $N_i$  and  $N_j$  microstates, is calculated by numerically solving an implicit function of  $\Delta V_{ij}$ :

$$\frac{1}{\langle 1 + e^{\beta(\Delta V_{ij} - C)} \rangle_i} = \frac{1}{\langle 1 + e^{-\beta(\Delta V_{ji} - C)} \rangle_j} \quad (3.47)$$

with

$$C = \Delta F_{ij} + \frac{1}{\beta} \ln \left( \frac{N_j}{N_i} \right) \quad (3.48)$$

It has to be noted that in BAR both forward and direct  $\Delta V_{ij}$  and  $\Delta V_{ji}$  potential energy differences are included in the analysis.

### 3.1.1.7 Umbrella sampling

In case the continuous parameter which links the two thermodynamic states is defined in geometric terms, *e.g.* as a direction (vector) or a torsion, an *umbrella sampling* simulation can be performed.<sup>25</sup> The path along which the system evolves is called *reaction coordinate* ( $\zeta$ ). In this case, the partition function  $Q$  is dependent from  $\zeta$  and can be defined as the probability of finding the system in an interval  $d\zeta$  around  $\zeta$ . The free energy along the reaction coordinate, defined as  $F(\xi) = -\frac{1}{\beta} \ln Q(\xi)$ , is called *potential of mean force* (PMF). Sampling of different configurations along  $\zeta$  can be done by means of a bias, an additional energy term that is applied to the system to make it passing from one state to another. Each window can be then simulated independently by constraining the system in one state with a harmonic potential, which also allows oscillation and overlap within each window.<sup>26</sup> To calculate the PMF, results from different windows can be combined in different ways like the weighted histogram analysis method (WHAM)<sup>27</sup> or by umbrella integration.<sup>28</sup>

## 3.1.2 *Ab initio* Molecular Dynamics

Strictly speaking, in classical MD the total interaction potential is made by additive pair potentials that are determined in advance, either empirically or based on fitting procedures of *ab initio* data. Otherwise, different methods have been proposed to include also the electronic degrees of freedom in the dynamics of the system. For example, in *Born-Oppenheimer Molecular Dynamics* (BOMD) the time-independent Schrödinger equation for a given set of nuclear coordinates is iteratively solved for each step of the dynamics. By assuming Newton's notation for partial derivatives, the equations of motion are given by:

$$m_i \ddot{\mathbf{r}}_i = -\nabla_i \min_{\Psi} \langle \Psi | \hat{H} | \Psi \rangle; \hat{H}\Psi = E\Psi \quad (3.49)$$

where  $m_i$  masses and  $r_i$  positions are referred to the  $i$ -th nucleus, while  $\hat{H}$ ,  $\Psi$  and  $E$  are respectively the electronic Hamiltonian, wave function and energy. The  $\min_{\Psi}$  notation indicates that in each MD step the minimum of  $\langle \hat{H} \rangle$  has to be reached, *i.e.* the electronic wave function is optimized at a desired level of theory. This task is very computational demanding, making BOMD a difficultly affordable technique.

A suitable alternative is *Car-Parrinello Molecular Dynamics* (CPMD).<sup>29</sup> Here the basic idea is that the electronic degrees of freedom can evolve in time classically along with nuclear motion. This can be done by means of a quantum-mechanical adiabatic time-scale separation between the fast electronic and slow nuclear motion by transforming this into a classical-mechanical adiabatic energy-scale separation in the framework of molecular dynamics.<sup>30</sup> To do so, Car and Parrinello introduced new  $\mathcal{L}_{CP}$  Lagrangians expressed as:

$$\mathcal{L}_{CP} = \sum_{i=1}^N \frac{1}{2} m_i \dot{\mathbf{r}}_i^2 + \sum_{j=1}^{N_e} \frac{1}{2} \mu_j \langle \dot{\psi}_j | \dot{\psi}_j \rangle - \langle \Psi | \hat{H} | \Psi \rangle + \text{constraints} \quad (3.50)$$

where  $T_n = \sum_{i=1}^N \frac{1}{2} m_i \dot{\mathbf{r}}_i^2$  and  $T_e = \sum_{j=1}^{N_e} \frac{1}{2} \mu_j \langle \dot{\psi}_j | \dot{\psi}_j \rangle$  are the kinetic energies of the  $N$  nuclei and fictitious kinetic energies of  $N_e$  electronic orbitals  $\psi_j$ .  $V_e = \langle \Psi | \hat{H} | \Psi \rangle$  is the potential energy related to the electronic wavefunction  $\Psi$ . The ‘‘constraints’’ are functions of the nuclear positions and of the set of orbitals, introduced to guarantee conservation of orbitals orthonormality.  $\mu_j$  are the fictitious masses assigned to the orbital degrees of freedom. The Newtonian equations of motion become:

$$\frac{d}{dt} \frac{\partial \mathcal{L}}{\partial \dot{\mathbf{r}}_i} = \frac{\partial \mathcal{L}}{\partial \mathbf{r}_i}; \quad \frac{d}{dt} \frac{\partial \mathcal{L}}{\partial \dot{\psi}_j^*} = \frac{\partial \mathcal{L}}{\partial \psi_j^*} \quad (3.51)$$

with  $\psi_j^* = \langle \psi_j |$ . The equations of motion in the CPMD approach are therefore given by:

$$m_i \ddot{\mathbf{r}}_i = - \frac{\partial}{\partial \mathbf{r}_i} \langle \Psi | \hat{H} | \Psi \rangle + \frac{\partial}{\partial \mathbf{r}_i} (\text{constraints}) \quad (3.52)$$

$$m_j \ddot{\psi}_j = - \frac{\partial}{\partial \psi_j^*} \langle \Psi | \hat{H} | \Psi \rangle + \frac{\partial}{\partial \psi_j^*} (\text{constraints}) \quad (3.53)$$

Basically, in the Car-Parrinello method the nuclei evolve in time at a definite physical temperature, while a fictitious temperature is associated to the electronic degrees of freedom. If this fictitious temperature is low enough, the electronic ensemble stays close to its (instantaneous) minimum energy  $\min_{\Psi} \langle \Psi | \hat{H} | \Psi \rangle$  (*i.e.* close to the *Born-Oppenheimer surface*). If the system is in its electronic ground-state corresponding to the nuclear configuration of that time-step, forces acting on electrons vanish.<sup>3</sup> Therefore, a CPMD run must always start with an optimization of the wave function of the system to reach the ground-state for the initial configuration of nuclear positions. Such an optimized wave function is supposed to stay close to its Born-Oppenheimer surface for each step of the dynamics if kept fixed to a sufficiently low temperature. Given that the Lagrangian in **Eq. 3.50** is time-independent, there should be a conserved energy quantity  $E_{cons}$  defined as:

$$E_{cons} = T_n + T_e + V_e \quad (3.54)$$

while the physical energy of the system  $E_{phys}$  can be expressed as:

$$E_{phys} = T_n + V_e = E_{cons} - T_e \quad (3.55)$$

Therefore, if  $T_e \ll E_{cons}$ , *i.e.* if the fictitious electronic kinetic energy  $T_e$  is very small in comparison to the total energy,  $E_{phys}$  remains constant on the desired time scale. Strictly speaking, the validity of the Car-Parrinello approach is guaranteed by the maintenance of adiabaticity between the fictitious electrons dynamics and nuclear motion. In poor terms, if no heat exchange occurs between the “hot nuclei” and the “cold electrons”. This adiabatic condition is maintained if  $T_e$  is kept oscillating around a small and constant value. Thus,  $T_e$  can be considered as a measure of the deviation from the Born-Oppenheimer surface.

## 3.2 X-ray absorption spectroscopy

In an X-ray absorption spectroscopy (XAS) experiment, a sample is exposed to an electromagnetic radiation in the X-ray energy field. Some of these X-rays are absorbed and an *absorption coefficient*  $\mu(E)$  is measured as a function of the incident photon energy  $E = \hbar\omega$ . This causes the excitation and/or ejection of a core electron of the absorbing atom, which is called *photoabsorber*. In a XAS spectrum, an overall decrease of the absorption with increasing energy can be observed, with the exception of

some sharp peaks called *edges*. These edges are provoked by transitions of core electrons to an unoccupied level or to the continuum. This occurs when the incident photon energy is greater than the energy that is necessary to remove the electron from its ground state ( $E_0$ ). The electron is ejected from the photoabsorber and is now called a *photoelectron*, leaving behind him a *core-hole*. In this way, each absorption edge can be associated to a specific element and this makes XAS a selective technique that allows understanding the atomic species in a material. The nomenclature of the various edges is related to the origin of the excited electron: K-edge is referred to the innermost  $1s$  electron,  $L_1$ -edge to the  $2s$  electron,  $L_2$ - and  $L_3$ -edge to the  $2p$  electrons with  $^2P_{1/2}$  and  $^2P_{3/2}$  electronic states, respectively (**Fig. 3.3**).

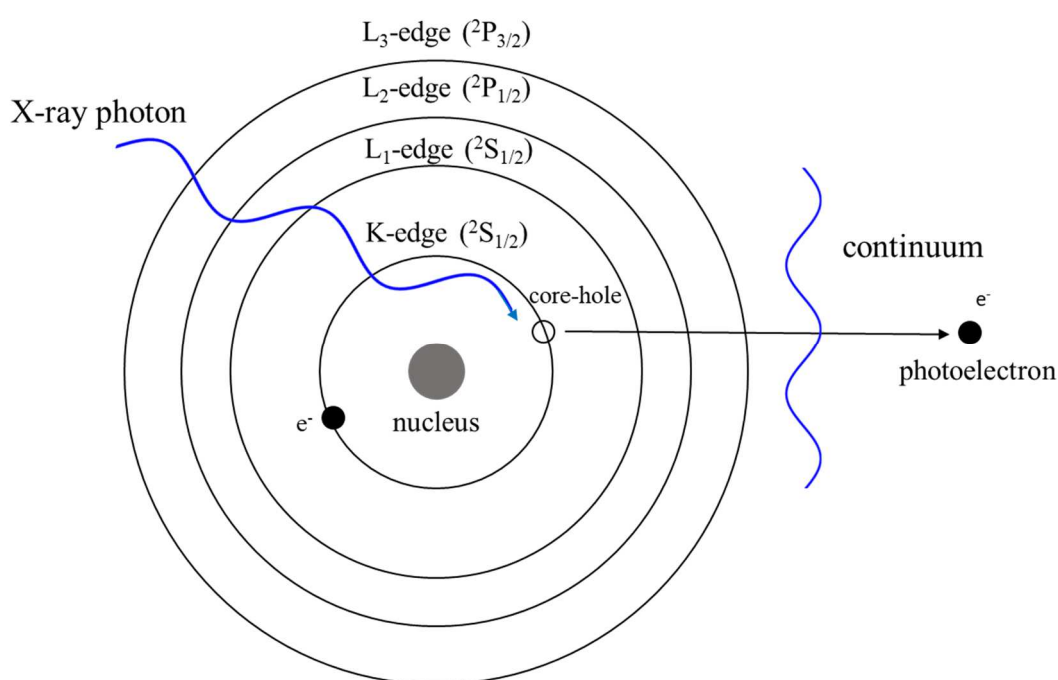


**Figure 3.3.** Pictorial representation of the transitions that can take place at the various absorption edges.

Once ejected, the photoelectron possesses a kinetic energy  $E_k = E - E_0$ , *i.e.* equal to the energy  $E$  of the incident photon minus whatever energy was necessary to remove it from its ground state. The photoelectron can be now described as a spherical wave radiating out in all directions with a  $\lambda$  wavelength given by:

$$\lambda = \frac{h}{p} \quad (3.56)$$

with  $h$  Planck's constant and  $p$  momentum of the photoelectron. The momentum is related to the kinetic energy by:

$$E_k = \frac{p^2}{2m_e} \quad (3.57)$$

where  $m_e$  is the mass of an electron. The photoelectron wavenumber  $k$  is equal to  $2\pi/\lambda$ , so it can be put in relationship with the photon energy by:

$$k = \frac{1}{\hbar} \sqrt{2m_e(E - E_0)} \quad (3.58)$$

Therefore, when we are scanning through the incident photon energy, we are also scanning through the photoelectron wavenumber.

A XAS spectrum can be divided into two regions: the XANES (*X-ray Absorption Near Edge Structure*), usually considered as that located up to 50 eV after the absorption edge, and the EXAFS part (*Extended X-ray Absorption Fine Structure*) which is higher in energy (**Fig. 3.4**). This arbitrary division is made because XANES and EXAFS can provide different, although complementary, structural information, the former being more sensitive to the three-dimensional displacement of the scattering atoms around the photoabsorber, the latter to their average distances.<sup>31</sup> In addition, a different treatment of the photoelectron phenomenology is usually needed between XANES and EXAFS. In both cases, approximations have to be made since a full quantum-mechanical description of the X-ray absorption is not possible. The ejected electron is usually treated as a quasi-particle moving in an effective potential taking into account both the interactions with the other electrons of the photoabsorber and the potential generated by the scattering atoms. In general, the higher the kinetic energy of the photoelectron, the less it will be influenced by this local potential. Consequently, XANES should need a more precise description of the potential affecting the photoelectron, while further approximations can be made for EXAFS.<sup>31</sup> For example, this description can be made in the framework of the widely employed *muffin-tin approximation*, where a spherical potential is centered on each scattering atom and a constant value is present in the interstitial regions.

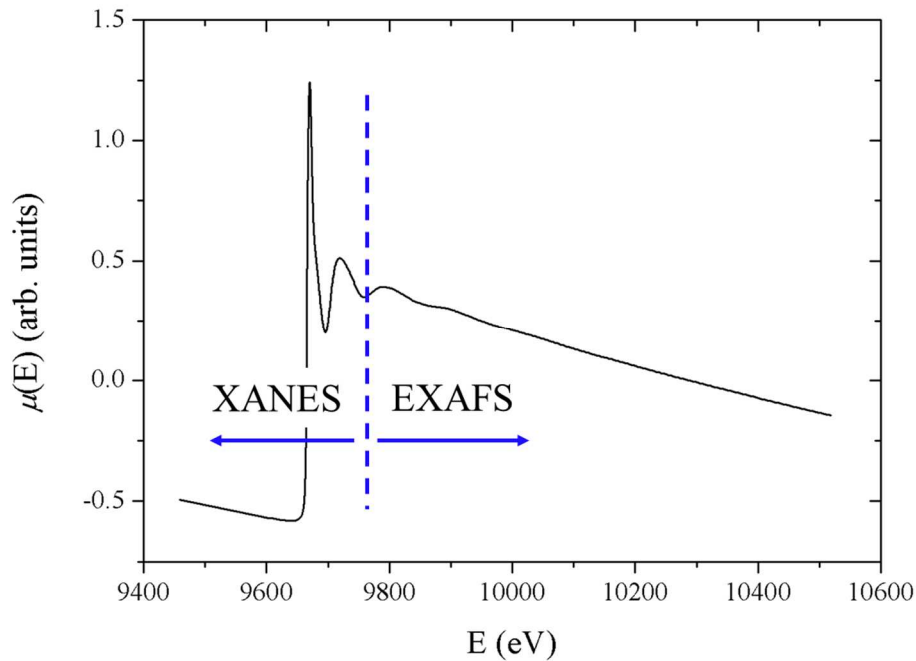


**Figure 3.4.** Division of a XAS spectrum into the XANES and EXAFS energy regions.

As regards the destiny of the photoelectron, once it has passed the continuum it can be scattered by the neighboring atoms and return back to the photoabsorber.<sup>32</sup> Being a quasi-particle, we can imagine it as doing different paths between these neighboring atoms. Being also a wave, it can interfere constructively or destructively, this process producing the typical oscillatory structures in the XAS spectrum above the threshold energy. Given the relationship between absorption coefficient and *cross-section*, this part of the spectrum can be defined in function of  $k$  as the relative oscillation with respect to a total atomic cross-section  $\sigma_0^t$  normalized for the atomic cross section of the considered edge  $\sigma_0$ :<sup>33</sup>

$$\chi(k) = \frac{[\sigma(E) - \sigma_0^t(E)]}{\sigma_0(E)} \quad (3.59)$$

A general expression which gives a quantitative parametrization of the  $\chi(k)$  signal has been proposed by Sayers *et al.*:<sup>34</sup>

$$\chi(k) = S_0^2 \sum_i N_i \frac{f_i(k)}{kR_i^2} e^{-\frac{2R_i}{\lambda(k)}} e^{-2k^2\sigma_i^2} \sin[2kR_i + \varphi_i(k)] \quad (3.60)$$

The first observation is that the EXAFS spectrum is a sum of contributions, each derived from a different neighboring atom. In case the photoelectron path involves the same type of atom at the same average distance, we talk about the *degeneracy* of that path, which is taken into account by the term  $N_i$ . In addition, the description given until now is based on the assumption that the photoelectron scatters *elastically* on a neighboring atom surrounding the photoabsorber. However, other things can happen to the photoelectron, *e.g.* it can scatter *inelastically* such that some of its energy is lost and its wavelength is changed, or it could not scatter at all. Each of these phenomena possess a probability which is included in the  $f_i(k)$  term, being this related to the probability of scattering elastically. It has to be underlined that this term depends directly on  $k$  and this dependence is different for different elements. For example, it comes obvious that a big atom with a huge number of electrons possess a higher scatter probability than an atom with smaller atomic number. This statement points out that the selectivity of EXAFS is not only about the photoabsorber, but also for the scattering atoms, at least if their atomic numbers are not very close.

Furthermore, the scattering atom is not expected to reverse the direction of the photoelectron instantaneously, but in reality the photoelectron phase is shifted of a certain extent after the interaction with a neighboring atom. The *phase-shift* parameter  $\varphi_i(k)$  is related to this issue. This dephasing term is still a function associated to both the photoabsorber and the scattering atom, therefore introducing further selectivity in XAS.

Another information that makes EXAFS a useful technique is its high sensitivity (usually up to 0.02 Å) on the average distance of the scattering atoms from the photoabsorber. This quantity is expressed by  $R_i$ , representing half the path length of the photoelectron. The presence of  $R_i^2$  dividing the  $f_i(k)$  term means that the scattering probability drops with the square of the distance, as the spherical wave of the photoelectron spreads out as the distance from the photoabsorber increases.

Besides the fall of the amplitude with  $R_i^2$ , many other events can damage the wave function of the photoelectron. For example, it can scatter inelastically and excite a valence electron from a scattering atom. In addition, the core-hole has a limited lifetime and eventually an electron from a higher orbital will fall into it, resulting in a fluorescence phenomenon or in the ejection of another electron. These effects have a strong dependence on  $R_i$ , since the farther the photoelectron goes, the higher is the probability for these events to occur. This probability is included in the  $\lambda(k)$  function called *mean free path* of the photoelectron. It is primarily because of this term that EXAFS is a short-range sensitive method, *i.e.* among 4 - 5 Å from the photoabsorber.<sup>32</sup>

In addition, the initial state of the photoabsorber is not the same as the final state. In the final state, the ejected photoelectron has left a core-hole in the photoabsorber. As a consequence, the other electrons feel a higher positive charge from the nucleus because of a smaller shielding effect and there

is a contraction of their orbits. These issues may attenuate the amplitude of the oscillating signal and are taken into account by the *amplitude reduction factor*  $S_0^2$ . Typical values for this parameter should be comprised between 0.85 and 1.0 in a fitting procedure, *i.e.* its spectral weight should not go beyond 15 % of the total amplitude, otherwise the starting model is probably wrong. All these phenomena described since here can be divided into two groups: *extrinsic losses*, related to events after the formation of the core-hole (included in  $\lambda(k)$ ), and *intrinsic losses*, which are connected with the formation of the core-hole and (included in  $S_0^2$ ).

The  $e^{-2k^2\sigma_i^2}$  term introduces a dumping of the XAS signal with the square of the so-called *Debye-Waller factor*  $\sigma^2$ , often referred to also as *second cumulant*. It is equivalent to a mean square relative displacement (MSRD), that is the square of the standard deviation of half the path length. This takes into account two kinds of disorder in the cluster: static and thermal. *Static disorder* can arise from defects in a crystal, which are basically scattered at random distances throughout all the material. *Thermal disorder* is due to oscillations of atoms around equilibrium positions due to thermal vibrations. Amorphous materials and liquids are the extreme case, since no long-range order can be discerned and the distinction between static and thermal disorder is not possible anymore.

### 3.2.1 EXAFS analysis

If the photoelectron scatters only on one single neighboring atom and comes back to the photoabsorber, a *single-scattering* (SS) has occurred. If its path includes two or more scattering atoms, we talk about *multiple-scattering* (MS). SS terms probe a two-particle distribution, while MS terms are able to probe the presence of several atoms around the photoabsorber, *i.e.* they probe the  $n$ -body distribution. MS effects are dominant in the XANES region, and this is what makes the low-energy part of the XAS spectrum so sensitive to the three-dimensional arrangement of the scattering atoms. However, the treatment of MS paths has been for a long time the subject of some debate also for what concerns the EXAFS region, limiting the applicability of standard methods for EXAFS analysis to SS approximation for many years. The general problem is that of finding a linear relationship between the geometry of the analyzed cluster and the XAS signal. In terms of a MS series, the XAS cross-section  $\sigma(\omega)$  can be expressed as follows:<sup>33</sup>

$$\sigma(\omega) = \sigma_0 \left( 1 + \sum_{i \neq 0} \chi_2^{0i0} + \sum_{\substack{i \neq j \\ i \neq 0, j \neq 0}} \chi_3^{0ij0} + \sum_{\substack{i \neq j \neq k \\ i \neq 0, k \neq 0}} \chi_4^{0ijk0} + \dots \right) \quad (3.61)$$

where each  $\chi_n$  term is related to a scattering path starting and ending at the photoabsorber  $0$ , with the only constraint that successive sites  $i, j, k, \dots$  must be different. A linear relationship between geometry and signal is preserved up to  $n = 3$ , since the  $\chi_2$  and  $\chi_3$  terms probe a two- and three-particle distributions:  $\chi_2$  probe the relative positions of particles  $0$  and  $i$ ,  $\chi_3$  of particles  $0, i$  and  $j$ . However, starting from  $\chi_4$ , this linearity is lost and the relationship between geometry and signal starts to be cumbersome. In fact,  $\chi_4$  probes not only the four-body distribution between  $0, i, j$  and  $k$ , but also lower-order distributions with paths like  $0i0i0$  or  $0i0k0$  (two- and three-particle order, respectively) (**Fig. 3.5**). In general, for order  $n$  we have paths involving  $2 \dots n$  particles if  $n$  is even,  $3 \dots n$  particles if  $n$  is odd.

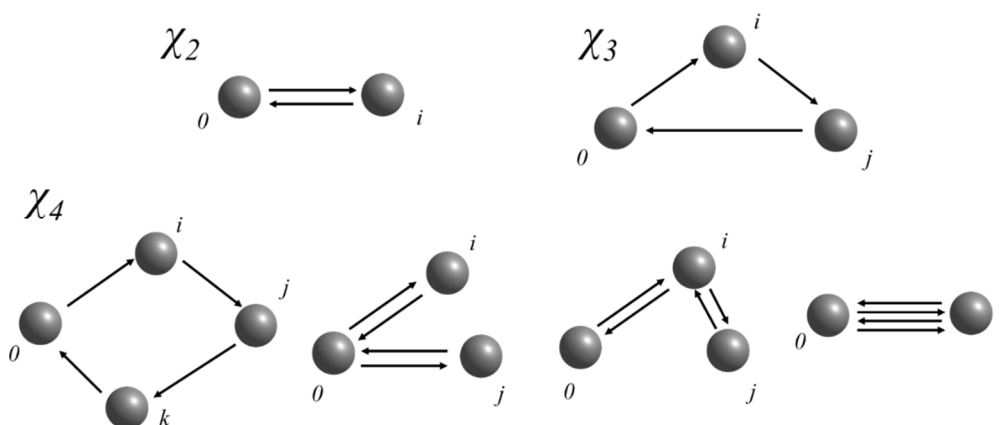


**Figure 3.5.** Pictorial view of the possible photoelectron paths included in the  $\chi_2$ ,  $\chi_3$  and  $\chi_4$  terms.

For this reason, reorder of the MS series seems necessary. Strictly speaking, it can be affirmed that the different approaches in EXAFS data analysis differ among each other basically for the different treatment of the MS theory. One of the first packages to be developed with the aim of being user-oriented was the EXCURVE software by the Daresbury research group.<sup>35</sup> Another popular code is the FEFF package,<sup>36</sup> which uses *ad hoc* amplitude cut-off criteria to select the most relevant MS paths and reduce their prohibitive high number.

A total different approach has been followed in the GNXAS method.<sup>33,37</sup> Here the total cross-section  $\sigma(0, i, j, \dots, n)$  for a system of  $n + 1$  atoms ( $n$  neighbors plus the photoabsorber) has been reordered as:

$$\sigma(0, i, j, \dots n) = \sigma_0 + \sum_i \sigma^{(2)}(0, i) + \sum_{i,j} \sigma^{(3)}(0, i, j) + \sum_{i,j,k} \sigma^{(4)}(0, i, j, k) + \dots + \sigma^{(n)}(0, i, j, \dots n) \quad (3.62)$$

where  $\sigma(0, i)$  is the cross section of the structure including particles 0 and  $i$  only,  $\sigma(0, i, j)$  including 0,  $i$  and  $j$  and so on. Therefore, the total cross section is expressed as a sum of the atomic cross-section in addition to all the possible 2-body, 3-body ... contributions. This series has a finite number of terms only for a finite number of atoms, but the  $n$ -body contributions are expected to be smaller and smaller as  $n$  and/or the atomic distances increase. Therefore, it can be easily argued that the sum possesses excellent convergence properties, so that relative small numbers of atoms can be considered in a practical case.<sup>38</sup>

Provided that the XAS oscillation is defined as in **Eq. 3.59** and by introducing the dimensionless quantities  $\gamma^{(n)} = \sigma^{(n)}/\sigma_0$ , XAS structural signal can be rewritten as:

$$\chi(0, i, j, \dots n) = \sum_i \gamma^{(2)}(0, i) + \sum_{i,j} \gamma^{(3)}(0, i, j) + \sum_{i,j,k} \gamma^{(4)}(0, i, j, k) + \dots + \gamma^{(n)}(0, i, j, \dots n) \quad (3.63)$$

The  $\gamma^{(n)}$  signals are the central quantities in the GNXAS approach, as each of them is related to a precise  $n$ -body arrangement. Like the  $\chi_n$  terms, they are oscillating functions of the photoelectron wave-vector modulus  $k$  of the type  $A(k)\sin[2kR+\varphi(k,R)]$ , where  $A(k)$  is the amplitude function characteristic of the backscattering atom and  $\varphi(k)$  is the already described phase function. In the two-body case,  $\gamma^{(2)}$  can be expanded in the MS series as:

$$\gamma^{(2)}(0, i) = \chi_2^{0i0} + \chi_4^{0i0i0} + \chi_6^{0i0i0i0} + \chi_8^{0i0i0i0i0} + \dots \quad (3.64)$$

while for  $\gamma^{(3)}$ :

$$\begin{aligned} \gamma^{(3)}(0, i, j) = & 2\chi_3^{0ij0} + 2\chi_4^{0i0j0} + \chi_4^{0ijj0} + \chi_4^{0jij0} + 2(\chi_5^{0i0ij0} + \chi_5^{0j0ji0} + \chi_5^{0i0ji0} + \\ & + \chi_5^{0j0i0} + \chi_5^{0ijji0}) + \dots \end{aligned} \quad (3.65)$$

In other words,  $\gamma^{(n)}$  is the sum of all the possible MS signals involving *all and only* the considered  $n$ -bodies in any possible sequence (**Fig. 3.6**). Being each of these series potentially infinite, in a fitting procedure they have to be cut to a certain limit. Usually, the number of required MS terms depends

on bond distances and atomic numbers of the involved species. For short bonds, terms up to  $\chi_6$  may be required, while for long bonds terms up to  $\chi_4$  may suffice.

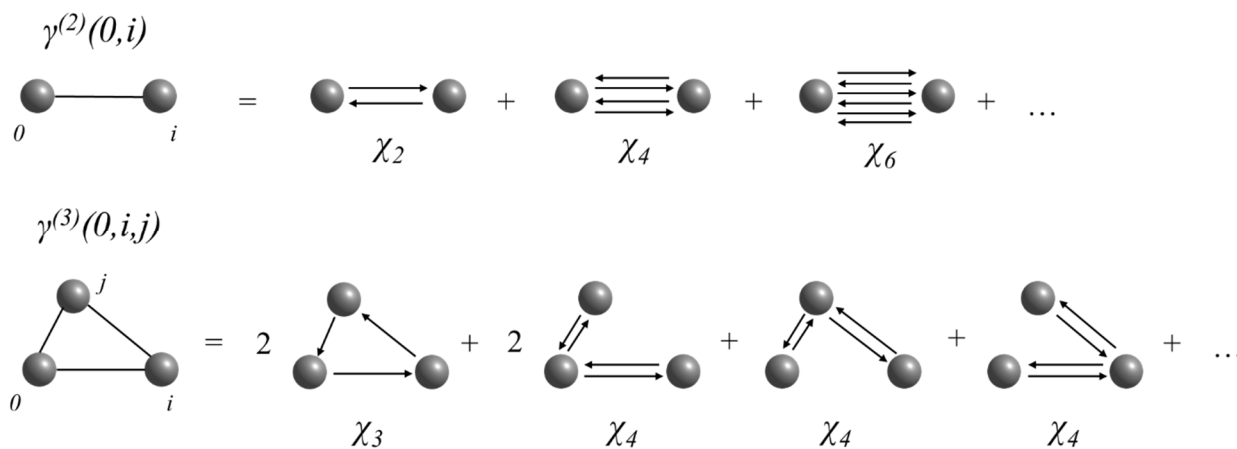


**Figure 3.6.** Pictorial view of the MS expansion for the  $\gamma^{(2)}$  and  $\gamma^{(3)}$  signals including terms up to  $\chi_6$  and  $\chi_4$ , respectively.

To simulate a XAS signal for a given cluster, the analysis of the  $n$ -body distribution functions around the photoabsorber is therefore required. For the two-body case, this means defining only one distance between the photoabsorber and the scattering atom. For a three-body distribution, the two shortest distances  $r_1$  and  $r_2$  within the  $\varphi$  angle in between can be considered. This choice is physically meaningful, since the two shortest bonds are usually real chemical bonds and the angle between them is the real bond angle. Since these distances and angle are correlated, a covariance matrix containing bond and angle variances as well as bond-angle correlations is also required:

$$M = \begin{pmatrix} \sigma_{r_1}^2 & \rho_{r_1 r_2}^2 & \rho_{r_1 \varphi}^2 \\ - & \sigma_{r_2}^2 & \rho_{r_2 \varphi}^2 \\ - & - & \sigma_{\varphi}^2 \end{pmatrix} \quad (3.66)$$

where the  $\rho_{ij}$  terms are defined as  $\rho_{ij} = \sigma_{ij}^2 / \sqrt{\sigma_i^2 \sigma_j^2}$  and  $-1 \leq \rho_{ij} \leq 1$ . For  $\rho_{ij} = 0$ , bonds (or angles) vibrate independently, while for  $\rho_{ij} = \pm 1$  there is full correlation between the parameters, which both expand or contract at the same time for +1, while one expands the other contracts in case of -1.

### 3.2.1.1 Liquid systems

As previously reported, the structural environment around the photoabsorber can be described in terms of  $n$ -body distribution functions. In case of a disordered system, like an amorphous solid or a liquid, information on the relative particle positions is meaningful only in a probabilistic sense. Basically, the sum of **Eq. 3.63** expressed in terms of atomic positions has to be turned into integrals over the atomic distributions.<sup>38</sup> The average XAS signal can be written as:

$$\begin{aligned} \langle \chi(k) \rangle = & \int_0^{\infty} dr 4\pi r^2 \rho g(r) \gamma^{(2)}(r, k) \\ & + \int_0^{\infty} dr_1 dr_2 d\varphi 8\pi^2 r_1^2 r_2^2 \sin(\varphi) \rho^2 g_3(r_1, r_2, \varphi) \gamma^{(3)}(r_1, r_2, \varphi, k) + \dots \end{aligned} \quad (3.67)$$

where  $\rho$  is the density of the considered scattering atoms. It has to be noted that the integrals are formally extended to the whole coordinates domain, but in practice are limited to EXAFS short-range sensitivity.

The average distribution of atoms around the photoabsorber is now expressed by means of a collection of *radial distribution functions*.<sup>38-40</sup> Here only the two- and three-body cases have been reported, so that pair and triplet distributions  $g(r)$  and  $g(r_1, r_2, \varphi)$  appear. In disordered systems, a radial distribution function usually present peaks with a broad shape and tend to 1 in the long range region due to lack of correlation between positions of distant atoms. In addition, asymmetric distributions are often obtained, which are not well approximated by Gaussian functions with width directly proportional to the Debye-Waller factor as in case of crystal structures at room temperature. Particles distribution in liquid systems can instead be modelled as a set of Gamma functions depending on four parameters: average distance  $R$ , coordination number  $N$  (degeneracy), standard deviation  $\sigma^2$  and asymmetry factor  $\beta = 2p^{-1/2}$ . They can be expressed as:

$$g(r) = \frac{2N}{\sigma |\beta| \Gamma(4\beta^{-2})} \left[ 4\beta^{-2} + \frac{2(r-R)}{\beta\sigma} \right]^{4\beta^{-2}-1} e^{-\left(4\beta^{-2} + \frac{2(r-R)}{\beta\sigma}\right)} \quad (3.68)$$

Where  $\Gamma(x)$  is the Euler's Gamma function. **Eq. 3.68** is defined in a wide interval of positive and negative asymmetry values and falls in the Gaussian limit for  $\beta \rightarrow 0$ .

With the GNXAS method, a theoretical spectrum can be therefore generated for an average particle distribution provided by several radial distribution functions. Least-squares fits of the model spectrum

can be performed on the experimental one by minimizing a residual function  $R_{sq}$  running on the square differences between the experimental  $\alpha(E_i)$  points and the model  $\alpha_m(E_i)$ , which also depend on the array of the optimized parameters  $p$ :

$$R_{sq} = \sum_i [\alpha(E_i) - \alpha_m(E_i, \{p\})]^2 \times W(E_i) \quad (3.69)$$

where  $W(E_i)$  is a statistical weight. This can be carried out for an arbitrary structural model or for that provided by any method who can produce distribution functions between the photoabsorber and the scattering atoms. In this way, it is possible to couple molecular simulation techniques like MD with XAS in a synergic approach, comparing the obtained theoretical results with the experimental data and assessing the validity of the simulation.<sup>41-45</sup>

### 3.2.2 XANES analysis

As already stated, the XANES region of the XAS spectrum is extremely sensitive to the geometrical environment around the photoabsorber including the overall symmetry, distances and angles. This should allow in principle a complete recovery of the three-dimensional arrangement of the scattering atoms. In addition, EXAFS is usually not particularly sensible to coordination numbers in disordered systems due to their strong correlation with the Debye-Waller factor. On the contrary, atomic thermal disorder is very limited for low  $k$  values,<sup>46</sup> thus XANES can provide complementary information and address some drawbacks with respect to the analysis of the high energy part of the spectrum. However, XANES analysis presents some dramatic difficulties that limited its employment to a qualitative level (*i.e.* comparison between spectra collected on different samples) for many years. These difficulties derive in particular from the treatment of the local potential felt by the photoelectron and the employment of very time-demanding algorithms for the calculation of the absorption cross section in a full MS treatment, since multiple-scattering phenomena are dominant in this spectral region.<sup>31</sup> In the last years, some methods have been proposed for a quantitative XANES data analysis. For example, in the MXAN code<sup>47</sup> a comparison between the experimental spectrum and several theoretical ones is performed starting from a putative geometrical configuration of the scattering atoms around the photoabsorber. This is performed by varying selected structural parameters like angles and bond distances and minimizing a residual function similar to **Eq. 3.69**. The X-ray absorption cross-section is calculated with a general MS scheme in the muffin-tin approximation.<sup>46,48</sup> The exchange and correlation parts of the potential are determined in the local density approximation

(LDA) of the self-energy of the photoelectron, *i.e.* for a certain spatial coordinate they depend only on the value of the electronic density at that point. This can be done by employing an appropriate complex optical potential.<sup>49</sup> Actually, MXAN supports the  $X_\alpha$  energy-independent or the energy-dependent complex Hedin-Lundqvist (HL) potentials.<sup>50</sup> However, the complex part of HL potential can introduce an excessive loss in the transition amplitude for the primary channel.<sup>51</sup> To avoid for this over-damping at low energies, it is possible to account for the inelastic processes by means of a convolution of the total cross section with a Lorentzian broadening having an energy-dependent  $\Gamma_{tot}(E)$  width given by:

$$\Gamma_{tot}(E) = \Gamma_c + \Gamma_{mfp}(E) \quad (3.70)$$

Here the constant part  $\Gamma_c$  takes into account both the experimental resolution and core-hole lifetime, while the  $\Gamma_{mfp}(E)$  energy-dependent term includes all the intrinsic and extrinsic inelastic processes (*mfp* stands for “mean free path” of the photoelectron).<sup>49</sup>  $\Gamma_{mfp}(E)$  is zero below the Fermi energy and starts increasing from a definite value that corresponds to the plasmon excitation energy.<sup>49</sup> The values of these energies introduce three non-structural parameters that are continuously adjusted at each computational step by means of a Monte Carlo fit.

## Bibliography

- 1 F. Jensen, *Introduction to Computational Chemistry*, John Wiley & Sons, Inc., USA, 2006.
- 2 C. J. Cramer, *Essentials of computational chemistry: theories and models*, West Sussex, England; New York: J. Wiley, 2002.
- 3 R. Car, F. de Angelis, P. Giannozzi and N. Marzari, in *Handbook of Materials Modeling: Methods*, ed. S. Yip, Springer Netherlands, Dordrecht, 2005, pp. 59–76.
- 4 W. L. Maxwell, David S.; Tirado-Rives, Julian; Jorgensen, Development and Testing of the OPLS All-Atom Force Field on Conformational Energetics and Properties of Organic Liquids, *J. Am. Chem. Soc.*, 1996, **118**, 11225–11236.
- 5 P. P. Ewald, Die Berechnung optischer und elektrostatischer Gitterpotentiale, *Ann. Phys.*, 1921, **369**, 253–287.
- 6 T. Darden, D. York and L. Pedersen, Particle mesh Ewald: An Nlog(N) method for Ewald sums in large systems, *J. Chem. Phys.*, 1993, **98**, 10089.
- 7 J.-P. Ryckaert, G. Ciccotti and H. J. C. Berendsen, Numerical integration of the cartesian equations of motion of a system with constraints: molecular dynamics of n-alkanes, *J. Comput. Phys.*, 1977, **23**, 327–341.
- 8 B. Hess, H. Bekker, H. J. C. Berendsen and J. G. E. M. Fraaije, LINCS: A linear constraint solver for molecular simulations, *J. Comput. Chem.*, 1997, **18**, 1463–1472.
- 9 R. W. Hockney, S. P. Goel and J. W. Eastwood, Quiet high-resolution computer models of a plasma, *J. Comput. Phys.*, 1974, **14**, 148–158.
- 10 W. C. Swope, H. C. Andersen, P. H. Berens and K. R. Wilson, A computer simulation method for the calculation of equilibrium constants for the formation of physical clusters of molecules: Application to small water clusters, *J. Chem. Phys.*, 1982, **76**, 637–649.
- 11 H. J. C. Berendsen, J. P. M. Postma, W. F. van Gunsteren, A. DiNola and J. R. Haak, Molecular dynamics with coupling to an external bath, *J. Chem. Phys.*, 1984, **81**, 3684–3690.
- 12 S. Nosé, A molecular dynamics method for simulations in the canonical ensemble, *Mol. Phys.*, 1984, **52**, 255–268.
- 13 W. G. Hoover, Canonical dynamics: Equilibrium phase-space distributions, *Phys. Rev. A*, 1985, **31**, 1695–1697.
- 14 M. Parrinello and A. Rahman, Polymorphic transitions in single crystals: A new molecular dynamics method, *J. Appl. Phys.*, 1981, **52**, 7182–7190.

- 15 J. Koca, Z. Jirouskova, R. Svobodova Varekova and J. Vanek, Basic Ingredients of Free Energy Calculations: A Review, *J. Comput. Chem.*, 2009, **30**, 1174–1178.
- 16 A. Pohorille, C. Jarzynski and C. Chipot, Good practices in free-energy calculations, *J. Phys. Chem. B*, 2010, **114**, 10235–10253.
- 17 N. Hansen and W. F. Van Gunsteren, Practical aspects of free-energy calculations: A review, *J. Chem. Theory Comput.*, 2014, **10**, 2632–2647.
- 18 P. V. Klimovich, M. R. Shirts and D. L. Mobley, Guidelines for the analysis of free energy calculations, *J. Comput. Aided. Mol. Des.*, 2015, **29**, 397–411.
- 19 T. Steinbrecher, D. L. Mobley and D. A. Case, Nonlinear scaling schemes for Lennard-Jones interactions in free energy calculations, *J. Chem. Phys.*, 2007, **127**, 214108.
- 20 T. C. Beutler, A. E. Mark, R. C. van Schaik, P. R. Gerber and W. F. van Gunsteren, Avoiding singularities and numerical instabilities in free energy calculations based on molecular simulations, *Chem. Phys. Lett.*, 1994, **222**, 529–539.
- 21 J. Pillardy and L. Piela, Molecular Dynamics on Deformed Potential Energy Hypersurfaces, *J. Phys. Chem.*, 1995, **99**, 11805–11812.
- 22 M. Zacharias, T. P. Straatsma and J. A. McCammon, Separation-shifted scaling, a new scaling method for Lennard-Jones interactions in thermodynamic integration, *J. Chem. Phys.*, 1994, **100**, 9025–9031.
- 23 C.-S. Shao, R. Byrd, E. Eskow and R. B. Schnabel, Global Optimization For Molecular Clusters Using A New Smoothing Approach, *J. Glob. Optim.*, 2000, **16**, 167–196.
- 24 C. H. Bennett, Efficient estimation of free energy differences from Monte Carlo data, *J. Comput. Phys.*, 1976, **22**, 245–268.
- 25 G. M. Torrie and J. P. Valleau, Nonphysical sampling distributions in Monte Carlo free-energy estimation: Umbrella sampling, *J. Comput. Phys.*, 1977, **23**, 187–199.
- 26 J. Kästner, Umbrella sampling, *Wiley Interdiscip. Rev. Comput. Mol. Sci.*, 2011, **1**, 932–942.
- 27 S. Kumar, J. M. Rosenberg, D. Bouzida, R. H. Swendsen and P. A. Kollman, The weighted histogram analysis method for free-energy calculations on biomolecules. I. The method, *J. Comput. Chem.*, 1992, **13**, 1011–1021.
- 28 J. Kästner and W. Thiel, Bridging the gap between thermodynamic integration and umbrella sampling provides a novel analysis method: “Umbrella integration”, *J. Chem. Phys.*, 2005, **123**, 144104.
- 29 R. Car and M. Parrinello, Unified Approach for Molecular Dynamics and Density-Functional Theory, *Phys. Rev. Lett.*, 1985, **55**, 2471–2474.
- 30 D. Marx and J. Hutter, *Ab Initio Molecular Dynamics: Basic Theory and Advanced Methods*,

Cambridge University Press, 2009.

- 31 J. J. Rehr and R. C. Albers, Theoretical approaches to x-ray absorption fine structure, *Rev. Mod. Phys.*, 2000, **72**, 621–654.
- 32 S. Calvin, *XAFS for Everyone*, CRC Press, Boca Raton, 2013.
- 33 A. Filipponi, A. Di Cicco and C. R. Natoli, X-ray-absorption spectroscopy and n-body distribution functions in condensed matter. I. Theory, *Phys. Rev. B*, 1995, **52**, 15122–15134.
- 34 D. E. Sayers, E. A. Stern and F. W. Lytle, New Technique for Investigating Noncrystalline Structures: Fourier Analysis of the Extended X-Ray-Absorption Fine Structure, *Phys. Rev. Lett.*, 1971, **27**, 1204–1207.
- 35 N. Binsted, J. W. Campbell, S. J. Gurman and P. C. Stephenson, *The Daresbury Laboratory EXCURVE program*, Daresbury Laboratory, Warrington, England, WA4 4AD.
- 36 J. J. Rehr, J. J. Kas, F. D. Vila, M. P. Prange and K. Jorissen, Parameter-free calculations of X-ray spectra with FEFF9, *Phys. Chem. Chem. Phys.*, 2010, **12**, 5503–5513.
- 37 A. Filipponi and A. Di Cicco, X-ray-absorption spectroscopy and n-body distribution functions in condensed matter. II. Data analysis and applications, *Phys. Rev. B*, 1995, **52**, 15135–15149.
- 38 A. Filipponi and P. D'Angelo, in *X-Ray Absorption and X-Ray Emission Spectroscopy*, John Wiley & Sons, Ltd, 2016, pp. 745–771.
- 39 A. Filipponi, The radial distribution function probed by X-ray absorption spectroscopy, *J. Phys. Condens. Matter*, 1994, **6**, 8415–8427.
- 40 A. Di Cicco, EXAFS in liquids and disordered systems: a personal review, *XAS Res. Rev.*, 2016, **15**, 1–7.
- 41 P. D'Angelo, A. Di Nola, A. Filipponi, N. V. Pavel and D. Roccatano, An extended x-ray absorption fine structure study of aqueous solutions by employing molecular dynamics simulations, *J. Chem. Phys.*, 1994, **100**, 985–994.
- 42 P. D'Angelo, M. Benfatto, S. Della Longa and N. V. Pavel, Combined XANES and EXAFS analysis of  $\text{Co}^{2+}$ ,  $\text{Ni}^{2+}$ , and  $\text{Zn}^{2+}$  aqueous solutions, *Phys. Rev. B - Condens. Matter Mater. Phys.*, 2002, **66**, 642091–642097.
- 43 G. Chillemi, P. D'Angelo, N. V. Pavel, N. Sanna and V. Barone, Development and validation of an integrated computational approach for the study of ionic species in solution by means of effective two-body potentials. The case of  $\text{Zn}^{2+}$ ,  $\text{Ni}^{2+}$ , and  $\text{Co}^{2+}$  in aqueous solutions, *J. Am. Chem. Soc.*, 2002, **124**, 1968–1976.
- 44 P. D'Angelo, V. Barone, G. Chillemi, N. Sanna, W. Meyer-Klaucke and N. V. Pavel, Hydrogen and higher shell contributions in  $\text{Zn}^{2+}$ ,  $\text{Ni}^{2+}$ , and  $\text{Co}^{2+}$  aqueous solutions: An X-ray absorption fine structure and molecular dynamics study, *J. Am. Chem. Soc.*, 2002, **124**,

- 1958–1967.
- 45 P. D'Angelo and R. Spezia, Hydration of lanthanoids(III) and actinoids(III): An experimental/theoretical saga, *Chem. - A Eur. J.*, 2012, **18**, 11162–11178.
- 46 M. Benfatto, C. R. Natoli, A. Bianconi, J. Garcia, A. Marcelli, M. Fanfoni and I. Davoli, Multiple-scattering regime and higher-order correlations in x-ray-absorption spectra of liquid solutions, *Phys. Rev. B*, 1986, **34**, 5774–5781.
- 47 M. Benfatto, S. Della Longa and C. R. Natoli, The MXAN procedure: a new method for analysing the XANES spectra of metallo-proteins to obtain structural quantitative information, *J. Synchrotron Radiat.*, 2003, **10**, 51–57.
- 48 T. A. Tyson, K. O. Hodgson, C. R. Natoli and M. Benfatto, General multiple-scattering scheme for the computation and interpretation of x-ray-absorption fine structure in atomic clusters with applications to SF<sub>6</sub>, GeCl<sub>4</sub> and Br<sub>2</sub> molecules, *Phys. Rev. B*, 1992, **46**, 5997–6019.
- 49 M. Benfatto and S. Della Longa, Geometrical fitting of experimental XANES spectra by a full multiple-scattering procedure, *J. Synchrotron Radiat.*, 2001, **8**, 1087–1094.
- 50 L. Hedin and S. Lundqvist, Effects of Electron-Electron and Electron-Phonon Interactions on the One-Electron States of Solids, *Solid State Phys.*, 1969, **23**, 1–15.
- 51 M. Benfatto, J. A. Solera, J. Chaboy, M. G. Proietti and J. Garcia, Theoretical analysis of x-ray absorption near-edge structure of transition-metal aqueous complexes in solution at the metal K edge, *Phys. Rev. B*, 1997, **56**, 2447–2452.



# Chapter 4

## Zn<sup>2+</sup> ion in Tf<sub>2</sub>N<sup>-</sup>- and BF<sub>4</sub><sup>-</sup>-based imidazolium RTILs

### 4.1 Introduction

Many technological, environmental and energy-related applications involve the presence of the Zn<sup>2+</sup> ion in RTILs. For example, it has been proven that the dissolution of the Zn(Tf<sub>2</sub>N)<sub>2</sub> salt in RTILs carrying the [Tf<sub>2</sub>N]<sup>-</sup> anion can provide a solution with high catalytic activity for Friedel-Crafts acylation.<sup>1</sup> In addition, the electrochemical behavior of the Zn/Zn<sup>2+</sup> redox couple in various RTILs has been studied to electrodeposit zinc metallic films<sup>2</sup> and for zinc-air rechargeable batteries.<sup>3-7</sup>

Zinc is also involved in many kinds of industrial processes, therefore its removal from aqueous solutions has become an important issue for wastewater treatment technologies.<sup>8,9</sup> Selective extractions of Zn<sup>2+</sup> ion employing RTILs have already been tested.<sup>10-15</sup> According to these works, Zn<sup>2+</sup> seems to be poorly separated by pure Tf<sub>2</sub>N-based ionic liquids and the presence of auxiliary extractants is needed.<sup>11,14,15</sup> Differently, the extraction with RTILs carrying the [BF<sub>4</sub>]<sup>-</sup> anion seems to a certain extent more promising.<sup>11,14,16</sup> This is in agreement with the previously reported experimental Gibbs free energies of transfer from water to these families of RTILs (**Tab. 1.2** of **Chapter 1**), showing positive values for transfer to Tf<sub>2</sub>N-based RTILs and negative values for BF<sub>4</sub>-RTILs. Data for the RTILs studied in this work are here reported again for sake of clarity (**Tab. 4.1**).

As regards the coordination in solution, Zn<sup>2+</sup> structural features in Tf<sub>2</sub>N-based RTILs in dry conditions have been unambiguously determined by XAS measurements coupled with MD simulations, resulting in the [Zn(Tf<sub>2</sub>N)<sub>6</sub>]<sup>4+</sup> species where zinc is coordinated by six monodentate [Tf<sub>2</sub>N]<sup>-</sup> in an octahedral field.<sup>17</sup> However, it is known that in a real application, *e.g.* a liquid-liquid extraction, water is present in the RTIL at high concentrations. Therefore, metal ion coordination in the “wet” ionic liquid can be in principle very different to that in “dry” conditions. In addition, no structural data are present for Zn<sup>2+</sup> coordination in BF<sub>4</sub>-based RTILs. For these reasons, a study about the Zn<sup>2+</sup> ion in RTILs carrying the [Tf<sub>2</sub>N]<sup>-</sup> and [BF<sub>4</sub>]<sup>-</sup> anions within 1-alkyl-3-methylimidazolium cations has been carried out.

In the first part, Zn<sup>2+</sup> in Tf<sub>2</sub>N-based RTILs has been used as a test case to verify if an accurate description of single-ion structural and thermodynamic solvation properties can be obtained by means

of MD simulations. To this purpose, the metal ion coordination as well as Gibbs free energies of solvation in the RTILs and transfer from water have been calculated employing different LJ parameters for  $\text{Zn}^{2+}$  and RTILs force fields and the results compared with the experimental data (**Tab. 4.1**). To understand the reasons of the unfavorable transfer to  $\text{Tf}_2\text{N}$ -RTILs, also the enthalpies and entropies of solvation and transfer were obtained for  $[\text{C}_4\text{mim}][\text{Tf}_2\text{N}]$ . Umbrella sampling simulations have been performed to understand the energetics related to the two possible binding modes of the  $[\text{Tf}_2\text{N}]^-$  anion, namely mono- and bidentate. This technique has been employed also to study the transfer of  $\text{Zn}^{2+}$  in a water/ $[\text{C}_4\text{mim}][\text{Tf}_2\text{N}]$  biphasic system. In addition, to get insights into  $\text{Zn}^{2+}$  coordination in wet RTILs, XAS measures along with EXAFS data analysis have been performed on  $\text{Zn}(\text{Tf}_2\text{N})_2$  solutions in  $[\text{C}_4\text{mim}][\text{Tf}_2\text{N}]$  in presence of different amounts of water.

In the second part, MD simulations have been employed to obtain a structural and thermodynamic description of  $\text{Zn}^{2+}$  solvation in  $[\text{C}_4\text{mim}][\text{BF}_4]$ . Also in this case, two force fields for the RTIL have been tested. In addition, an explanation of the favorable Gibbs free energy of transfer from water to this RTIL is given thanks to the interpretation of the calculated enthalpies and entropies of solvation and transfer.

**Table 4.1.**  $\text{Zn}^{2+}$  experimental Gibbs free energies of solvation ( $\Delta G_{\text{solv}}$ ) and transfer from water ( $\Delta G_{\text{trans}}$ ) for the RTILs studied in this work obtained as reported in **Sec. 1.3.3** of **Chapter 1** at 298.15 K. Values in  $\text{kcal mol}^{-1}$ .

RTIL	$\Delta G_{\text{solv}}$	$\Delta G_{\text{trans}}$
$[\text{C}_2\text{mim}][\text{Tf}_2\text{N}]$	-457.1	10.2
	-473.6	
$[\text{C}_4\text{mim}][\text{Tf}_2\text{N}]$	-457.2	10.0
	-473.7	
$[\text{C}_4\text{mim}][\text{BF}_4]$	-479.2	-12.0
	-495.7	

## 4.2 Methods

### 4.2.1 Zn<sup>2+</sup> in [C<sub>n</sub>mim][Tf<sub>2</sub>N] (n = 2, 4)

#### 4.2.1.1 MD simulations details

MD simulations have been carried out for the Zn<sup>2+</sup> ion in the [C<sub>n</sub>mim][Tf<sub>2</sub>N] (n = 2, 4) RTILs. To this purpose, cubic boxes with one Zn<sup>2+</sup>, 216 [C<sub>2</sub>mim]<sup>+</sup>/[C<sub>4</sub>mim]<sup>+</sup> cations and 218 [Tf<sub>2</sub>N]<sup>-</sup> anions with respectively 45.3 Å and 47.3 Å initial side lengths were built. These box dimensions and number of ions were chosen to reproduce neat [C<sub>2</sub>mim][Tf<sub>2</sub>N] and [C<sub>4</sub>mim][Tf<sub>2</sub>N] experimental densities and infinite dilution conditions for the metal ion. Three force fields were tested for [C<sub>4</sub>mim][Tf<sub>2</sub>N], namely the all-atom non-polarizable force fields by Canongia Lopes and Padua (CL&P),<sup>18–20</sup> Ludwig *et al.* (KPL)<sup>21</sup> and Müller-Plathe *et al.* (MP).<sup>22</sup> For [C<sub>2</sub>mim][Tf<sub>2</sub>N], simulations have been performed with CL&P<sup>18–20</sup> and KPL.<sup>21</sup> For each RTIL force field, simulations were carried out testing also three LJ parameter sets for Zn<sup>2+</sup> taken from Merz *et al.* (Merz),<sup>23</sup> Stote and Karplus (SK),<sup>24</sup> and from those implemented by Merz *et al.* in the AMBER force field (AMBER).<sup>25</sup> Non-bonded parameters for Zn<sup>2+</sup> and the oxygen atom of the [Tf<sub>2</sub>N]<sup>-</sup> anion taken from the force fields employed in this work are reported in **Tab. 4.2**. In case of Merz parameters, which will be employed for the rest of the calculations (*vide infra*), we choose the “CM” set for TIP3P water parametrized to reproduce a good compromise between structural (CN and average bond distance) and thermodynamic ( $\Delta G_{\text{hyd}}$ ) parameters in aqueous solution. Cross terms in vdW interactions were constructed with geometric average combining rules. A 10 Å cut-off has been employed for all non-bonded interactions, being this length comprised in the optimal range in order to perform free energy calculations.<sup>26</sup> No substantial differences in the calculated free energies have been observed by varying the cut-off between 10 and 12 Å. Long-range electrostatic interactions were taken into account with the PME method.<sup>27,28</sup>

After an energy minimization, each box was equilibrated in NVT conditions for 10 ns at 700 K and then cooled back to 298.15 K for 20 ns. NPT equilibration and final production runs were carried out each for 10 ns at 298.15 K and 1 atm to obtain data for structural analysis. The temperature was kept constant with the thermostat implicitly handled by the stochastic dynamics (sd) leap-frog integrator,<sup>29</sup> while in NPT the pressure was coupled to the Parrinello-Rahman barostat<sup>30</sup> both with relaxation constants of 1 ps. In all simulations, a 1 fs time step has been employed. Stretching vibrations involving hydrogen atoms have been constrained with the LINCS algorithm.<sup>31</sup> All calculations have been performed with the Gromacs 5.1.6 package.<sup>32</sup>

$\text{Zn}^{2+}$   $\Delta G_{\text{solv}}$  in the RTILs have been calculated for all the possible combinations of the tested force fields and LJ parameters. A decoupling of  $\text{Zn}^{2+}$  non-bonded interactions with the solvent has been performed by multiplying the Hamiltonian by a decoupling parameter  $\lambda$ . In particular, 20  $\lambda$  windows have been chosen to change  $\text{Zn}^{2+}$  non-bonded interactions from  $\lambda = 0$  (dummy metal ion in solution without interactions) to  $\lambda = 1$  (full Coulomb and vdW-interacting metal ion). The first 10  $\lambda$  correspond to turning on vdW interactions, while the successive 10 are related to the electrostatic part. This number of windows was selected as it allowed to reproduce  $\text{Zn}^{2+}$   $\Delta G_{\text{hyd}}$  in good agreement with the values obtained by Merz *et al.*<sup>23</sup> in the optimization of the LJ parameters for the metal. LJ transformation has been treated via the soft-core potential to avoid singularities when the ion is close to appear ( $\lambda \sim 0$ ). For each  $\lambda$ , an NPT equilibration and a production run for data collection were carried out at 1 atm and 298.15 K each for 2 ns.

To calculate  $\text{Zn}^{2+}$  free energies of transfer between water and the RTILs, Gibbs free energies of hydration for the metal ion were also calculated by representing  $\text{Zn}^{2+}$  with all the tested LJ parameters. To this purpose, boxes containing one  $\text{Zn}^{2+}$  ion and 500 TIP3P water molecules<sup>33</sup> were first equilibrated, then 20  $\lambda$  windows were employed for  $\Delta G_{\text{hyd}}$  calculation. For each  $\lambda$ , 100 ps NPT equilibrations and 1 ns runs for data collection were performed.

Final free energies have been calculated with the BAR method.<sup>34</sup> From the obtained values, Gibbs free energies of transfer have been calculated as  $\Delta G_{\text{trans}} = \Delta G_{\text{solv}} - \Delta G_{\text{hyd}}$ .

To calculate  $\text{Zn}^{2+}$  solvation enthalpy and entropy in  $[\text{C}_4\text{mim}][\text{Tf}_2\text{N}]$ , free energy calculations were also carried out at 7 temperatures in the 290 - 340 K range. This protocol has turned out to be the most accurate for the calculation of the entropy change for metal ions in water by means of MD.<sup>35-37</sup> In this case, Merz parameters were employed for  $\text{Zn}^{2+}$  within the CL&P force field for the RTIL. For each temperature, the box was equilibrated for 10 ns in NVT and for 20 ns in NPT, then free energy calculations were performed after 5 ns equilibrations and 10 ns production runs for each  $\lambda$  in NPT conditions. A similar procedure has been employed to calculate  $\text{Zn}^{2+}$  hydration enthalpy and entropy, which gave access to enthalpy and entropy of transfer.

**Table 4.2.** Non-bonded parameters for  $\text{Zn}^{2+}$  and the oxygen atom of the  $[\text{Tf}_2\text{N}]^-$  anion taken from the force fields employed in this work.

Atom	Potential	$q$ (e)	$\sigma$ (Å)	$\epsilon$ (kcal mol <sup>-1</sup> )
$\text{Zn}^{2+}$	Merz <sup>23</sup>	2.00	2.265	0.0033
	SK <sup>24</sup>	2.00	1.949	0.250
	AMBER <sup>25</sup>	2.00	1.960	0.0125
O( $\text{Tf}_2\text{N}$ )	CL&P <sup>18-20</sup>	-0.53	2.96	0.21
	KPL <sup>21</sup>	-0.53	3.46	0.063
	MP <sup>22</sup>	-0.53	3.18	0.21

#### 4.2.1.2 Umbrella sampling simulations

The free energy related to the phase transfer of  $\text{Zn}^{2+}$  from water to an RTIL has been studied by pulling the metal ion from the aqueous phase to  $[\text{C}_4\text{mim}][\text{Tf}_2\text{N}]$  in a biphasic system. A  $36.47 \text{ \AA} \times 36.47 \text{ \AA} \times 72.95 \text{ \AA}$  box was filled with 100  $[\text{C}_4\text{mim}]^+/102 [\text{Tf}_2\text{N}]^-$  ions and 1618 TIP3P<sup>33</sup> water molecules with a preformed biphasic system where the RTIL and water occupy initially the same volumes. One  $\text{Zn}^{2+}$  was set in the middle of the aqueous phase in the starting configuration. The box was equilibrated for 20 ns in NPT at 298.15 K and 1 atm and then in NVT for 10 ns at the same temperature. Sampling of the configurations along the path of interest was performed by pulling  $\text{Zn}^{2+}$  for 400 ps along the  $z$ -axis connecting the two phases by applying between the metal and the center of mass (COM) of the  $[\text{C}_4\text{mim}][\text{Tf}_2\text{N}]$  phase a force constant of  $1000 \text{ kJ mol}^{-1} \text{ nm}^{-2}$ . From the result of this simulation, 35 configurations were collected to cover a path of  $\sim 36 \text{ \AA}$  connecting the two phases with  $\sim 1 \text{ \AA}$  step size. Each configuration has been simulated for data collection for 15 ns in NPT (1 atm, 298.15 K) by constraining the  $z$ -component of  $\text{Zn}^{2+}$  position by means of an harmonic potential with  $2000 \text{ kJ mol}^{-1} \text{ nm}^{-2}$  force constant. The first 2 ns of each run were discarded as equilibration time.

Umbrella sampling simulations were employed also to assess a possible solvation equilibrium between a species formed by  $[\text{Tf}_2\text{N}]^-$  anions coordinating  $\text{Zn}^{2+}$  with monodentate-only fashion ( $[\text{Zn}(\text{Tf}_2\text{N})_6]^{4+}$ ) and a species with a mixed coordination presenting one bidentate and four monodentate coordinating anions ( $[\text{Zn}(\text{Tf}_2\text{N})_5]^{3-}$ ). A box with one  $\text{Zn}^{2+}$  ion, 80  $[\text{C}_4\text{mim}]^+$  cations and 82  $[\text{Tf}_2\text{N}]^-$  anions was employed in this case. Configurations along the reaction coordinate were generated with a 400 ps NVT simulation by applying a  $200 \text{ kJ mol}^{-1} \text{ nm}^{-2}$  force constant between the oxygen atom of the incoming  $[\text{Tf}_2\text{N}]^-$  anion and  $\text{Zn}^{2+}$ . During this run, the approach of  $[\text{Tf}_2\text{N}]^-$  to  $[\text{Zn}(\text{Tf}_2\text{N})_5]^{3-}$  provoked the formation of a new Zn-O( $\text{Tf}_2\text{N}$ ) bond and the aperture of the bidentate

$[\text{Tf}_2\text{N}]^-$  to monodentate, giving  $[\text{Zn}(\text{Tf}_2\text{N})_6]^{4+}$ . From the results of this simulation, 20 configurations were collected along the reaction coordinate for Zn-O( $\text{Tf}_2\text{N}$ ) distances from 6.86 Å to 1.88 Å with  $\sim 0.25$  Å step. Each of these configurations was equilibrated for 5 ns and simulated for data collection for 10 ns in NPT ensemble (298.15 K, 1 atm) by applying between  $\text{Zn}^{2+}$  and the oxygen atom of the approaching  $[\text{Tf}_2\text{N}]^-$  a harmonic potential going from 20000  $\text{kJ mol}^{-1} \text{nm}^{-2}$  for the longer distances to 220000  $\text{kJ mol}^{-1} \text{nm}^{-2}$  for the shorter ones.

In all the umbrella sampling simulations, the Merz and CL&P parameters for respectively  $\text{Zn}^{2+}$  and  $[\text{C}_4\text{mim}][\text{Tf}_2\text{N}]$  were employed. Free energies related to each process were obtained by the PMF profiles calculated with the WHAM method.<sup>38</sup>

#### 4.2.1.3 X-ray absorption measurements

0.1 M  $\text{Zn}(\text{Tf}_2\text{N})_2$  solutions in water, dry  $[\text{C}_4\text{mim}][\text{Tf}_2\text{N}]$ ,  $[\text{C}_4\text{mim}][\text{Tf}_2\text{N}]$  with 1 M water and in water-saturated conditions were prepared by adding weighted amounts of metallic salt into the correspondent solvent.  $\text{Zn}(\text{Tf}_2\text{N})_2$  was purchased from Solvionic and  $[\text{C}_4\text{mim}][\text{Tf}_2\text{N}]$  from Iolitec GmbH (purities > 99%). For dry  $[\text{C}_4\text{mim}][\text{Tf}_2\text{N}]$ , the resulting solution was sonicated for 10 minutes and dried under vacuum for 36 hours. A final water content between 150 and 300 ppm was determined by Karl-Fischer titration. A precise amount of MilliQ water was added to a part of this solution to obtain the  $[\text{C}_4\text{mim}][\text{Tf}_2\text{N}]$  sample with 1 M water. Water-saturated  $[\text{C}_4\text{mim}][\text{Tf}_2\text{N}]$  has been prepared by shaking the RTIL with water in a separating funnel for 3 minutes, letting the two phases separate overnight and collecting the organic phase.

Zn K-edge XAS spectra were collected in transmission mode at the 11.1 beamline of Elettra Synchrotron.<sup>39</sup> Cells with Kapton windows were filled with the solutions and kept under  $\text{N}_2$ -flux during data collection to avoid contact with moisture from the air. A Si(111) double crystal was employed as monochromator, while the storage ring was working at 2 GeV and beam current was maintained between 300 and 200 mA. At least two spectra were recorded and averaged for each sample.

#### 4.2.1.4 EXAFS data analysis

Analysis of the EXAFS part of the spectra was carried with the GNXAS method and software.<sup>33,37</sup> To this purpose, theoretical signals have been generated and subsequent refinement of the structural parameters has been performed in order to get the best agreement with the experimental data. Amplitudes  $A(k,r)$  and phase shifts  $\varphi(k,r)$  have been calculated in the muffin-tin approximation

employing advanced models for the exchange-correlation self-energy (Hedin-Lundqvist).<sup>41</sup> In this way, inelastic losses in the final state are intrinsically accounted by the complex potential. The imaginary part also includes a constant factor accounting for the core-hole width (1.67 eV). Given the similarity of the XANES spectra of  $\text{Zn}^{2+}$  in wet  $[\text{C}_4\text{mim}][\text{Tf}_2\text{N}]$  and in pure water (*vide infra*), EXAFS data analysis of these samples has been carried out starting from the results of a previous EXAFS investigation performed on a 0.2 M  $\text{Zn}(\text{NO}_3)_2$  aqueous solution,<sup>42</sup> showing the presence of an octahedral hydration shell with six oxygen atoms at 2.078(2) Å and twelve hydrogens at 2.78(2) Å. Also in this case, both the Zn-O and Zn-H SS contributions have been considered, as well as MS contributions associated to three-body O-Zn-O distributions with 180° and 90° bond angles. Each two-body distribution has been modeled as a  $\Gamma$ -like function characterized by coordination number CN, average distance R, variance  $\sigma^2$  (Debye-Waller-like factor) and asymmetry factor  $\beta$ . Least-squares fits have been carried out on the raw data directly, without preliminary background subtraction or Fourier filtering, by changing all the structural parameters with the exception of the coordination numbers and angles, being known that  $\text{Zn}^{2+}$  forms well defined octahedral complexes with water.<sup>42</sup> Moreover, non-structural parameters have been optimized, namely  $E_0$  which is the K-edge ionization energy, and the  $\text{KM}_1$  and  $\text{KM}_2$  double-electron excitation channels identified respectively at 103 and 160 eV above the first inflection point of the spectra on the basis of the Z+1 approximation. Owing to the inclusion of double-electron excitations, the  $S_0^2$  amplitude reduction factor was kept constrained to 0.99.

## 4.2.2 $\text{Zn}^{2+}$ in $[\text{C}_4\text{mim}][\text{BF}_4]$

### 4.2.2.1 MD simulations details

MD simulations have been carried out on  $\text{Zn}^{2+}$  in the  $[\text{C}_4\text{mim}][\text{BF}_4]$  RTIL. A cubic box with one  $\text{Zn}^{2+}$  ion, 198  $[\text{C}_4\text{mim}]^+$  cations and 200  $[\text{BF}_4]^-$  anions with 38.97 Å initial side length was built.  $\text{Zn}^{2+}$  was represented with LJ parameters taken from Merz *et al.* “CM set” for TIP3P water, while two force fields were tested for  $[\text{C}_4\text{mim}][\text{BF}_4]$ : CL&P<sup>18</sup> and CL&P with the parameters for  $[\text{BF}_4]^-$  taken from Wang *et al.*<sup>43</sup> Non-bonded parameters for boron and fluorine atoms of the anion are reported in **Tab. 4.3**. Cross terms in vdW interactions were constructed with the Lorentz-Berthelot combining rules. A 12 Å cut-off has been employed for all non-bonded interactions and long-range electrostatics was taken into account with the PME method.<sup>27,28</sup>

After an energy minimization, the box was first equilibrated in NVT conditions for 10 ns at 700 K and then cooled to 298.15 K for 12 ns. An equilibration in NPT conditions (1 atm, 298.15 K) has

been performed for further 10 ns.  $\text{Zn}^{2+}$  solvation free energy in  $[\text{C}_4\text{mim}][\text{BF}_4]$  was calculated by decoupling the metal ion non-bonded interactions with the solvent in 15  $\lambda$  windows, the first 5  $\lambda$  corresponding to vdW interactions and the successive 10 to the electrostatic part. The number of windows related to the vdW part has been reduced with respect to calculations in  $\text{Tf}_2\text{N}$ -based RTILs since it was observed that only a negligible contribute to the free energy is provided by the LJ interaction (*vide infra*). For each  $\lambda$  value, production runs at 1 atm and 298.15 K in NPT were performed for 15 ns, with the first 5 ns discarded as equilibration time. Simulations of each window up to 50 ns did not show any relevant change in the computed free energy value. The same protocol was employed to obtain solvation enthalpy and entropy in  $[\text{C}_4\text{mim}][\text{BF}_4]$  by free energy calculations at different temperatures (300 – 420 K). Temperature was kept constant with the thermostat implicitly handled by the sd leap-frog integrator,<sup>29</sup> while in NPT the pressure was coupled to the Parrinello-Rahman barostat<sup>30</sup> with relaxation constants of respectively 0.5 and 1 ps. In all simulations, a 1 fs time step has been employed. Stretching vibrations involving hydrogen atoms have been constrained with the LINCS algorithm.<sup>31</sup>

Final free energies have been calculated with the BAR method.<sup>34</sup> Structural parameters were obtained from the Zn-F and Zn-B  $g(r)$  calculated on the simulations with  $\lambda = 1$ . All calculations have been performed with the Gromacs 5.1.6 program.<sup>32</sup>

**Table 4.3.** Non-bonded parameters for the  $[\text{BF}_4]^-$  anion taken from the force fields employed in this work.

Force field	Atom	$q$ (e)	$\sigma$ (Å)	$\epsilon$ (kcal mol <sup>-1</sup> )
CL&P <sup>18</sup>	F	-0.49	3.12	1.0678
	B	0.96	3.58	1.6631
CL&P + Wang <sup>18,43</sup>	F	-0.5376	3.58	1.0678
	B	1.1504	3.12	1.6631

## 4.3 Results

### 4.3.1 Zn<sup>2+</sup> in [C<sub>n</sub>mim][Tf<sub>2</sub>N] (n = 2, 4)

#### 4.3.1.1 Zn<sup>2+</sup> coordination

MD simulations of Zn<sup>2+</sup> in [C<sub>2</sub>mim][Tf<sub>2</sub>N] and [C<sub>4</sub>mim][Tf<sub>2</sub>N] employing different RTILs force fields and LJ parameters for the metal have been carried out. The obtained structural parameters for Zn<sup>2+</sup> first coordination shell are reported in **Tab. 4.4**, while the calculated  $g(r)$ 's for the Zn–O(Tf<sub>2</sub>N) and Zn–N(Tf<sub>2</sub>N) pairs are reported in **Fig. 4.1** and **Fig. 4.2** for [C<sub>2</sub>mim][Tf<sub>2</sub>N] and [C<sub>4</sub>mim][Tf<sub>2</sub>N], respectively. As regards the Zn–O distribution, a first intense peak integrating six oxygen atoms is obtained with all the tested parameter sets. The average bond distance between Zn<sup>2+</sup> and the coordinating oxygen atoms shows a clear dependence from the employed potential. In particular, keeping constant the metal LJ parameters, the Zn–O distance decreases with the RTIL force field following the KPL > MP > CL&P trend. This order can be attributed to the different value of  $\sigma$ , which is smaller following the same KPL (3.46 Å) > MP (3.18 Å) > CL&P (2.96 Å) order. On the other side, keeping constant the RTIL force field and changing Zn<sup>2+</sup> LJ parameters, the average bond distance decreases following the SK > Merz > AMBER trend, even if the  $\sigma$  value for zinc decreases in a different order. Also for the Zn–N pairs distribution a single intense peak integrating six nitrogen atoms is observed. This picture implies that each of the coordinating oxygen atoms is provided by a monodentate [Tf<sub>2</sub>N]<sup>−</sup> and reports the presence of the octahedral [Zn(Tf<sub>2</sub>N)<sub>6</sub>]<sup>4+</sup> species in solution (**Fig. 4.3 A**). This result is in agreement with what was found by D'Angelo *et al.* on 0.1 M Zn<sup>2+</sup> solutions in [C<sub>4</sub>mim][Tf<sub>2</sub>N] by means of MD simulations validated on EXAFS data employing SK parameters for Zn<sup>2+</sup> and the CL&P force field.<sup>17</sup> However, an exception is given in case the MP force field is employed for [C<sub>4</sub>mim][Tf<sub>2</sub>N] in combination with AMBER parameters for zinc. In fact, in this case the Zn–N(Tf<sub>2</sub>N)  $g(r)$  is split into two peaks, a first one of lower and a second of higher intensity (**Fig. 4.2**). The overall integration reports 5.0 nitrogen atoms in Zn<sup>2+</sup> first solvation shell (**Tab. 4.4**), thus the [Zn(Tf<sub>2</sub>N)<sub>5</sub>]<sup>3+</sup> species where one [Tf<sub>2</sub>N]<sup>−</sup> binds the metal in a bidentate way and four [Tf<sub>2</sub>N]<sup>−</sup> are monodentate (**Fig. 4.3 B**). The former coordination gives rise to the first peak of the  $g(r)$ , the latter to the second one.

**Table 4.4.** MD results of  $\text{Zn}^{2+}$  first solvation shell structure in  $[\text{C}_2\text{mim}][\text{Tf}_2\text{N}]$  and  $[\text{C}_4\text{mim}][\text{Tf}_2\text{N}]$  employing all the tested  $\text{Zn}^{2+}$  LJ parameters<sup>23–25</sup> and RTILs force fields.<sup>18–22</sup>

RTIL	RTIL force field	$\text{Zn}^{2+}$ LJ parameters	$r_{\text{Zn-O}}(\text{\AA})^{\text{a}}$	$\text{CN}_{\text{O}}^{\text{b}}$	$\text{CN}_{\text{N}}^{\text{c}}$	
$[\text{C}_2\text{mim}][\text{Tf}_2\text{N}]$	CL&P	Merz	1.90	6.0	6.0	
		SK	2.02	6.0	6.0	
		AMBER	1.88	6.0	6.0	
	KPL	Merz	2.00	6.0	6.0	
		SK	2.14	6.0	6.0	
		AMBER	1.98	6.0	6.0	
	$[\text{C}_4\text{mim}][\text{Tf}_2\text{N}]$	CL&P	Merz	1.88	6.0	6.0
			SK	2.00	6.0	6.0
			AMBER	1.86	6.0	6.0
KPL		Merz	2.00	6.0	6.0	
		SK	2.14	6.0	6.0	
		AMBER	1.98	6.0	6.0	
MP		Merz	2.00	6.0	6.0	
		SK	2.12	6.0	6.0	
		AMBER	1.96	6.0	5.0	

<sup>a</sup>Average bond distance between the  $\text{Zn}^{2+}$  ion and the coordinating oxygen atoms of the first solvation shell  $[\text{Tf}_2\text{N}]^-$  anions;

<sup>b</sup> $\text{Zn-O}(\text{Tf}_2\text{N})$  first  $g(r)$  peak integration number; <sup>c</sup> $\text{Zn-N}(\text{Tf}_2\text{N})$  first  $g(r)$  peak integration number.

# [C<sub>2</sub>mim][Tf<sub>2</sub>N]

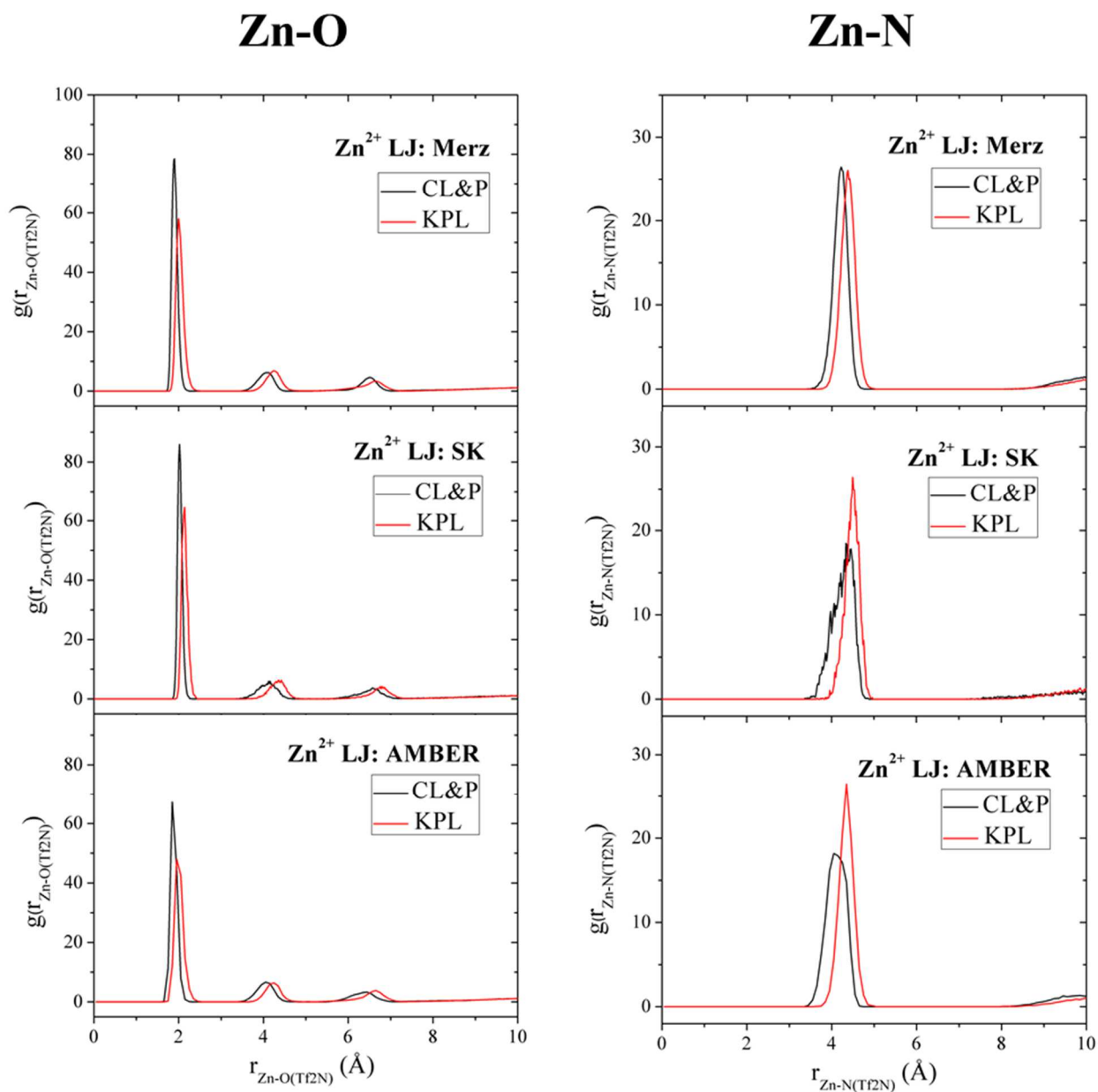


**Figure 4.1.** Zn-O(Tf<sub>2</sub>N) and Zn-N(Tf<sub>2</sub>N) pairs  $g(r)$ 's radial distribution functions calculated for Zn<sup>2+</sup> in [C<sub>2</sub>mim][Tf<sub>2</sub>N] employing different Zn<sup>2+</sup> LJ parameters and RTILs force fields.

# [C<sub>4</sub>mim][Tf<sub>2</sub>N]

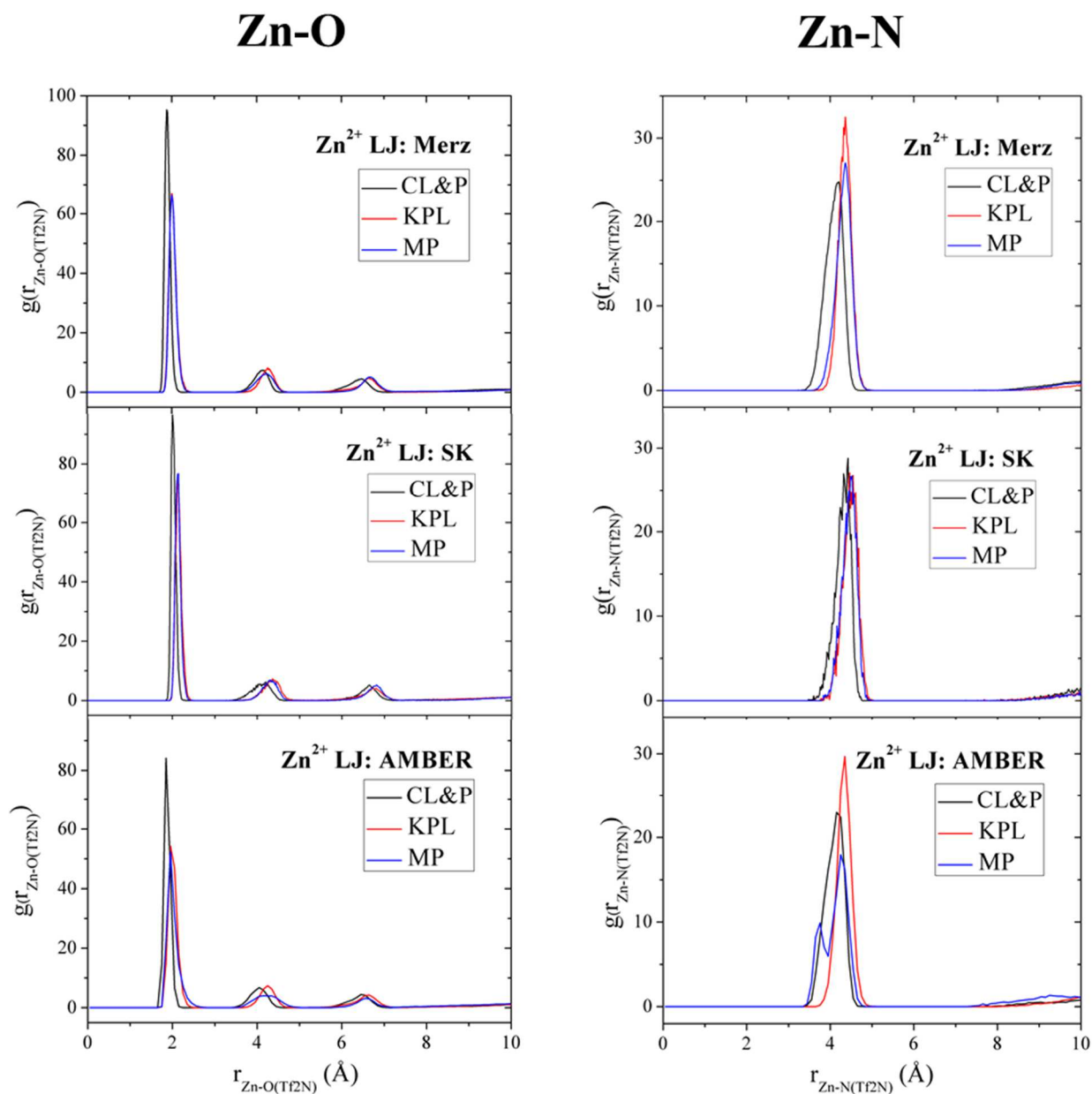


**Figure 4.2.** Zn-O(Tf<sub>2</sub>N) and Zn-N(Tf<sub>2</sub>N) pairs radial distribution functions calculated for Zn<sup>2+</sup> in [C<sub>4</sub>mim][Tf<sub>2</sub>N] employing different Zn<sup>2+</sup> LJ parameters and RTILs force fields.

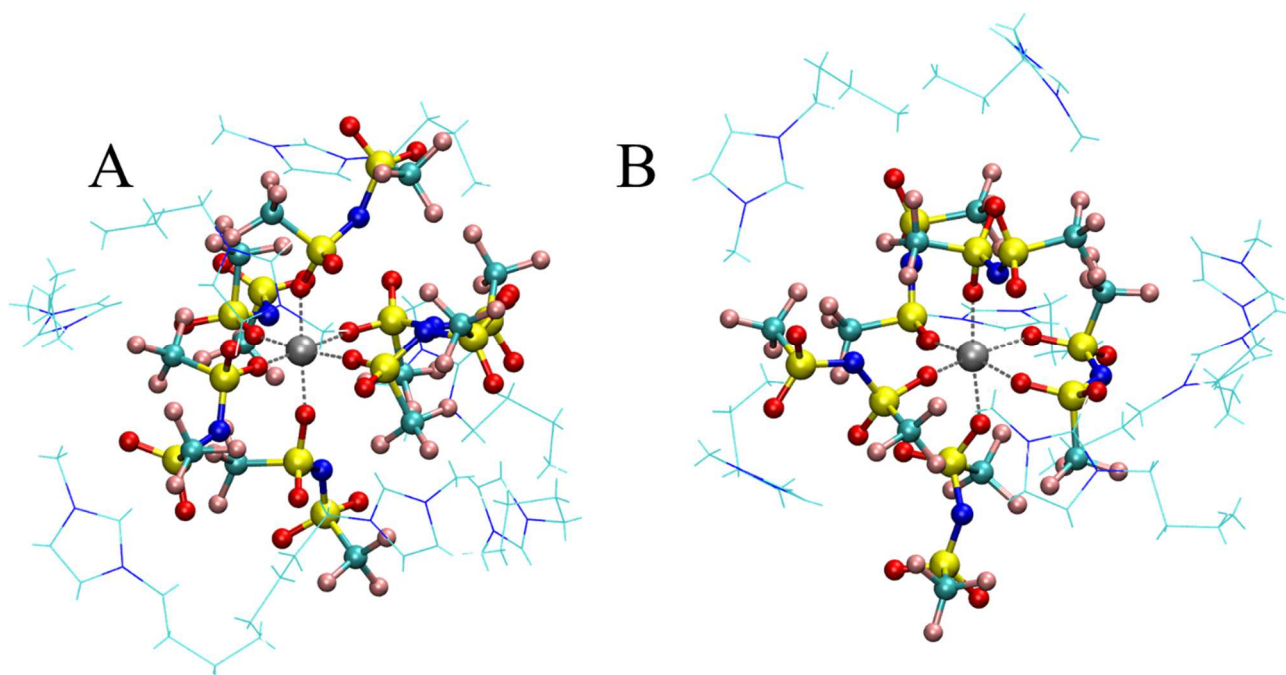
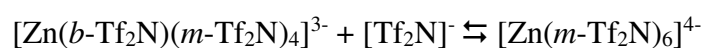


**Figure 4.3.** MD snapshots of  $\text{Zn}^{2+}$  in  $[\text{C}_4\text{mim}][\text{Tf}_2\text{N}]$  giving A)  $[\text{Zn}(\text{Tf}_2\text{N})_6]^{4-}$  ( $\text{Zn}^{2+}$  LJ parameters: Merz; RTIL force field: CL&P) and B)  $[\text{Zn}(\text{Tf}_2\text{N})_5]^{3-}$  ( $\text{Zn}^{2+}$  LJ parameters: AMBER; RTIL force field: MP). Balls and sticks:  $\text{Zn}^{2+}$  and coordinating  $[\text{Tf}_2\text{N}]^-$ ; wireframe: second shell  $[\text{C}_4\text{mim}]^+$ .

The obtained structural results show that even though monodentate  $[\text{Tf}_2\text{N}]^-$  coordination is preferred, the choice of the force field can also give rise to different coordination modes of the RTIL anion. To understand if a possible solvation equilibrium could be present, umbrella sampling simulations for the following process have been performed:



where  $b$  is bidentate and  $m$  is monodentate ligand. The studied thermodynamic path implies the approach of one  $[\text{Tf}_2\text{N}]^-$  forming a new Zn-O( $\text{Tf}_2\text{N}$ ) bond causing the detachment of one oxygen atom of the bidentate  $[\text{Tf}_2\text{N}]^-$  from the metal to give  $[\text{Zn}(\text{Tf}_2\text{N})_6]^{4-}$ , as can be observed from the snapshots reported in **Fig. 4.4**.

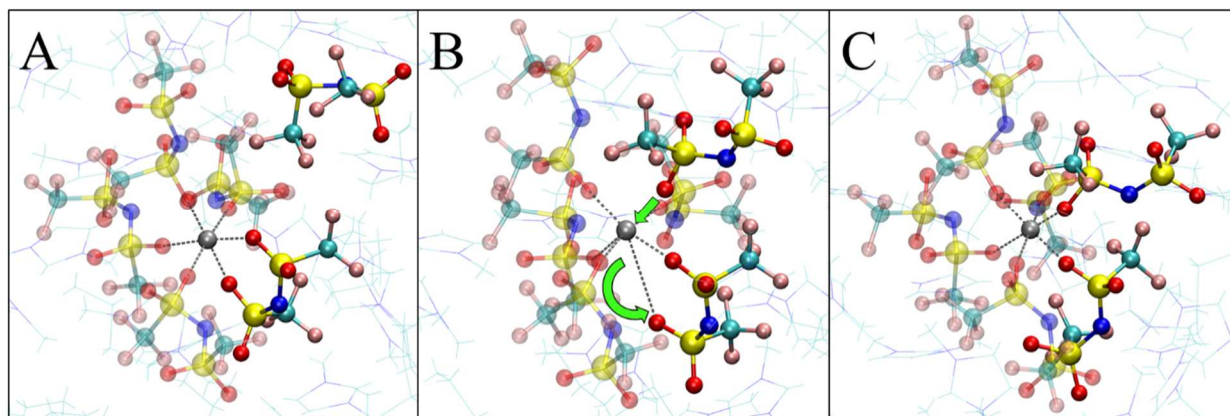


**Figure 4.4.** Selected MD snapshots from the umbrella sampling simulation showing A) the  $[\text{Zn}(\text{Tf}_2\text{N})_5]^{3-}$  unit and the  $[\text{Tf}_2\text{N}]^-$  anion set in the second solvation shell, B) the approach of the  $[\text{Tf}_2\text{N}]^-$  anion leading to the aperture of the bidentate  $[\text{Tf}_2\text{N}]^-$  ligand and C) the resulting  $[\text{Zn}(\text{Tf}_2\text{N})_6]^{4-}$  species.

After the simulation of each configuration, the analysis evidenced a reasonable overlap between the histograms of the selected windows (**Fig. C.1** in **Appendix C**). Here it is also possible to observe the effect of the different constant for the harmonic potential that have been employed for different Zn-O( $\text{Tf}_2\text{N}$ ) distances between the metal and the approaching  $[\text{Tf}_2\text{N}]^-$ . For longer distances, smaller constants show higher oscillations around the imposed value of the reaction coordinate  $\xi$ . On the other hand, higher constants had to be employed for small Zn-O( $\text{Tf}_2\text{N}$ ) distances to contrast the strong electrostatic interaction and to prevent the oxygen atom falling around the equilibrium bond distance. The obtained PMF profile is reported in **Fig. 4.5**. The minimum is located at 1.88 Å, which is the average Zn-O( $\text{Tf}_2\text{N}$ ) distance obtained for  $\text{Zn}^{2+}$  in  $[\text{C}_4\text{mim}][\text{Tf}_2\text{N}]$  with Merz and CL&P parameter sets (**Tab. 4.4**). The PMF profile shows that when the  $[\text{Tf}_2\text{N}]^-$  anion approaches  $[\text{Zn}(\text{Tf}_2\text{N})_5]^{3-}$  there is an energy barrier of 5.2 kcal mol<sup>-1</sup> at ~3 Å, corresponding to the opening of the bidentate  $[\text{Tf}_2\text{N}]^-$ . Given that the final potential minimum value is -7.8 kcal mol<sup>-1</sup>,  $[\text{Zn}(\text{Tf}_2\text{N})_6]^{4-}$  seems to be the favored species in comparison to  $[\text{Zn}(\text{Tf}_2\text{N})_5]^{3-}$ . To further confirm this observation, the calculated energy difference obtained at DFT level<sup>i</sup> for interconverting  $[\text{Tf}_2\text{N}]^-$  from mono- to bidentate binding conformation resulted to be 3.4 kcal mol<sup>-1</sup>. Furthermore, the estimated  $\Delta G_{\text{solv}}$  of the  $[\text{Zn}(\text{Tf}_2\text{N})_6]^{4-}$  and  $[\text{Zn}(\text{Tf}_2\text{N})_5]^{3-}$  complexes in SMD continuum solvent resulted to be -325.6 and -189.9 kcal mol<sup>-1</sup>,

<sup>i</sup>DFT calculations carried out for  $[\text{Zn}(\text{Tf}_2\text{N})_5]^{3-}$  and  $[\text{Zn}(\text{Tf}_2\text{N})_6]^{4-}$  complexes with  $\omega\text{B97XD}$  functional<sup>47</sup> and 6-31+G(d) basis set coupled with Stuttgart-Dresden pseudopotentials for Zn.<sup>48</sup> Triple-zeta 6-311+G(d) basis set was employed for  $[\text{Tf}_2\text{N}]^-$  in its mono- and bidentate binding configurations. Simulations carried out using the SMD continuum model<sup>49</sup> with the specific parameters developed for  $[\text{C}_4\text{mim}][\text{Tf}_2\text{N}]$ .<sup>50</sup> Calculations performed with Gaussian 16 program.<sup>51</sup>

respectively. This further indicates that the more favorable solvation of the hexa-monodentate species could be responsible of its higher stability, highlighting the role of the solvent in the formation of this coordination. Such difference should be able to compensate also the increase in entropy of the anion when released to the bulk ionic liquid in the  $[\text{Zn}(\text{Tf}_2\text{N})_6]^{4-} \rightarrow [\text{Zn}(\text{Tf}_2\text{N})_5]^{3-} + [\text{Tf}_2\text{N}]^-$  process.

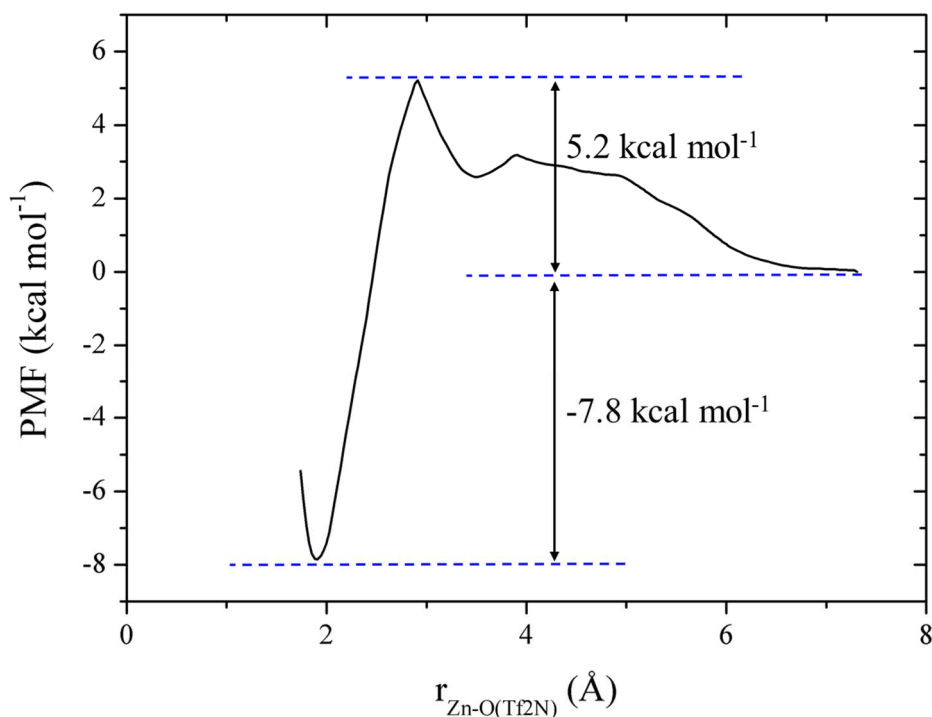


**Figure 4.5.** Calculated PMF profile for the addition of a  $[\text{Tf}_2\text{N}]^-$  anion to a  $[\text{Zn}(\text{Tf}_2\text{N})_5]^{3-}$  unit to give  $[\text{Zn}(\text{Tf}_2\text{N})_6]^{4-}$ .

#### 4.3.1.2 $\text{Zn}^{2+}$ Solvation thermodynamics

$\text{Zn}^{2+}$  Gibbs free energies of solvation in  $[\text{C}_2\text{mim}][\text{Tf}_2\text{N}]$  and  $[\text{C}_4\text{mim}][\text{Tf}_2\text{N}]$  have been calculated with all the tested RTILs force fields and LJ parameters for the metal and the results are reported in **Tab. 4.5**. The output of the BAR module providing the relative free energy differences between neighboring  $\lambda$  windows is reported in **Fig. C.2** of **Appendix C**. From this output, it can be observed that the process of turning on vdW interactions provides only a negligible contribute to the total free energy, while the largest part is given by the electrostatic interaction. The values reported in **Tab. 4.5** show that at constant  $\text{Zn}^{2+}$  LJ parameters,  $\Delta G_{\text{solv}}$  becomes more negative by changing the RTIL force field following the  $\text{KPL} < \text{MP} < \text{CL\&P}$  trend. Since  $[\text{Tf}_2\text{N}]^-$  oxygen partial charge is the same in the tested force fields (**Tab. 4.2**), it can be concluded that the more negative value calculated with CL&P is due to the smaller value of the LJ parameter  $\sigma$  for oxygen, thus bringing to shorter Zn-O( $\text{Tf}_2\text{N}$ )

average distances (**Tab. 4.4**) and stronger non-bonded interactions between the metal ion and the solvent. On the other hand, for a given RTIL force field,  $\Delta G_{\text{solv}}$  becomes more negative with  $\text{Zn}^{2+}$  LJ parameters in the SK < Merz < AMBER order, following once again the calculated average Zn-O(Tf<sub>2</sub>N) distance as expected. Interestingly, the values obtained with MP force field in combination with AMBER LJ parameters do not follow this trend. This exception can be attributed to the different [Tf<sub>2</sub>N]<sup>-</sup> coordination towards zinc ([Zn(Tf<sub>2</sub>N)<sub>5</sub>]<sup>3+</sup> instead of [Zn(Tf<sub>2</sub>N)<sub>6</sub>]<sup>4+</sup>) observed with this set of potentials. As regards the absolute values,  $\Delta G_{\text{solv}}$  results to be best reproduced in comparison with the experimental (**Tab. 4.1**) with CL&P force field in combination with Merz and AMBER parameters. On the other hand, KPL and MP tend to underestimate  $\Delta G_{\text{solv}}$  regardless of the employed LJ for  $\text{Zn}^{2+}$ . In order to obtain the  $\Delta G_{\text{trans}}$  from water to the RTILs,  $\text{Zn}^{2+}$   $\Delta G_{\text{hyd}}$  employing all the tested LJ parameters for the metal were also calculated and the values are reported in **Tab. 4.6**. It can be observed that the obtained values are well in agreement with those calculated by Merz *et al.*<sup>23</sup> in the parametrization of their new sets of LJ for  $\text{Zn}^{2+}$ . In addition, it is evident that an underestimation of  $\Delta G_{\text{solv}}$  (**Tab. 4.5**) is accompanied by an equal underestimation of  $\Delta G_{\text{hyd}}$  for a given set of LJ. In particular, the slight underestimation of  $\Delta G_{\text{solv}}$  with Merz parameters and CL&P is caused by an equal underestimation of  $\Delta G_{\text{hyd}}$  (-447.2 kcal mol<sup>-1</sup> vs. -467.4<sup>44</sup> and -483.7 kcal mol<sup>-1</sup>)<sup>45</sup> due to the employment of the “CM set”<sup>23</sup> parametrized to provide a compromise between structural and thermodynamic properties in water. The choice of the “HFE” set, capable of reproducing  $\Delta G_{\text{hyd}}$  in almost perfect agreement with the experimental, was discarded since to obtain such a negative free energy the authors had to reduce the Zn-O(H<sub>2</sub>O) bond distance and a CN of 4.0 also resulted,<sup>23</sup> which is deeply incorrect for  $\text{Zn}^{2+}$  in water.<sup>42</sup> As regards the calculated  $\Delta G_{\text{trans}}(\text{water} \rightarrow \text{RTIL})$ , values are positive for both the ionic liquids in most cases and this result shows that MD simulations were able to reproduce  $\text{Zn}^{2+}$  as less solvated in the RTILs than in water, in agreement with the picture arising from the experimental data (**Tab. 4.1**). Also in this case, the best reproduction of experimental  $\Delta G_{\text{trans}}$  is provided by Merz LJ parameters in combination with CL&P.

**Table 4.5.** Calculated  $\text{Zn}^{2+}$  Gibbs free energies of solvation  $\Delta G_{\text{solv}}$  ( $\text{kcal mol}^{-1}$ ) in  $[\text{C}_2\text{mim}][\text{Tf}_2\text{N}]$  and  $[\text{C}_4\text{mim}][\text{Tf}_2\text{N}]$  and free energies of transfer from water to the RTILs employing all the tested  $\text{Zn}^{2+}$  LJ parameters<sup>23–25</sup> and RTIL force fields.<sup>18–22</sup>  $T = 298.15 \text{ K}$ ,  $P = 1 \text{ atm}$ . Errors given by BAR module.

RTIL	RTIL force field	$\text{Zn}^{2+}$ LJ: Merz		$\text{Zn}^{2+}$ LJ: SK		$\text{Zn}^{2+}$ LJ: AMBER	
		$\Delta G_{\text{solv}}^{\text{a}}$	$\Delta G_{\text{trans}}$ (water $\rightarrow$ RTIL) <sup>b</sup>	$\Delta G_{\text{solv}}^{\text{a}}$	$\Delta G_{\text{trans}}$ (water $\rightarrow$ RTIL) <sup>b</sup>	$\Delta G_{\text{solv}}^{\text{a}}$	$\Delta G_{\text{trans}}$ (water $\rightarrow$ RTIL) <sup>b</sup>
$[\text{C}_2\text{mim}][\text{Tf}_2\text{N}]$	CL&P	$-437.7 \pm 0.4$	$9.5 \pm 0.5$	$-412.7 \pm 1.1$	$1.6 \pm 1.2$	$-452.4 \pm 1.1$	$1.3 \pm 1.3$
	KPL	$-397.6 \pm 1.1$	$49.6 \pm 1.2$	$-379.2 \pm 0.6$	$35.1 \pm 0.7$	$-397.7 \pm 1.7$	$56.0 \pm 1.9$
$[\text{C}_4\text{mim}][\text{Tf}_2\text{N}]$	CL&P	$-441.4 \pm 0.3$	$5.8 \pm 0.5$	$-415.5 \pm 1.1$	$-0.2 \pm 1.2$	$-454.7 \pm 0.7$	$-0.9 \pm 0.9$
	KPL	$-393.8 \pm 0.9$	$53.4 \pm 1.1$	$-375.0 \pm 0.8$	$39.3 \pm 0.9$	$-398.5 \pm 0.7$	$55.2 \pm 0.9$
	MP	$-413.3 \pm 1.1$	$33.9 \pm 1.3$	$-391.8 \pm 1.4$	$22.4 \pm 1.5$	$-402.9 \pm 0.6$	$50.8 \pm 0.8$

<sup>a</sup> $\text{Zn}^{2+}$  Gibbs free energy of solvation in RTILs; <sup>b</sup> $\text{Zn}^{2+}$  Gibbs free energy of transfer from water to the RTILs calculated as  $\Delta G_{\text{trans}}(\text{water}\rightarrow\text{RTIL}) = \Delta G_{\text{solv}}(\text{g}\rightarrow\text{RTIL}) - \Delta G_{\text{hyd}}$  with the  $\Delta G_{\text{hyd}}$  values reported in **Tab. 4.6**.

**Table 4.6.** MD calculated  $\text{Zn}^{2+}$  Gibbs free energy of hydration ( $\Delta G_{\text{hyd}}$ , kcal mol<sup>-1</sup>) with the LJ parameters<sup>23–25</sup> tested in this work at  $T = 298.15$  K and  $P = 1$  atm. Errors given by BAR module.

$\text{Zn}^{2+}$ LJ parameters	$\Delta G_{\text{hyd}}$
Merz	$-447.2 \pm 0.2$
SK	$-414.3 \pm 0.1$
AMBER	$-453.8 \pm 0.2$

An estimation about the spontaneity of the transfer process of  $\text{Zn}^{2+}$  from water to  $[\text{C}_4\text{mim}][\text{Tf}_2\text{N}]$  has been obtained also by means of umbrella sampling simulations for the pulling of one  $\text{Zn}^{2+}$  ion from an aqueous phase to  $[\text{C}_4\text{mim}][\text{Tf}_2\text{N}]$  in a biphasic system (**Fig. 4.6**).

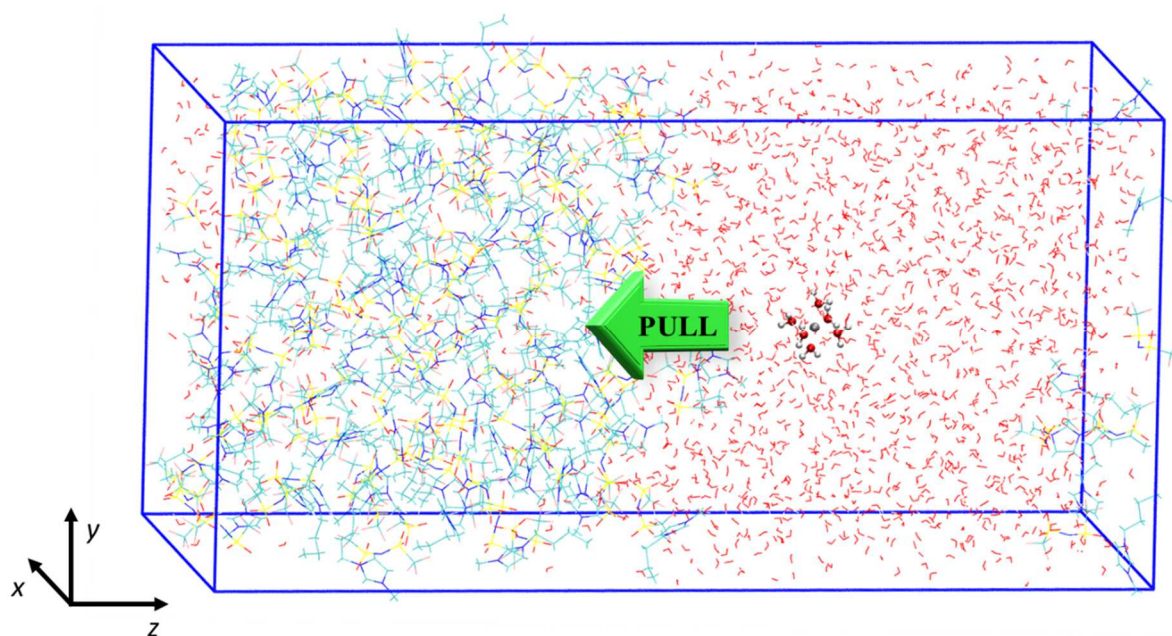


**Figure 4.6.** Initial configuration of the simulated system for the pulling of  $\text{Zn}^{2+}$  through a water/ $[\text{C}_4\text{mim}][\text{Tf}_2\text{N}]$  interphase (balls and sticks:  $\text{Zn}^{2+}$  and coordinating water molecules, wireframe: bulk water and  $[\text{C}_4\text{mim}][\text{Tf}_2\text{N}]$ ).

After the simulation of each configuration and the calculation of the PMF, a good overlap between the histograms of the selected windows was observed (**Fig. C.3** in **Appendix C**). The calculated PMF profile reported in **Fig. 4.7** shows a plateau from the  $\sim 34$  Å reaction coordinate (distance between  $\text{Zn}^{2+}$  and  $[\text{C}_4\text{mim}][\text{Tf}_2\text{N}]$  COM) to  $\sim 23$  Å, corresponding to the  $\text{Zn}^{2+}$  ion in the aqueous phase. After, the energy starts increasing sharply at about  $18$  Å, which is the coordinate corresponding to the interphase. In the RTIL, the energy rises until a value comprised between  $5.0$  and  $5.5$  kcal mol<sup>-1</sup>, which is the PMF associated to the transfer of the metal ion between the two phases. The obtained

value is still in agreement with the experimental and calculated  $\Delta G_{\text{trans}}(\text{water} \rightarrow [\text{C}_4\text{mim}][\text{Tf}_2\text{N}])$  between the two pure solvents (**Tab. 4.1** and **Tab. 4.5**) and also with the observation that  $\text{Zn}^{2+}$  is poorly extracted from water employing the ionic liquid without auxiliary ligands.<sup>11,14,15</sup>

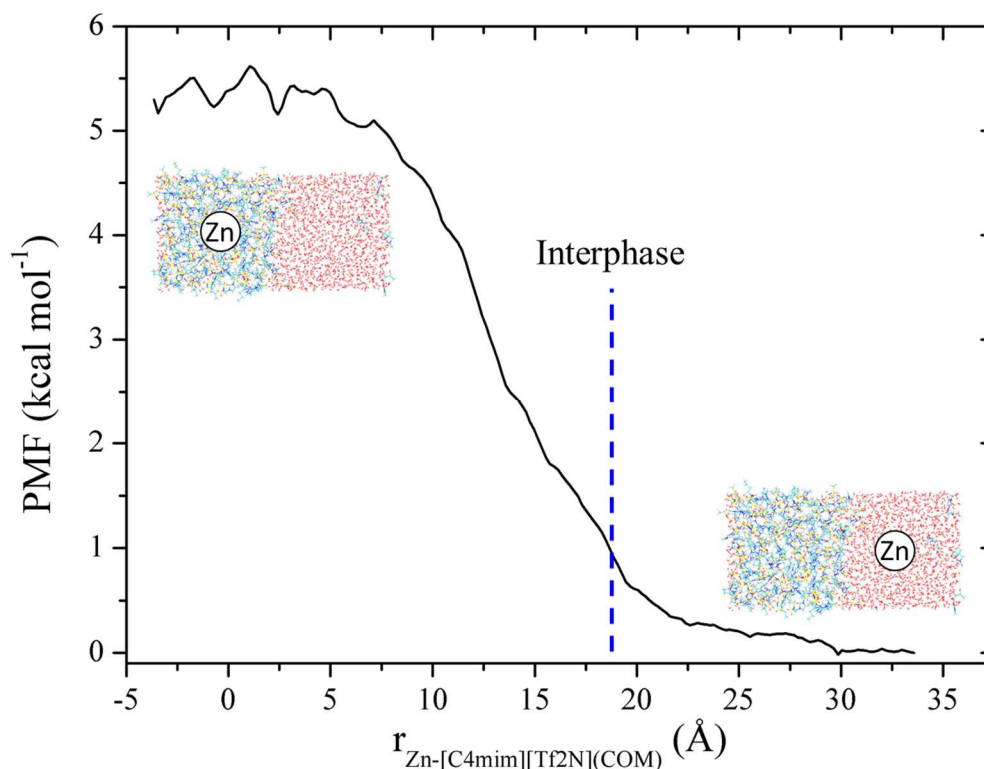


**Figure 4.7.** Calculated PMF profile for the umbrella sampling simulation of one  $\text{Zn}^{2+}$  ion pulled through a water/[ $\text{C}_4\text{mim}$ ][ $\text{Tf}_2\text{N}$ ] biphasic system.

As regards  $\text{Zn}^{2+}$  coordination along the reaction coordinate, MD simulations reproduced the metal ion as always coordinated by six water molecules in an octahedral fashion along the entire reaction coordinate. This can be observed from the  $\text{Zn-O}(\text{H}_2\text{O})$   $g(r)$  in the RTIL phase (**Fig. C.4** in **Appendix C**), showing overlapping strong peaks at  $1.98 \text{ \AA}$  which integrate six oxygen atoms in each umbrella window. In addition, the  $\text{Zn-O}(\text{Tf}_2\text{N})$   $g(r)$  in the RTIL phase report a second solvation shell formed by a mixture of water molecules and  $[\text{Tf}_2\text{N}]^-$  anions starting approximately at  $4.2 \text{ \AA}$  from the metal center, thus indicating that no  $[\text{Tf}_2\text{N}]^-$  are present in the first solvation shell.

To understand the origin of the unfavorable transfer,  $\text{Zn}^{2+}$  enthalpies and entropies of hydration and solvation in [ $\text{C}_4\text{mim}$ ][ $\text{Tf}_2\text{N}$ ] have been calculated using the set of potentials providing the best compromise between structural and thermodynamic experimental data (CL&P for the RTIL and Merz for  $\text{Zn}^{2+}$ ). This was performed by means of free energy calculations at different temperatures and the employment of  $\Delta G/T$  vs.  $1/T$  plots (**Fig. 4.8**). The obtained values for hydration are reported in **Tab.**

**4.7.** The calculated  $\Delta H_{\text{hyd}}$  and  $\Delta S_{\text{hyd}}$  are in good agreement with the experimental and are typical for divalent metal ions in water,<sup>44–46</sup> showing large negative enthalpy and small negative entropy due to the ordering of the solvent around the solute. The calculation of enthalpy and entropy of solvation in [C<sub>4</sub>mim][Tf<sub>2</sub>N] also allowed to obtain the enthalpy and entropy of transfer from water to the RTIL. The results are reported in **Tab. 4.8**.  $\Delta H_{\text{solv}}$  in [C<sub>4</sub>mim][Tf<sub>2</sub>N] resulted to be more negative than  $\Delta H_{\text{hyd}}$  and the same happens for the entropy term. As a consequence, both the enthalpy and entropy of transfer from water to the RTIL are negative. The negative enthalpy seems to favor the transfer of Zn<sup>2+</sup>, but the unfavorable contribution is given by the negative  $\Delta S_{\text{trans}}(\text{water} \rightarrow [\text{C}_4\text{mim}][\text{Tf}_2\text{N}])$  term which determines the global positive Gibbs free energy of transfer. This result can be explained by the higher order imposed to the liquid structure by the solvated metal ion in the case of [C<sub>4</sub>mim][Tf<sub>2</sub>N] with respect to water.

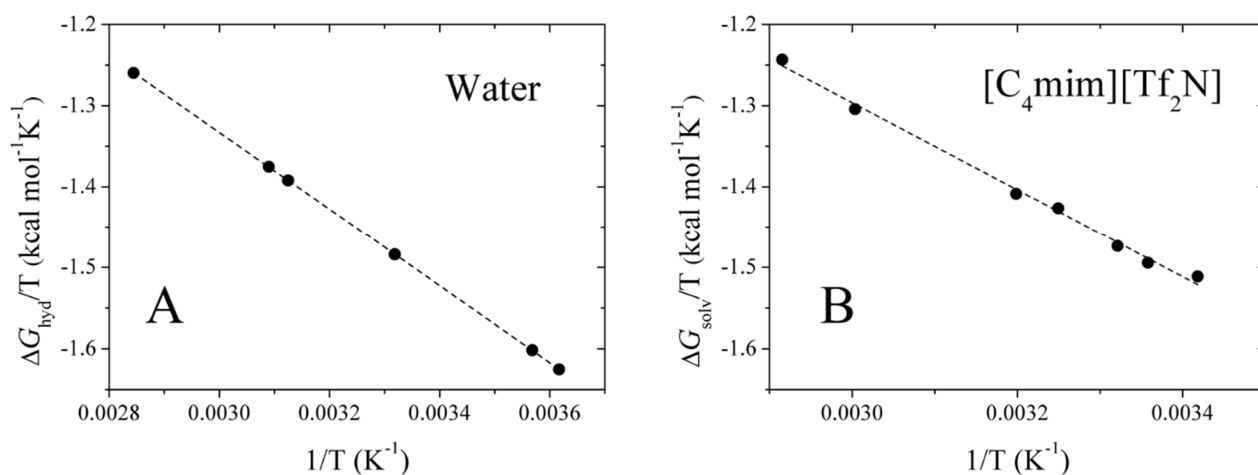


**Figure 4.8.**  $\Delta G/T$  vs.  $1/T$  plots obtained from calculated Zn<sup>2+</sup> Gibbs free energies A) in water and B) in [C<sub>4</sub>mim][Tf<sub>2</sub>N] at different temperatures ( $R^2 = 0.99$ ).

**Table 4.7.** Hydration enthalpies (kcal mol<sup>-1</sup>) and entropies (kcal mol<sup>-1</sup> K<sup>-1</sup>) for Zn<sup>2+</sup> calculated from MD simulations (obtained from plot in **Fig. 4.8 A**) and from experimental data.

MD calculated		Experimental	
$\Delta H_{\text{hyd}}$	$\Delta S_{\text{hyd}}$	$\Delta H_{\text{hyd}}$	$\Delta S_{\text{hyd}}$
$-473.2 \pm 0.4$	$-0.086 \pm 0.001$	$-486.7^{\text{a}}$	$-0.065^{\text{46}}$
		$-493.1^{\text{45}}$	$-0.031^{\text{b}}$

<sup>a</sup> $\Delta H_{\text{hyd}}$  calculated from Marcus'  $\Delta G_{\text{hyd}}$ <sup>44</sup> and  $\Delta S_{\text{hyd}}$ .<sup>46</sup> <sup>b</sup> $\Delta S_{\text{hyd}}$  calculated from Ahrland's  $\Delta G_{\text{hyd}}$  and  $\Delta H_{\text{hyd}}$ .<sup>45</sup>

**Table 4.8.** MD calculated enthalpy (kcal mol<sup>-1</sup>) and entropy (kcal mol<sup>-1</sup> K<sup>-1</sup>) of solvation for Zn<sup>2+</sup> in [C<sub>4</sub>mim][Tf<sub>2</sub>N] and transfer from water to the RTIL obtained from the plot in **Fig. 4.8 B**.

$\Delta H_{\text{solv}}$	$\Delta S_{\text{solv}}$	$\Delta H_{\text{trans}}^{\text{a}}$ (water→[C <sub>4</sub> mim][Tf <sub>2</sub> N])	$\Delta S_{\text{trans}}^{\text{b}}$ (water→[C <sub>4</sub> mim][Tf <sub>2</sub> N])
-538.1 ± 16.8	-0.318 ± 0.054	-64.9 ± 17.2	-0.232 ± 0.055

<sup>a</sup>Enthalpy of transfer from water to [C<sub>4</sub>mim][Tf<sub>2</sub>N] calculated as  $\Delta H_{\text{trans}}(\text{water} \rightarrow [\text{C}_4\text{mim}][\text{Tf}_2\text{N}]) = \Delta H_{\text{solv}} - \Delta H_{\text{hyd}}$ ;

<sup>b</sup>Entropy of transfer from water to [C<sub>4</sub>mim][Tf<sub>2</sub>N] calculated as  $\Delta S_{\text{trans}}(\text{water} \rightarrow [\text{C}_4\text{mim}][\text{Tf}_2\text{N}]) = \Delta S_{\text{solv}} - \Delta S_{\text{hyd}}$  using the MD calculated values reported in **Tab. 4.7** for hydration.

#### 4.3.1.3 Zn<sup>2+</sup> coordination in wet [C<sub>4</sub>mim][Tf<sub>2</sub>N]: XAS results

To better characterize Zn<sup>2+</sup> first solvation shell composition and structure in water-saturated [C<sub>4</sub>mim][Tf<sub>2</sub>N] and verify the reliability of the biphasic system umbrella sampling simulation representing zinc as coordinated by six water molecules, XAS measures have been performed on Zn<sup>2+</sup> solutions in the RTIL in presence of water (1 M and water-saturated). The XANES part of the spectra of the wet [C<sub>4</sub>mim][Tf<sub>2</sub>N] solutions has been compared with those of dry [C<sub>4</sub>mim][Tf<sub>2</sub>N] and pure water solutions, and the results are shown in **Fig. 4.9**. From this comparison, it can be observed that the XANES spectrum of Zn<sup>2+</sup> in dry [C<sub>4</sub>mim][Tf<sub>2</sub>N] presents slight differences as compared to the wet solutions, while spectra from RTIL solutions containing either 1 M water or up to the saturation limit are identical. This finding suggests that, if water is present at high concentration, Zn<sup>2+</sup> is preferentially coordinated by water in the RTIL. The origin of these small but detectable differences of the dry RTIL XANES spectrum as compared with the wet samples can be explained by taking into account that both water and the [Tf<sub>2</sub>N]<sup>-</sup> coordinate Zn<sup>2+</sup> with the oxygen atom at approximately the same distance (2.078(2) Å for water<sup>42</sup> and 2.07 Å for [Tf<sub>2</sub>N]<sup>-</sup>).<sup>17</sup> However, in dry [C<sub>4</sub>mim][Tf<sub>2</sub>N] there is an additional second shell Zn-S SS contribution associated with the [Tf<sub>2</sub>N]<sup>-</sup> ion.<sup>17</sup> In addition, XANES is known to be strongly sensitive to MS contributions. Therefore, further differences can be attributed to the Zn-O-S MS, which has been found to possess a detectable amplitude in the dry RTIL.<sup>17</sup> A further proof of the presence of a hexa-aquo Zn<sup>2+</sup> complex in wet [C<sub>4</sub>mim][Tf<sub>2</sub>N] has been obtained comparing the XANES spectra of this sample with that of Zn(Tf<sub>2</sub>N)<sub>2</sub> in pure water. The comparison is shown in **Fig. 4.9 B**. As expected, the two spectra are almost identical.

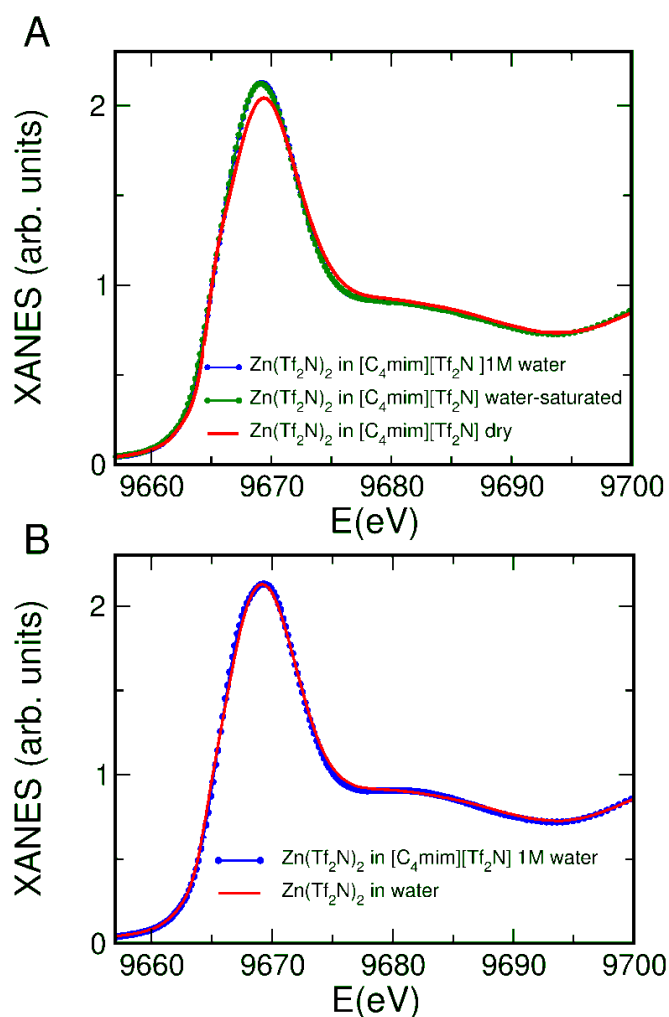


**Figure 4.9.** A) Zn K-edge XANES spectra of  $\text{Zn}(\text{Tf}_2\text{N})_2$  0.1 M solutions in  $[\text{C}_4\text{mim}][\text{Tf}_2\text{N}]$  in dry conditions (red line), with 1 M water (blue line) and water-saturated (green line). B) Zn K-edge XANES spectra of  $\text{Zn}(\text{Tf}_2\text{N})_2$  0.1 M in water (red line) and in  $[\text{C}_4\text{mim}][\text{Tf}_2\text{N}]$  with 1 M water content (blue line).

A quantitative determination of  $\text{Zn}^{2+}$  coordination in the wet RTIL has been obtained by the analysis of the EXAFS part of the spectra. To this purpose, a fitting procedure has been carried out on the 0.1 M  $\text{Zn}(\text{Tf}_2\text{N})_2$  sample in  $[\text{C}_4\text{mim}][\text{Tf}_2\text{N}]$  with 1 M water content. To validate the results from the umbrella sampling simulations and the qualitative observations of XANES, the fitting procedure has been carried out for a  $\text{Zn}^{2+}$  ion as coordinated by six water molecules in an octahedral fashion. To this extent, SS contributions associated with 6 Zn-O and 12 Zn-H paths have been included, within MS signals coming from O-Zn-O  $90^\circ$  and  $180^\circ$  paths. Least-squares fits of the EXAFS data have been carried out in the  $2.3 - 15.0 \text{ \AA}^{-1} k$  range by varying the structural parameters associated with the Zn-O and Zn-H contributions, whereas O-Zn-O angles have been kept fixed in an octahedral configuration. The full list of the final optimized parameters is reported in **Tab. 4.9**, whereas the calculated  $\chi(k)$  signals are reported in **Fig. 4.10** within the best-fit results compared with the

experimental spectrum and the resulting residuals. The agreement between the theoretical and experimental data is very good, as also showed by the Fourier-transformed spectra. The average distances for the Zn-O and Zn-H paths of respectively 2.07 and 2.80 Å, as well as the  $\sigma^2$  Debye-Waller factors and asymmetry indexes  $\beta$ , are almost identical to that of the  $[\text{Zn}(\text{H}_2\text{O})_6]^{2+}$  species formed by  $\text{Zn}^{2+}$  in pure water,<sup>42</sup> while  $E_0$  was found at 0.8 eV above the first inflection point of the spectrum. Such results show that the  $\text{Zn}^{2+}$  ion is preferentially coordinated by water in the wet  $[\text{C}_4\text{mim}][\text{Tf}_2\text{N}]$  ionic liquid, as suggested by MD simulations.

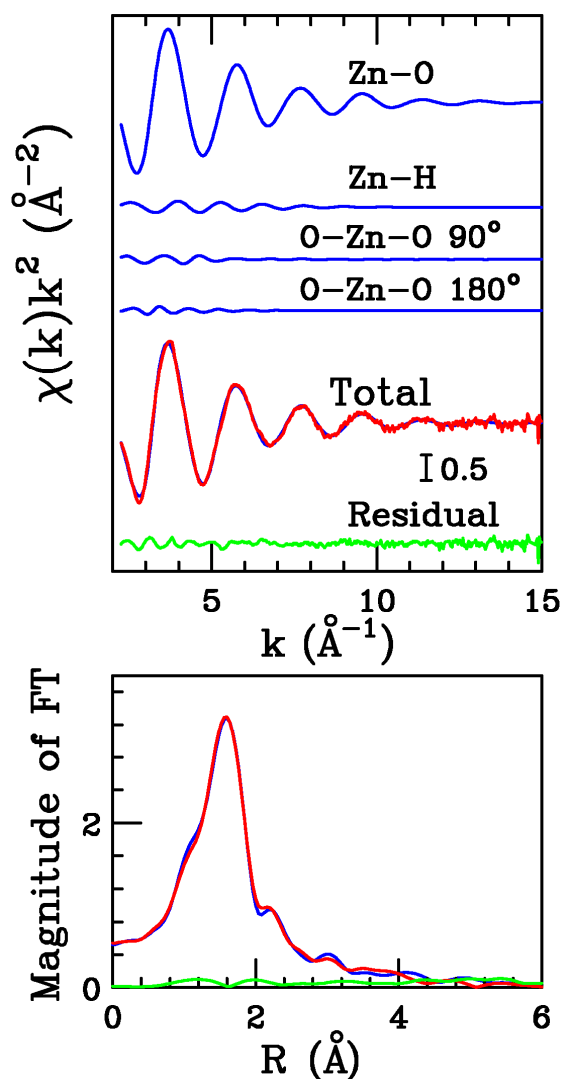


**Figure 4.10.** Upper panel: EXAFS analysis of the Zn K-edge EXAFS spectrum of the 0.1  $\text{Zn}(\text{Tf}_2\text{N})_2$  solution in  $[\text{C}_4\text{mim}][\text{Tf}_2\text{N}]$  with 1 M water content. From the top the following curves are reported: best fit theoretical Zn-O and Zn-H SS contributions, O-Zn-O MS signals, total theoretical signal (blue line) together with the experimental spectrum (red line) and the correspondent residuals (green line). Lower panel: non-phase shift corrected Fourier Transforms of the best-fit EXAFS theoretical signal (blue line) of the experimental data (red line) and of the residual curve (green line).

**Table 4.9.** Coordination number CN, average distance R, Debye-Waller factor  $\sigma^2$  and asymmetry index  $\beta$  optimized during the EXAFS fitting procedure for 0.1 M Zn(Tf<sub>2</sub>N)<sub>2</sub> in [C<sub>4</sub>mim][Tf<sub>2</sub>N] with 1 M water content. Standard deviation in parenthesis.

	CN	R (Å)	$\sigma^2$ (Å <sup>2</sup> )	$\beta$
Zn-O	6.0	2.07(2)	0.008(3)	0.15(5)
Zn-H	12.0	2.80(3)	0.015(4)	0.09(5)

### 4.3.2 Zn<sup>2+</sup> in [C<sub>4</sub>mim][BF<sub>4</sub>]

MD simulations of Zn<sup>2+</sup> in [C<sub>4</sub>mim][BF<sub>4</sub>] have been carried out by representing the RTIL with two different force fields. The obtained structural parameters for Zn<sup>2+</sup> first coordination shell are reported in **Tab. 4.10**, while the  $g(r)$ 's calculated for the Zn-F and Zn-B pairs are showed in **Fig. 4.11**. As regards the Zn-F distribution, a first intense peak integrating 6.0 fluorine atoms at an average distance of 1.85 Å is obtained with both force fields. The Zn-B  $g(r)$ , also integrating 6.0 atoms, indicates the formation of the [Zn(BF<sub>4</sub>)<sub>6</sub>]<sup>4-</sup> octahedral species where six tetrafluoroborate anions are able to coordinate the metal in a monodentate fashion (**Fig. 4.12**). Therefore, the same coordination is obtained with both the tested force fields, as is expectable given the same LJ part between these two potential sets (**Tab. 4.3**).

**Table 4.10.** MD results of Zn<sup>2+</sup> first solvation shell structure in [C<sub>4</sub>mim][BF<sub>4</sub>] employing the tested RTIL force fields.<sup>18,43</sup>

RTIL force field	$r_{\text{Zn-F}}$ (Å) <sup>a</sup>	CN <sub>F</sub> <sup>b</sup>	CN <sub>B</sub> <sup>c</sup>
CL&P	1.85	6.0	6.0
CL&P + Wang anion	1.85	6.0	6.0

<sup>a</sup>Average bond distance between the Zn<sup>2+</sup> ion and the coordinating fluorine atoms of the first solvation shell [BF<sub>4</sub>]<sup>-</sup> anions;

<sup>b</sup>Zn-F first  $g(r)$  peak integration number; <sup>c</sup>Zn-B first  $g(r)$  peak integration number.

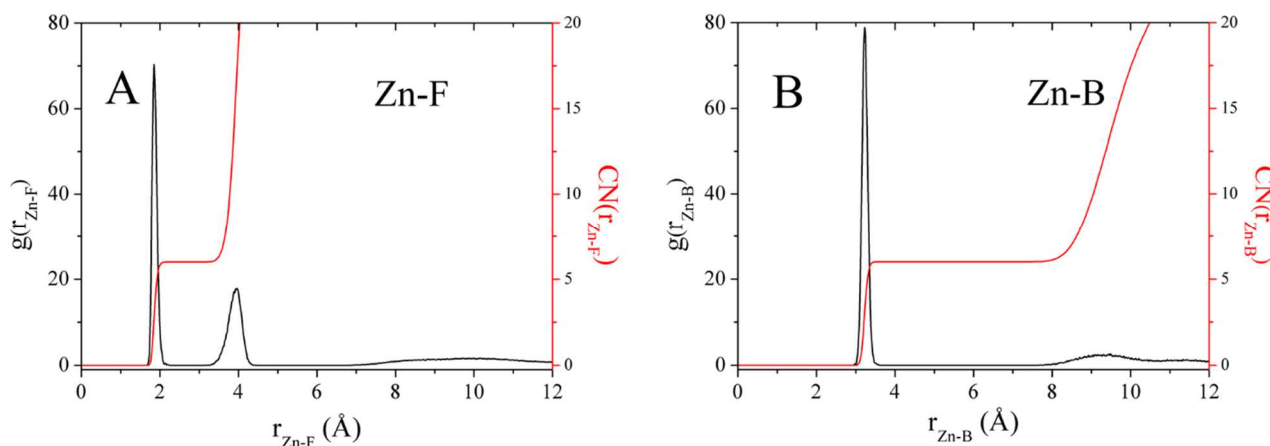


**Figure 4.11.** MD calculated A) Zn-F and B) Zn-B pairs  $g(r)$ 's radial distribution functions (black lines, left scale) and corresponding integration numbers (red lines, right scales) for  $\text{Zn}^{2+}$  in  $[\text{C}_4\text{mim}][\text{BF}_4]$  (RTIL force field: CL&P).

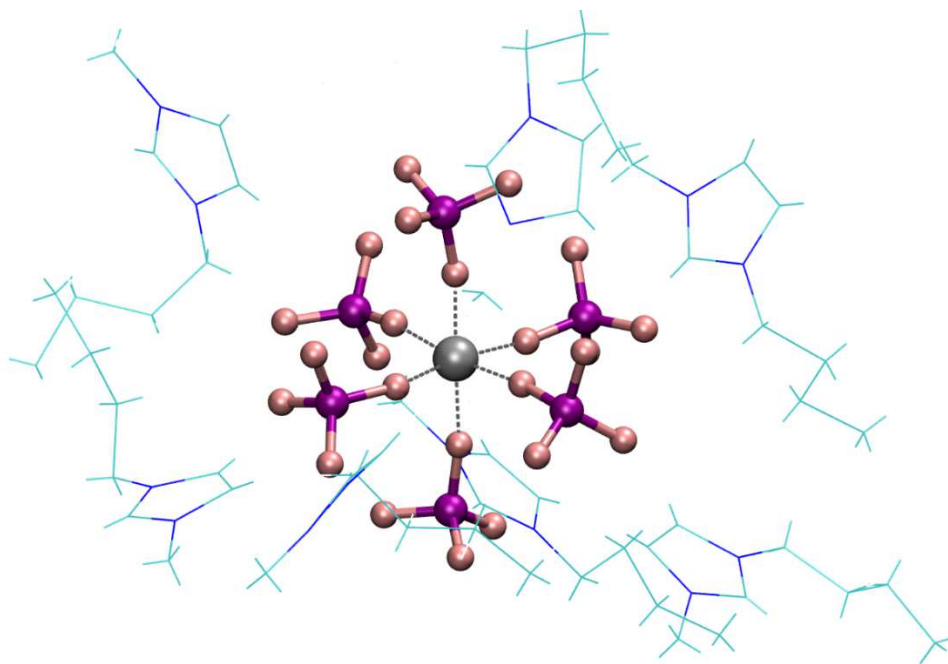


**Figure 4.12.** MD snapshot of  $\text{Zn}^{2+}$  in  $[\text{C}_4\text{mim}][\text{BF}_4]$  forming the  $[\text{Zn}(\text{BF}_4)_6]^{4-}$  species (RTIL force field: CL&P). Balls and sticks:  $\text{Zn}^{2+}$  and coordinating  $[\text{BF}_4]^-$ ; wireframe: second shell  $[\text{C}_4\text{mim}]^+$ .

$\text{Zn}^{2+}$  Gibbs free energies of solvation in  $[\text{C}_4\text{mim}][\text{BF}_4]$  and transfer from water to the RTIL have also been calculated and the obtained values are reported in **Tab. 4.11**. As can be observed,  $\Delta G_{\text{solv}}$  calculated with CL&P force field resulted to be less negative than that obtained with Wang *et al.* parameters for  $[\text{BF}_4]^-$ , as is expectable from the less negative partial charge on the fluorine atoms in case of the former force field (**Tab. 4.3**). In addition, Wang anion reproduced a  $\Delta G_{\text{solv}}$  which is more close to the experimental ( $-479.2$  and  $-495.7$  kcal mol $^{-1}$ , **Tab. 4.1**). As a consequence, this force field

provided also a better estimation of  $\Delta G_{\text{trans}}$  in comparison with the experimental data (-12.0 kcal mol<sup>-1</sup>), even though both the force fields were able to reproduce Zn<sup>2+</sup> as more solvated in [C<sub>4</sub>mim][BF<sub>4</sub>] than in water and therefore a favorable transfer from the aqueous solution to this RTIL.

**Table 4.11.** MD calculated Gibbs free energies of solvation in [C<sub>4</sub>mim][BF<sub>4</sub>] ( $\Delta G_{\text{solv}}$ ) and transfer from water ( $\Delta G_{\text{trans}}$ ) obtained at T = 298.15 K and P = 1 atm for Zn<sup>2+</sup> with the tested RTIL force fields.<sup>18,43</sup> Errors given by the BAR module. Values in kcal mol<sup>-1</sup>.

RTIL force field	$\Delta G_{\text{solv}}$	$\Delta G_{\text{trans}}^{\text{a}}$
CL&P	-450.2 ± 0.8	-2.9 ± 1.1
CL&P + Wang anion	-461.1 ± 0.8	-13.8 ± 1.1

<sup>a</sup>Zn<sup>2+</sup> Gibbs free energy of transfer from water to the RTIL calculated as  $\Delta G_{\text{trans}} = \Delta G_{\text{solv}} - \Delta G_{\text{hyd}}$  with the values for hydration reported in **Tab. 4.6** (Merz LJ).

Also in this case, the contributions to the free energies of solvation and transfer were explored by obtaining the enthalpies and entropies of solvation in [C<sub>4</sub>mim][BF<sub>4</sub>] and of transfer from water to this RTIL. To this purpose, free energy calculations were performed at six different temperatures in the 300 – 420 K range by representing Zn<sup>2+</sup> with Merz *et al.* LJ parameters and [C<sub>4</sub>mim][BF<sub>4</sub>] with CL&P plus Wang *et al.* anion. The obtained  $\Delta G/T$  vs.  $1/T$  plot is showed in **Fig. 4.13**, while the calculated values are reported in **Tab. 4.12**. Here it can be observed that the obtained  $\Delta H_{\text{solv}}$  is more negative than  $\Delta H_{\text{hyd}}$  (**Tab. 4.7**) and the same happens for the entropic term. As a consequence, both  $\Delta H_{\text{trans}}$  and  $\Delta S_{\text{trans}}$  are negative, as was found for [C<sub>4</sub>mim][Tf<sub>2</sub>N] (**Tab. 4.8**). However,  $\Delta S_{\text{trans}}$  is much lower in comparison with that obtained for the previously studied RTIL. As a consequence, the favorable  $\Delta G_{\text{trans}}$  towards [C<sub>4</sub>mim][BF<sub>4</sub>] can be attributed to the negative  $\Delta H_{\text{trans}}$ , while the slightly unfavorable  $\Delta S_{\text{trans}}$  is not negative enough to compensate the favorable enthalpic effect. In other words, it seems that a higher order to the liquid structure is still imposed by the solvated metal ion in case of [C<sub>4</sub>mim][BF<sub>4</sub>] with respect to water, but of a lower extent with respect to what was found for [C<sub>4</sub>mim][Tf<sub>2</sub>N].

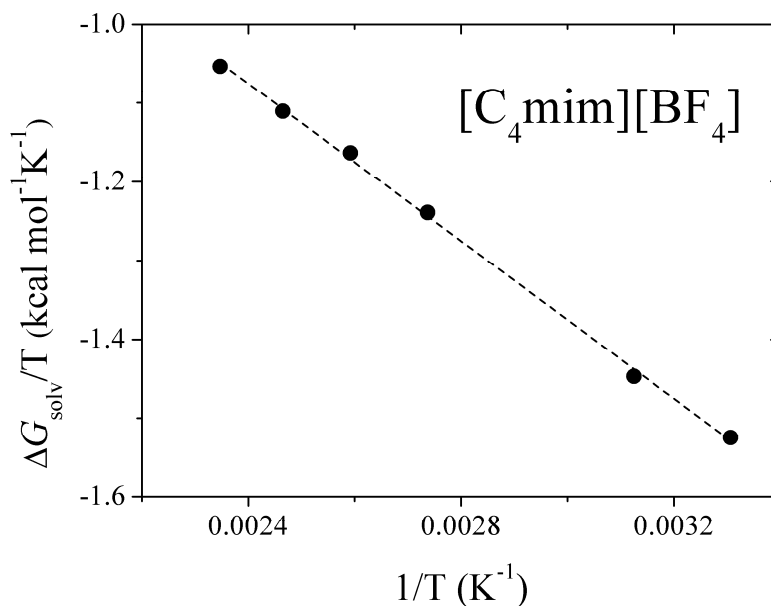


**Figure 4.13.**  $\Delta G/T$  vs.  $1/T$  plot obtained from calculated  $\text{Zn}^{2+}$  Gibbs free energies in  $[\text{C}_4\text{mim}][\text{BF}_4]$  at different temperatures ( $R^2 = 0.99$ ).

**Table 4.12.** MD calculated enthalpy ( $\text{kcal mol}^{-1}$ ) and entropy ( $\text{kcal mol}^{-1} \text{K}^{-1}$ ) of solvation for  $\text{Zn}^{2+}$  in  $[\text{C}_4\text{mim}][\text{BF}_4]$  and transfer from water to the RTIL obtained from the plot in **Fig. 4.13**.

$\Delta H_{\text{solv}}$	$\Delta S_{\text{solv}}$	$\Delta H_{\text{trans}}^{\text{a}}$ (water $\rightarrow$ $[\text{C}_4\text{mim}][\text{BF}_4]$ )	$\Delta S_{\text{trans}}^{\text{b}}$ (water $\rightarrow$ $[\text{C}_4\text{mim}][\text{BF}_4]$ )
$-499.6 \pm 8.7$	$-0.124 \pm 0.024$	$-26.4 \pm 9.1$	$-0.038 \pm 0.025$

<sup>a</sup>Enthalpy of transfer from water to  $[\text{C}_4\text{mim}][\text{BF}_4]$  calculated as  $\Delta H_{\text{trans}}(\text{water}\rightarrow[\text{C}_4\text{mim}][\text{BF}_4]) = \Delta H_{\text{solv}} - \Delta H_{\text{hyd}}$ ; <sup>b</sup>Entropy of transfer from water to  $[\text{C}_4\text{mim}][\text{BF}_4]$  calculated as  $\Delta S_{\text{trans}}(\text{water}\rightarrow[\text{C}_4\text{mim}][\text{BF}_4]) = \Delta S_{\text{solv}} - \Delta S_{\text{hyd}}$  using the MD calculated values reported in **Tab. 4.7** for hydration.

## 4.4 Conclusions

MD simulations have been carried out on the  $\text{Zn}^{2+}$  ion in the  $[\text{C}_n\text{mim}][\text{Tf}_2\text{N}]$  ( $n = 2, 4$ ) and  $[\text{C}_4\text{mim}][\text{BF}_4]$  ionic liquids. The results showed that a description of structural and thermodynamic properties of a metal ion solvation in RTILs in good agreement with experimental data can be obtained by means of MD calculations. From a thermodynamic point of view, the positive transfer free energies  $\Delta G_{\text{trans}}(\text{water}\rightarrow[\text{C}_n\text{mim}][\text{Tf}_2\text{N}])$  indicate that  $\text{Zn}^{2+}$  is more favorably solvated in water than in this class of ionic liquids. The unfavorable  $\Delta G_{\text{trans}}$  arises from an entropy-enthalpy balance where the negative  $\Delta S_{\text{trans}}(\text{water}\rightarrow[\text{C}_4\text{mim}][\text{Tf}_2\text{N}])$  is able to overcome a favorable  $\Delta H_{\text{trans}}(\text{water}\rightarrow[\text{C}_4\text{mim}][\text{Tf}_2\text{N}])$  contribution and could be explained by the higher liquid ordering

due to ion solvation in the case of [C<sub>4</sub>mim][Tf<sub>2</sub>N] with respect to water. Also the free energy associated to the transfer of a Zn<sup>2+</sup> ion in a water/[C<sub>4</sub>mim][Tf<sub>2</sub>N] biphasic system is positive, in agreement with the poor extraction rates from aqueous solutions obtained experimentally. From a structural point of view, umbrella sampling simulations for the addition of a [Tf<sub>2</sub>N]<sup>-</sup> anion to a [Zn(Tf<sub>2</sub>N)<sub>5</sub>]<sup>3-</sup> unit to give [Zn(Tf<sub>2</sub>N)<sub>6</sub>]<sup>4-</sup> showed that the coordination including only monodentate [Tf<sub>2</sub>N]<sup>-</sup> is largely energetically favored. In addition, simulations predict that Zn<sup>2+</sup> in water saturated [C<sub>4</sub>mim][Tf<sub>2</sub>N] is coordinated by six water molecules. This finding is confirmed by XAS experimental results, which clearly show that water completely solvates the metal ion when present at high concentrations in the ionic liquid.

As regards [C<sub>4</sub>mim][BF<sub>4</sub>], MD simulations reproduce a Zn<sup>2+</sup> ion still coordinated by six monodentate anions, thus the [Zn(BF<sub>4</sub>)<sub>6</sub>]<sup>4-</sup> species. In addition, the trend showed by the experimental data is confirmed, *i.e.* a favorable transfer from water to BF<sub>4</sub>-based RTILs is obtained. In this case the favorable  $\Delta G_{\text{trans}}(\text{water} \rightarrow [\text{C}_4\text{mim}][\text{BF}_4])$  is due to the negative enthalpy of transfer, with a still unfavorable  $\Delta S_{\text{trans}}(\text{water} \rightarrow [\text{C}_4\text{mim}][\text{BF}_4])$  that however is not enough negative to counterbalance the enthalpic effect.

## Bibliography

- 1 M. J. Earle, U. Hakala, B. J. Mcauley and M. Nieuwenhuyzen, Metal bis{(trifluoromethyl)sulfonyl}amide complexes: highly efficient Friedel – Crafts acylation catalysts, *Chem. Commun.*, 2004, **0**, 1368–1369.
- 2 Z. Liu, S. Z. El Abedin and F. Endres, Electrodeposition of zinc films from ionic liquids and ionic liquid/water mixtures, *Electrochim. Acta*, 2013, **89**, 635–643.
- 3 T. J. Simons, P. M. Bayley, Z. Zhang, P. C. Howlett, D. R. Macfarlane, L. A. Madsen and M. Forsyth, Influence of Zn<sup>2+</sup> and water on the transport properties of a pyrrolidinium dicyanamide ionic liquid, *J. Phys. Chem. B*, 2014, **118**, 4895–4905.
- 4 M. Xu, D. G. Ivey, W. Qu and Z. Xie, Improved Zn/Zn(II) redox kinetics, reversibility and cyclability in 1-ethyl-3-methylimidazolium dicyanamide with water and dimethyl sulfoxide added, *J. Power Sources*, 2014, **252**, 327–332.
- 5 M. Xu, D. G. Ivey, Z. Xie, W. Qu and E. Dy, The state of water in 1-butyl-1-methylpyrrolidinium bis(trifluoromethanesulfonyl)imide and its effect on Zn/Zn(II) redox behavior, *Electrochim. Acta*, 2013, **97**, 289–295.
- 6 T. J. Simons, P. C. Howlett, A. A. J. Torriero, D. R. MacFarlane and M. Forsyth, Electrochemical, transport, and spectroscopic properties of 1-ethyl-3-methylimidazolium ionic liquid electrolytes containing zinc dicyanamide, *J. Phys. Chem. C*, 2013, **117**, 2662–2669.
- 7 T. J. Simons, A. A. J. Torriero, P. C. Howlett, D. R. MacFarlane and M. Forsyth, High current density, efficient cycling of Zn<sup>2+</sup> in 1-ethyl-3-methylimidazolium dicyanamide ionic liquid: The effect of Zn<sup>2+</sup> salt and water concentration, *Electrochem. commun.*, 2012, **18**, 119–122.
- 8 M. Regel-Rosocka, A review on methods of regeneration of spent pickling solutions from steel processing, *J. Hazard. Mater.*, 2010, **177**, 57–69.
- 9 M. Regel-Rosocka, A. Cieszyńska and M. Wiśniewski, Methods of regeneration of spent pickling solutions from steel treatment plants, *Polish J. Chem. Technol.*, 2007, **9**, 42–45.
- 10 Ł. Nowak, M. Regel-Rosocka, B. Marszałkowska and M. Wiśniewski, Removal of Zn(II) from chloride acidic solutions with hydrophobic quaternary salts, *Polish J. Chem. Technol.*, 2010, **12**, 24–28.
- 11 P. A. De Los Rios, F. J. Hernandez-Fernandez, S. Sanchez-Segado, L. J. Lozano, J. I.

- Moreno and C. Godínez, Selective Separation of Zn(II) and Fe(III) from Acidic Media Using Ionic Liquids as Sole Extraction Agents, *Chem. Eng. Trans.*, 2010, **21**, 625–630.
- 12 B. Marszakowska, M. Regel-Rosocka, Ł. Nowak and M. Wioeniewski, Quaternary phosphonium salts as effective extractants of zinc(II) and iron(III) ions from acidic pickling solutions, *Polish J. Chem. Technol.*, 2010, **12**, 1–5.
- 13 M. Regel-Rosocka, Extractive removal of zinc(II) from chloride liquors with phosphonium ionic liquids/toluene mixtures as novel extractants, *Sep. Purif. Technol.*, 2009, **66**, 19–24.
- 14 A. P. De Los Ríos, F. J. Hernández-Fernández, L. J. Lozano, S. Sánchez, J. I. Moreno, C. Godínez, F. J. Herna and C. Godínez, Removal of Metal Ions from Aqueous Solutions by Extraction with Ionic Liquids, *J. Chem. Eng. Data*, 2010, **55**, 605–608.
- 15 K. Kidani, N. Hirayama and H. Imura, Extraction behavior of divalent metal cations in ionic liquid chelate extraction systems using 1-alkyl-3-methylimidazolium bis(trifluoromethanesulfonyl)imides and thenoyltrifluoroacetone, *Anal. Sci.*, 2008, **24**, 1251–4.
- 16 S. T. M. Vidal, M. J. N. Correia, M. M. Marques, M. R. Ismael and M. T. A. Reis, Studies on the Use of Ionic Liquids as Potential Extractants of Phenolic Compounds and Metal Ions, *Sep. Sci. Technol.*, 2004, **39**, 2155–2169.
- 17 F. Sessa, V. Migliorati, A. Serva, A. Lapi, G. Aquilanti, G. Mancini and P. D'Angelo, On the coordination of Zn<sup>2+</sup> ion in Tf<sub>2</sub>N<sup>-</sup> based ionic liquids: structural and dynamic properties depending on the nature of the organic cation, *Phys. Chem. Chem. Phys.*, 2018, **20**, 2662–2675.
- 18 J. N. Canongia Lopes, A. A. H. Padua and J. Dechamps, Modeling ionic liquids using a systematic all-atom force field, *J. Phys. Chem. B*, 2004, **108**, 2038–2047.
- 19 J. N. Canongia Lopes, A. A. H. Padua and J. Dechamps, Additions and corrections., *J. Phys. Chem. B*, 2004, **108**, 11250.
- 20 J. N. Canongia Lopes and A. A. H. Padua, Molecular Force Field for Ionic Liquids Composed of Triflate or Bistriflyimide Anions, *J. Phys. Chem. B*, 2004, **108**, 16893–16898.
- 21 T. Köddermann, D. Paschek and R. Ludwig, Molecular dynamic simulations of ionic liquids: A reliable description of structure, thermodynamics and dynamics, *ChemPhysChem*, 2007, **8**, 2464–2470.
- 22 W. Zhao, E. Hossein, W. L. Cavalcanti and F. Müller-Plathe, A Refined All-Atom Model for the Ionic Liquid 1-n-Butyl 3-Methylimidazolium bis(Trifluoromethylsulfonyl)imide [bmim][Tf<sub>2</sub>N], *Z. Phys. Chem.*, 2007, **221**, 1549–1567.
- 23 P. Li, B. P. Roberts, D. K. Chakravorty and K. M. Merz, Rational design of particle mesh

- ewald compatible lennard-jones parameters for +2 metal cations in explicit solvent, *J. Chem. Theory Comput.*, 2013, **9**, 2733–2748.
- 24 R. H. Stote and M. Karplus, Zinc binding in proteins and solution: a simple but accurate nonbonded representation., *Proteins*, 1995, **23**, 12–31.
- 25 S. C. Hoops, K. W. Anderson and K. M. Merz, Force Field Design for Metalloproteins, *J. Am. Chem. Soc.*, 1991, **113**, 8262–8270.
- 26 M. R. Shirts, J. W. Pitner, W. C. Swope and V. S. Pande, Extremely precise free energy calculations of amino acid side chain analogs: Comparison of common molecular mechanics force fields for proteins, *J. Chem. Phys.*, 2003, **119**, 5740–5761.
- 27 T. Darden, D. York and L. Pedersen, Particle mesh Ewald: An Nlog(N) method for Ewald sums in large systems, *J. Chem. Phys.*, 1993, **98**, 10089.
- 28 U. Essmann, L. Perera, M. L. Berkowitz, T. Darden, H. Lee and L. G. Pedersen, A smooth particle mesh Ewald method, *J Chem Phys*, 1995, **103**, 8577–8593.
- 29 R. W. Hockney, S. P. Goel and J. W. Eastwood, Quiet high-resolution computer models of a plasma, *J. Comput. Phys.*, 1974, **14**, 148–158.
- 30 M. Parrinello and A. Rahman, Polymorphic transitions in single crystals: A new molecular dynamics method, *J. Appl. Phys.*, 1981, **52**, 7182–7190.
- 31 B. Hess, H. Bekker, H. J. C. Berendsen and J. G. E. M. Fraaije, LINCS: A linear constraint solver for molecular simulations, *J. Comput. Chem.*, 1997, **18**, 1463–1472.
- 32 M. J. Abraham, T. Murtola, R. Schulz, S. Páll, J. C. Smith, B. Hess and E. Lindahl, Gromacs: High performance molecular simulations through multi-level parallelism from laptops to supercomputers, *SoftwareX*, 2015, **1–2**, 19–25.
- 33 W. L. Jorgensen, J. Chandrasekhar, J. D. Madura, R. W. Impey and M. L. Klein, Comparison of simple potential functions for simulating liquid water, *J. Chem. Phys.*, 1983, **79**, 926.
- 34 C. H. Bennett, Efficient estimation of free energy differences from Monte Carlo data, *J. Comput. Phys.*, 1976, **22**, 245–268.
- 35 S. Wan, R. H. Stote and M. Karplus, Calculation of the aqueous solvation energy and entropy, as well as free energy, of simple polar solutes, *J. Chem. Phys.*, 2004, **121**, 9539–9548.
- 36 J. Carlsson and J. Åqvist, Calculations of solute and solvent entropies from molecular dynamics simulations, *Phys. Chem. Chem. Phys.*, 2006, **8**, 5385–5395.
- 37 J. Carlsson and J. Åqvist, Absolute hydration entropies of alkali metal ions from molecular dynamics simulations, *J. Phys. Chem. B*, 2009, **113**, 10255–10260.
- 38 S. Kumar, J. M. Rosenberg, D. Bouzida, R. H. Swendsen and P. A. Kollman, The weighted

- histogram analysis method for free-energy calculations on biomolecules. I. The method, *J. Comput. Chem.*, 1992, **13**, 1011–1021.
- 39 A. Di Cicco, G. Aquilanti, M. Minicucci, E. Principi, N. Novello, A. Cognigni and L. Olivi, Novel XAFS capabilities at ELETTRA synchrotron light source, *J. Phys. Conf. Ser.*, 2009, **190**, 12043.
- 40 A. Filipponi and A. Di Cicco, X-ray-absorption spectroscopy and  $n$ -body distribution functions in condensed matter. II. Data analysis and applications, *Phys. Rev. B*, 1995, **52**, 15135–15149.
- 41 L. Hedin and B. I. Lundqvist, Explicit local exchange-correlation potentials, *J. Phys. C Solid State Phys.*, 1971, **4**, 2064–2082.
- 42 P. D'Angelo, V. Barone, G. Chillemi, N. Sanna, W. Meyer-Klaucke and N. V. Pavel, Hydrogen and higher shell contributions in Zn<sup>2+</sup>, Ni<sup>2+</sup>, and Co<sup>2+</sup>-aqueous solutions: An X-ray absorption fine structure and molecular dynamics study, *J. Am. Chem. Soc.*, 2002, **124**, 1958–1967.
- 43 Z. Liu, S. Huang and W. Wang, A refined force field for molecular simulation of imidazolium-based ionic liquids, *J. Phys. Chem. B*, 2004, **108**, 12978–12989.
- 44 Y. Marcus, Thermodynamics of Solvation of Ions, *J. Chem. Soc., Faraday Trans.*, 1991, **87**, 2995–2999.
- 45 S. Ahrland, Solvation and Complex Formation-Competing and Cooperative Processes in Solution, *Pure Appl. Chem.*, 1982, **54**, 1451–1468.
- 46 Y. Marcus and A. Loewenschuss, Standard Entropies of Hydration of Ions, *A. Annu. Rep. Prog. Chem. Sect. C Phys. Chem.*, 1984, **81**, 81–135.
- 47 J. Da Chai and M. Head-Gordon, Systematic optimization of long-range corrected hybrid density functionals, *J. Chem. Phys.*, , DOI:10.1063/1.2834918.
- 48 M. Dolg, U. Wedig, H. Stoll and H. Preuss, Energy-adjusted ab initio pseudopotentials for the first row transition elements, *J. Chem. Phys.*, 1987, **86**, 866–872.
- 49 A. V Marenich, C. J. Cramer and D. G. Truhlar, Universal Solvation Model Based on Solute Electron Density and on a Continuum Model of the Solvent Defined by the Bulk Dielectric Constant and Atomic Surface Tensions, *J. Phys. Chem. B*, 2009, **113**, 6378–6396.
- 50 R. Contreras, C. J. Cramer, D. G. Truhlar, V. S. Bernales and A. V. Marenich, Quantum mechanical continuum solvation models for ionic liquids, *J. Phys. Chem. B*, 2012, **116**, 9122–9129.
- 51 M. J. Frisch, G. W. Trucks, H. B. Schlegel, G. E. Scuseria, M. A. Robb, J. R. Cheeseman, G. Scalmani, V. Barone, G. A. Petersson, H. Nakatsuji, X. Li, M. Caricato, A. V Marenich, J.

Bloino, B. G. Janesko, R. Gomperts, B. Mennucci, H. P. Hratchian, J. V Ortiz, A. F. Izmaylov, J. L. Sonnenberg, D. Williams-Young, F. Ding, F. Lipparini, F. Egidi, J. Goings, B. Peng, A. Petrone, T. Henderson, D. Ranasinghe, V. G. Zakrzewski, J. Gao, N. Rega, G. Zheng, W. Liang, M. Hada, M. Ehara, K. Toyota, R. Fukuda, J. Hasegawa, M. Ishida, T. Nakajima, Y. Honda, O. Kitao, H. Nakai, T. Vreven, K. Throssell, J. A. Montgomery Jr., J. E. Peralta, F. Ogliaro, M. J. Bearpark, J. J. Heyd, E. N. Brothers, K. N. Kudin, V. N. Staroverov, T. A. Keith, R. Kobayashi, J. Normand, K. Raghavachari, A. P. Rendell, J. C. Burant, S. S. Iyengar, J. Tomasi, M. Cossi, J. M. Millam, M. Klene, C. Adamo, R. Cammi, J. W. Ochterski, R. L. Martin, K. Morokuma, O. Farkas, J. B. Foresman and D. J. Fox, *Gaussian 16 Rev. A03*, Wallingford, CT, 2016.



# Chapter 5

## Co<sup>2+</sup> ion in [C<sub>4</sub>mim][Tf<sub>2</sub>N]

### 5.1 Introduction

Applications involving the Co<sup>2+</sup> ion in RTILs seems to provide promising results. For example, Co<sup>2+</sup> complexes in RTILs have been tested as catalysts for sustainable chemistry and energy applications such as the oxidation of lignin to obtain high-value products<sup>1</sup> or for the desulfurization of petroleum.<sup>2</sup> Co(Tf<sub>2</sub>N)<sub>2</sub> dissolved in [C<sub>4</sub>mim][Tf<sub>2</sub>N] showed a high catalytic activity for the acylation of chloro- and fluorobenzene,<sup>3</sup> while Co<sup>2+</sup> phthalocyanine complexes in [C<sub>4</sub>mim][Br] exhibited excellent yields and high recycling capabilities for the aerobic oxidation of alkyl-arenes and alcohols.<sup>4</sup> In addition, the electrochemical behavior of the Co/Co<sup>2+</sup> redox couple has been studied in several RTILs for electrodepositions.<sup>5,6</sup> Metallic cobalt has been successfully electrodeposited from [C<sub>4</sub>mpyr][Tf<sub>2</sub>N] and [C<sub>4</sub>mim][BF<sub>4</sub>].<sup>7-9</sup> The extraction of Co<sup>2+</sup> from aqueous solutions with ionic liquids has also been tested.<sup>10-12</sup>

For what concerns RTILs containing the [Tf<sub>2</sub>N]<sup>-</sup> anion, at the solid state Co<sup>2+</sup> results to be bound *via* the oxygen atoms of the -SO<sub>2</sub> moieties as shown by the crystal structure of [C<sub>4</sub>mpyr]<sub>2</sub>[Co(Tf<sub>2</sub>N)<sub>4</sub>].<sup>13</sup> In the [Co(Tf<sub>2</sub>N)<sub>4</sub>]<sup>2-</sup> unit, the metal ion is bound by two bidentate [Tf<sub>2</sub>N]<sup>-</sup> anions each binding with two oxygen atoms of two different -SO<sub>2</sub> moieties on the equatorial plane, in addition to two monodentate [Tf<sub>2</sub>N]<sup>-</sup> in apical positions. In a Raman spectroscopy work on Co(Tf<sub>2</sub>N)<sub>2</sub> in [C<sub>2</sub>mim][Tf<sub>2</sub>N], the ratio of the peak areas related to “free” and coordinating [Tf<sub>2</sub>N]<sup>-</sup> provided a number of RTIL anions in the metal first solvation sphere of ~3, thus suggesting the presence in solution of the octahedral [Co(Tf<sub>2</sub>N)<sub>3</sub>]<sup>-</sup> species with three bidentate [Tf<sub>2</sub>N]<sup>-</sup>.<sup>14</sup> The same coordination has been proposed for solutions in [P<sub>2225</sub>][Tf<sub>2</sub>N] in another recent work.<sup>15</sup> This [Co(Tf<sub>2</sub>N)<sub>3</sub>]<sup>-</sup> species was also the only detectable in gas phase as found by ESI-MS experiments.<sup>16</sup> However, previous studies have showed that the coordination of a metal ion in solution can be significantly different from that obtained for the solid state and different structures came out also for the liquid phases according to the method employed to analyze the metal first solvation sphere structure.<sup>17-20</sup> As a consequence, the nature of the species formed by the Co<sup>2+</sup> ion in several RTILs as well as most of the important thermodynamic parameters describing its solvation in these media are still unknown.

In this work, XAS measures have been combined with MD simulations to shed light on the still uncertain coordination of the  $[\text{Tf}_2\text{N}]^-$  anions towards  $\text{Co}^{2+}$  in RTILs. To this purpose, the  $[\text{C}_4\text{mim}][\text{Tf}_2\text{N}]$  ionic liquid was considered. The structure of the first solvation shell provided by MD has been validated directly on XAS experiments in a synergic approach. In addition, thermodynamic data such as the metal ion  $\Delta G_{\text{solv}}$  in  $[\text{C}_4\text{mim}][\text{Tf}_2\text{N}]$  and  $\Delta G_{\text{trans}}$  from water to the RTIL have been calculated. Free energy calculations performed at different temperatures allowed also to obtain information about the enthalpies and entropies of solvation and transfer. Furthermore, spectroscopic data in the UV-Vis region have been collected for  $\text{Co}(\text{Tf}_2\text{N})_2$  solutions in  $[\text{C}_4\text{mim}][\text{Tf}_2\text{N}]$  with an increasing amount of water to get more insight into the metal ion solvation tendencies also in the “wet” RTIL.

## 5.2 Methods

### 5.2.1 MD simulations details

For  $\text{Co}^{2+}$  simulations in  $[\text{C}_4\text{mim}][\text{Tf}_2\text{N}]$ , two different protocols have been employed in order to obtain structural and thermodynamic data. The composition of the simulated boxes for the two sets of calculations is reported in **Tab. 5.1**. For the structural part, the number of species was set up to reproduce the density of the 0.1 M  $\text{Co}(\text{Tf}_2\text{N})_2$  solution employed for the XAS measurements. As regards the thermodynamic calculations, the system has been designed to reproduce pure RTIL density and infinite dilution conditions for the metal.

**Table 5.1.** MD boxes details for the calculation of  $\text{Co}^{2+}$  structural and thermodynamic properties in  $[\text{C}_4\text{mim}][\text{Tf}_2\text{N}]$ .

	Structure	Thermodynamics
$\text{Co}^{2+}$	5	1
$[\text{C}_4\text{mim}]^+$	170	198
$[\text{Tf}_2\text{N}]^-$	180	200
Box edge (Å)	44.15	45.90*

\*Initial side length before NPT equilibration.

The CL&P force field was employed for [C<sub>4</sub>mim][Tf<sub>2</sub>N],<sup>21–23</sup> while LJ parameters for Co<sup>2+</sup> were taken from Merz *et al.*<sup>24</sup> This set was selected as that providing the best compromise between structural and thermodynamic description for the solvation of Zn<sup>2+</sup> in RTILs (see **Chapter 4**).<sup>25</sup> For the structural part, Merz “IOD set” reproducing the average Co-O bond distance in water in almost perfect agreement with the experimental was employed, while for the thermodynamic part the “HFE set” that best reproduces Co<sup>2+</sup> Gibbs free energy of hydration was chosen. Both sets of parameters provide a CN of 6.0 for Co<sup>2+</sup>, since it is well-known that this ion is hexa-coordinated in water.<sup>26</sup>

A similar simulation protocol to that employed for Zn<sup>2+</sup> as specified in **Sec. 4.2.1.1** was used, with some exceptions. For the structural part, the production run for data acquisition was performed for 100 ns in NVT conditions at 298.15 K with configurations saved every 100 time steps. For the thermodynamic calculations, Co<sup>2+</sup> single-ion  $\Delta G_{\text{solv}}$  in [C<sub>4</sub>mim][Tf<sub>2</sub>N] has been calculated with 15  $\lambda$  windows: the first 5  $\lambda$  correspond to turn on vdW interactions and the successive 10 are related to the electrostatic part. The number of vdW windows has been reduced because it was observed that the majority of the contribution to the calculated free energy is provided by the electrostatic part, while for vdW it is almost negligible (**Sec. 4.3.1.2** of **Chapter 4**). Longer simulation times were employed with respect to Zn<sup>2+</sup>: for each  $\lambda$ , an NPT equilibration was performed for 5 ns and a production run for data collection was carried out for 60 ns. Longer runs resulted to be necessary as, differently from the Zn<sup>2+</sup> case, a derive in the computed free energy has been observed with simulation time.

To calculate  $\Delta G_{\text{trans}}$ , simulations were carried out also in water. To this purpose, Co<sup>2+</sup> was represented with the same Merz “HFE set”<sup>24</sup> employed for calculations in the RTIL and water with the SPC/E model.<sup>27</sup>  $\Delta G_{\text{hyd}}$  was calculated by employing a 26.2 Å side length box containing one Co<sup>2+</sup> and 600 water molecules still with 15  $\lambda$  windows. For each  $\lambda$ , 2 ns equilibrations and 5 ns runs for data collection were performed.

Co<sup>2+</sup> Enthalpies and entropies of hydration and solvation in [C<sub>4</sub>mim][Tf<sub>2</sub>N] were obtained by performing free energy calculations at 6 different temperatures in the 280 – 340 K range for water and at 5 temperatures in the 300 – 420 K range for the RTIL. A slightly longer cut-off radius with respect to the Zn<sup>2+</sup> case was employed for non-bonded interactions (12 Å). Cross-terms were constructed with the Lorentz-Berthelot combining rules. Simulations have been performed with the Gromacs 5.1.6 program.<sup>28</sup>

## 5.2.2 X-ray absorption measurements

[C<sub>4</sub>mim][Tf<sub>2</sub>N] was purchased by Sigma-Aldrich with a >99% stated purity. Co(Tf<sub>2</sub>N)<sub>2</sub> was synthesized following the procedure reported by Earle *et al.*<sup>29</sup> A 0.1 M solution of Co(Tf<sub>2</sub>N)<sub>2</sub> in

[C<sub>4</sub>mim][Tf<sub>2</sub>N] was prepared with a procedure similar to that employed for Zn<sup>2+</sup> in the same dry RTIL (Sec. 4.2.1.3 of Chapter 4). In addition, solid Co(Tf<sub>2</sub>N)<sub>2</sub> was diluted with boron nitride, carefully grained in an agate mortar and put in 1.5 mm aluminum frames with a Mylar tape covering the sample. Co K-edge XAS spectra of the RTIL solution and solid Co(Tf<sub>2</sub>N)<sub>2</sub> were collected in transmission mode at the 11.1 beamline of Elettra Synchrotron with the same operating conditions employed for Zn<sup>2+</sup>. Three spectra have been recorded and averaged for each sample.

### 5.2.3 EXAFS data analysis

EXAFS data analysis has been carried out with the GNXAS method with the same level of theory employed for Zn<sup>2+</sup> (Sec. 4.2.1.4 of Chapter 4). For the analysis of the Co(Tf<sub>2</sub>N)<sub>2</sub> salt spectrum, the crystallographic structure of [C<sub>4</sub>mpyr]<sub>2</sub>[Co(Tf<sub>2</sub>N)<sub>4</sub>] has been employed as starting point.<sup>13</sup> Co-O first shell SS signal accounting for the six coordinating oxygen atoms has been calculated as well as the Co-S and Co-N signals related to the four [Tf<sub>2</sub>N]<sup>-</sup> binding the metal. In addition, a strong MS contribution associated to the Co-O-S three-body configurations has been found. In particular, both bidentate and monodentate [Tf<sub>2</sub>N]<sup>-</sup> are coordinated to Co<sup>2+</sup> in such a way that the Co-O-S angle is 134°, thus providing a MS signal with a multiplicity of six. The O-S distance of [Tf<sub>2</sub>N]<sup>-</sup> as determined from the crystallographic structure is 1.47 Å. The MS contribution associated with the three collinear O-Co-O configurations has been also found to have a detectable amplitude. All the other three-body configurations involving Co<sup>2+</sup> showed negligible amplitude.

Differently, the analysis of the Co(Tf<sub>2</sub>N)<sub>2</sub> solution in [C<sub>4</sub>mim][Tf<sub>2</sub>N] has been carried out starting from the structural results of the MD simulation. In particular, the Co-O, Co-N and Co-S pairs  $g(r)$ 's have been modeled as  $\Gamma$ -like functions. SS signals for these pair distributions have been calculated starting from the structural parameters obtained from the MD simulation. In this case, as was found for Zn(Tf<sub>2</sub>N)<sub>2</sub> in [C<sub>4</sub>mim][Tf<sub>2</sub>N],<sup>20</sup> there are six monodentate ligands coordinating Co<sup>2+</sup> in an octahedral fashion. At variance with the crystallographic structure, in the RTIL the [Tf<sub>2</sub>N]<sup>-</sup> ligands assume a quasi-linear geometry around the metal ion with Co-O-S angles of ~180° and O-S distance of 1.46 Å. Also in this case, the MS contribution associated with O-Co-O collinear configurations has been included in the analysis. Structural parameters obtained from MD have been varied during the fitting procedure to obtain the best agreement with the  $\chi(k)$  experimental spectrum. In this way, the structural results deriving from the simulation have been compared directly with the EXAFS experimental evidence.

Besides  $E_0$ , also the  $KM_1$  and  $KM_{2,3}$  double-electron excitation energies were optimized starting from values of respectively 66 – 68 and 111 eV above the first inflection point of the experimental spectra on the basis of the  $Z+1$  approximation.

## 5.2.4 UV-Vis absorption spectra

A spectrophotometric titration of a  $\text{Co}(\text{Tf}_2\text{N})_2$  (Alfa Aesar, >98%) solution in  $[\text{C}_4\text{mim}][\text{Tf}_2\text{N}]$  (Iolitec, >99%) with water was carried out. To this purpose, all chemicals were dried under vacuum for 48 h at 70 °C. An amount of metallic salt was dissolved in  $[\text{C}_4\text{mim}][\text{Tf}_2\text{N}]$  to form a  $\text{Co}(\text{Tf}_2\text{N})_2$  0.05 M solution and the residual water was determined to be less than 50 ppm after Karl-Fischer titration. Manipulations of the samples was performed in a  $\text{N}_2$ -filled glove box (water content < 1 ppm). Absorbance spectra were recorded in the 200 – 900 nm region on a Cary 50 UV-Vis spectrophotometer employing a rectangular quartz cell of 10 mm path length with Teflon stopper. Neat  $[\text{C}_4\text{mim}][\text{Tf}_2\text{N}]$  has been employed as blank sample. After recording the  $\text{Co}(\text{Tf}_2\text{N})_2$  sample in the dry RTIL, precise amounts of a 0.5 M water solution in  $[\text{C}_4\text{mim}][\text{Tf}_2\text{N}]$  were added to reach Co:H<sub>2</sub>O ratios from 1:1 to a 1:8 excess, since this metal is hexa-coordinated by water.<sup>26</sup> In addition, spectra of 0.05 M  $\text{Co}(\text{Tf}_2\text{N})_2$  in pure water and in water-saturated  $[\text{C}_4\text{mim}][\text{Tf}_2\text{N}]$  were recorded as comparison. The water-saturated RTIL has been prepared by shaking  $[\text{C}_4\text{mim}][\text{Tf}_2\text{N}]$  with an equal volume of MilliQ water in a separating funnel for 3 minutes, letting the two liquids separate overnight and then collecting the organic phase.

## 5.3 Results

### 5.3.1 $\text{Co}^{2+}$ coordination

$\text{Co}^{2+}$  coordination in the  $\text{Co}(\text{Tf}_2\text{N})_2$  crystal has been determined on the basis of the crystallographic structure reported in literature.<sup>13</sup> The metal ion results to be coordinated by two monodentate and two bidentate  $[\text{Tf}_2\text{N}]^-$  (**Fig. 5.1 A**) both assuming a bent configuration with a Co-O-S angle of 134°. The first coordination shell consists in six oxygen atoms arranged in an octahedral fashion at a Co-O distance of 2.07 Å. In addition, six sulfur atoms are present at 3.24 Å and four Co-N paths at 3.63 Å.

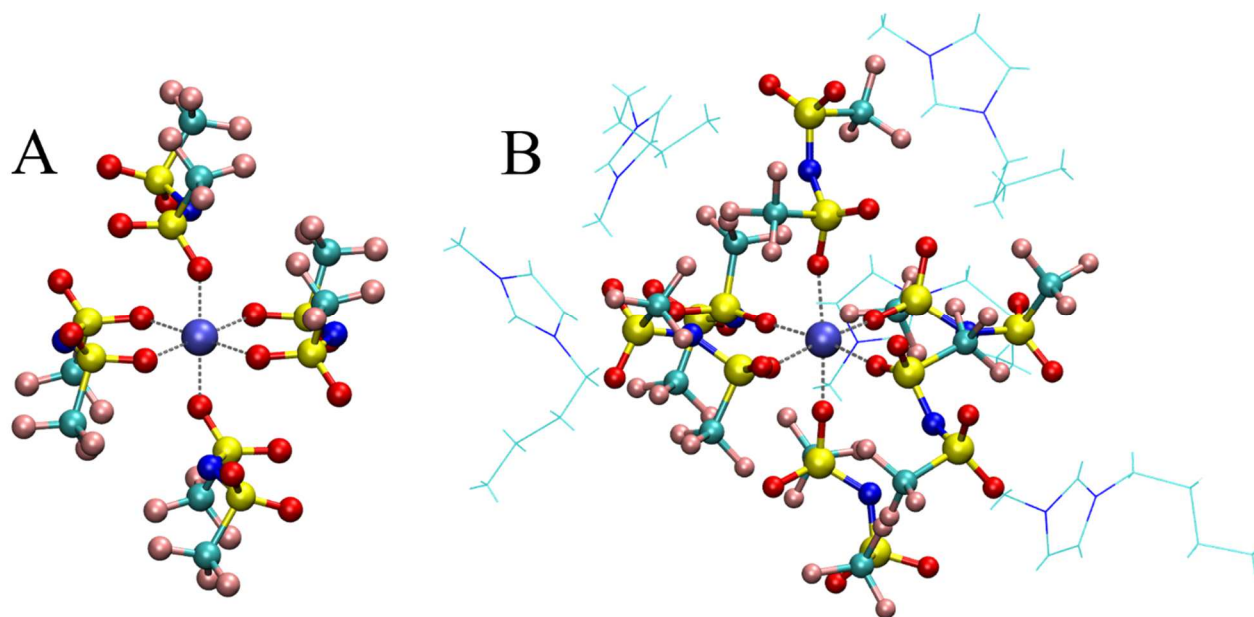


**Figure 5.1.** Structural arrangement of the  $[\text{Tf}_2\text{N}]^-$  anions around  $\text{Co}^{2+}$  A) in the  $\text{Co}(\text{Tf}_2\text{N})_2$  crystal as determined starting from the crystallographic structure of Ref.<sup>13</sup> and B) in the  $[\text{C}_4\text{mim}][\text{Tf}_2\text{N}]$  ionic liquid as showed by a snapshot from the MD simulation (balls and sticks:  $\text{Co}^{2+}$  and coordinating  $[\text{Tf}_2\text{N}]^-$ , wireframe: second shell  $[\text{C}_4\text{mim}]^+$ ).

As regards the  $\text{Co}(\text{Tf}_2\text{N})_2$  solution in  $[\text{C}_4\text{mim}][\text{Tf}_2\text{N}]$ , the local structure around the metal has been characterized starting from the Co-O, Co-S and Co-N pairs  $g(r)$ 's obtained from the analysis of the MD simulation (**Fig. 5.2**). To compare the MD results with the crystallographic structure of  $\text{Co}(\text{Tf}_2\text{N})_2$  and provide a quantitative description of the local coordination around  $\text{Co}^{2+}$ , the  $g(r)$ 's have been modeled with  $\Gamma$ -like functions as previously described. The results of this analysis are shown in **Fig. C.5** of **Appendix C**, while the obtained structural parameters are listed in **Tab. 5.2**. As can be observed, the Co-O  $g(r)$  shows a sharp first peak indicating the existence of a well-defined first solvation shell of oxygen atoms around  $\text{Co}^{2+}$  with a number of coordinating atoms equal to six and an average Co-O distance of 2.07 Å (**Fig. 5.2 A**). As regards the Co-S  $g(r)$  (**Fig. 5.2 B**), a well-defined first peak is obtained with a CN of six and an average Co-S distance of 3.48 Å. Conversely, the Co-N  $g(r)$  is wider as compared to the other pair distribution functions (**Fig. 5.2 C**) and two asymmetric peaks had to be used to obtain a proper fit, both comprising three nitrogen atoms (see **Fig. C.5 B** of **Appendix C**). This finding suggests that three  $[\text{Tf}_2\text{N}]^-$  ligands coordinate the metal in a slightly different way with respect to the other three anions. This effect is probably due to the organization of the first solvation sphere and to the steric hindrance provoked by the contemporary presence of six large anions like the bis(trifluoromethylsulfonyl)imide in a restricted space around the metal ion. These results altogether suggest that in the RTIL solution the  $\text{Co}^{2+}$  cation is coordinated by six monodentate  $[\text{Tf}_2\text{N}]^-$  ligands arranged to form a linear Co-O-S configuration. Note that the

different Co-O-S angle of the monodentate ligands found in the  $\text{Co}(\text{Tf}_2\text{N})_2$  crystal as compared to the RTIL solution is inferred by the different Co-S distance of the sulfonyl groups that are found at smaller values in the crystallographic structure as compared to the solution. Moreover, the existence of a small structural disorder in the arrangement of the ligands is shown by the wider Co-N pair distribution.

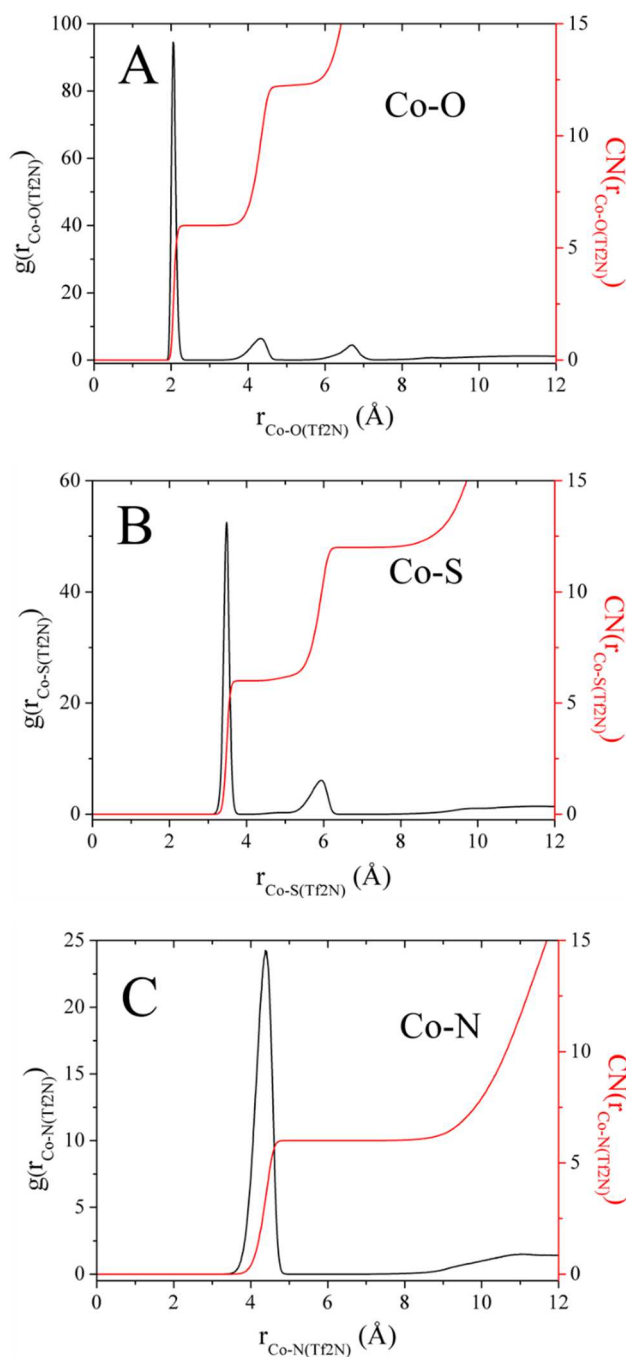


**Figure 5.2.** Radial distribution functions  $g(r)$ 's (black lines, left scale) and corresponding integration number (red lines, right scale) for the A) Co-O, B) Co-S and C) Co-N pairs calculated from the MD simulation of the  $\text{Co}(\text{Tf}_2\text{N})_2$  solution in  $[\text{C}_4\text{mim}][\text{Tf}_2\text{N}]$  for the structural part.

**Table 5.2.** Coordination number CN, average distance R, Debye-Waller factor  $\sigma^2$  and asymmetry index  $\beta$  of the first peaks of the Co-O, Co-S and Co-N  $g(r)$ 's as obtained by modeling the peaks with  $\Gamma$ -like functions for the  $\text{Co}(\text{Tf}_2\text{N})_2$  0.1 M solution in  $[\text{C}_4\text{mim}][\text{Tf}_2\text{N}]$ .

Path	CN	R (Å)	$\sigma^2$ (Å <sup>2</sup> )	$\beta$
Co-O	6.0	2.07	0.003	0.44
Co-S	6.0	3.48	0.005	0.02
Co-N <sub>1</sub>	3.0	4.22	0.035	-0.03
Co-N <sub>2</sub>	3.0	4.45	0.017	0.00

The results of the MD simulation show  $\text{Co}^{2+}$  as coordinated by six oxygen atoms in the first shell assuming an octahedral geometry as in the crystal. Nevertheless, while in the metallic salt there are two monodentate and two bidentate  $[\text{Tf}_2\text{N}]^-$ , in solution the ligands are only monodentate and they are arranged differently. This suggests that the  $[\text{C}_4\text{mim}][\text{Tf}_2\text{N}]$  RTIL is able to dissolve the  $\text{Co}(\text{Tf}_2\text{N})_2$  salt giving rise to a different structural arrangement as compared to the solid state. A first qualitative proof of this has been obtained by comparing the XANES parts of the absorption spectra of the  $\text{Co}(\text{Tf}_2\text{N})_2$  salt and RTIL solution (**Fig. 5.3**). As can be observed, the XANES spectrum of the  $\text{Co}(\text{Tf}_2\text{N})_2$  crystal shows small but detectable differences from that of the RTIL solution. As it is known, this spectral region is influenced by the higher distance contributions and by MS effects. The similarity between the two XANES spectra therefore confirms the existence of a similar octahedral first coordination shell around  $\text{Co}^{2+}$ . However, the small but detectable differences such as the presence of the bump at about 7740 eV in the XANES spectrum of the solution, not present in the crystal, are consistent with a different arrangement of the ligands in the two cases. In fact, the  $[\text{Tf}_2\text{N}]^-$  anion is known to be able to coordinate both in a mono- and bidentate fashion. The average distance of first shell oxygen atoms with respect to the metal ion has been found to be approximately the same for the two coordination modes.<sup>20,30</sup> However, the different organization of the  $[\text{Tf}_2\text{N}]^-$  ligand gives rise to a different distance between the metal ion and the nitrogen atoms as well as to different MS paths.<sup>20</sup> Therefore, the differences in the XANES spectra between the solid and the solution suggest a different number of bidentate-coordinating ligands in the two cases.

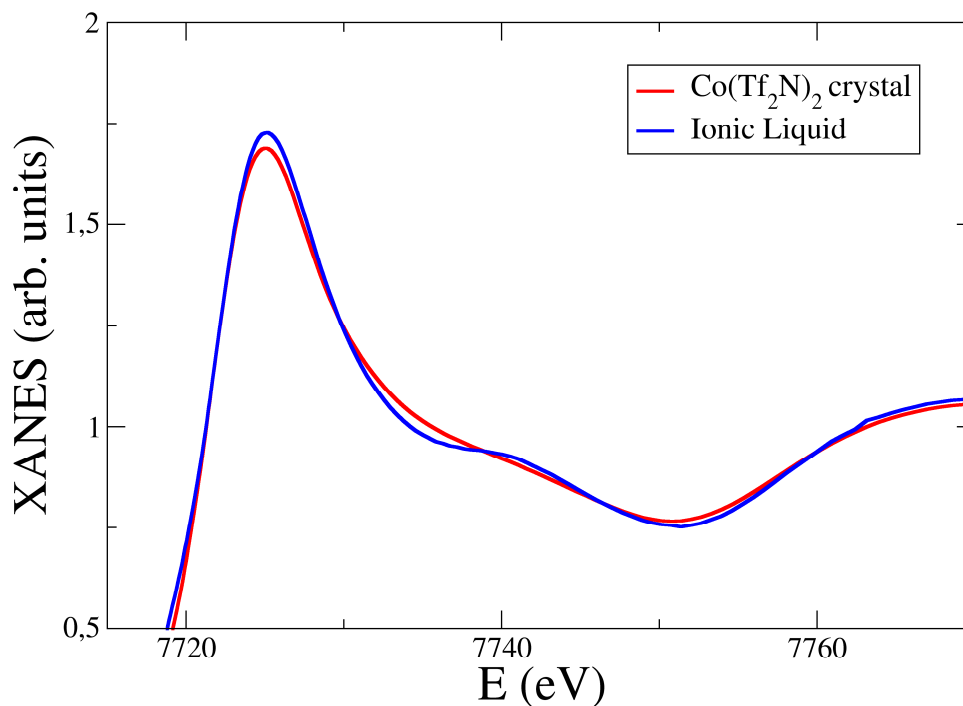


**Figure 5.3.** Co K-edge XANES experimental spectra of solid  $\text{Co}(\text{Tf}_2\text{N})_2$  as compared to the 0.1 M solution of  $\text{Co}(\text{Tf}_2\text{N})_2$  in  $[\text{C}_4\text{mim}][\text{Tf}_2\text{N}]$ .

A more quantitative determination of the structural arrangement around  $\text{Co}^{2+}$  has been obtained from the analysis of the EXAFS spectra. EXAFS data analysis for the  $\text{Co}(\text{Tf}_2\text{N})_2$  crystal has been carried out on the basis of the crystallographic structure reported in literature.<sup>13</sup> To this purpose, two-body signals associated with the Co-O, Co-S and Co-N paths have been considered while MS signals with a detectable amplitude resulted those associated with the three linear O-Co-O contributions and six Co-O-S paths with  $134^\circ$  bond angle. For the Co-N paths coming from mono- and bidentate  $[\text{Tf}_2\text{N}]^-$  the same distance was employed, since they are found at distances that differ of a quantity comprised in EXAFS uncertainty on bond distances ( $3.62 \text{ \AA}$  and  $3.65 \text{ \AA}$ , respectively). Least-squares fits have been carried out in the  $2.1 - 15.0 \text{ \AA}^{-1} k$  range on the raw spectrum of the  $\text{Co}(\text{Tf}_2\text{N})_2$  salt and the best-fit results are shown in **Fig. 5.4**. The agreement between the theoretical and experimental data is very good, and this is also evident from the corresponding FT spectra shown in the lower panel. The complete list of the optimized structural parameters is reported in **Tab. 5.3**, while among the non-structural ones  $E_0$  resulted to be 2.0 eV above the first inflection point of the experimental spectrum. The structural results obtained from the EXAFS analysis are equal to the crystallographic structure reported in literature within the experimental error.<sup>13</sup>

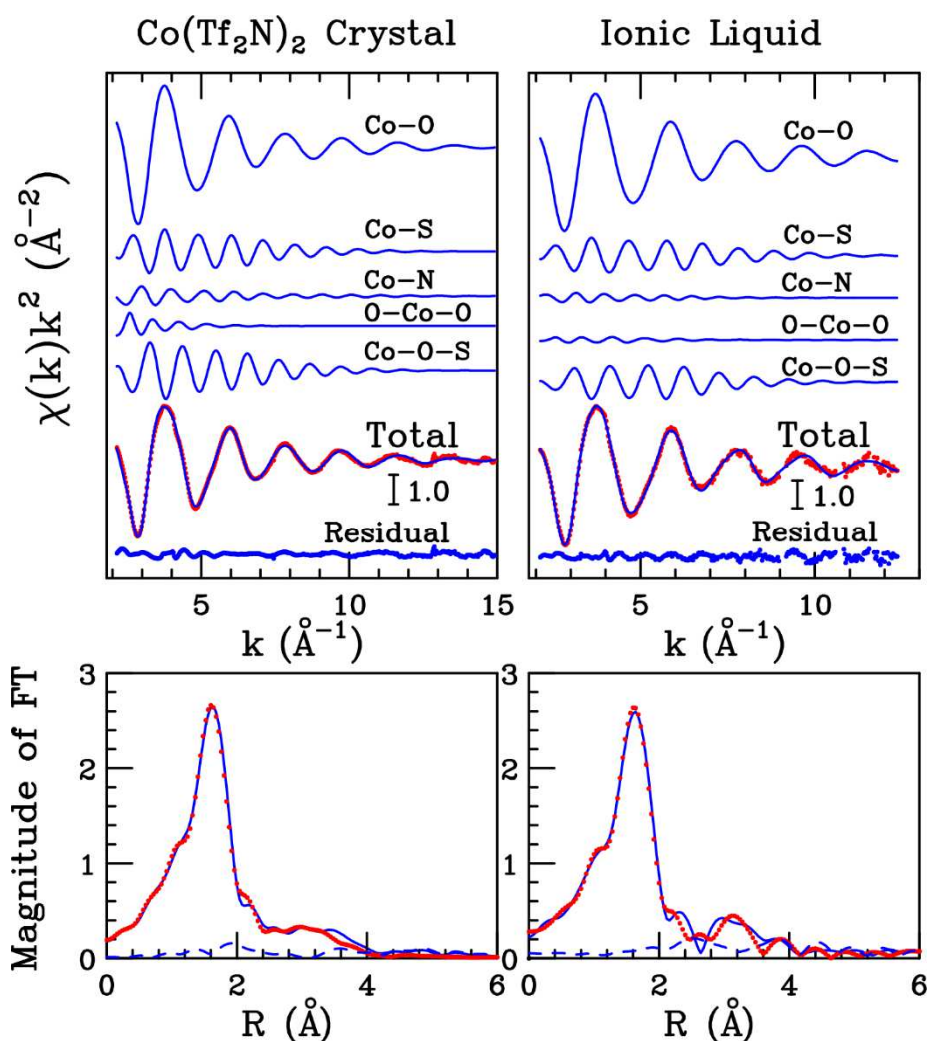


**Figure 5.4.** Upper panels: fit of Co K-edge EXAFS spectra of Co(Tf<sub>2</sub>N)<sub>2</sub> crystal (left panel) and of the 0.1 M solution of Co(Tf<sub>2</sub>N)<sub>2</sub> in [C<sub>4</sub>mim](Tf<sub>2</sub>N) (right panel). From the top to the bottom: Co-O, Co-S and Co-N SS theoretical signals, O-Co-O and Co-O-S MS three-body theoretical signals, total theoretical signal (blue line) compared with the experimental spectrum (red dotted line) and resulting residual. Lower panels: non-phase shift corrected Fourier transforms of the experimental data (red dotted line), of the total theoretical signals (blue line) and of the residuals (blue dashed line).

**Table 5.3.** Coordination number CN, average distance R (Å), Debye-Waller factor  $\sigma^2$  (Å<sup>2</sup>) and asymmetry index  $\beta$  as obtained from the EXAFS data analysis for the Co(Tf<sub>2</sub>N)<sub>2</sub> crystal and the Co(Tf<sub>2</sub>N)<sub>2</sub> 0.1 M solution in [C<sub>4</sub>mim][Tf<sub>2</sub>N].

Path		Co(Tf <sub>2</sub> N) <sub>2</sub> crystal	Co(Tf <sub>2</sub> N) <sub>2</sub> in [C <sub>4</sub> mim][Tf <sub>2</sub> N]
Co-O	CN	6	6
	R	2.07(1)	2.08(1)
	$\sigma^2$	0.006(1)	0.005(1)
	$\beta$	0.0(1)	0.0(1)
Co-S	CN	6	6
	R	3.29(3)	3.49(3)
	$\sigma^2$	0.008(2)	0.009(3)
	$\beta$	0.0(1)	0.0(1)
Co-N	CN	4	6
	R	3.60(4)	4.39(4)
	$\sigma^2$	0.009(2)	0.014(4)
	$\beta$	0.1(1)	0.1(1)

A quantitative determination of the coordination involving Co<sup>2+</sup> in the [C<sub>4</sub>mim][Tf<sub>2</sub>N] solution has been also carried out from EXAFS experimental data. To this purpose,  $\chi(k)$  theoretical signals have been calculated for the Zn-O, Zn-S and Zn-N contributions as well as for the six Zn-O-S paths starting from the parameters obtained from the MD simulation (**Tab. 5.2**). Least-squares fits of the EXAFS data have been carried out in the 2.0 – 13.0 Å<sup>-1</sup>  $k$  range. The best-fit results are shown in the right panel of **Fig. 5.4**, while the optimized parameters are reported in **Tab. 5.3**. Also in this case, the agreement between the theoretical and experimental data is good both for the  $\chi(k)$  and FT spectra and this strongly supports the presence of the [Co(Tf<sub>2</sub>N)<sub>6</sub>]<sup>4+</sup> species in solution, as found from the MD simulation. In addition, it can be observed that the EXAFS spectra of the Co(Tf<sub>2</sub>N)<sub>2</sub> salt and the RTIL solution are quite similar among each other, as the high energy region of a XAS spectra is dominated by first shell SS contribution that is similar in the two samples. In fact, from the theoretical signals shown in **Fig. 5.4** it can be observed that the Co-O signals are quite similar between the solid and the solution. Indeed, the main difference in the two cases is provided by the different coordination modes of the [Tf<sub>2</sub>N]<sup>-</sup> anion, that implies also the bidentate fashion for Co(Tf<sub>2</sub>N)<sub>2</sub>, while monodentate-only coordination is found for the solution. This gives rise to MS signals for the O-Co-O and Co-O-S paths that are different in amplitude and phase, as can be appreciated in **Fig. 5.4**.

In addition, it has to be noted that while Co-O and Co-S distances obtained from EXAFS analysis are equal to those obtained from the MD simulation, the Debye-Waller factor obtained from the experimental data fitting are larger. This finding suggests that the potentials used in the simulations for the Co<sup>2+</sup>-RTIL interaction are too rigid, giving rise to a structure in solution that is less flexible as compared to the experimental results. This behavior has to be attributed to the employment of the LJ potential for the Co-[Tf<sub>2</sub>N]<sup>-</sup> interaction, as already pointed out when the LJ function is used in MD simulations of liquids containing metal cations.<sup>26,31,32</sup>

Also for the solution, E<sub>0</sub> was found at 2.0 eV above the first inflection point of the experimental spectrum.

### 5.3.2 Co<sup>2+</sup> solvation thermodynamics

MD simulations for the thermodynamic part have been also carried out. The resulting metal species in [C<sub>4</sub>mim][Tf<sub>2</sub>N] was [Co(Tf<sub>2</sub>N)<sub>6</sub>]<sup>4+</sup> with an average Co-O(Tf<sub>2</sub>N) distance of 1.84 Å, as can be deduced from the Co-O, Co-S and Co-N *g(r)*'s (**Fig. C.6** of **Appendix C**). Therefore, the same type of [Tf<sub>2</sub>N]<sup>-</sup> coordination towards Co<sup>2+</sup> with respect to that observed in the structural part has been obtained also in this case. The underestimated bond distance with respect to that obtained previously is due to the employment of the “HFE” LJ parameters instead of the “IOD” set used for the structural part.

The calculated  $\Delta G_{\text{solv}}$  resulted to be -451.3 kcal mol<sup>-1</sup> (**Tab. 5.4**), which is similar to that previously obtained for Zn<sup>2+</sup>. This was expected on the basis of the dominating electrostatic term in free energy calculations as discussed in **Chapter 4 (Sec. 4.3.1.2)**. As regards the aqueous solution, the obtained  $\Delta G_{\text{hyd}}$  for Co<sup>2+</sup> in SPC/E water (**Tab. 5.4**) is very close to that obtained by Merz and Li (-456.9 kcal mol<sup>-1</sup>)<sup>24</sup> as well as to the experimental (-457.7 kcal mol<sup>-1</sup>),<sup>33</sup> showing the goodness of the employed protocol for free energy calculations. The calculated  $\Delta G_{\text{solv}}$  in [C<sub>4</sub>mim][Tf<sub>2</sub>N] resulted to be less negative than  $\Delta G_{\text{hyd}}$  and as a consequence a positive  $\Delta G_{\text{trans}}$  of 6.6 kcal mol<sup>-1</sup> is obtained, suggesting that Co<sup>2+</sup> is more favorably solvated in water than in the RTIL. This is qualitatively in agreement with the previously obtained  $\Delta G_{\text{trans}}$  for Zn<sup>2+</sup> and confirms the unfavorable transfer from an aqueous solution to neat [C<sub>4</sub>mim][Tf<sub>2</sub>N] for these metal ions.

**Table 5.4.** MD calculated Gibbs free energies of hydration ( $\Delta G_{\text{hyd}}$ ), solvation in  $[\text{C}_4\text{mim}][\text{Tf}_2\text{N}]$  ( $\Delta G_{\text{solv}}$ ) and transfer from water to the RTIL ( $\Delta G_{\text{trans}}$ ) obtained at  $T = 298.15$  K and  $P = 1$  atm for the  $\text{Co}^{2+}$  ion. Values in  $\text{kcal mol}^{-1}$ .

$\Delta G_{\text{hyd}}$	$\Delta G_{\text{solv}}$	$\Delta G_{\text{trans}}^{\text{a}}$
$-457.9 \pm 0.1$	$-451.3 \pm 1.5$	$6.6 \pm 1.6$

<sup>a</sup>Gibbs free energy of transfer from water to the RTIL calculated as  $\Delta G_{\text{trans}} = \Delta G_{\text{solv}} - \Delta G_{\text{hyd}}$ .

As for  $\text{Zn}^{2+}$ , to understand the origin of the unfavorable transfer, enthalpies and entropies of hydration and solvation were obtained by performing free energy calculations at different temperatures. The obtained  $\Delta G/T$  vs.  $1/T$  plots are showed in **Fig. 5.5**, while the calculated values are reported in **Tab. 5.5** for hydration and in **Tab. 5.6** for solvation in  $[\text{C}_4\text{mim}][\text{Tf}_2\text{N}]$ .  $\Delta H_{\text{hyd}}$  and  $\Delta S_{\text{hyd}}$  are in good agreement with the experimental<sup>33,34</sup> and are typical for the formation of divalent metal ions aquo-complexes.<sup>35</sup>  $\Delta H_{\text{solv}}$  in  $[\text{C}_4\text{mim}][\text{Tf}_2\text{N}]$  is more negative than in water and the same happens for the entropic term. As a consequence, both  $\Delta H_{\text{trans}}$  and  $\Delta S_{\text{trans}}$  from water to  $[\text{C}_4\text{mim}][\text{Tf}_2\text{N}]$  are negative. The negative  $\Delta H_{\text{trans}}$  suggests that the transfer of  $\text{Co}^{2+}$  from water to  $[\text{C}_4\text{mim}][\text{Tf}_2\text{N}]$  is enthalpically favorable. Therefore, the term that causes the overall positive  $\Delta G_{\text{trans}}$  is the unfavorable  $\Delta S_{\text{trans}}$ , as was found for  $\text{Zn}^{2+}$ . The negative entropy of transfer has been previously explained with the higher order imposed to the liquid structure by the solvated metal ion in the case of  $[\text{C}_4\text{mim}][\text{Tf}_2\text{N}]$  with respect to water. The almost identical picture obtained in the  $\text{Zn}^{2+}$  and  $\text{Co}^{2+}$  cases can be reasonably explained by taking into account their similar ionic radii<sup>36</sup> and coordination mode in the two liquids.<sup>20</sup>

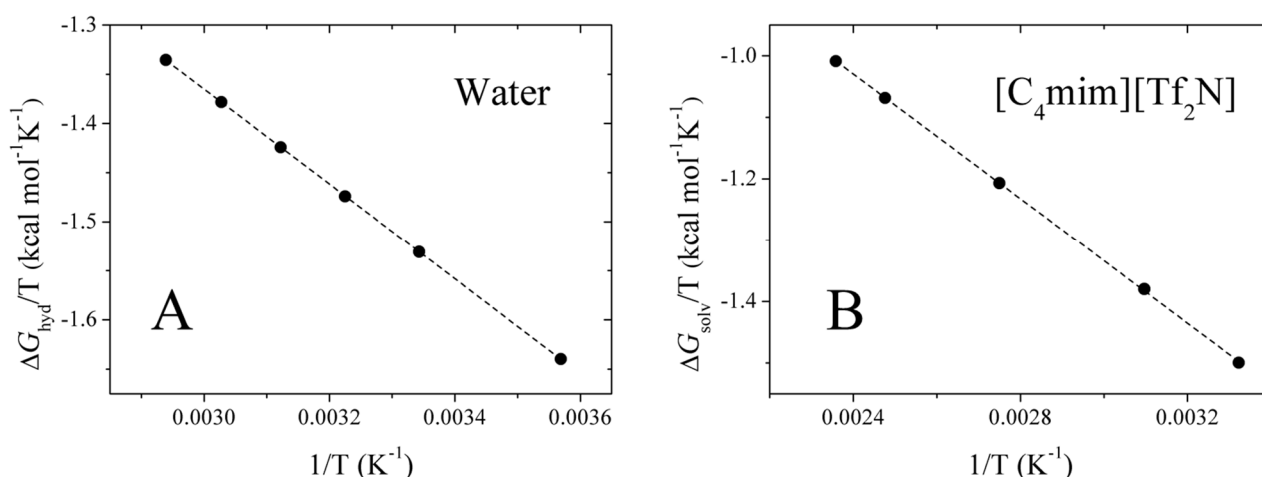


**Figure 5.5.**  $\Delta G/T$  vs.  $1/T$  plots obtained from MD calculated  $\text{Co}^{2+}$  Gibbs free energies A) in water and B) in  $[\text{C}_4\text{mim}][\text{Tf}_2\text{N}]$  at different temperatures ( $R^2 = 0.99$ ).

**Table 5.5.** Hydration enthalpies (kcal mol<sup>-1</sup>) and entropies (kcal mol<sup>-1</sup> K<sup>-1</sup>) for Co<sup>2+</sup> calculated from MD simulations (obtained from plot in **Fig. 5.5 A**) and from experimental data.

	MD		Experimental	
	$\Delta H_{\text{hyd}}$	$\Delta S_{\text{hyd}}$	$\Delta H_{\text{hyd}}$	$\Delta S_{\text{hyd}}$
Co <sup>2+</sup>	-483.2 ± 0.6	-0.085 ± 0.002	-478.6 <sup>a</sup>	-0.070 <sup>34</sup>

<sup>a</sup>Co<sup>2+</sup> experimental  $\Delta H_{\text{hyd}}$  calculated from Marcus'  $\Delta G_{\text{hyd}}$ <sup>33</sup> and  $\Delta S_{\text{hyd}}$ .<sup>34</sup>

**Table 5.6.** MD calculated enthalpy (kcal mol<sup>-1</sup>) and entropy (kcal mol<sup>-1</sup> K<sup>-1</sup>) of solvation for Co<sup>2+</sup> in [C<sub>4</sub>mim][Tf<sub>2</sub>N] and transfer from water to the RTIL obtained from the plot in **Fig. 5.5 B**.

	$\Delta H_{\text{solv}}$	$\Delta S_{\text{solv}}$	$\Delta H_{\text{trans}}$ <sup>a</sup>	$\Delta S_{\text{trans}}$ <sup>b</sup>
Co <sup>2+</sup>	-507.4 ± 2.6	-0.188 ± 0.007	-24.2 ± 3.2	-0.103 ± 0.009

<sup>a</sup>Enthalpy of transfer from water to [C<sub>4</sub>mim][Tf<sub>2</sub>N] calculated as  $\Delta H_{\text{trans}} = \Delta H_{\text{solv}} - \Delta H_{\text{hyd}}$ ; <sup>b</sup>Entropy of transfer from water to [C<sub>4</sub>mim][Tf<sub>2</sub>N] calculated as  $\Delta S_{\text{trans}} = \Delta S_{\text{solv}} - \Delta S_{\text{hyd}}$  using values reported in **Tab. 5.5** for hydration.

### 5.3.3 Co<sup>2+</sup> in wet [C<sub>4</sub>mim][Tf<sub>2</sub>N]: UV-Vis titration

Electronic spectra have been collected on Co(Tf<sub>2</sub>N)<sub>2</sub> solutions in [C<sub>4</sub>mim][Tf<sub>2</sub>N] in dry conditions as well as with increasing water content (Co:H<sub>2</sub>O from 1:1 to 1:8), in water-saturated [C<sub>4</sub>mim][Tf<sub>2</sub>N] and in pure aqueous solution. The obtained spectra are shown in **Fig. 5.6**. The spectrum of Co(Tf<sub>2</sub>N)<sub>2</sub> in water-saturated [C<sub>4</sub>mim][Tf<sub>2</sub>N] presents a maximum at  $\lambda_{\text{max}} = 510$  nm ( $\epsilon = 5.3$  mol<sup>-1</sup> L cm<sup>-1</sup>) and is nearly superimposable to that obtained in pure water ( $\lambda_{\text{max}} = 511$  nm;  $\epsilon = 4.0$  mol<sup>-1</sup> L cm<sup>-1</sup>). This trend suggests that Co<sup>2+</sup> is preferentially coordinated by water instead of [Tf<sub>2</sub>N]<sup>-</sup> in the wet RTIL and is compatible with the obtained positive  $\Delta G_{\text{trans}}$  (**Tab. 5.4**). The same has been previously evidenced for Zn<sup>2+</sup> by means of MD simulations and XAS measures (**Sec. 4.3.1.3 of Chapter 4**).

UV-Vis spectra provide also additional information. By increasing the water content, the maximum of the *d-d* transition is blue-shifted from  $\lambda_{\text{max}} = 549$  nm ( $\epsilon = 33.1$  mol<sup>-1</sup> L cm<sup>-1</sup>) in dry [C<sub>4</sub>mim][Tf<sub>2</sub>N] to  $\lambda_{\text{max}} = 512$  nm ( $\epsilon = 11.9$  mol<sup>-1</sup> L cm<sup>-1</sup>) in the solution with the 1:8 Co:H<sub>2</sub>O ratio, therefore a blue-shift is observed by passing from [Tf<sub>2</sub>N]<sup>-</sup> to water coordination. In other words, water results to be a stronger ligand than [Tf<sub>2</sub>N]<sup>-</sup> for Co<sup>2+</sup>. To compare the relative strength associated to the pure metal-ligand interaction, also the energy difference ( $\Delta E$ ) for the ligand-exchange reaction  $[\text{Co}(\text{H}_2\text{O})_6]^{2+} + 6$

$[\text{Tf}_2\text{N}]^- \rightarrow [\text{Co}(\text{Tf}_2\text{N})_6]^{4+} + 6 \text{H}_2\text{O}$  has been computed at DFT level of theory.<sup>i</sup> The calculated  $\Delta E$  resulted to be 48.6 and 88.2 kcal mol<sup>-1</sup> in gas phase and in SMD continuum solvent, respectively. Note that these positive  $\Delta E$  values seem somewhat contradictory with respect to the negative  $\Delta H_{\text{trans}}(\text{water} \rightarrow [\text{C}_4\text{mim}][\text{Tf}_2\text{N}])$  data obtained by MD simulations both in the  $\text{Co}^{2+}$  and  $\text{Zn}^{2+}$  cases. The whole results indirectly suggest that the negative  $\Delta H_{\text{trans}}(\text{water} \rightarrow [\text{C}_4\text{mim}][\text{Tf}_2\text{N}])$  cannot be attributed to a stronger metal-ligand interaction, rather to a different reorganization energy of the outer-sphere solvent around the metal ion in the two cases. In fact, transfer enthalpy is known to be related not only to the solute-solvent interaction, but also to the interactions within the solvent molecules.<sup>37-39</sup> For example, for the transfer of  $\text{Co}^{2+}$  from water to methanol and dimethyl sulfoxide a  $\Delta H_{\text{trans}}(\text{water} \rightarrow \text{solvent})$  of -11.2 and -16.7 kcal mol<sup>-1</sup> has been obtained, respectively.<sup>40</sup> In this case, the negative  $\Delta H_{\text{trans}}(\text{water} \rightarrow \text{solvent})$  have been justified by supposing that, when the metal is introduced in water, the breaking of the network of strong H-bonds requires a higher energy cost with respect to the solvent-solvent interactions present in the other solvents.<sup>37,40</sup> This explanation could fit also the  $\text{Zn}^{2+}$  case, where the same trend has been obtained for the transfer data.

---

<sup>i</sup> $[\text{Co}(\text{Tf}_2\text{N})_6]^{4+}$  and  $[\text{Co}(\text{H}_2\text{O})_6]^{2+}$  complexes as well as single ligands optimized in gas phase with the B3LYP functional<sup>41,42</sup> and the 6-31G(*d*, *p*) basis set for main group elements, while the Stuttgart-Dresden pseudopotential coupled with the relative basis set for the valence electrons was used for Co.<sup>43</sup> Vibrational analysis was carried out to confirm that stationary points were minima.  $\text{Co}^{2+}$  always considered in its high-spin state ( $S = 3/2$ ). Single-point calculations also performed including solvent effects by the SMD continuum model<sup>44</sup> with parameters developed for  $[\text{C}_4\text{mim}][\text{Tf}_2\text{N}]$ .<sup>45</sup> Simulations carried out with the Gaussian 16 program.<sup>46</sup>

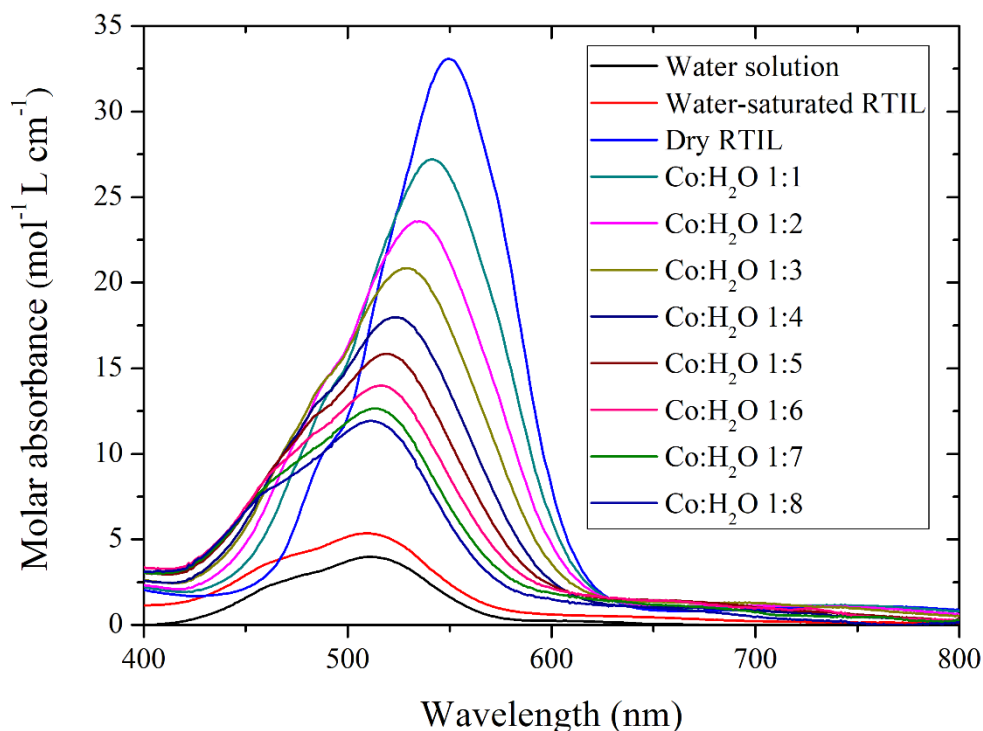


**Figure 5.6.** From the top to the bottom: absorption spectra of  $\text{Co}(\text{Tf}_2\text{N})_2$  0.05 M solutions in dry  $[\text{C}_4\text{mim}][\text{Tf}_2\text{N}]$  and with increasing content of water. The spectrum in pure water is also reported. The molar absorbance corresponds to the experimental absorbance divided by the total  $\text{Co}^{2+}$  concentration.

## 5.4 Conclusions

The solvation of the  $\text{Co}^{2+}$  ion in the  $[\text{C}_4\text{mim}][\text{Tf}_2\text{N}]$  ionic liquid has been studied both from a structural and thermodynamic point of view. The analysis of X-ray absorption data for the solution combined with MD simulations shows that the metal ion is coordinated by six monodentate  $[\text{Tf}_2\text{N}]^-$  anions to form  $[\text{Co}(\text{Tf}_2\text{N})_6]^{4+}$ . This differs from the spectrum of the solid compound, presenting a  $[\text{Co}(\text{Tf}_2\text{N})_4]^{2-}$  unit with two bidentate and two monodentate anions.

Free energy calculations provided a  $\Delta G_{\text{solv}}$  that is close to that previously obtained for the  $\text{Zn}^{2+}$  ion in the same RTIL with the same simulation protocol. Negative  $\Delta H_{\text{solv}}$  and  $\Delta S_{\text{solv}}$  have been obtained by means of free energy calculations carried out at variable temperature. Negative  $\Delta S_{\text{solv}}$  are found for bivalent metal ions in various solvents and reflect the increased order of the liquid by the introduction of the metal ion. On the other hand, the overall solvation enthalpy is the result of several contributions, such as the nature of the  $\text{Co}^{2+}-[\text{Tf}_2\text{N}]^-$  interaction, ionic liquid reorganization and interaction between

the solvate and outer sphere ions. The positive  $\Delta G_{\text{trans}}$  obtained here is the result of the compensation between both negative  $\Delta S_{\text{trans}}$  and  $\Delta H_{\text{trans}}$  terms in qualitative agreement with those obtained for the  $\text{Zn}^{2+}$  ion. The positive  $\Delta G_{\text{trans}}$  suggests  $\text{Co}^{2+}$  preferential solvation by water with respect to  $[\text{C}_4\text{mim}][\text{Tf}_2\text{N}]$ , as is also shown by the UV-Vis spectral changes of RTIL solutions containing increasing amounts of water up to the saturation limit. The spectrum of the saturated solution is nearly the same as that in pure water, indicating that the  $\text{Co}^{2+}$  ion is fully hydrated as also shown for  $\text{Zn}^{2+}$  by EXAFS spectra.

The  $\Delta S_{\text{trans}}$  could be explained by the higher liquid order imposed when the metal ion is introduced in  $[\text{C}_4\text{mim}][\text{Tf}_2\text{N}]$  with respect to water. The largely positive  $\Delta E$  for the ligand exchange calculated for the replacement of  $\text{H}_2\text{O}$  by  $[\text{Tf}_2\text{N}]^-$  in the  $\text{CoL}_6$  complexes is in agreement with the general assumption that  $[\text{Tf}_2\text{N}]^-$  is a weaker ligand as compared to water, but in apparent contrast with the calculated negative  $\Delta H_{\text{trans}}$ . This evidence suggests that the energetic contributions to the overall solvation enthalpy due to outer sphere effects are markedly different in water and  $[\text{C}_4\text{mim}][\text{Tf}_2\text{N}]$ , so that the final  $\Delta H_{\text{trans}}$  results to be negative despite the  $[\text{Tf}_2\text{N}]^-$  anion is a weaker ligand than  $\text{H}_2\text{O}$ .

## Bibliography

- 1 Z. Zhang, J. Song and B. Han, Catalytic Transformation of Lignocellulose into Chemicals and Fuel Products in Ionic Liquids, *Chem. Rev.*, 2017, **117**, 6834–6880.
- 2 D. W. Scott, D. L. Myers, H. Hill and O. Omadoko, Sodium cobalt(II) tetrasulfophthalocyanine and catalytic oxidation of ethanethiol, *Fuel*, 2019, **242**, 573–579.
- 3 M. J. Earle, U. Hakala, B. J. Mcauley and M. Nieuwenhuyzen, Metal bis{(trifluoromethyl)sulfonyl}amide complexes: highly efficient Friedel – Crafts acylation catalysts, *Chem. Commun.*, 2004, 1368–1369.
- 4 A. Shaabani, E. Farhangi and A. Rahmati, Aerobic oxidation of alkyl arenes and alcohols using cobalt(II) phthalocyanine as a catalyst in 1-butyl-3-methyl-imidazolium bromide, *Appl. Catal. A Gen.*, 2008, **338**, 14–19.
- 5 M. Tułodziecki, J.-M. Tarascon, P.-L. Taberna and C. Guéry, Non-Equilibrium Ionic Liquid-Electrode Interface at Elevated Temperature and Its Influence on Co<sup>2+</sup> Reduction Process, *J. Electrochem. Soc.*, 2016, **163**, D355–D365.
- 6 S. Schaltin, P. Nockemann, B. Thijs, K. Binnemans and J. Fransaer, Influence of the Anion on the Electrodeposition of Cobalt from Imidazolium Ionic Liquids, *Electrochem. Solid-State Lett.*, 2007, **10**, D104.
- 7 Y. Katayama, R. Fukui and T. Miura, Electrodeposition of Cobalt from an Imide-Type Room-Temperature Ionic Liquid, *J. Electrochem. Soc.*, 2007, **154**, D534.
- 8 C. Su, M. An, P. Yang, H. Gu and X. Guo, Electrochemical behavior of cobalt from 1-butyl-3-methylimidazolium tetrafluoroborate ionic liquid, *Appl. Surf. Sci.*, 2010, **256**, 4888–4893.
- 9 M. Li, Z. Shi, Z. Wang and R. G. Reddy, in *EPD Congress 2015*, John Wiley & Sons, Ltd, 2015, pp. 21–30.
- 10 B. Onghena, S. Valgaeren, T. Vander Hoogerstraete and K. Binnemans, Cobalt(II)/nickel(II) separation from sulfate media by solvent extraction with an undiluted quaternary phosphonium ionic liquid, *RSC Adv.*, 2017, **7**, 35992–35999.
- 11 A. Rout and K. Binnemans, Efficient separation of transition metals from rare earths by an undiluted phosphonium thiocyanate ionic liquid, *Phys. Chem. Chem. Phys.*, 2016, **18**, 16039–16045.
- 12 J. Fliieger, M. Tatarczak-Michalewska, E. Blicharska, A. Madejska, W. Fliieger and A. Adamczuk, Extraction of cobalt (II) using ionic liquid-based bi-phase and three-phase

- systems without adding any chelating agents with new recycling procedure, *Sep. Purif. Technol.*, 2019, **209**, 984–989.
- 13 P. Nockemann, M. Pellens, K. Van Hecke, L. Van Meervelt, J. Wouters, B. Thijs, E. Vanecht, T. N. Parac-Vogt, H. Mehdi, S. Schaltin, J. Fransaer, S. Zahn, B. Kirchner and K. Binnemans, Cobalt(II) complexes of nitrile-functionalized ionic liquids, *Chem. - A Eur. J.*, 2010, **16**, 1849–1858.
- 14 K. Fujii, T. Nonaka, Y. Akimoto, Y. Umebayashi and S. Ishiguro, Solvation Structures of Some Transition Metal(II) Ions in a Room-Temperature Ionic Liquid, 1-Ethyl-3-methylimidazolium Bis(trifluoromethanesulfonyl)amide, *Anal. Sci.*, 2008, **24**, 1377–1380.
- 15 Y. Tsuchida, M. Matsumiya and K. Tsunashima, Solvation structure for Fe(II), Co(II) and Ni(II) complexes in [P2225][NTf2] ionic liquids investigated by Raman spectroscopy and DFT calculation, *J. Mol. Liq.*, 2018, **269**, 8–13.
- 16 O. Bortolini, C. Chiappe, T. Ghilardi, A. Massi and C. S. Pomelli, Dissolution of metal salts in bis(trifluoromethylsulfonyl)imide-based ionic liquids: Studying the affinity of metal cations toward a ‘weakly coordinating’ anion, *J. Phys. Chem. A*, 2015, **119**, 5078–5087.
- 17 Y. Umebayashi, T. Mitsugi, S. Fukuda, T. Fujimori, K. Fujii, R. Kanzaki, M. Takeuchi and S. I. Ishiguro, Lithium ion solvation in room-temperature ionic liquids involving bis(trifluoromethanesulfonyl)imide anion studied by Raman spectroscopy and DFT calculations, *J. Phys. Chem. B*, 2007, **111**, 13028–13032.
- 18 Y. Umebayashi, T. Yamaguchi, S. Fukuda, T. Mitsugi, M. Takeuchi, K. Fujii and S. Ishiguro, Raman Spectroscopic Study on Alkaline Metal Ion Solvation in 1-Butyl-3-methylimidazolium Bis(trifluoromethanesulfonyl)amide Ionic Liquid, *Anal. Sci.*, 2008, **24**, 1297–1304.
- 19 G. A. Giffin, A. Moretti, S. Jeong and S. Passerini, Complex Nature of Ionic Coordination in Magnesium Ionic Liquid-Based Electrolytes: Solvates with Mobile Mg<sup>2+</sup> Cations, *J. Phys. Chem. C*, 2014, **118**, 9966–9973.
- 20 F. Sessa, V. Migliorati, A. Serva, A. Lapi, G. Aquilanti, G. Mancini and P. D’Angelo, On the coordination of Zn<sup>2+</sup> ion in Tf<sub>2</sub>N<sup>-</sup> based ionic liquids: structural and dynamic properties depending on the nature of the organic cation, *Phys. Chem. Chem. Phys.*, 2018, **20**, 2662–2675.
- 21 J. N. Canongia Lopes, A. A. H. Padua and J. Dechamps, Modeling ionic liquids using a systematic all-atom force field, *J. Phys. Chem. B*, 2004, **108**, 2038–2047.
- 22 J. N. Canongia Lopes, A. A. H. Padua and J. Dechamps, Additions and corrections., *J. Phys. Chem. B*, 2004, **108**, 11250.

- 23 J. N. Canongia Lopes and A. A. H. Padua, Molecular Force Field for Ionic Liquids Composed of Triflate or Bistriflyimide Anions, *J. Phys. Chem. B*, 2004, **108**, 16893–16898.
- 24 P. Li, B. P. Roberts, D. K. Chakravorty and K. M. Merz, Rational design of particle mesh ewald compatible lennard-jones parameters for +2 metal cations in explicit solvent, *J. Chem. Theory Comput.*, 2013, **9**, 2733–2748.
- 25 M. Busato, P. D'Angelo and A. Melchior, Solvation of Zn<sup>2+</sup> ion in 1-alkyl-3-methylimidazolium bis(trifluoromethylsulfonyl)imide ionic liquids: a molecular dynamics and X-Ray absorption study, *Phys. Chem. Chem. Phys.*, 2019, **21**, 6958–6969.
- 26 P. D'Angelo, V. Barone, G. Chillemi, N. Sanna, W. Meyer-Klaucke and N. V. Pavel, Hydrogen and higher shell contributions in Zn<sup>2+</sup>, Ni<sup>2+</sup>, and Co<sup>2+</sup> aqueous solutions: An X-ray absorption fine structure and molecular dynamics study, *J. Am. Chem. Soc.*, 2002, **124**, 1958–1967.
- 27 H. J. C. Berendsen, J. R. Grigera and T. P. Straatsma, The missing term in effective pair potentials, *J. Phys. Chem.*, 1987, **91**, 6269–6271.
- 28 M. J. Abraham, T. Murtola, R. Schulz, S. Páll, J. C. Smith, B. Hess and E. Lindah, Gromacs: High performance molecular simulations through multi-level parallelism from laptops to supercomputers, *SoftwareX*, 2015, **1–2**, 19–25.
- 29 *W. Pat.*, 2002.
- 30 A. Melchior, C. Gaillard, S. Gràcia Lanas, M. Tolazzi, I. Billard, S. Georg, L. Sarrasin and M. Boltoeva, Nickel(II) Complexation with Nitrate in Dry [C<sub>4</sub>mim][Tf<sub>2</sub>N] Ionic Liquid: A Spectroscopic, Microcalorimetric, and Molecular Dynamics Study, *Inorg. Chem.*, 2016, **55**, 3498–3507.
- 31 P. D'Angelo and R. Spezia, Hydration of lanthanoids(III) and actinoids(III): An experimental/theoretical saga, *Chem. - A Eur. J.*, 2012, **18**, 11162–11178.
- 32 A. Filipponi and P. D'Angelo, in *X-Ray Absorption and X-Ray Emission Spectroscopy*, John Wiley & Sons, Ltd, 2016, pp. 745–771.
- 33 Y. Marcus, Thermodynamics of Solvation of Ions, *J. Chem. Soc., Faraday Trans.*, 1991, **87**, 2995–2999.
- 34 Y. Marcus and A. Loewenschuss, Standard Entropies of Hydration of Ions, *A. Annu. Rep. Prog. Chem. Sect. C Phys. Chem.*, 1984, **81**, 81–135.
- 35 I. Persson, Hydrated metal ions in aqueous solution: How regular are their structures?, *Pure Appl. Chem.*, 2010, **82**, 1901–1917.
- 36 R. D. Shannon, Revised effective ionic radii and systematic studies of interatomic distances in halides and chalcogenides, *Acta Crystallogr. Sect. A*, 1976, **32**, 751–767.

- 37 E. Kamieńska-Piotrowicz, Solvation of cobalt(II) and perchlorate ions in binary mixtures of donor solvents, *J. Chem. Soc. Faraday Trans.*, 1995, **91**, 71–75.
- 38 E. Kamieńska-Piotrowicz and J. Stangret, VIS spectroscopy studies of pseudooctahedral solvation complexes of cobalt(II) ion in mixed solvents, *J. Mol. Struct.*, 1998, **440**, 131–139.
- 39 A. Melchior and M. Tolazzi, Thermodynamics of complex formation in dimethylsulfoxide: the case of Co(II) complexes with nitrogen donor ligands and their O<sub>2</sub> adducts, *Inorg. Chim. Acta*, 2019, **493**, 91–101.
- 40 E. Kamieńska-Piotrowicz, Analysis of the enthalpies of transfer of Co(II) ion in mixed solvents by means of the theory of preferential solvation, *Thermochim. Acta*, 2005, **427**, 1–7.
- 41 A. D. Becke, A new mixing of Hartree–Fock and local density-functional theories, *J. Chem. Phys.*, 1993, **98**, 1372–1377.
- 42 C. Lee, W. Yang and R. G. Parr, Development of the Colle-Salvetti correlation-energy formula into a functional of the electron density, *Phys. Rev. B*, 1988, **37**, 785–789.
- 43 M. Dolg, U. Wedig, H. Stoll and H. Preuss, Energy-adjusted ab initio pseudopotentials for the first row transition elements, *J. Chem. Phys.*, 1987, **86**, 866–872.
- 44 A. V Marenich, C. J. Cramer and D. G. Truhlar, Universal Solvation Model Based on Solute Electron Density and on a Continuum Model of the Solvent Defined by the Bulk Dielectric Constant and Atomic Surface Tensions, *J. Phys. Chem. B*, 2009, **113**, 6378–6396.
- 45 R. Contreras, C. J. Cramer, D. G. Truhlar, V. S. Bernales and A. V. Marenich, Quantum mechanical continuum solvation models for ionic liquids, *J. Phys. Chem. B*, 2012, **116**, 9122–9129.
- 46 M. J. Frisch, G. W. Trucks, H. B. Schlegel, G. E. Scuseria, M. A. Robb, J. R. Cheeseman, G. Scalmani, V. Barone, G. A. Petersson, H. Nakatsuji, X. Li, M. Caricato, A. V Marenich, J. Bloino, B. G. Janesko, R. Gomperts, B. Mennucci, H. P. Hratchian, J. V Ortiz, A. F. Izmaylov, J. L. Sonnenberg, D. Williams-Young, F. Ding, F. Lipparini, F. Egidi, J. Goings, B. Peng, A. Petrone, T. Henderson, D. Ranasinghe, V. G. Zakrzewski, J. Gao, N. Rega, G. Zheng, W. Liang, M. Hada, M. Ehara, K. Toyota, R. Fukuda, J. Hasegawa, M. Ishida, T. Nakajima, Y. Honda, O. Kitao, H. Nakai, T. Vreven, K. Throssell, J. A. Montgomery Jr., J. E. Peralta, F. Ogliaro, M. J. Bearpark, J. J. Heyd, E. N. Brothers, K. N. Kudin, V. N. Staroverov, T. A. Keith, R. Kobayashi, J. Normand, K. Raghavachari, A. P. Rendell, J. C. Burant, S. S. Iyengar, J. Tomasi, M. Cossi, J. M. Millam, M. Klene, C. Adamo, R. Cammi, J. W. Ochterski, R. L. Martin, K. Morokuma, O. Farkas, J. B. Foresman and D. J. Fox, *Gaussian 16 Rev. A03*, Wallingford, CT, 2016.



# Chapter 6

## Ag<sup>+</sup> ion between water and RTILs

### 6.1 Introduction

Available literature data about Ag<sup>+</sup> solvation in RTILs provide a quite encouraging picture for the potential applications involving this metal ion in these solvents. This is particularly true for what concerns the employment of RTILs as receiving phase for chemical separations, since high extraction rates of Ag<sup>+</sup> have been obtained both with Tf<sub>2</sub>N<sup>-</sup> and PF<sub>6</sub><sup>-</sup>-based ionic liquids.<sup>1,2</sup> Solvation thermodynamics data seem to confirm this trend, showing favorable Gibbs free energies of transfer from water to [C<sub>4</sub>mim][Tf<sub>2</sub>N] and [C<sub>n</sub>mim][BF<sub>4</sub>] (n = 2, 4) for this metal ion (see **Sec. 1.3.3 of Chapter 1, Tab. 1.2**).  $\Delta G_{\text{solv}}$  and  $\Delta G_{\text{trans}}$  values for the RTILs studied in this work are here reported for sake of clarity (**Tab. 6.1**). As regards Ag<sup>+</sup> coordination in RTILs, according to an IR/Raman spectroscopies and DFT study in [C<sub>2</sub>mim][Tf<sub>2</sub>N], the tetrahedral [Ag(Tf<sub>2</sub>N)<sub>3</sub>]<sup>2-</sup> species has been supposed.<sup>3</sup> On the other hand, in a recent study by Bortolini *et al.*,<sup>4</sup> the still tetrahedral [Ag(Tf<sub>2</sub>N)<sub>2</sub>]<sup>-</sup> has been proposed on the basis of mass spectra and DFT calculations in gas-phase. No data are available about Ag<sup>+</sup> coordination in BF<sub>4</sub>-based RTILs.

However, to understand the properties of a metal ion in a molecular solvent, a definite picture of its hydration properties in aqueous solution is an essential starting point. As has been showed in the previous chapters, a continuous comparison of the studied metal ions between water and RTILs has been traced, not only from a structural but also from a thermodynamic point of view. The latter point is particular important for the interpretation of  $\Delta G_{\text{trans}}$  from water, which is essential to understand the employment of RTILs as extracting phase. While hydration properties of transition metal ions like Zn<sup>2+</sup> and Co<sup>2+</sup> are well-known,<sup>5</sup> this is not totally true for Ag<sup>+</sup>. In fact, even though Ag<sup>+</sup> coordination in water has been a matter of interest of many research groups, no general agreement on its structure in aqueous solution seems to have been reached yet. In particular, its coordination number is far from being unambiguously determined. The general picture arising from the earliest experimental data is that of a tetrahedrally coordinated metal ion. This is the case of neutron diffraction studies reporting CNs of 3.7(5) and 4.1(3) within average Ag-O(H<sub>2</sub>O) distances of 2.40(2) and 2.41(2) Å, respectively.<sup>6,7</sup> EXAFS measures have also been employed. In particular, Yamaguchi

*et al.*<sup>8</sup> found  $\text{Ag}^+$  as coordinated by three to four water molecules at a 2.31 - 2.36 Å distance. In addition, Funahashi *et al.*<sup>9</sup> presented a fitting of an EXAFS spectrum for  $\text{Ag}^+$  in water providing a CN of 4.0 and a 2.41 Å bond distance, even though the authors pointed out that these structural parameters have been kept fixed during the fitting procedure. On the other hand, more recent works have started questioning the tetrahedral coordination. In particular, by means of large-angle X-ray scattering (LAXS) and EXAFS measures, Persson *et al.*<sup>10</sup> proposed a "2 + 2" model that should come from a linearly-distorted tetrahedral structure with two waters set at 2.32 Å and two at 2.48 Å. Differently, CNs higher than four have been proposed by Ag K- and L<sub>2</sub>-edge EXAFS measures by Fulton *et al.*<sup>11</sup> Here the authors argued that the K-edge spectrum analysis could not distinguish between different CNs and that in particular a MS feature in the Fourier-transformed spectrum consisting in a peak at 3.5 Å could not be fitted by any of the examined geometries. On the contrary, the L<sub>2</sub>-edge spectrum resulted to be more sensible to the CN and only the insertion of O-Ag-O 90° MS paths could provide a good fit, therefore suggesting a trigonal bipyramidal or octahedral coordination. High CNs have been obtained also by many theoretical works. In particular, both classical MD or Monte Carlo simulations and hybrid techniques like QM/MM and AIMD reproduced an  $\text{Ag}^+$  ion as always coordinated by at least five or six water molecules with Ag-O distances ranging from 2.3 to 2.6 Å.<sup>12-17</sup> The parametrization of  $\text{Ag}^+$ -water potentials with the aim of reproducing some experimental hydration properties in classical MD simulations has been also an effort of many groups. In this respect, it can be observed a general difficulty in reproducing a target CN alongside with the experimental Ag-O bond distance. In addition, the contemporary reproduction of such structural properties with thermodynamic ones can be very challenging. In this regard, Spezia *et al.*<sup>15</sup> presented a set of LJ parameters for classical MD simulations able to reproduce an Ag-O bond distance of 2.36 Å and a good Gibbs hydration free energy with respect to the experimental. However, a CN of 5.55 was also obtained, while the goal in the fitting procedure was 4.5. In their work about the parametrization of LJ parameters for several monovalent cations, Merz and Li<sup>18</sup> proposed two sets of LJ couples for  $\text{Ag}^+$ : an "HFE set" reproducing good  $\Delta G_{\text{hyd}}$  but an underestimated Ag-O bond (2.10-2.14 Å) together with a CN of 4.9-5.3, and an "IOD set" providing good bond distance (2.40 Å) but underestimated  $\Delta G_{\text{hyd}}$  and CN of 5.7-5.9. The compromises that have to be taken in case of the employment of simple forms of pair-interaction potentials like the LJ one are well-known<sup>5,19,20</sup> and has been already underlined also in the previous Chapters of this thesis. In addition, some authors also tried to employ more complex potential forms for the  $\text{Ag}^+$ -H<sub>2</sub>O interaction. For example, Rode *et al.*<sup>12</sup> developed a polynomial 6-8-9-12 potential for classical MD simulations from an *ab initio* fitting procedure. However, also in this case a high CN of 4.9 is obtained, alongside with a Ag-O bond of 2.59 Å.

For these reasons, in the first part of the work, a study about  $\text{Ag}^+$  in aqueous solution was carried out. To obtain a clear picture about this metal ion coordination, a fitting procedure of the XANES and EXAFS spectra collected on an  $\text{Ag}^+$  solution in water have been carried out. AIMD simulations with the Car-Parrinello approach have been performed on the same system to check the coordination reproduced at quantum-mechanical level of theory. In the second part, the task of reproducing  $\text{Ag}^+$  structural and thermodynamic hydration properties in classical MD simulations has been faced with different strategies. To this purpose, a scan of  $\text{Ag}^+$  LJ parameters was performed to check the dependency of  $\text{Ag}^+$  CN and bond distance with water upon  $\sigma$  and  $\epsilon$  variation and if the employment of a simple LJ potential is still justified. In addition, the generation of a new  $\text{Ag-H}_2\text{O}$  potential obtained from an *ab initio* fitting procedure has been carried out and is reported in **Appendix A**.

It has to be underlined that improvements in the liquid structure description of  $\text{AgCl}$  by means of dipolar and quadrupolar polarization has been discussed in literature.<sup>21</sup> This is beyond the purpose of this study, aimed to explore the advantages and limits of classical MD and provide a reliable model based on experimental data without the inclusion of explicit polarizability.

In the second part, the knowledge acquired from the study of  $\text{Ag}^+$  in water has been applied to MD simulations in the RTILs. In particular, MD simulations have been performed in order to obtain structural and thermodynamic data about  $\text{Ag}^+$  solvation in  $[\text{C}_4\text{mim}][\text{Tf}_2\text{N}]$  and  $[\text{C}_4\text{mim}][\text{BF}_4]$ .

**Table 6.1.**  $\text{Ag}^+$  literature experimental Gibbs free energies of solvation ( $\Delta G_{\text{solv}}$ ) and transfer from water ( $\Delta G_{\text{trans}}$ ) for the RTILs studied in this work obtained as reported in **Sec. 1.3.3** of **Chapter 1** at 298.15 K. Data in  $\text{kcal mol}^{-1}$ .

RTIL	$\Delta G_{\text{solv}}$	$\Delta G_{\text{trans}}$
[C <sub>4</sub> mim][Tf <sub>2</sub> N]	-107.1	-4.4
	-118.4	
[C <sub>4</sub> mim][BF <sub>4</sub> ]	-115.2	-12.4
	-126.4	
	-106.7	
	-118.0	

## 6.2 Methods

### 6.2.1 Ag<sup>+</sup> in water

#### *6.2.1.1 X-Ray absorption measurements*

A weighed amount of anhydrous silver perchlorate AgClO<sub>4</sub> (G. F. Smith) was dissolved in Millipore Q filtered water to obtain a 2.0 M solution. Silver K-edge XAS were collected in transmission mode at the 4-1 beamline of the Stanford Synchrotron Radiation Laboratory (SSRL). The EXAFS station was equipped with a Si[220] double-crystal monochromator while the storage ring was operating at 3.0 GeV with a maximum current of 100 mA. The energy scales of the XAS spectra were calibrated by assigning the first inflection point of the K-edge of a silver foil to 25514 eV. Three scans were averaged to obtain a satisfactory spectral quality.

#### *6.2.1.2 EXAFS data analysis*

Data analysis of the EXAFS part of the spectrum has been carried out with the GNXAS method. For the generation of the interatomic potential in the muffin-tin approximation, two structures consisting in a linear [Ag(H<sub>2</sub>O)<sub>2</sub>]<sup>+</sup> and trigonal bipyramidal [Ag(H<sub>2</sub>O)<sub>5</sub>]<sup>+</sup> clusters were employed in order to represent the low and high CNs case, as it has been proven that the potential is only weakly dependent on the selected geometry.<sup>22</sup> SS signals coming from first shell oxygen atoms as well as with hydrogens were included in the fitting procedure. Signals from a second shell of oxygen atoms and the O-Ag-O three-body 180° MS have been found to have negligible amplitude. Each two-body distribution has been modelled as a  $\Gamma$ -like function. During the fitting procedure, all structural parameters have been optimized with the exception of CN, which has been constrained with values ranging from 1.7 to 6.0 every ~0.1 units. In addition, the "2 + 2" model was also tested by including an additional Ag-O SS signal from two distal oxygen atoms initially set at 2.48 Å. Among non-structural parameters, E<sub>0</sub> and the K<sub>N2&3</sub>, K<sub>N1</sub> and K<sub>M4&5</sub> double-electron excitation channels identified respectively at 64, 110 and 409 eV above the threshold energy were optimized. S<sub>0</sub><sup>2</sup> was kept fixed to 0.99.

#### *6.2.1.3 XANES data analysis*

The analysis of the XANES part of the spectrum collected on the Ag<sup>+</sup> aqueous solution has been carried out with the MXAN code.<sup>23</sup> The interatomic potential has been calculated in the framework

of the MT approximation using a complex optical potential based on the local density approximation of the excited photoelectron self-energy. The self-energy has been calculated with the HL scheme using only the real part of the HL potential, while inelastic losses are accounted by convolution of the theoretical spectrum with a Lorentzian function having an energy-dependent width (see **Sec. 3.2.2 of Chapter 3**).

The XANES spectrum has been analyzed starting from clusters with CNs of 2, “2+2”, 4 and 6 with an average Ag-O bond distance of 2.34 Å, as found from the EXAFS analysis (*vide infra*). The fitting procedure has been carried out by optimizing both the structural and non-structural parameters by minimizing the residual function  $R_{sq}$  between the theoretically generated and experimental spectra.

#### 6.2.1.4 Car-Parrinello Molecular Dynamics

*Ab initio* MD simulations of Ag<sup>+</sup> in water have been carried out with the Car-Parrinello approach by means of the CPMD code.<sup>24</sup> The BLYP functional combining Becke’s GGA approximation<sup>25</sup> for exchange and Lee-Yang-Parr<sup>26</sup> for correlation energies was employed with Grimme’s empirical correction for dispersion.<sup>27</sup> This functional has been already shown to give good results for the structure and dynamics of water<sup>28,29</sup> and has been already employed in the study of Ag<sup>+</sup> in aqueous solution.<sup>14–16</sup> Norm-conserving Troullier-Martins pseudo-potentials<sup>30</sup> have been used for the Ag, O and H atoms with a 70 Ry energy cut-off. Tests with higher cut-offs up to 100 Ry have been carried out and did not show any difference in the coordination tendencies of the metal ion. Electronic degrees of freedom have been associated with a fictitious mass of 400 a.u. and a time step of 4 a.u. was employed for all the simulations. This augmented mass for electrons has been demonstrated to be necessary for the correct representation of bulk water dynamic properties in AIMD.<sup>31,32</sup>

The system consisting in a periodic cubic box of 14.7 Å edge with one Ag<sup>+</sup> ion and 100 water molecules was previously equilibrated with a 10 ns classical MD run in NVT conditions at 298 K. Different initial geometries for Ag<sup>+</sup> coordination, *i.e.* CNs of 4 and 6, were employed to check the dependence from the starting configuration. A geometry optimization was performed with the CPMD code and the system was equilibrated in NVT for 2 ps at 298 K, then for 2 ps at 400 K and brought again to 298 K for further 4 ps. A production run was carried out for 30 ps at 298 K. Temperature was kept constant with the Nosé-Hoover thermostat with a coupling frequency of 1500 cm<sup>-1</sup>. The fictitious electronic kinetic energy was constantly monitored during all simulation time not to display any relevant drift.

Information about the second hydration sphere was also obtained by means of combined distribution functions (CDFs) between distances and angles. CDFs has been turned out to be a useful tool for the

inspection of the three-dimensional arrangement of water molecules around metal ions in aqueous solutions.<sup>33</sup> To this purpose,  $O_{1st}-Ag-O_{2nd}$  angles were considered as those formed between the vector going from  $Ag^+$  to one of the first shell coordinating oxygens (that was kept fixed) and vectors connecting  $Ag^+$  with second shells oxygen atoms. These angles were plotted against the  $Ag-O_{2nd}$  distances between the silver atom and outer-sphere oxygens. The same procedure was applied on hydrogen atoms. In addition, the spatial distribution function (SDF) of O atoms around  $Ag^+$  was calculated. The TRAVIS code<sup>34</sup> was employed for CDF and SDF calculation.

#### 6.2.1.5 Lennard-Jones parameters for the $Ag^+$ ion

The dependency of  $Ag^+$  coordination in classical MD upon the employed LJ parameters was checked by performing simulations of the metal ion in water with different combinations of  $Ag^+$   $\sigma$  and  $\epsilon$  values. To this purpose, a box with one  $Ag^+$  and 500 TIP3P<sup>35</sup> water molecules was built and first minimized, then for each LJ couple a 500 ps equilibration and 1 ns production run were carried out in NPT conditions (298.15 K, 1 atm). LJ parameter  $\sigma$  was varied between 0.4 and 2.8 Å at constant  $\epsilon$  (1.6736 kcal mol<sup>-1</sup>), while  $\epsilon$  was varied between 0.4184 and 1087.84 kcal mol<sup>-1</sup> at constant  $\sigma$  (1.07 Å). For each couple of parameters,  $Ag^+$  CN and average  $Ag-O(H_2O)$  bond distance were calculated from  $Ag-O(H_2O)$  pairs  $g(r)$ . Free energy calculations were carried out with the chosen LJ final values by means of a 15  $\lambda$  windows decoupling. The obtained LJ parameters were tested for both TIP3P and SPC/E water models. Simulations have been performed with Gromacs 5.1.6 program.<sup>36</sup>

### 6.2.2 $Ag^+$ in RTILs

Classical MD simulations of  $Ag^+$  have been performed in the  $[C_4mim][Tf_2N]$  and  $[C_4mim][BF_4]$  RTILs. The composition of the simulated boxes is reported in **Tab. 6.2**. These numbers of ions and box dimensions were chosen in order to reproduce pure RTILs densities and infinite dilution conditions for the metal.

**Table 6.2.** MD boxes details for the simulation of  $\text{Ag}^+$  in the  $[\text{C}_4\text{mim}][\text{Tf}_2\text{N}]$  and  $[\text{C}_4\text{mim}][\text{BF}_4]$  RTILs.

	$[\text{C}_4\text{mim}][\text{Tf}_2\text{N}]$	$[\text{C}_4\text{mim}][\text{BF}_4]$
$\text{Ag}^+$	1	1
$[\text{C}_4\text{mim}]^+$	217	199
$[\text{Tf}_2\text{N}]^-/[\text{BF}_4]^-$	218	200
Box edge ( $\text{\AA}$ )*	47.277	39.01

\*Initial side length before NPT equilibration.

The CL&P force field<sup>37–39</sup> was employed for  $[\text{C}_4\text{mim}][\text{Tf}_2\text{N}]$ . For  $[\text{C}_4\text{mim}][\text{BF}_4]$ , CL&P was used in combination with Wang *et al.*<sup>40</sup> parameters for  $[\text{BF}_4]^-$ , as this combination was demonstrated to provide the best results for  $\text{Zn}^{2+}$  in this RTIL (Sec. 4.3.2 of Chapter 4).  $\text{Ag}^+$  was represented with the LJ parameters obtained in this work reproducing a tetrahedral coordination in water (*vide infra*) and with Merz and Li “HFE” set.<sup>18</sup>

The same simulation protocol employed for  $\text{Zn}^{2+}$  thermodynamic calculations was used (Sec. 4.2.1.1).  $\text{Ag}^+$  single-ion solvation free energies in the RTILs have been calculated with a  $15 \lambda$  windows decoupling by performing 5 ns equilibrations and 10 ns production runs for each  $\lambda$  value. Simulations have been carried out with Gromacs 5.1.6 program.<sup>36</sup>

## 6.3 Results

### 6.3.1 $\text{Ag}^+$ in water

#### 6.3.1.1 XAS results

A fitting procedure of the Ag K-edge EXAFS spectrum collected on the  $\text{AgClO}_4$  solution in water has been carried out. To this purpose,  $\chi(k)$  theoretical signals associated with first shell Ag-O and Ag-H SS paths have been generated, while the contribution from a second shell of oxygen atoms has turned out to provide negligible amplitude. First, least-squares fits were performed in the  $2.7 - 15.0 \text{ \AA}^{-1} k$  range for fixed CNs of the  $\text{Ag}^+$  ion comprised between 1.7 and 6.0. The goodness of the fit upon CN variation has been evaluated by checking the evolution of the obtained residual function  $R_{sq}$  and of the  $\sigma^2$  Debye-Waller factor for the Ag-O path, which are reported in Fig. 6.1. As can be observed, the smallest residual between the theoretical and experimental spectra is obtained for a CN of 2.0,

while  $R_{sq}$  tends to increase exponentially for greater coordination numbers (**Fig. 6.1 A**). For what concerns  $\sigma^2$ , the  $0.013 \text{ \AA}^2$  value obtained for  $\text{CN} = 2.0$  is in line with typical Debye-Waller factors usually observed for metal ions in disordered liquid systems,<sup>5,20,41,42</sup> while it tends to rise linearly reaching values of  $\sim 0.05 \text{ \AA}^2$  for CNs close to 6.0 (**Fig. 6.1 B**).

As a consequence, the best-fit is obtained for a CN of 2.0, which is shown in **Fig. 6.2** together with the single theoretical signals, the total theoretical contribution compared with the experimental spectra and the resulting residuals. A complete list of the optimized parameters is reported in **Tab. 6.3**. As can be observed, the agreement between the theoretical and experimental data is very good, as is also evident from the comparison of the FT spectra reported in the lower panel of **Fig. 6.2**. From the generated theoretical signals, it is evident that the EXAFS oscillation is largely dominated by the Ag-O SS, while the Ag-H path provides a much little contribution. The mean Ag-O bond distance resulted to be  $2.34(2) \text{ \AA}$  and is in line with previous determinations reported in literature,<sup>6-8,10</sup> while the obtained Ag-H distance of  $3.02(4) \text{ \AA}$  is in agreement with the geometry of the water molecule. As regards the tetrahedral distorted "2 + 2" model, the SS signal related to an additional Ag-O path arising from two distal oxygen atoms initially placed at  $2.48 \text{ \AA}$  resulted to provide a worst fit. A special mention has to be devoted to the collinear O-Ag-O MS, which turned out to provide negligible amplitude to the EXAFS oscillation. It is known that this kind of three-body path can have a marked contribution only if a focusing effect (bond angle  $\sim 180^\circ$ ) is present or for particularly short bond distances.<sup>5,20,41,42</sup> In our case, the long Ag-O bond distance of  $2.34 \text{ \AA}$  is probably responsible for the negligible contribution provided by this MS path.

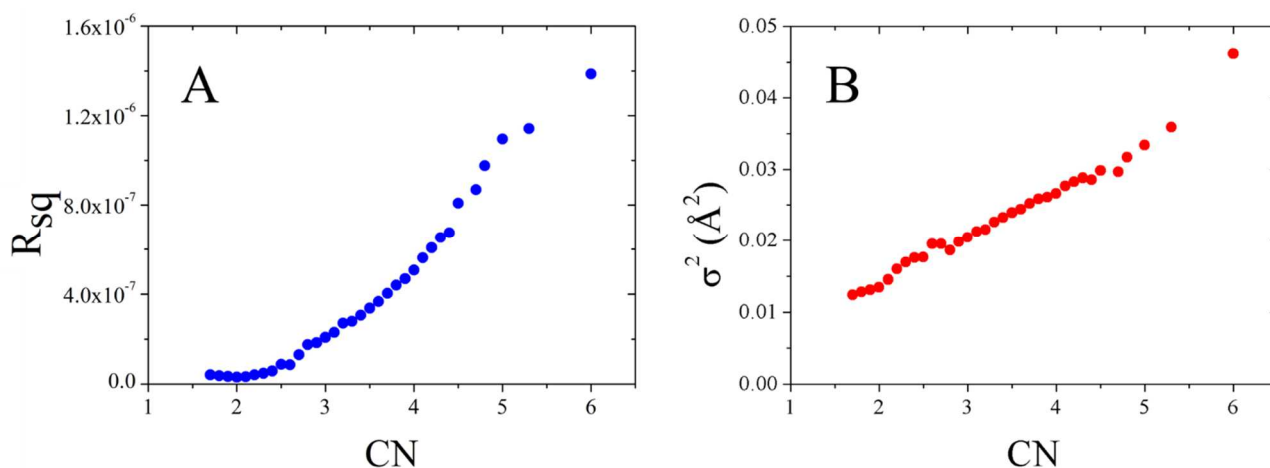


**Figure 6.1.** Values of the A)  $R_{sq}$  residual function and of the B)  $\sigma^2$  Debye-Waller factor obtained from the EXAFS fitting procedure for all the tested  $\text{Ag}^+$  coordination numbers (CN).

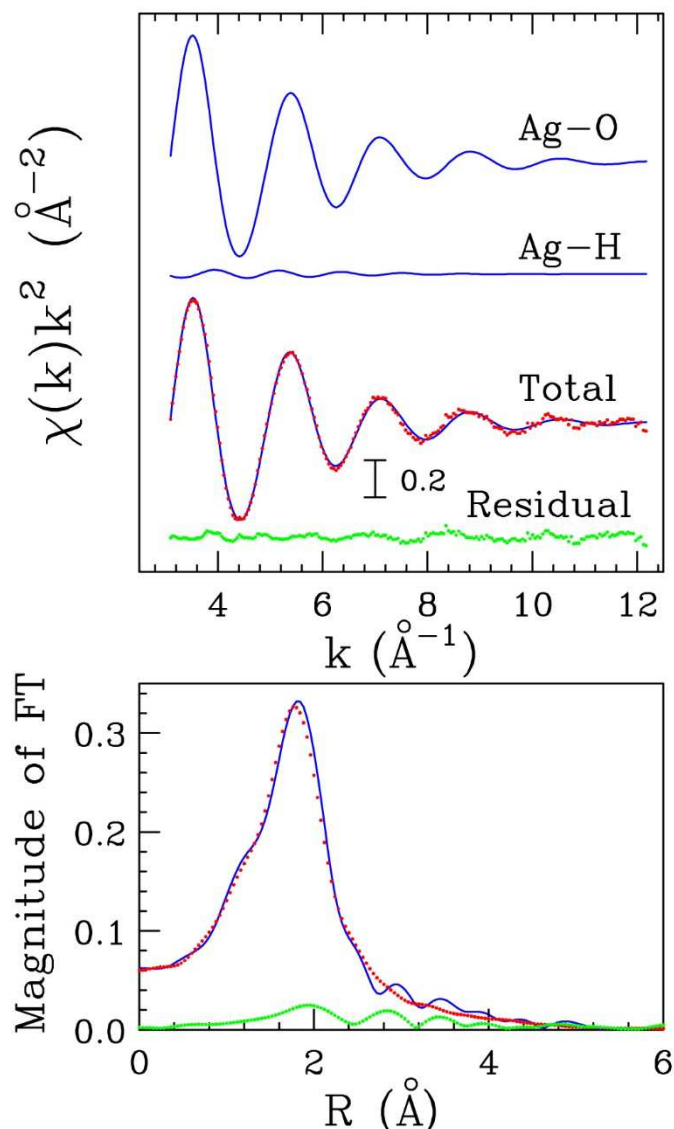


**Figure 6.2.** Upper panel: analysis of the Ag K-edge EXAFS spectrum of the 2 M  $\text{AgClO}_4$  in water. From the top the theoretical Ag-O and Ag-H SS signals are shown, as well as the total theoretical signal (blue line) together with the experimental spectrum (red dots) and the correspondent residuals (green line). Lower panel: non-phase shift corrected Fourier Transforms of the best-fit EXAFS theoretical signal (blue line) of the experimental data (red dots) and of the residual curve (green line).

**Table 6.3.** Best-fit coordination number CN, average distance R, Debye-Waller factor  $\sigma^2$  and asymmetry index  $\beta$  of the Ag-O and Ag-H distributions as obtained during the EXAFS fitting procedure for the 2 M  $\text{AgClO}_4$  solution in water.

Path	CN	R (Å)	$\sigma^2$ (Å <sup>2</sup> )	$\beta$
Ag-O	2.0	2.34	0.013	0.14
Ag-H	4.0	3.02	0.020	0.00

It is known that a complete recovery of the three-dimensional displacement of the scattering atoms around the photoabsorber can be obtained by the analysis of the XANES part of the X-ray absorption spectrum.<sup>43</sup> Therefore, to further confirm the results obtained with the EXAFS analysis, a fitting procedure of the XANES spectrum of the  $\text{Ag}^+$  solution in water has been performed. To shed light into the different potential CNs of the metal ion, a fitting procedure was carried out by optimizing the structural parameters starting from clusters with CNs of 2 (linear), “2+2” (linearly-distorted tetrahedral), 4 (tetrahedral) and 6 (octahedral) for the metal ion. The result of the fitting procedures is showed in **Fig. 6.3**. As can be observed, the best fitting is obtained for the cluster with the linear coordination, which shows a very good agreement between the experimental and theoretical spectra ( $R_{sq} = 1.1$ ). Differently, the value of the residual function tends to increase following the increase in the CN, up to a very poor fit obtained with the octahedral coordination ( $R_{sq} = 1.9$ ). In particular, a clear mismatch in the first and third oscillations after the threshold energy is observed for CNs higher than two. Therefore, XANES seems to confirm the preference for the linear coordination of the  $\text{Ag}^+$  ion in water solution already suggested by the EXAFS analysis.

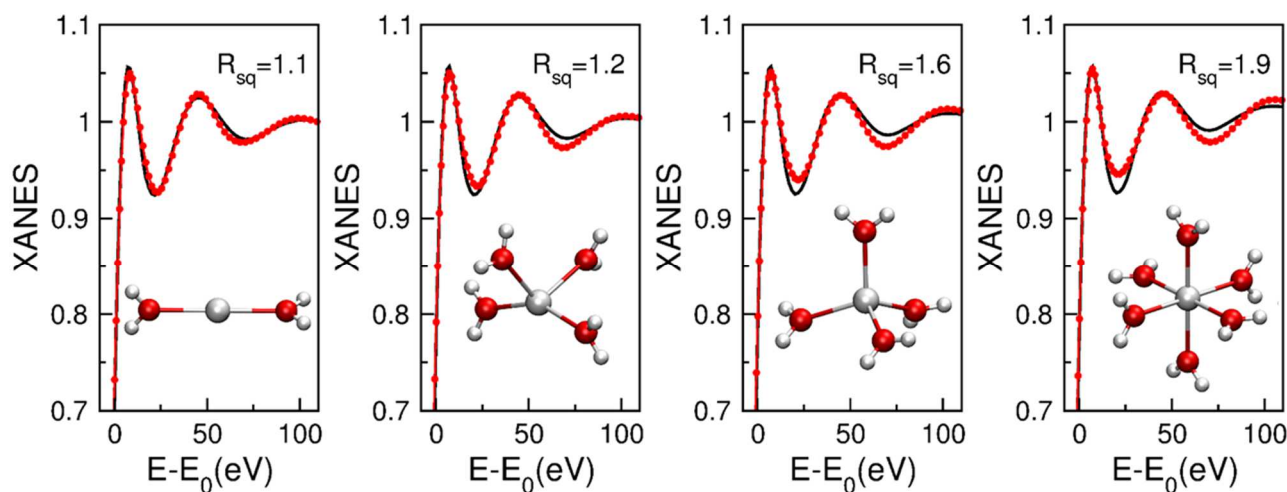


**Figure 6.3.** From left to the right: comparison of the XANES experimental spectrum (red dots) with the theoretical ones (black lines) optimized by starting from clusters with  $\text{Ag}^+$  CN of 2 (linear), “2+2” (linearly-distorted tetrahedral), 4 (tetrahedral) and 6 (octahedral). For each CN, the corresponding optimized cluster is shown as well as inset.

### 6.3.1.2 CPMD simulation results

The structural properties of  $\text{Ag}^+$  in water have been investigated also by means of *ab initio* MD simulations with the CPMD method.<sup>24</sup> The calculated Ag-O  $g(r)$  is shown in **Fig. 6.4 A**. As can be

observed, the Ag-O distribution presents a first intense peak centered at 2.20 Å integrating 2.0 oxygen atoms. This result shows that CPMD is able to reproduce the Ag<sup>+</sup> ion as linearly coordinated, as can also be observed from the snapshot reported in **Fig. 6.4 B**. It has to be noted that the choice of the initial configuration, *i.e.* starting from clusters with pre-fixed tetrahedral or octahedral geometries, resulted to have no effect on the description of Ag<sup>+</sup> first hydration shell, as water coordination towards the metal turned out to become linear after a few picoseconds already during equilibration time.

However, the Ag-O bond distance is underestimated with respect to that determined by the EXAFS analysis (**Tab. 6.3**). In addition, the Ag-O and Ag-H distributions obtained from the EXAFS fitting have been modelled as  $\Gamma$ -like functions and compared with the Ag-O and Ag-H  $g(r)$ 's calculated from the CPMD simulation. The comparison is shown in **Fig. C.7** of **Appendix C**. Firstly, here it can be observed that the Ag-O and Ag-H distributions from CPMD have a first maximum at shorter distances with respect to the experimental. However, the mismatch between the simulation and the experimental data is not only about average bond distances. In fact, from **Fig. C.7** it can also be observed that the Debye-Waller factor is smaller for the distributions obtained from the CPMD simulation, provoking peaks that are much more intense with respect to those found from EXAFS data analysis. In other words, the AIMD simulation reproduces an Ag-H<sub>2</sub>O interaction that is too stiff with respect to the experimental. This is a quite surprising result, if we take into account that this interaction is derived from *ab initio* principles in case of CPMD.

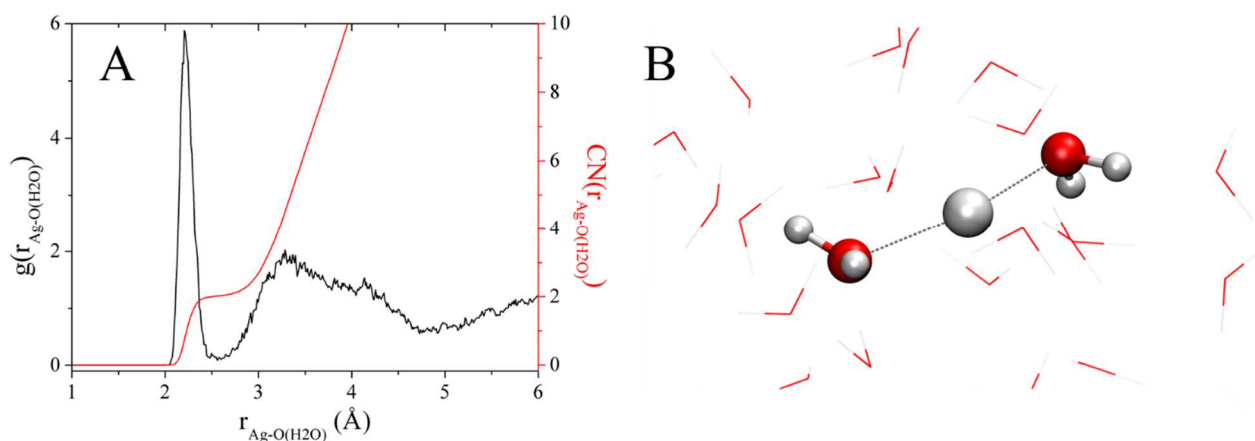


**Figure 6.4.** A) Ag-O pairs radial distribution function  $g(r)$  (black line, left scale) and corresponding integration number (red line, right scale) and B) trajectory snapshot (balls and sticks: Ag<sup>+</sup> and coordinating water molecules, wireframe: bulk water) as obtained by the CPMD simulation.

**Fig. 6.4 A** also shows the presence of a second shell at approximately 3.5 Å, but it consists in a very broad peak due to the short simulation time characteristic of AIMD. To get further insights into the arrangement of the outer-sphere solvent, Ag-O and Ag-H CDFs were calculated as reported in **Sec.**

**6.2.1.4** and the results are shown in **Fig. 6.5**. As can be observed, a first intense area in the Ag-O distribution results at  $\sim 3.25$  Å, these water molecules forming a  $90^\circ$  angle with the vector formed by  $\text{Ag}^+$  and first shell oxygen atoms. In addition, two areas of high probability are observed at a  $\sim 4$  Å distance for angles of  $\sim 45^\circ$  and  $\sim 135^\circ$ , respectively. Therefore, the CDF analysis was able to separate the contributions from the second hydration sphere that were convoluted in one broad peak in **Fig. 6.4 A**. Our supposition is that the second hydration sphere set at  $\sim 3.25$  Å is represented by water molecules that could partially weakly interact with the  $\text{Ag}^+$  ion and partially be caught in the H-bonds network formed by the outer-sphere waters. As regards the area at  $\sim 4$  Å, it could belong to water molecules forming H-bonds with the two coordinating waters of the first hydration sphere. In addition, from the CDF in **Fig. 6.5 B** it can be observed that the higher probability areas for hydrogens are at distances comparable with those obtained for the oxygen atoms of the corresponding waters. This result could mean that outer-sphere water molecules are oriented in a planar manner with respect to the  $\text{O}_{1\text{st}}\text{-Ag-O}_{1\text{st}}$  axis, this being a further proof that their disposition is more governed by water-water interactions with respect to the Ag- $\text{H}_2\text{O}$  one. A representative snapshot of this picture is reported in **Fig. C.8** of **Appendix C**.

The SDF between silver and outer-sphere water is shown in **Fig. 6.6**. The SDF results in a first area of density forming a ring around the  $\text{Ag}^+$  ion, while the two coordinating waters are embedded by two further rings. This confirms the picture supposed by the CDF analysis (**Fig. 6.5**), being the ring around  $\text{Ag}^+$  connected with the density area set at  $\sim 3.25$  Å, and the latter two rings with the two areas at  $\sim 4$  Å in **Fig. 6.5** representing water molecules forming H-bonds with the coordinating ones.

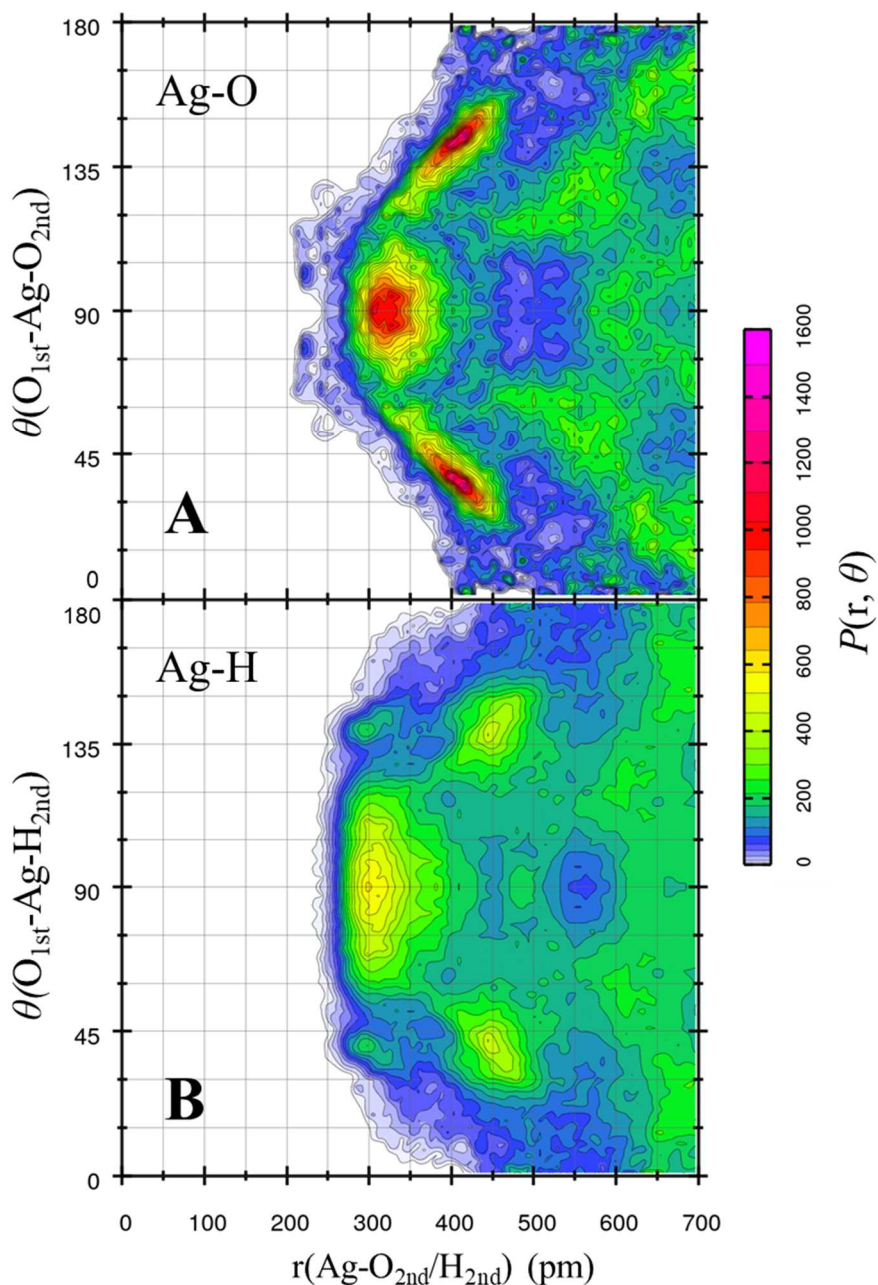


**Figure 6.5.** Combined distributions functions (CDFs) between the  $O_{1st}-Ag-O_{2nd}/H_{2nd}$  angles and  $Ag-O_{2nd}/H_{2nd}$  distances calculated from the CPMD simulation. Angles were considered as those formed between the vector going from  $Ag^+$  to one of the first shell coordinating oxygens and vectors connecting  $Ag^+$  with second shells oxygen/hydrogen atoms. The  $Ag-O_{2nd}$  and  $Ag-H_{2nd}$  distances are those between the silver atom and outer-sphere oxygens/hydrogens.  $P(r, \theta)$  is the probability function of finding the inspected particle at that distance and angle. Note that no information about the first hydration shell is here reported, as can be observed from the blank area up to  $\sim 2.5 \text{ \AA}$ .

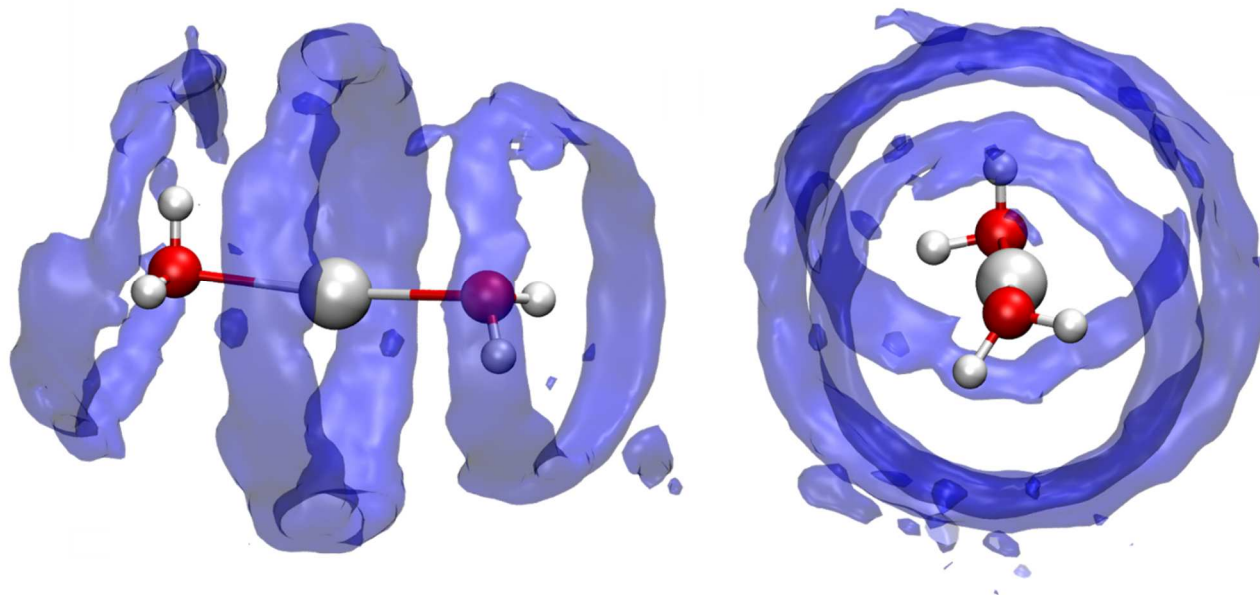


**Figure 6.6.** Spatial distribution function (SDF) between the  $O_{1st}\text{-Ag-}O_{1st}$  vector and outer-sphere oxygen atoms. Balls and sticks:  $\text{Ag}^+$  and first shell water molecules, solid surface: SDF (isovalue = 105). Two different orientations are shown.

### 6.3.1.3 Reproduction of $\text{Ag}^+$ coordination in water with classical MD

Classical MD simulations of  $\text{Ag}^+$  in water have been carried out by varying the metal ion LJ parameters to check the dependency of the reproduced coordination upon  $\sigma$  and  $\epsilon$ . The obtained  $\text{Ag}^+$  coordination number and Ag-O average bond distance are reported in **Fig. 6.7** in function of the varied LJ parameter. A direct proportionality between CN and bond distances against  $\sigma$  and  $\epsilon$  is observed. In particular, to reproduce a bond length which is close to the experimental (2.34 Å, **Tab. 6.3**), a CN between 5 and 6 is obtained. Otherwise, to get a CN lower than ~5, the bond distance results to be underestimated.

This was an expected result, as it is related to the employment of the simple LJ potential form that has already been underlined. Taking into account this trend, the reproduction of a linear coordination and thus a CN of 2 seems to be impossible to obtain with this kind of function. In addition, the generation of a new Ag- $\text{H}_2\text{O}$  interaction potential has been carried out and the results are reported in **Appendix A**. To this purpose, *ab initio* data were fitted with a polynomial 4-6-8-12 potential form. The resulting coordination consists in 6.0 water molecules at an average Ag-O distance of 2.31 Å. A bond in good agreement with the experimental (**Tab. 6.3**) was therefore obtained together with an overestimated CN. This result shows that also the employment of a more complex, but still spherical potential, is not sufficient to reproduce asymmetric coordinations like for example the linear case.

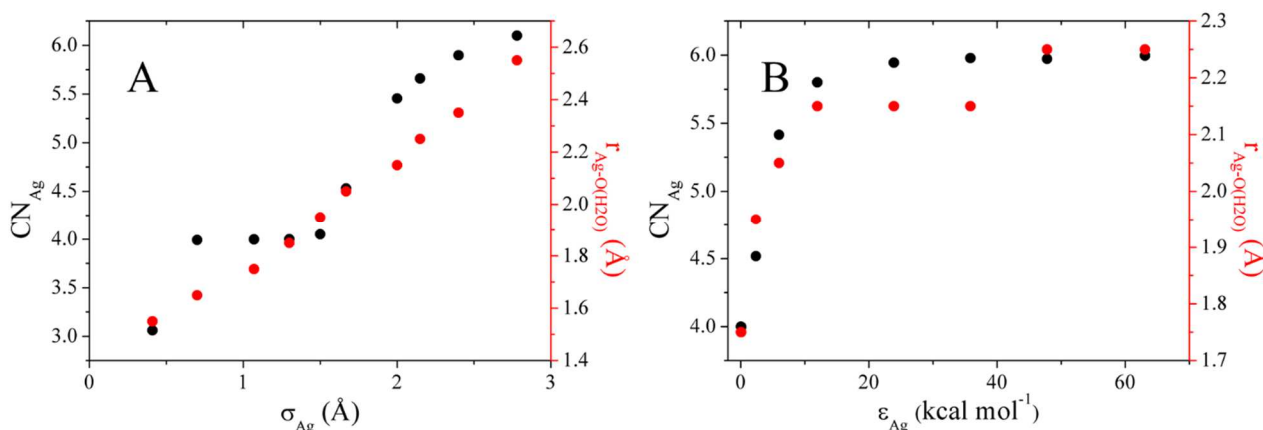


**Figure 6.7.** MD calculated Ag<sup>+</sup> coordination number CN (black dots, left scales) and average distance with coordinating water oxygen atoms (red dots, right scales) against Ag<sup>+</sup> LJ parameters A)  $\sigma$  and B)  $\epsilon$ .

As a consequence, LJ parameters that seemed to reproduce a CN of  $\sim 4$  ( $\sigma_{\text{Ag}} = 1.50 \text{ \AA}$ ,  $\epsilon_{\text{Ag}} = 0.0956 \text{ kcal mol}^{-1}$ ) were chosen and MD simulations were carried out to further test the performance of this set in the reproduction of structural and thermodynamic properties of Ag<sup>+</sup> in water. Simulations were performed both in TIP3P and SPC/E water and compared with Merz *et al.* “IOD” and “HFE” LJ sets for Ag<sup>+</sup>.<sup>18</sup> The results are reported in **Tab. 6.4**. As can be observed, a CN of 4.0 reproducing a tetrahedral coordination for Ag<sup>+</sup> is obtained with both the employed water models, as can also be observed from the snapshot and the Ag-O pairs  $g(r)$  shown in **Fig. 6.8**. The  $r_{\text{Ag-O}}$  average distance resulted of 1.93 Å with TIP3P water and 1.91 Å with SPC/E (**Tab. 6.4**), thus underestimated with respect to the bond distance obtained by EXAFS data analysis (**Tab. 6.3**). Every attempt of increasing this bond length has turned out to provide CNs higher than 4.0 and the loss of the tetrahedral coordination. The calculated  $\Delta G_{\text{hyd}}$  (**Tab. 6.4**) are in well agreement with the experimental values of -102.8 and -114.0 kcal mol<sup>-1</sup>.<sup>44,45</sup> It has to be noted that, according to us, a set of LJ parameters reproducing a tetrahedrally-coordinated Ag<sup>+</sup> ion in water together with good estimation of  $\Delta G_{\text{hyd}}$  is not still present in literature for classical MD.

As regards the results obtained with the parameters from Merz *et al.*,<sup>18</sup> they are very close to those obtained by the authors in the parametrization of the LJ set, providing a five-fold coordinated Ag<sup>+</sup>, good  $\Delta G_{\text{hyd}}$  and slight underestimated bond distance for the “HFE” set (**Tab. 6.4**). As expected, the “IOD” set best matches the experimental Ag-O(H<sub>2</sub>O) bond, but this is traduced in an increase of the CN and an underestimation of  $\Delta G_{\text{hyd}}$ .

**Table 6.4.** MD calculated  $\text{Ag}^+$  coordination in water and Gibbs free energy of hydration ( $\Delta G_{\text{hyd}}$ , kcal mol<sup>-1</sup>) with the LJ parameters obtained in this work and from Merz *et al.*<sup>18</sup>

LJ parameters	Water	CN <sub>O</sub> <sup>a</sup>	$r_{\text{Ag-O}}$ (Å) <sup>b</sup>	$\Delta G_{\text{hyd}}$ (kcal mol <sup>-1</sup> )*
This work	TIP3P	4.0	1.93	-118.3
	SPC/E	4.0	1.91	-117.3
Merz “HFE”	SPC/E	4.9	2.09	-102.7
Merz “IOD”	SPC/E	5.8	2.37	-84.3

<sup>a</sup>Ag-O(H<sub>2</sub>O) first  $g(r)$  peak integration number; <sup>b</sup>average bond distance between  $\text{Ag}^+$  and the coordinating oxygen atoms.

\*Errors below the first decimal digit.

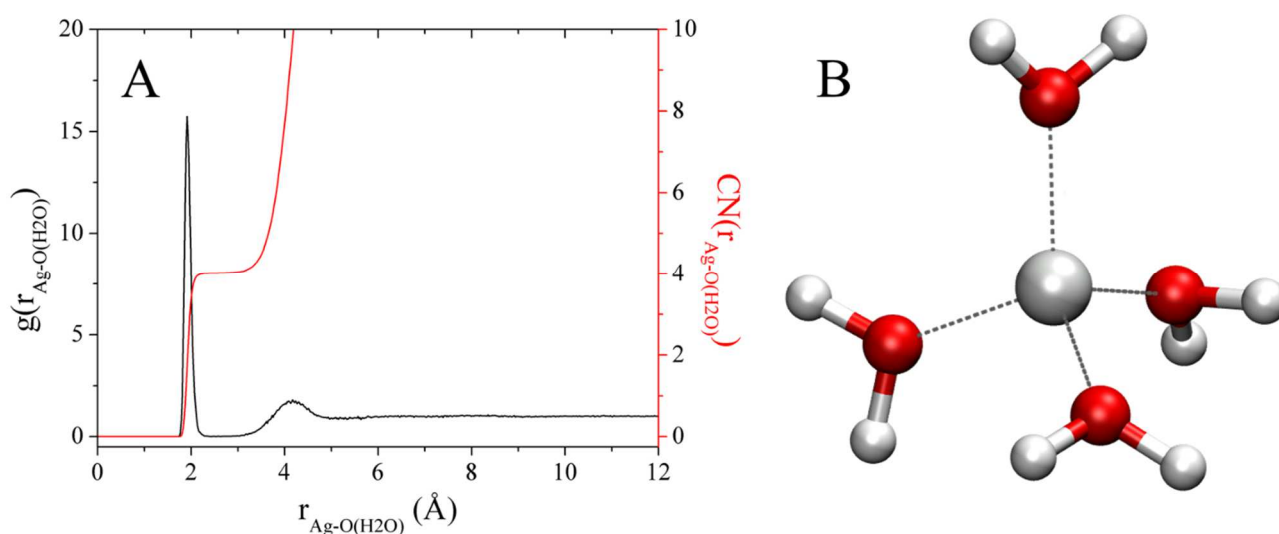


**Figure 6.8.** A) Ag-O(H<sub>2</sub>O) pair  $g(r)$  radial distribution function (black line, left scale) and corresponding integration number (red line, right scale) within B) MD snapshot obtained from the simulation of  $\text{Ag}^+$  in water with the LJ parameters found in this work (data showed for the simulation with SPC/E water).

The LJ parameters set obtained in this work was furtherly tested by calculating  $\text{Ag}^+$  hydration enthalpy and entropy in SPC/E water. To this purpose, free energy calculations were performed for five different temperatures in the 280 – 360 K range. The resulting  $\Delta G/T$  vs.  $1/T$  plot is shown in **Fig. 6.9**, while the calculated  $\Delta H_{\text{hyd}}$  and  $\Delta S_{\text{hyd}}$  are reported in **Tab. 6.5** together with the experimental data. Also in this case large negative enthalpy and small negative entropy are obtained, as expected for metal ion hydration.<sup>44–46</sup> The MD calculated  $\Delta H_{\text{hyd}}$  is well in agreement with the experimental, in particular with the value reported by Ahrland.<sup>45</sup> As regards  $\Delta S_{\text{hyd}}$ , the calculated value matches very well the experimental of Marcus *et al.*,<sup>46</sup> while the value obtained by Ahrland’s data is more underestimated. It has to be noted that in their works Ahrland and Marcus provided a direct

determination of  $\Delta H_{\text{hyd}}$  and  $\Delta S_{\text{hyd}}$  respectively, while  $\Delta S_{\text{hyd}}$  has been calculated in this work by  $\Delta G_{\text{hyd}}^{45}$  and  $\Delta H_{\text{hyd}}^{45}$  for Ahrlund and  $\Delta H_{\text{hyd}}$  was calculated by  $\Delta G_{\text{hyd}}^{44}$  and  $\Delta S_{\text{hyd}}^{46}$  for Marcus.

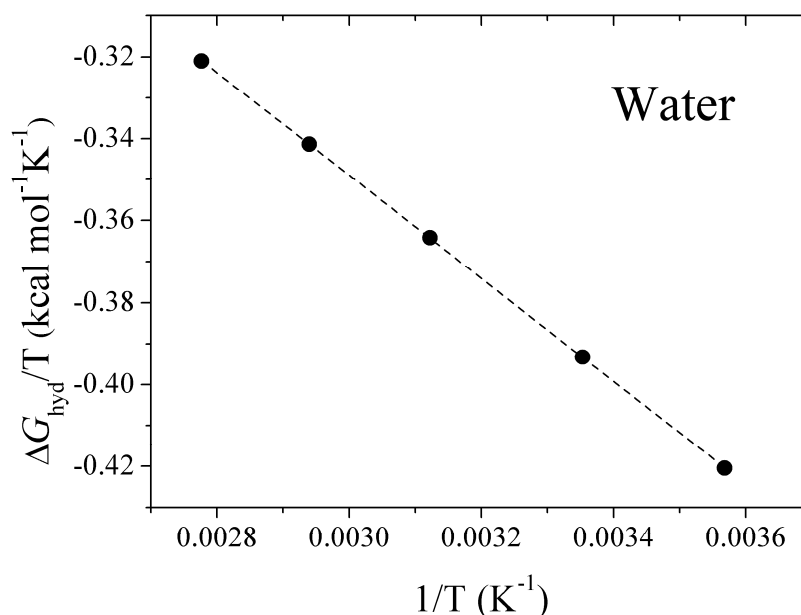


**Figure 6.9.**  $\Delta G/T$  vs.  $1/T$  plots obtained from calculated  $\text{Ag}^+$  Gibbs free energies in water at different temperatures ( $R^2 = 0.99$ ).  $\text{Ag}^+$  represented with LJ parameters obtained in this work.

**Table 6.5.** Hydration enthalpies ( $\text{kcal mol}^{-1}$ ) and entropies ( $\text{kcal mol}^{-1} \text{K}^{-1}$ ) for  $\text{Ag}^+$  calculated from MD simulations (obtained from plot in **Fig. 6.9**) and from experimental data.

MD calculated		Experimental	
$\Delta H_{\text{hyd}}$	$\Delta S_{\text{hyd}}$	$\Delta H_{\text{hyd}}$	$\Delta S_{\text{hyd}}$
$-125.9 \pm 0.2$	$-0.029^*$	$-109.6^a$	$-0.023^{46}$
		$-115.4^{45}$	$-0.005^b$

<sup>a</sup> $\Delta H_{\text{hyd}}$  calculated from Marcus'  $\Delta G_{\text{hyd}}^{44}$  and  $\Delta S_{\text{hyd}}^{46}$  <sup>b</sup> $\Delta S_{\text{hyd}}$  calculated from Ahrlund's  $\Delta G_{\text{hyd}}$  and  $\Delta H_{\text{hyd}}^{45}$  \*Error below the third decimal digit.

### 6.3.2 $\text{Ag}^+$ in RTILs

Classical MD simulations have been performed to obtain data about  $\text{Ag}^+$  solvation in  $[\text{C}_4\text{mim}][\text{Tf}_2\text{N}]$  and  $[\text{C}_4\text{mim}][\text{BF}_4]$ . As was reported in **Sec. 6.3.1.1**, an experimental evidence for a linear coordination of  $\text{Ag}^+$  in water has been obtained. However, this study also showed the impossibility of reproducing a linear coordination for this metal ion with the employment of a spherical potential, in particular in the LJ case (**Sec. 6.3.1.3**). In addition, in absence of XAS data about  $\text{Ag}^+$  in these RTILs, the only experimental evidence points out a tetrahedral coordination for this metal ion in

Tf<sub>2</sub>N-based ionic liquids,<sup>3,4</sup> while no information is available for BF<sub>4</sub>-based ones. For these reasons, to get thermodynamic data about Ag<sup>+</sup> solvation in [C<sub>4</sub>mim][Tf<sub>2</sub>N] and [C<sub>4</sub>mim][BF<sub>4</sub>], the metal ion was represented both with the LJ obtained in this work providing a tetrahedral coordination in water (Sec. 6.3.1.3) and with Merz *et al.* “HFE” set.<sup>18</sup>

The obtained Ag-O(Tf<sub>2</sub>N) and Ag-N(Tf<sub>2</sub>N)  $g(r)$ 's for simulations in [C<sub>4</sub>mim][Tf<sub>2</sub>N] with both the LJ sets are reported in Fig. 6.10, while the Ag-F(BF<sub>4</sub>) and Ag-B(BF<sub>4</sub>)  $g(r)$ 's for [C<sub>4</sub>mim][BF<sub>4</sub>] are shown in Fig. 6.12. Details of the first solvation sphere structure in the two RTILs are reported in Tab. 6.6. In [C<sub>4</sub>mim][Tf<sub>2</sub>N], a tetrahedral coordination with four monodentate [Tf<sub>2</sub>N]<sup>-</sup> is reproduced with the LJ obtained in this work, while with Merz *et al.* parameters a five-fold coordination with one bidentate and three monodentate [Tf<sub>2</sub>N]<sup>-</sup> is obtained, as can also be observed from the snapshots reported in Fig. 6.11. The mixed coordination in case of Merz *et al.* parameters can be also observed from the Ag-N  $g(r)$  in Fig. 6.10 D. Here two peaks are present, the less intense relative to bidentate coordination (integrating one anion) and the more intense to the monodentate-binding form (integrating three).

As regards [C<sub>4</sub>mim][BF<sub>4</sub>], a similar picture is observed. Here Ag<sup>+</sup> is bound in a tetrahedral fashion by four monodentate [BF<sub>4</sub>]<sup>-</sup> with the LJ obtained in this work, while five anions coordinate the metal (one bidentate and three monodentate) when Merz *et al.* parameters are employed. The correspondent snapshots are reported in Fig. 6.13. Also in this case, the mixed coordination mode is evident from the Ag-B  $g(r)$  in Fig. 6.12 D. As expected, for both RTILs a higher average bond distance between Ag<sup>+</sup> and the coordinating atoms of the anions is obtained with Merz *et al.* parameters with respect of the LJ couple of our work (Tab. 6.6).

**Table 6.6.** MD results of Ag<sup>+</sup> first solvation shell structure in [C<sub>4</sub>mim][Tf<sub>2</sub>N] and [C<sub>4</sub>mim][BF<sub>4</sub>] with both the tested LJ sets for the metal ion.

RTIL	Ag <sup>+</sup> LJ parameters	r <sub>Ag-O</sub> (Å) <sup>a</sup>	CN <sub>O</sub> <sup>b</sup>	CN <sub>N</sub> <sup>c</sup>
[C <sub>4</sub> mim][Tf <sub>2</sub> N]	This work	1.87	4.0	4.0
	Merz “HFE”	2.09	5.1	4.0
		r <sub>Ag-F</sub> (Å) <sup>d</sup>	CN <sub>F</sub> <sup>e</sup>	CN <sub>B</sub> <sup>f</sup>
[C <sub>4</sub> mim][BF <sub>4</sub> ]	This work	1.85	4.2	4.0
	Merz “HFE”	2.01	5.0	4.0

<sup>a</sup>Average bond distance between the Ag<sup>+</sup> ion and the coordinating oxygen atoms of the first solvation shell [Tf<sub>2</sub>N]<sup>-</sup> anions;

<sup>b</sup>Ag-O(Tf<sub>2</sub>N) first  $g(r)$  peak integration number; <sup>c</sup>Ag-N(Tf<sub>2</sub>N) first  $g(r)$  peak integration number. <sup>d</sup>Average bond distance between the Ag<sup>+</sup> ion and the coordinating oxygen atoms of the first solvation shell [BF<sub>4</sub>]<sup>-</sup> anions; <sup>e</sup>Ag-F(BF<sub>4</sub>) first  $g(r)$  peak integration number; <sup>f</sup>Ag-B(BF<sub>4</sub>) first  $g(r)$  peak integration number. In case of Merz *et al.* sets, the cumulative integration between the first and second peaks has been calculated for Ag-N and Ag-B.

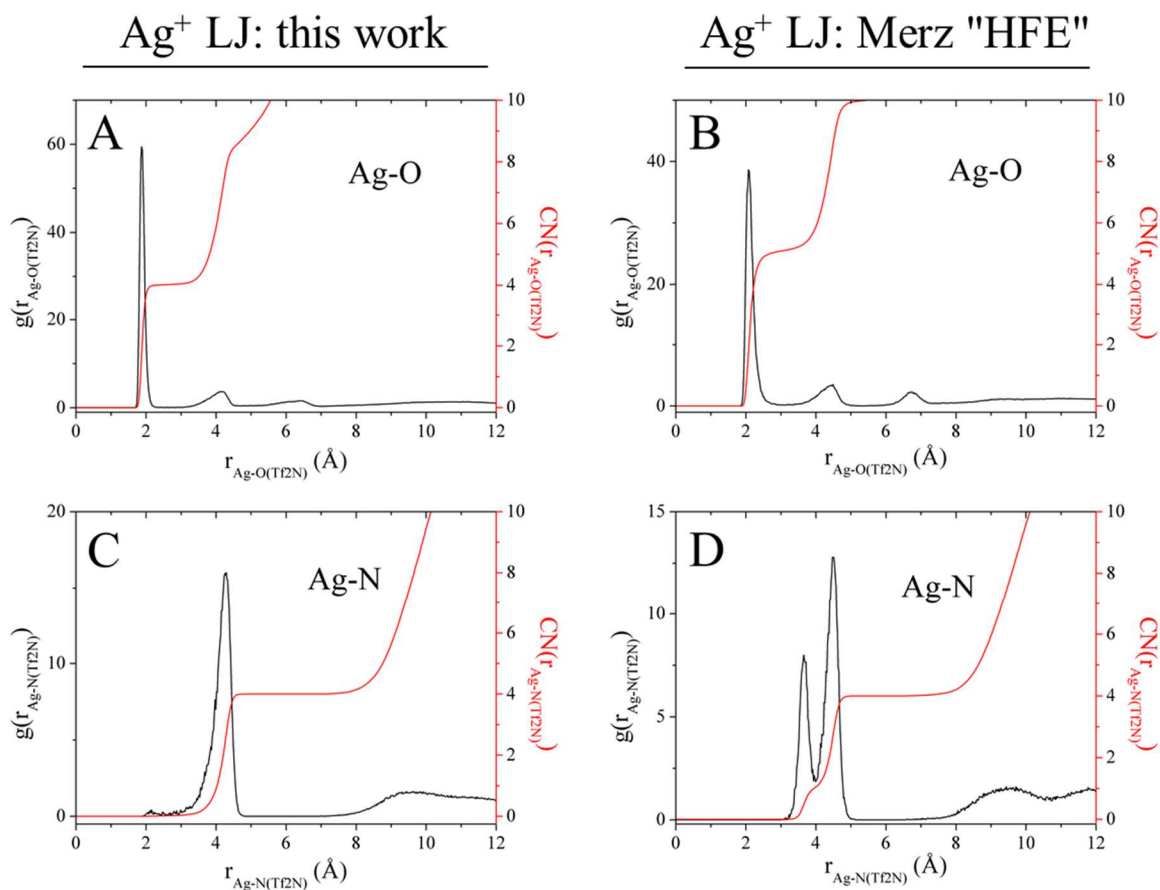


**Figure 6.10.** MD calculated Ag-O(Tf<sub>2</sub>N) and Ag-N(Tf<sub>2</sub>N) pairs radial distribution functions  $g(r)$ 's obtained from simulations in [C<sub>4</sub>mim][Tf<sub>2</sub>N] with LJ parameters for Ag<sup>+</sup> obtained in this work (A and C) and from Merz *et al.* "HFE" set (B and D) (black lines, left scales). The correspondent integration numbers (red lines, right scales) are also reported.

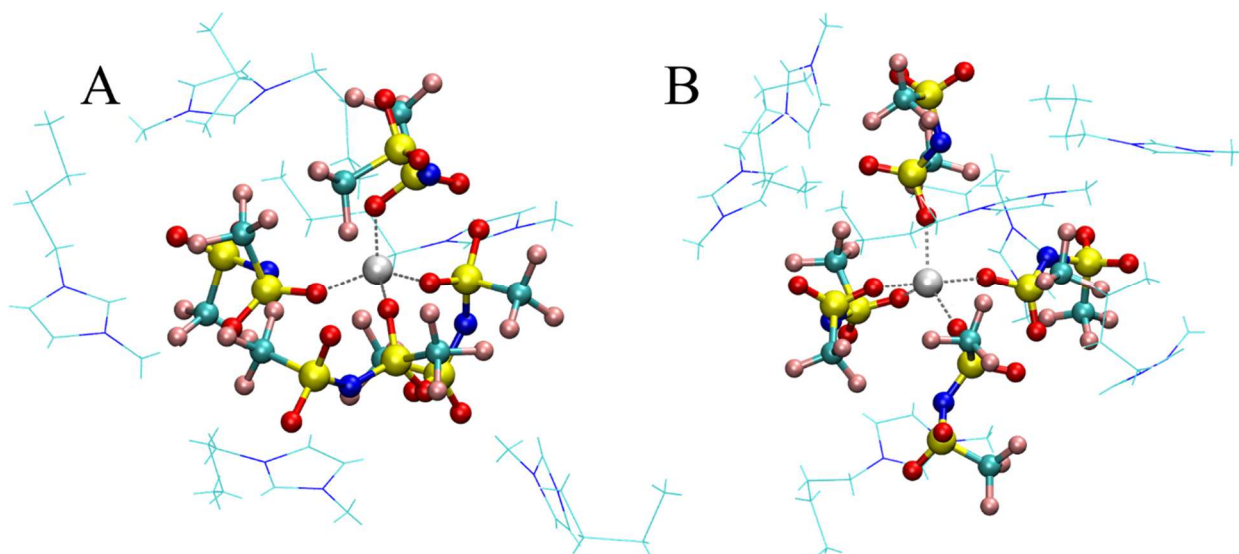


**Figure 6.11.** MD snapshots of  $\text{Ag}^+$  in  $[\text{C}_4\text{mim}][\text{Tf}_2\text{N}]$  obtained by representing the metal ion A) with the LJ parameters obtained in this work and B) from Merz *et al.* (balls and sticks:  $\text{Ag}^+$  and coordinating  $[\text{Tf}_2\text{N}]^-$ , wireframe: second shell  $[\text{C}_4\text{mim}]^+$ ).

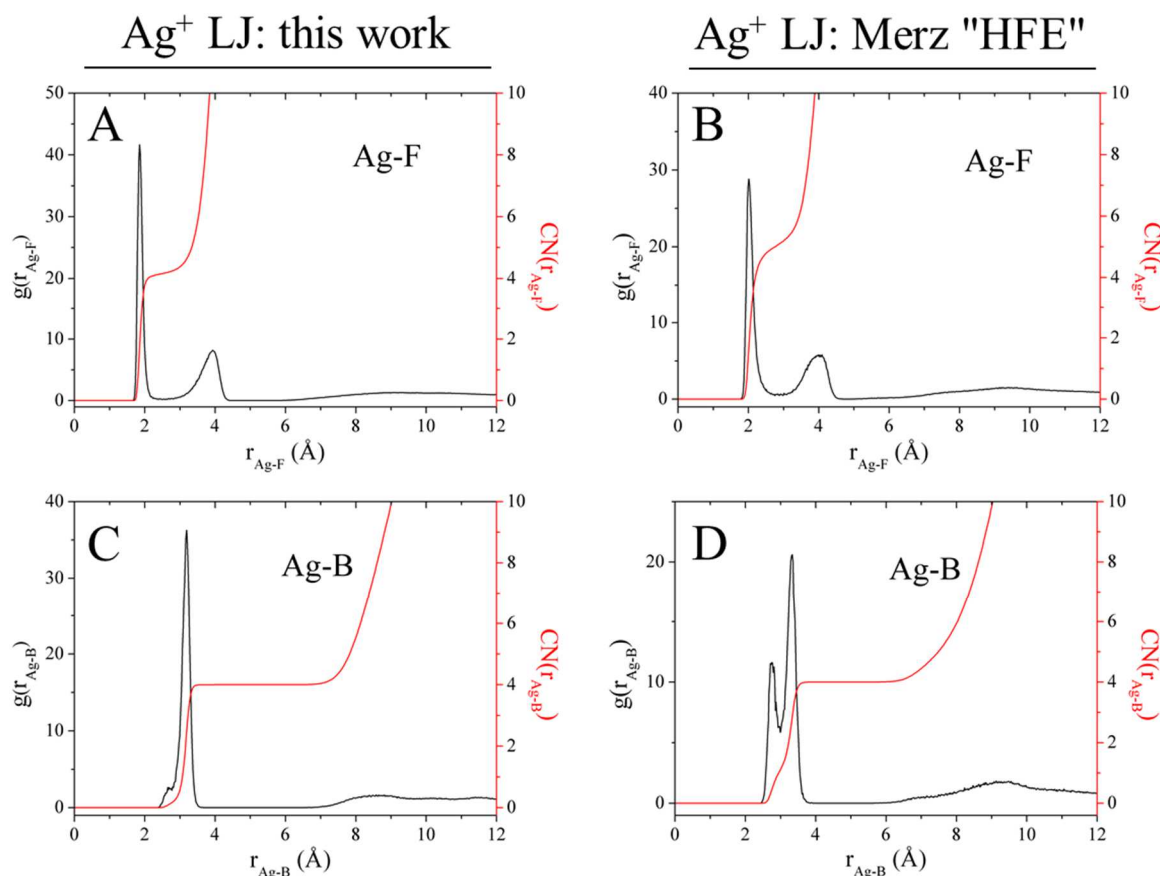


**Figure 6.12.** MD calculated  $\text{Ag-F}(\text{BF}_4)$  and  $\text{Ag-B}(\text{BF}_4)$  pairs radial distribution functions  $g(r)$ 's obtained from simulations in  $[\text{C}_4\text{mim}][\text{BF}_4]$  with LJ parameters for  $\text{Ag}^+$  obtained in this work (A and C) and from Merz *et al.* "HFE" set (B and D) (black lines, left scales). The correspondent integration numbers (red lines, right scales) are also reported.

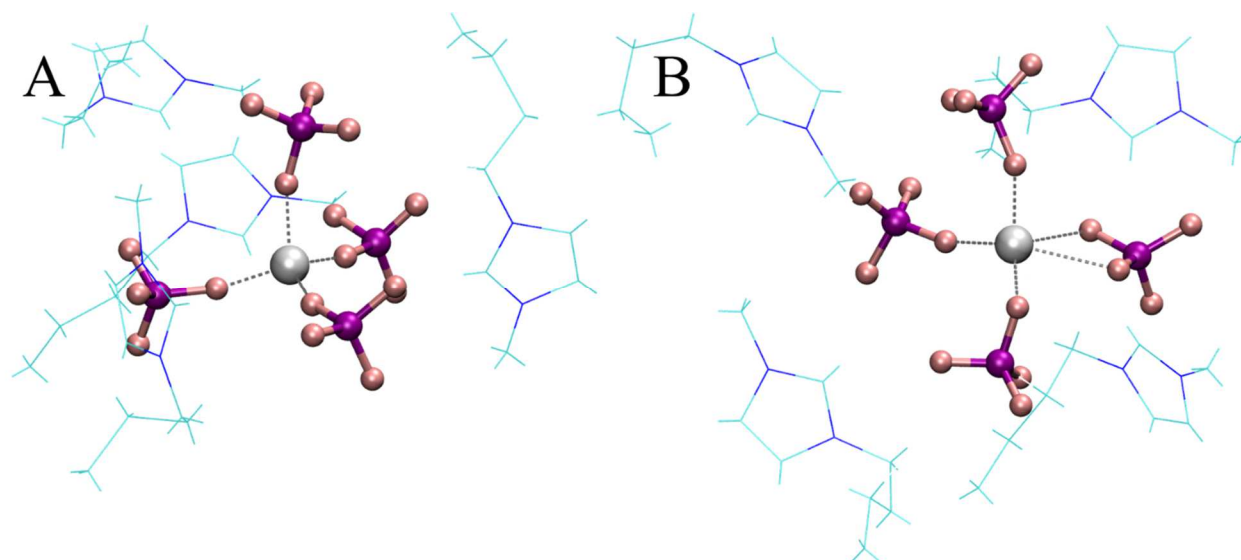


**Figure 6.13.** MD snapshots of  $\text{Ag}^+$  in  $[\text{C}_4\text{mim}][\text{BF}_4]$  obtained by representing the metal ion A) with the LJ parameters obtained in this work and B) from Merz *et al.* (balls and sticks:  $\text{Ag}^+$  and coordinating  $[\text{BF}_4]^-$ , wireframe: second shell  $[\text{C}_4\text{mim}]^+$ ).

### 6.3.2.1 Solvation thermodynamics

$\text{Ag}^+$  Gibbs free energies of solvation in  $[\text{C}_4\text{mim}][\text{Tf}_2\text{N}]$  and  $[\text{C}_4\text{mim}][\text{BF}_4]$  as well as free energies of transfer from water to the RTILs have been calculated. Also in this case, the metal ion has been represented both with LJ parameters obtained in this work and with Merz *et al* set.<sup>18</sup> The calculated values are reported in **Tab. 6.7**. As can be observed, free energies of solvation in good agreement with the experimental data (**Tab. 6.1**) are obtained for both the studied RTILs with the LJ from this work. In addition, the free energies of transfer from water to  $[\text{C}_4\text{mim}][\text{Tf}_2\text{N}]$  and  $[\text{C}_4\text{mim}][\text{BF}_4]$  result to be positive. Therefore, the picture of an  $\text{Ag}^+$  ion that is more favorably solvated in these RTILs than in water is confirmed, in agreement with the experimental data (**Tab. 6.1**). In addition,  $\Delta G_{\text{trans}}$  for  $[\text{C}_4\text{mim}][\text{BF}_4]$  is more negative than that for  $[\text{C}_4\text{mim}][\text{Tf}_2\text{N}]$ , thus MD simulations were also able to reproduce the more favorable solvation capabilities of the former RTIL in comparison with the latter.

**Table 6.7.** MD calculated Gibbs free energies of solvation in [C<sub>4</sub>mim][Tf<sub>2</sub>N] and [C<sub>4</sub>mim][BF<sub>4</sub>] ( $\Delta G_{\text{solv}}$ ) as well as transfer from water to the RTILs ( $\Delta G_{\text{trans}}$ ) obtained at T = 298.15 K and P = 1 atm for the Ag<sup>+</sup> ion. Values in kcal mol<sup>-1</sup>.

RTIL	Ag <sup>+</sup> LJ parameters	$\Delta G_{\text{solv}}$	$\Delta G_{\text{trans}}(\text{water} \rightarrow \text{RTIL})^{\text{a}}$
[C <sub>4</sub> mim][Tf <sub>2</sub> N]	This work	-125.0 ± 0.9	-7.7 ± 0.9
	Merz “HFE”	-109.1 ± 0.5	-6.5 ± 0.5
[C <sub>4</sub> mim][BF <sub>4</sub> ]	This work	-130.9 ± 0.4	-13.6 ± 0.4
	Merz “HFE”	-115.9 ± 0.4	-13.2 ± 0.4

<sup>a</sup>Gibbs free energy of transfer from water to the RTIL calculated as  $\Delta G_{\text{trans}} = \Delta G_{\text{solv}} - \Delta G_{\text{hyd}}$  with the correspondent value reported in **Tab. 6.4** for hydration.

To inspect the reasons of this favorable transfer, also the enthalpies and entropies of solvation in [C<sub>4</sub>mim][Tf<sub>2</sub>N] and [C<sub>4</sub>mim][BF<sub>4</sub>] were calculated by represented the Ag<sup>+</sup> ion with the LJ from this work. To this purpose, free energy calculations were performed for five different temperatures in each RTIL in the 300 – 400 K temperature range. The obtained  $\Delta G/T$  vs.  $1/T$  plots are shown in **Fig. 6.14**. Thanks to the data obtained for hydration with the same set of parameters (**Tab. 6.5**), also the enthalpies and entropies of transfer from water to the RTILs have been calculated and the obtained values are reported in **Tab. 6.8**. As can be observed,  $\Delta H_{\text{solv}}$  is more negative than  $\Delta H_{\text{hyd}}$  (**Tab. 6.5**) for both the RTILs and the same is found for the entropic term. As a consequence, both  $\Delta H_{\text{trans}}$  and  $\Delta S_{\text{trans}}$  are negative (**Tab. 6.8**). The enthalpic contribution seems therefore to favor the transfer of Ag<sup>+</sup> from water to [C<sub>4</sub>mim][Tf<sub>2</sub>N] and [C<sub>4</sub>mim][BF<sub>4</sub>], as was found for Zn<sup>2+</sup> and Co<sup>2+</sup>. However, differently from zinc and cobalt in [C<sub>4</sub>mim][Tf<sub>2</sub>N], the unfavorable  $\Delta S_{\text{trans}}$  is not negative enough to prevent the transfer and a favorable  $\Delta G_{\text{trans}}$  is therefore obtained (**Tab. 6.7**). The negative  $\Delta S_{\text{trans}}$  has been previously attributed to the higher order imposed by the metal ion to the RTIL phase with respect to the aqueous phase when the transfer occurs (**Sec. 4.3.1.2** of **Chapter 4** for Zn<sup>2+</sup> and **Sec. 5.3.2** of **Chapter 5** for Co<sup>2+</sup>). In addition, in a similar way to the picture obtained here, a favorable free energy of transfer caused by negative transfer enthalpy and only slight negative entropy has been found for Zn<sup>2+</sup> in [C<sub>4</sub>mim][BF<sub>4</sub>] (**Sec. 4.3.2** of **Chapter 4**). In this last case, the explanation was the less order imposed by Zn<sup>2+</sup> in the [C<sub>4</sub>mim][BF<sub>4</sub>] RTIL with respect to [C<sub>4</sub>mim][Tf<sub>2</sub>N], where the transfer was unfavorable. The only slight unfavorable  $\Delta S_{\text{trans}}$  of Ag<sup>+</sup> for both [C<sub>4</sub>mim][Tf<sub>2</sub>N] and [C<sub>4</sub>mim][BF<sub>4</sub>] could be instead be attributed to the different coordination obtained for this metal ion with respect to Zn<sup>2+</sup> and Co<sup>2+</sup> (tetrahedral instead of octahedral) and a consequent lower extent of order imposed by

the metal in the RTIL. Note that the degree of order imposed in the RTIL phase is still higher than that in water, since  $\Delta S_{\text{trans}}$  is negative.

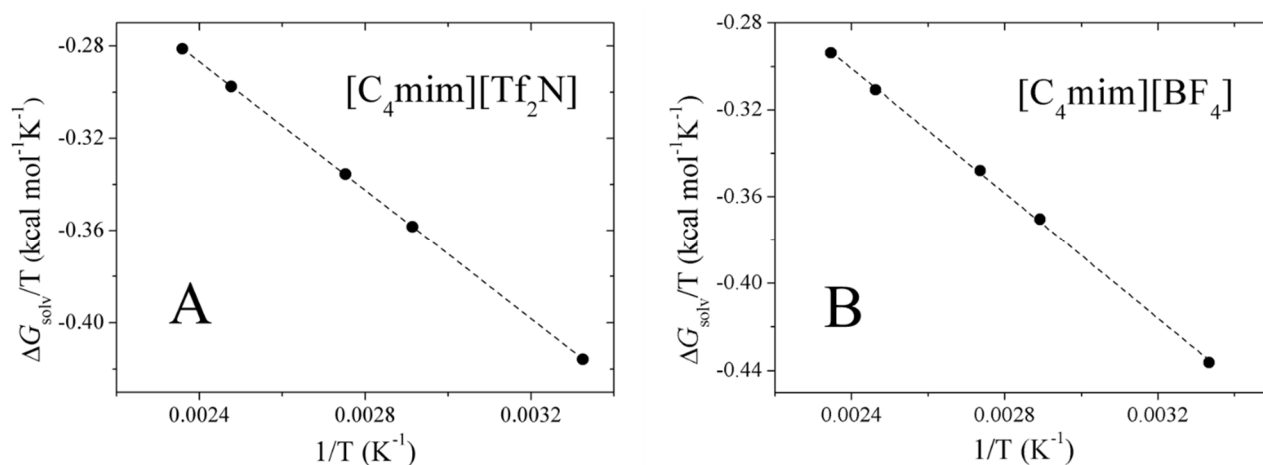


**Figure 6.14.**  $\Delta G/T$  vs.  $1/T$  plots obtained from calculated  $\text{Ag}^+$  Gibbs free energies A) in  $[\text{C}_4\text{mim}][\text{Tf}_2\text{N}]$  and B) in  $[\text{C}_4\text{mim}][\text{BF}_4]$  at different temperatures ( $R^2 = 0.99$ ).

**Table 6.8.** MD calculated enthalpy ( $\text{kcal mol}^{-1}$ ) and entropy ( $\text{kcal mol}^{-1} \text{K}^{-1}$ ) of solvation for  $\text{Ag}^+$  in  $[\text{C}_4\text{mim}][\text{Tf}_2\text{N}]$  and  $[\text{C}_4\text{mim}][\text{BF}_4]$  transfer from water to the RTILs obtained from the plots in **Fig. 6.14**.

RTIL	$\Delta H_{\text{solv}}$	$\Delta S_{\text{solv}}$	$\Delta H_{\text{trans}}(\text{water} \rightarrow \text{RTIL})^{\text{a}}$	$\Delta S_{\text{trans}}(\text{water} \rightarrow \text{RTIL})^{\text{b}}$
$[\text{C}_4\text{mim}][\text{Tf}_2\text{N}]$	$-139.3 \pm 0.3$	$-0.047 \pm 0.001$	$-13.4 \pm 0.5$	$-0.018 \pm 0.001$
$[\text{C}_4\text{mim}][\text{BF}_4]$	$-143.9 \pm 1.7$	$-0.045 \pm 0.005$	$-18.0 \pm 1.9$	$-0.016 \pm 0.005$

<sup>a</sup>Enthalpy of transfer from water to RTILs calculated as  $\Delta H_{\text{trans}}(\text{water} \rightarrow \text{RTIL}) = \Delta H_{\text{solv}} - \Delta H_{\text{hyd}}$ ; <sup>b</sup>Entropy of transfer from water to RTILs calculated as  $\Delta S_{\text{trans}}(\text{water} \rightarrow \text{RTILs}) = \Delta S_{\text{solv}} - \Delta S_{\text{hyd}}$  using the MD calculated values reported in **Tab. 6.5** for hydration.

## 6.4 Conclusions

A study about the  $\text{Ag}^+$  ion in the  $[\text{C}_4\text{mim}][\text{Tf}_2\text{N}]$  and  $[\text{C}_4\text{mim}][\text{BF}_4]$  RTILs has been carried out. As a preliminary part of this research, the hydration properties of  $\text{Ag}^+$  have been studied both from an experimental and theoretical point of view. In this respect, EXAFS and XANES data analysis performed on the X-ray absorption spectrum of  $\text{Ag}^+$  in aqueous solution seem to suggest a linear coordination of this metal ion in water. AIMD simulations with the Car-Parrinello approach confirmed this observation and provided a picture also about the second hydration sphere. However,

the simultaneous reproduction of  $\text{Ag}^+$  structural and thermodynamic hydration features in good agreement with the experimental data is found to be difficult in classical MD. In particular, when a LJ potential for the Ag-H<sub>2</sub>O interaction is employed, a compromise between the metal ion CN and average bond distance with water has to be taken into account. More complex potential forms, but still spherical, seem not to solve this issue. In this work, LJ parameters reproducing a tetrahedral coordinated  $\text{Ag}^+$  in water within good estimation of  $\Delta G_{\text{hyd}}$ , although underestimated Ag-O bond distance, have been obtained.

Classical MD simulations of  $\text{Ag}^+$  in [C<sub>4</sub>mim][Tf<sub>2</sub>N] and [C<sub>4</sub>mim][BF<sub>4</sub>] showed that thermodynamic data in good agreement with the experimental can be obtained. In particular,  $\Delta G_{\text{solv}}$  in the RTILs and  $\Delta G_{\text{trans}}$  from water to the ionic liquids have been calculated, depicting an  $\text{Ag}^+$  ion that is more favorably solvated in the RTILs than in water. Enthalpies and entropies of solvation and transfer have also been obtained by free energy calculations at different temperatures. The results showed that the transfer of  $\text{Ag}^+$  from an aqueous phase to the RTILs is favored by the enthalpic contribution, while a negative entropy of transfer is obtained. However, the latter contribute is not unfavorable enough and a negative (favorable) Gibbs free energy of transfer is obtained.

## Bibliography

- 1 U. Domańska and A. Rękawek, Extraction of metal ions from aqueous solutions using imidazolium based ionic liquids, *J. Solution Chem.*, 2009, **38**, 739–751.
- 2 K. Shimojo and M. Goto, Solvent extraction and stripping of silver ions in room-temperature ionic liquids containing calixarenes, *Anal. Chem.*, 2004, **76**, 5039–5044.
- 3 T. Liu, Y. Danten, J. Grondin and R. Vilar, Solvation of AgTFSI in 1-ethyl-3-methylimidazolium bis(trifluoromethylsulfonyl)imide ionic liquid investigated by vibrational spectroscopy and DFT calculations, *J. Raman Spectrosc.*, 2016, **47**, 449–456.
- 4 O. Bortolini, C. Chiappe, T. Ghilardi, A. Massi and C. S. Pomelli, Dissolution of Metal Salts in Bis(trifluoromethylsulfonyl)imide-Based Ionic Liquids: Studying the Affinity of Metal Cations Toward a “Weakly Coordinating” Anion, *J. Phys. Chem. A*, 2015, **119**, 5078–5087.
- 5 P. D’Angelo, V. Barone, G. Chillemi, N. Sanna, W. Meyer-Klaucke and N. V. Pavel, Hydrogen and higher shell contributions in Zn<sup>2+</sup>, Ni<sup>2+</sup>, and Co<sup>2+</sup> aqueous solutions: An X-ray absorption fine structure and molecular dynamics study, *J. Am. Chem. Soc.*, 2002, **124**, 1958–1967.
- 6 N. T. Skipper and G. W. Neilson, X-ray and neutron diffraction studies on concentrated aqueous solutions of sodium nitrate and silver nitrate, *J. Phys. Condens. Matter*, 1989, **1**, 4141–4154.
- 7 M. Sandström, G. W. Neilson, G. Johansson and T. Yamaguchi, Ag<sup>+</sup> hydration in perchlorate solution, *J. Phys. C Solid State Phys.*, 1985, **18**, L1115–L1121.
- 8 T. Yamaguchi, O. Lindqvist, J. B. Boyce and T. Claeson, Determination of the hydration structure of silver ions in aqueous silver perchlorate and nitrate solutions from EXAFS using synchrotron radiation, *Acta Chem. Scand.*, 1984, **38**, 423–428.
- 9 Y. Tsutsui, K.-I. Sugimoto, H. Wasada, Y. Inada and S. Funahashi, EXAFS and ab initio molecular orbital studies on the structure of solvated silver(I) ions, *J. Phys. Chem. A*, 1997, **101**, 2900–2905.
- 10 I. Persson and K. B. Nilsson, Coordination chemistry of the solvated silver(I) ion in the oxygen donor solvents water, dimethyl sulfoxide, and N,N'-dimethylpropyleneurea, *Inorg. Chem.*, 2006, **45**, 7428–7434.
- 11 J. L. Fulton, S. M. Kathmann, G. K. Schenter and M. Balasubramanian, Hydrated Structure of Ag ( I ) Ion from Symmetry- Dependent , K- and L-edge XAFS Multiple Scattering and

- Molecular Dynamics Simulations, *J. Phys. Chem. A*, 2009, **113**, 13976–13984.
- 12 R. Armunanto, C. F. Schwenk and B. M. Rode, Structure and Dynamics of Hydrated Ag (I): Ab Initio Quantum Mechanical-Molecular Mechanical Molecular Dynamics Simulation, *J. Phys. Chem. A*, 2003, **107**, 3132–3138.
- 13 V. Dubois, P. Archirel and A. Boutin, Monte Carlo Simulations of Ag<sup>+</sup> and Ag in Aqueous Solution. Redox Potential of the Ag<sup>+</sup>/Ag Couple, *J. Phys. Chem. B*, 2001, **105**, 9363–9369.
- 14 R. Spezia, C. Nicolas, A. Boutin and R. Vuilleumier, Molecular dynamics simulations of a silver atom in water: Evidence for a dipolar excitonic state, *Phys. Rev. Lett.*, 2003, **91**, 1–4.
- 15 R. Spezia, C. Nicolas, P. Archirel and A. Boutin, Molecular dynamics simulations of the Ag<sup>+</sup> or Na<sup>+</sup> cation with an excess electron in bulk water, *J. Chem. Phys.*, 2004, **120**, 5261–5268.
- 16 R. Vuilleumier and M. Sprik, Electronic properties of hard and soft ions in solution: Aqueous Na<sup>+</sup> and Ag<sup>+</sup> compared, *J. Chem. Phys.*, 2001, **115**, 3454–3468.
- 17 M. C. Blauth, A. B. Pribil, B. R. Randolph, B. M. Rode and T. S. Hofer, Structure and dynamics of hydrated Ag<sup>+</sup>: An ab initio quantum mechanical/charge field simulation, *Chem. Phys. Lett.*, 2010, **500**, 251–255.
- 18 P. Li, L. F. Song and K. M. Merz, Systematic parameterization of monovalent ions employing the nonbonded model, *J. Chem. Theory Comput.*, 2015, **11**, 1645–1657.
- 19 P. D'Angelo and R. Spezia, Hydration of lanthanoids(III) and actinoids(III): An experimental/theoretical saga, *Chem. - A Eur. J.*, 2012, **18**, 11162–11178.
- 20 A. Filipponi and P. D'Angelo, in *X-Ray Absorption and X-Ray Emission Spectroscopy*, John Wiley & Sons, Ltd, 2016, pp. 745–771.
- 21 M. Wilson, P. A. Madden and B. J. Costa-Cabral, Quadrupole polarization in simulations of ionic systems: Application to AgCl, *J. Phys. Chem.*, 1996, **100**, 1227–1237.
- 22 B. Ravel, Muffin-tin potentials in EXAFS analysis, *J. Synchrotron Radiat.*, 2015, **22**, 1258–1262.
- 23 M. Benfatto, S. Della Longa and C. R. Natoli, The MXAN procedure: a new method for analysing the XANES spectra of metallo-proteins to obtain structural quantitative information, *J. Synchrotron Radiat.*, 2003, **10**, 51–57.
- 24 R. Car and M. Parrinello, Unified Approach for Molecular Dynamics and Density-Functional Theory, *Phys. Rev. Lett.*, 1985, **55**, 2471–2474.
- 25 A. D. Becke, Density-functional exchange-energy approximation with correct asymptotic behavior, *Phys. Rev. A*, 1988, **38**, 3098–3100.
- 26 C. Lee, W. Yang and R. G. Parr, Development of the Colle-Salvetti correlation-energy formula into a functional of the electron density, *Phys. Rev. B*, 1988, **37**, 785–789.

- 27 S. Grimme, Semiempirical GGA-type density functional constructed with a long-range dispersion correction, *J. Comput. Chem.*, 2006, **27**, 1787–1799.
- 28 M. Sprik, J. Hutter and M. Parrinello, Ab initio molecular dynamics simulation of liquid water: Comparison of three gradient-corrected density functionals, *J. Chem. Phys.*, 1996, **105**, 1142–1152.
- 29 P. L. Silvestrelli and M. Parrinello, Structural, electronic, and bonding properties of liquid water from first principles, *J. Chem. Phys.*, 1999, **111**, 3572–3580.
- 30 N. Troullier and J. L. Martins, Efficient pseudopotentials for plane-wave calculations, *Phys. Rev. B*, 1991, **43**, 1993–2006.
- 31 J. C. Grossman, E. Schwegler, E. W. Draeger, F. Gygi and G. Galli, Towards an assessment of the accuracy of density functional theory for first principles simulations of water, *J. Chem. Phys.*, 2004, **120**, 300–311.
- 32 E. Schwegler, J. C. Grossman, F. Gygi and G. Galli, Towards an assessment of the accuracy of density functional theory for first principles simulations of water. II, *J. Chem. Phys.*, 2004, **121**, 5400–5409.
- 33 F. Sessa, P. D’Angelo and V. Migliorati, Combined distribution functions: A powerful tool to identify cation coordination geometries in liquid systems, *Chem. Phys. Lett.*, 2018, **691**, 437–443.
- 34 M. Brehm and B. Kirchner, TRAVIS - A free analyzer and visualizer for monte carlo and molecular dynamics trajectories, *J. Chem. Inf. Model.*, 2011, **51**, 2007–2023.
- 35 W. L. Jorgensen, J. Chandrasekhar, J. D. Madura, R. W. Impey and M. L. Klein, Comparison of simple potential functions for simulating liquid water, *J. Chem. Phys.*, 1983, **79**, 926.
- 36 M. J. Abraham, T. Murtola, R. Schulz, S. Páll, J. C. Smith, B. Hess and E. Lindah, Gromacs: High performance molecular simulations through multi-level parallelism from laptops to supercomputers, *SoftwareX*, 2015, **1–2**, 19–25.
- 37 J. N. Canongia Lopes, A. A. H. Padua and J. Dechamps, Modeling ionic liquids using a systematic all-atom force field, *J. Phys. Chem. B*, 2004, **108**, 2038–2047.
- 38 J. N. Canongia Lopes, A. A. H. Padua and J. Dechamps, Additions and corrections., *J. Phys. Chem. B*, 2004, **108**, 11250.
- 39 J. N. Canongia Lopes and A. A. H. Padua, Molecular Force Field for Ionic Liquids Composed of Triflate or Bistriflyimide Anions, *J. Phys. Chem. B*, 2004, **108**, 16893–16898.
- 40 Z. Liu, S. Huang and W. Wang, A refined force field for molecular simulation of imidazolium-based ionic liquids, *J. Phys. Chem. B*, 2004, **108**, 12978–12989.
- 41 P. D’Angelo, M. Benfatto, S. Della Longa and N. V. Pavel, Combined XANES and EXAFS

- analysis of  $\text{Co}^{2+}$ ,  $\text{Ni}^{2+}$ , and  $\text{Zn}^{2+}$  aqueous solutions, *Phys. Rev. B - Condens. Matter Mater. Phys.*, 2002, **66**, 642091–642097.
- 42 G. Chillemi, P. D'Angelo, N. V. Pavel, N. Sanna and V. Barone, Development and validation of an integrated computational approach for the study of ionic species in solution by means of effective two-body potentials. The case of  $\text{Zn}^{2+}$ ,  $\text{Ni}^{2+}$ , and  $\text{Co}^{2+}$  in aqueous solutions, *J. Am. Chem. Soc.*, 2002, **124**, 1968–1976.
- 43 P. D'Angelo, V. Migliorati, F. Sessa, G. Mancini and I. Persson, XANES reveals the flexible nature of hydrated strontium in aqueous solution, *J. Phys. Chem. B*, 2016, **120**, 4114–4124.
- 44 Y. Marcus, Thermodynamics of Solvation of Ions, *J. Chem. Soc., Faraday Trans.*, 1991, **87**, 2995–2999.
- 45 S. Ahrland, Solvation and Complex Formation-Competing and Cooperative Processes in Solution, *Pure Appl. Chem.*, 1982, **54**, 1451–1468.
- 46 Y. Marcus and A. Loewenschuss, Standard Entropies of Hydration of Ions, *A. Annu. Rep. Prog. Chem. Sect. C Phys. Chem.*, 1984, **81**, 81–135.



# Appendix A

## *Ab initio* generation of Ag<sup>+</sup>-H<sub>2</sub>O interaction potential

### A.1 Method

An *ab initio* fitting of the interaction potential between the Ag<sup>+</sup> ion and water has been carried out with the method proposed by Floris *et al.*<sup>1,2</sup> and more recently employed by other authors also for divalent transition metal ions in aqueous solution.<sup>3</sup> This method mainly consists in the calculation of an effective pair potential between the metal and one water molecule, with the effect induced by the remaining of the solvent taken into account by an implicit solvation model. The main advantage is that this does not need *a priori* knowledge about the number of molecules coordinating the metal ion, *i.e.* of the experimental coordination number.

This Ag<sup>+</sup>-H<sub>2</sub>O potential ( $V_{Agw}$ ) can be expressed as:

$$V_{Agw} = \langle \psi | \hat{H}^0 | \psi \rangle_{Agw} - \langle \psi | \hat{H}^0 | \psi \rangle_{Ag} - \langle \psi | \hat{H}^0 | \psi \rangle_w \quad (\text{A.1})$$

where  $\psi$  is the wave function perturbed by the solvent represented by the solvation model (CPCM in this case),<sup>4,5</sup> while the three Hamiltonians  $\hat{H}^0$  are referred to respectively the Ag-H<sub>2</sub>O cluster, the solely Ag<sup>+</sup> ion and to the water molecule in gas phase. This potential has been calculated for different configurations of the Ag-H<sub>2</sub>O dimer. In particular, a potential energy surface (PES) scan of the energies along the Ag-O(H<sub>2</sub>O) distance  $r_{AgO}$  from 1.2 to 12.0 Å every 0.02 Å has been carried out for variable Ag-Ô-H angles  $\theta$  (**Fig. A.1**) from 35° to 125° every 10°, for a total of 4860 grid points. Energies more repulsive than 30 kcal mol<sup>-1</sup> were not taken into account in the fitting.

Water geometry has been kept fixed to the SPC/E model,<sup>6</sup> since it has been successively employed for the MD simulations. In a first step, single-point energy calculations on the water molecule with different quantum-mechanical levels of theory have been carried out to verify which one was able to best reproduce water partial charges in agreement with the SPC/E model.

A central issue in Floris' method was also explored, that is the optimization of the effective radii of the implicit solvation model. In this work, standard CPCM radii for hydrogen and oxygen were employed, while the radius for Ag<sup>+</sup> ( $\rho_{Ag}$ ) was optimized. This has been carried out by running two

sets of simulations on the  $[\text{AgH}_2\text{O}]^+$  and  $[\text{Ag}(\text{H}_2\text{O})_2]^+$  clusters for different radii, to find the value that satisfied the following equation:

$$V_{wAgw} = 2V_{Agw} + V_{ww} \quad (\text{A.2})$$

where

$$V_{wAgw} = \langle \psi | \hat{H}^0 | \psi \rangle_{wAgw} - \langle \psi | \hat{H}^0 | \psi \rangle_{Ag} - 2 \langle \psi | \hat{H}^0 | \psi \rangle_w \quad (\text{A.3})$$

$V_{wAgw}$  is referred to the  $[\text{Ag}(\text{H}_2\text{O})_2]^+$  cluster, while  $V_{ww}$  is the water-water potential without the effect of the electric field of the ion and  $V_{Agw}$  is defined as in **Eq. A.1**. Both sides of **Eq. A.2** depend upon  $\rho_{Ag}$ , but taking into account that  $V_{Agw}$  is much more sensitive to the radius than  $V_{wAgw}$ , the equation is satisfied only for a specific value of  $\rho_{Ag}$ .

The Ag-H<sub>2</sub>O energies obtained from the potential scans were fitted with the following 4-6-8-12 potential form:

$$V_{Ag-H_2O} = f \frac{q_{Ag}q_O}{r_{AgO}} + \frac{A_O}{r_{AgO}^4} + \frac{B_O}{r_{AgO}^6} + \frac{C_O}{r_{AgO}^8} + \frac{D_O}{r_{AgO}^{12}} + \sum_{H=H_1, H_2} f \frac{q_{Ag}q_H}{r_{AgH}} + \frac{A_H}{r_{AgH}^4} + \frac{B_H}{r_{AgH}^6} + \frac{C_H}{r_{AgH}^8} + \frac{D_H}{r_{AgH}^{12}} \quad (\text{A.4})$$

where  $r_{AgO}$  and  $r_{AgH}$  are the ion-water distances (the second term containing distances for the two different hydrogen atoms),  $q_{Ag}$ ,  $q_O$  and  $q_H$  are the electrostatic charges and  $A_O$ ,  $B_O$ , ...  $D_H$  the fitted parameters. During the fitting, water charges have been kept fixed to the SPC/E model, while  $q_{Ag}$  was equal to 1. The quality of the fitting was assessed by comparing *ab initio* energies with those obtained by the fitting.

The obtained Ag-H<sub>2</sub>O interaction potential was implemented in the DLPOLY 2 package for classical MD simulations.<sup>7</sup> A box with one Ag<sup>+</sup> ion and 500 SPC/E waters was initially minimized, then an NVT simulation at 298.15 K was run for 1.5 ns with 1 fs time step and coordinates were saved every 100 frames. The first 500 ps were discarded as equilibration time. Temperature was kept constant with the Nosé-Hoover thermostat<sup>8,9</sup> with 0.5 ps relaxation constant. A cut-off of 12 Å was employed for all non-bonded interactions with long-range electrostatics taken into account with the PME method.<sup>10,11</sup> Bonds involving hydrogen atoms were constrained with the SHAKE algorithm.<sup>12</sup>

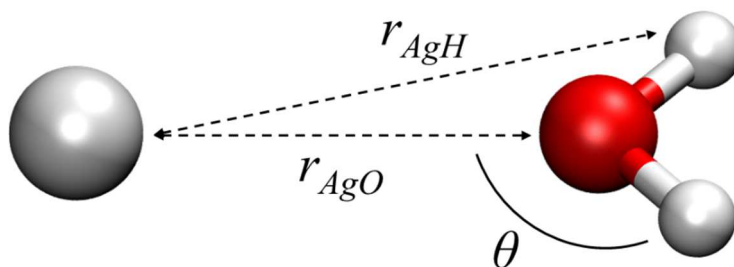


**Figure A.1.** Geometrical parameters definition for the Ag-H<sub>2</sub>O cluster employed to generate the interaction potential. The Ag- $\hat{O}$ -H angle  $\theta$  is defined in the plane containing Ag<sup>+</sup>, O and the considered H atom.

## A.2 Results

The calculated CHelpG charges for the water oxygen and hydrogen atoms at different levels of theory are reported in **Tab. A.1**. Since the set that provided the closest partial charges to those of the SPC/E model resulted to be B3LYP/6-311++G(*d,p*), these functional and basis set were employed in the subsequent generation of the *ab initio* potential.

**Table A.1.** Calculated CHelpG charges for water oxygen and hydrogen atoms obtained at different levels of theory compared with charges from the SPC/E water model.

	$q_O$ (au)	$q_H$ (au)
SPC/E	-0.848	0.424
MP2/6-311++G( <i>d,p</i> )	-0.898	0.449
MP2/cc-PVTZ	-0.823	0.412
B3LYP/6-311++G( <i>d,p</i> )	-0.870	0.435
B3LYP/cc-PVTZ	-0.783	0.391

In addition, Ag<sup>+</sup> CPCM radius was optimized as previously described. The evolution of the two members of **Eq. A.2** is plotted as a function of the effective radius  $\rho_{Ag}$  in **Fig. A.2**. The two curves intersect for  $\rho_{Ag} = 1.80 \text{ \AA}$ , therefore this value for Ag<sup>+</sup> CPCM radius was employed for the generation of the effective pair potential.

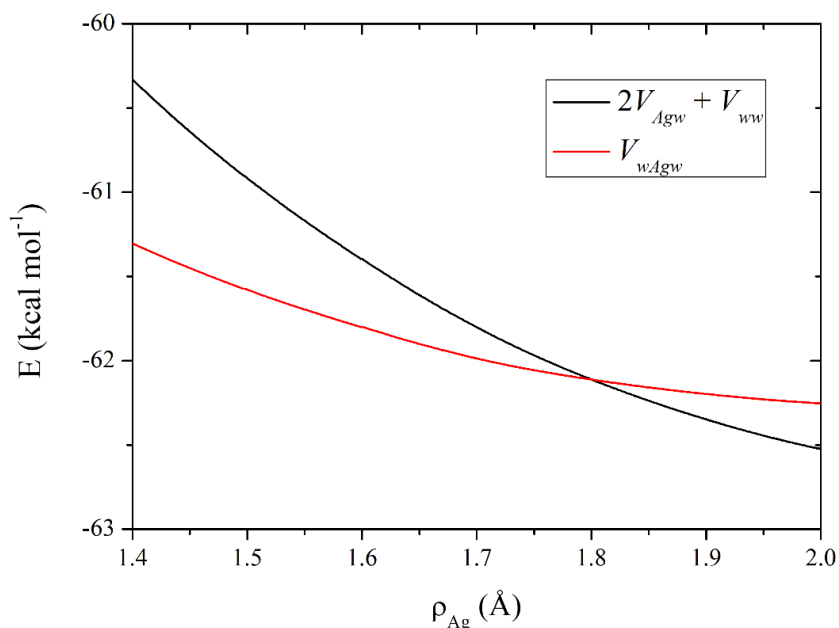


**Figure A.2.** CPCM cavity radius optimization curves for the  $\text{Ag}^+$  ion. The  $2V_{Agw} + V_{ww}$  (black line) and  $V_{wAgw}$  (red line) energies are plotted as a function of the effective radius  $\rho_{Ag}$ .

The fitting of the potential energy including all the studied configurations is reported in **Fig. A.3** together with the comparison between DFT calculated and fitted energies. The standard deviation between the two sets of energies resulted to be  $2.7 \text{ kcal mol}^{-1}$ . The obtained parameters for the 4-6-8-12 potential are reported in **Tab. A.2**.

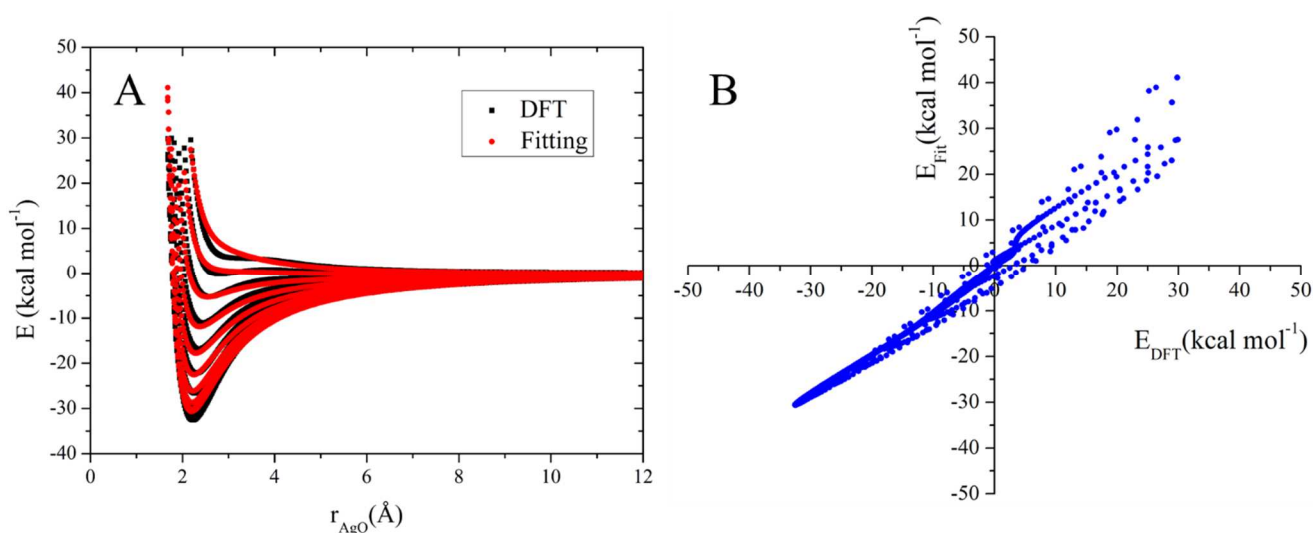


**Figure A.3.** A)  $\text{Ag}^+$ - $\text{H}_2\text{O}$  interaction energy curves vs. the ion-oxygen ( $r_{AgO}$ ) distance. All the curves for the various configurations with different  $\text{Ag}-\hat{\text{O}}-\text{H}$  angles  $\theta$  are reported (black dots: DFT calculated energies, red dots: energies from the fitted potential). B) Fitted vs. DFT calculated energies for the  $\text{Ag}^+$ - $\text{H}_2\text{O}$  pair potential.

**Table A.2.** Fitted parameters for the Ag-H<sub>2</sub>O 4-6-8-12 interaction potential.

Parameter	Value (kcal mol <sup>-1</sup> )
A <sub>O</sub>	$-4.995 \times 10^2$
B <sub>O</sub>	$1.519 \times 10^{-2}$
C <sub>O</sub>	$9.117 \times 10^3$
D <sub>O</sub>	$9.361 \times 10^{-5}$
A <sub>H</sub>	$3.272 \times 10^2$
B <sub>H</sub>	$-1.749 \times 10^3$
C <sub>H</sub>	$3.483 \times 10^3$
D <sub>H</sub>	$-3.916 \times 10^3$

An MD simulation of Ag<sup>+</sup> in 500 SPC/E water molecules has been carried out by employing the 4-6-8-12 potential of **Eq. A.4** for the Ag<sup>+</sup>-H<sub>2</sub>O interaction with the parameters obtained from the *ab initio* fitting (**Tab. A.2**). The results for Ag<sup>+</sup> first hydration shell obtained from the Ag-O  $g(r)$  (**Fig. A.4 A**) report a silver ion as coordinated by 6.0 water molecules at an average distance of 2.31 Å. This indicates the formation of an octahedral species, as can also be observed from the MD snapshot reported in **Fig. A.4 B**. Therefore, the obtained potential is able to reproduce the Ag-O average bond distance in good agreement with that determined by the EXAFS analysis (**Chapter 6**), but a high CN very far to that determined by the XAS data fitting is also obtained.

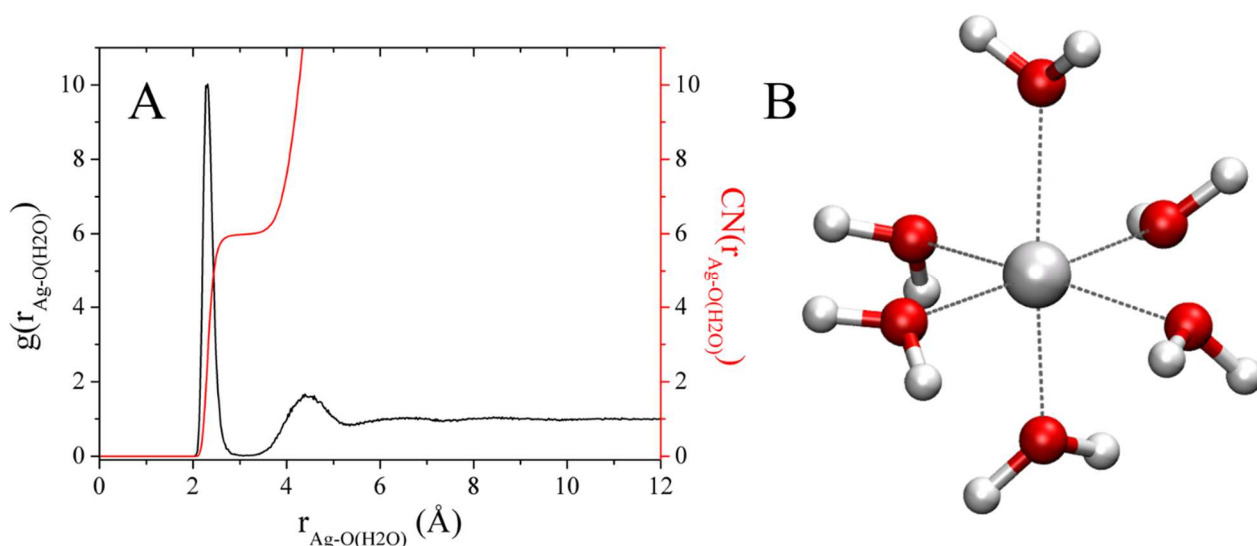


**Figure A.4.** A) Ag-O(H<sub>2</sub>O) pair  $g(r)$  radial distribution function (black line, left scale) and corresponding integration number (red line, right scale) within B) MD snapshot obtained from the simulation of Ag<sup>+</sup> in water with the fitted *ab initio* potential.

### A.3 Conclusions

The generation of a new Ag-H<sub>2</sub>O interaction potential for classical MD was carried out by means of a fitting procedure performed on *ab initio* calculations. As regards Ag<sup>+</sup> coordination, the new potential was able to reproduce the Ag-O bond distance in good agreement with the experimental data, but an overestimated CN was also obtained. This circumstance could arise from the nature of the PES generation, carried out on a Ag-H<sub>2</sub>O cluster and being therefore independent from any imposed CN. However, it could be also a proof that interaction potentials more complex than the LJ form, but still spherical, are not able to reproduce particular anisotropic coordinations like the linear case.

# Bibliography

- 1 F. Floris, M. Persico, A. Tani and J. Tomasi, Free energies and structures of hydrated cations, based on effective pair potentials, *Chem. Phys.*, 1995, **195**, 207–220.
- 2 F. Floris, M. Persico, A. Tani and J. Tomasi, Ab initio effective pair potentials for simulations of the liquid state, based on the polarizable continuum model of the solvent, *Chem. Phys. Lett.*, 1992, **199**, 518–524.
- 3 G. Chillemi, P. D'Angelo, N. V. Pavel, N. Sanna and V. Barone, Development and validation of an integrated computational approach for the study of ionic species in solution by means of effective two-body potentials. The case of Zn<sup>2+</sup>, Ni<sup>2+</sup>, and Co<sup>2+</sup> in aqueous solutions, *J. Am. Chem. Soc.*, 2002, **124**, 1968–1976.
- 4 V. Barone and M. Cossi, Quantum Calculation of Molecular Energies and Energy Gradients in Solution by a Conductor Solvent Model, *J. Phys. Chem. A*, 1998, **102**, 1995–2001.
- 5 M. Cossi, N. Rega, G. Scalmani and V. Barone, Energies, structures, and electronic properties of molecules in solution with the C-PCM solvation model, *J. Comput. Chem.*, 2003, **24**, 669–681.
- 6 H. J. C. Berendsen, J. R. Grigera and T. P. Straatsma, The missing term in effective pair potentials, *J. Phys. Chem.*, 1987, **91**, 6269–6271.
- 7 W. Smith, C. W. Yong and P. M. Rodger, DL\_POLY: Application to molecular simulation, *Mol. Simul.*, 2002, **28**, 385–471.
- 8 S. Nosé, A molecular dynamics method for simulations in the canonical ensemble, *Mol. Phys.*, 1984, **52**, 255–268.
- 9 W. G. Hoover, Canonical dynamics: Equilibrium phase-space distributions, *Phys. Rev. A*, 1985, **31**, 1695–1697.
- 10 T. Darden, D. York and L. Pedersen, Particle mesh Ewald: An Nlog(N) method for Ewald sums in large systems, *J. Chem. Phys.*, 1993, **98**, 10089.
- 11 U. Essmann, L. Perera, M. L. Berkowitz, T. Darden, H. Lee and L. G. Pedersen, A smooth particle mesh Ewald method, *J Chem Phys*, 1995, **103**, 8577–8593.
- 12 J.-P. Ryckaert, G. Ciccotti and H. J. C. Berendsen, Numerical integration of the cartesian equations of motion of a system with constraints: molecular dynamics of n-alkanes, *J. Comput. Phys.*, 1977, **23**, 327–341.



# Appendix B

## Zn<sup>2+</sup> ion in [C<sub>2</sub>mim][Tf<sub>2</sub>N]: adding explicit polarizability

### B.1 Introduction

Although the employment of non-polarizable force fields has provided very useful knowledge in the study of RTILs, in the last years the challenge of the inclusion of explicit many-body polarizability has been thrown.<sup>1,2</sup> This necessity arose from the observation that many popular non-polarizable force fields tend to underestimate some dynamical properties like the diffusion coefficients of the ions, while viscosities are overestimated even of one order of magnitude and conductivities are underestimated. The inclusion of polarizability, that some authors have referred to as an “inner solvent” or “lubricant”,<sup>3</sup> should be able to tackle these issues.

Actually, the effect induced by polarizability can be introduced also by refining non-polarizable models. For example, in their pioneering work, Ludwig *et al.*<sup>4</sup> re-parametrized many of the LJ terms of CL&P<sup>4</sup> and obtained a more accurate description of cations and anions self-diffusion coefficients in comparison with the experimental. This should be possible in principle because LJ terms already account implicitly for induction coming from parametrization on empirical data.<sup>5</sup> Another simple solution, often referred to as the “poor man’s way”,<sup>6</sup> is charges rescaling. This method takes its origin from the observation that ionic net charges of non-isolated ions of RTILs were found to be reduced as showed by *ab initio* calculations.<sup>7-9</sup> Both charge-transfer and polarization effects should be responsible for this phenomenon, but discriminating between them seems to be a difficult challenge.<sup>1</sup> Typical re-scaled values for the RTIL cation and anion are comprised between +/- 0.7 and 0.9 *e*. For RTILs, this strategy of including polarizability has been observed to yield good improvement on collective properties.<sup>6</sup> However, to obtain a more accurate description of local interactions, an explicit inclusion of many-body polarizability seems somewhat mandatory. This seems to be particularly true when the computation of thermodynamic quantities (*e.g.*  $\Delta G_{\text{solv}}$ ) of small solutes in RTILs is required, as was shown in a recent work for CO<sub>2</sub> and NH<sub>3</sub> in [C<sub>4</sub>mim][BF<sub>4</sub>].<sup>10</sup> In addition, carbon dioxide and ammonia can be considered in first approximation as vdW-interacting solutes, but it seems legit to suppose that for metal ions, where the electrostatic contribution to  $\Delta G_{\text{solv}}$  is massive (see **Sec. 4.3.1.2** of **Chapter 4**), this could be even more important.

Many methods have been proposed for the introduction of many-body polarizability in RTILs. For example, in the polarizable ion model (PIM), the interaction potential for the non-bonded part is described as following:<sup>11</sup>

$$V = \sum_{i < j} \left( f \frac{q_i q_j}{\epsilon_r r_{ij}} + A^{ij} e^{-b^{ij} r^{ij}} - f_6^{ij} \frac{C_6^{ij}}{r_{ij}^6} - f_8^{ij} \frac{C_8^{ij}}{r_{ij}^8} \right) + V_{pol} \quad (\text{B.1})$$

Here the first term corresponds to a normal Coulomb interaction among fixed charges, while the following terms are represented by a Born-Huggins-Mayer type potential accounting for repulsion and dispersion.  $C_6^{ij}$  and  $C_8^{ij}$  are the dipole-dipole and dipole-quadrupole dispersion coefficients and the  $f_n^{ij}$  terms are the Tang-Toennies damping functions<sup>12</sup> aimed at avoiding short-range penetration effects and the so-called ‘‘polarization catastrophe’’. They take the form:

$$f_n^{ij}(r^{ij}) = 1 - e^{-b_n^{ij} r^{ij}} \sum_{k=0}^n \frac{(b_n^{ij} r^{ij})^k}{k!} \quad (\text{B.2})$$

with the  $b_n^{ij}$  parameter setting the range of the damping. Instead, the  $V_{pol}$  term in the potential reads:

$$V_{pol} = \sum_{i,j} \left[ (q^i \mu_\alpha^j g^{ij}(r_{ij}) \mathbb{T}_\alpha^{ij} - q^j \mu_\alpha^i g^{ji}(r_{ij}) \mathbb{T}_\alpha^{ij} - \mu_\alpha^i \mu_\beta^j \mathbb{T}_{\alpha\beta}^{ij} \right] + \sum_i \frac{1}{2\alpha_i} \mu_i^2 \quad (\text{B.3})$$

where  $\mathbb{T}_\alpha$  and  $\mathbb{T}_{\alpha\beta}$  are respectively the charge-dipole and dipole-dipole tensors, while  $\alpha_i$  is the isotropic polarizability of atom  $i$ . The entity of the  $\mu^i$  induced dipoles is determined at each time step by minimizing the total polarization potential. Tang-Toennies functions  $g^{ij}$  are again introduced, but here they are expressed as:

$$g^{ij}(r^{ij}) = 1 - c^{ij} e^{-b_n^{ij} r^{ij}} \sum_{k=0}^n \frac{(b_n^{ij} r^{ij})^k}{k!} \quad (\text{B.4})$$

Note that these functions differ from the previously defined in **Eq. B.2** only for the parameter  $c_{ij}$ . The PIM model was successfully employed for the  $[\text{C}_2\text{mim}][\text{AlCl}_4]$  ionic liquid.<sup>11</sup> Besides this method, a more serial parametrization of polarizable force fields for RTILs were carried out also by other authors. One of the first polarizable force fields for a huge amount of RTILs cations and anions

was proposed by O. Borodin.<sup>13</sup> Here the non-bonded part is very similar to the PIM model, with the exception that Tang-Toennies functions are replaced by Thole screening<sup>14</sup> to smear induced dipoles at short distances:

$$T_{ij}(r_{ij}) = 1 - \left(1 + \frac{ar_{ij}}{2^6 \sqrt{\alpha_i \alpha_j}}\right) e^{-\frac{ar_{ij}}{\sqrt[6]{\alpha_i \alpha_j}}} \quad (\text{B.5})$$

Thole function depends on the polarizabilities of the two centers and by the  $a$  parameter that is fixed for all the interactions.

Another recent polarizable force field for several RTILs was proposed by Yethiraj *et al.*<sup>15,16</sup> Here the authors accounted for polarizability by means of Drude oscillators, consisting in particles with a partial charge and a small mass attached to a core atom by a harmonic bond. Their displacement with respect to the reference atom is determined at each time step and mimics the effect of an induced dipole.<sup>6</sup> This strategy was recently employed also by A. Padua<sup>5</sup> in the insertion of polarization in the popular CL&P force field. The bonded part of the original potential set is preserved, but the interesting point is that a LJ potential is still employed for the vdW part. Here the author re-scaled the  $\epsilon$  parameters from the non-polarizable set, since they implicitly already account for induction as previously said.

In this work, the CL&P polarizable force field<sup>5</sup> was employed in the study of  $\text{Zn}^{2+}$  in  $[\text{C}_2\text{mim}][\text{Tf}_2\text{N}]$ . Preliminary results are presented by showing the different strategies that have been employed to represent the Zn-RTIL interaction with the aim of reproducing the experimental coordination of the metal ion in solution.<sup>17</sup> This work has to be considered a very first step aimed at setting-up an interaction potential to perform also thermodynamic calculations of metal ions in RTILs with the inclusion of polarizability.

## B.2 Methods and Results

In a first part of the study, the CL&P polarizable force field was implemented in the “Metalwalls” in-house code for classical MD simulations developed by the PHENIX group (Physicochimie des Electrolytes et Nanosystèmes interfaciaux – Sorbonne Université, CNRS). Drude particles and Thole screening of the original force field were translated into the PIM model employing explicit dipoles for polarizability and Tang-Toennies functions for short-range correction. The  $c_{ij}$  values of **Eq. B.4** were set to 1 to coincide with Thole screening at the origin, while  $b_n^{ij}$  parameters were fitted for each

interacting couple to obtain the best matching between the two functions. The reproducibility of the force field in the new code was validated by checking forces acting on each atom in a box of 125 [C<sub>2</sub>mim]<sup>+</sup> cations and 125 [Tf<sub>2</sub>N]<sup>-</sup> anions.

In a second part, one Zn<sup>2+</sup> ion was introduced in a cubic box consisting of 123 [C<sub>2</sub>mim]<sup>+</sup> cations and 123 [Tf<sub>2</sub>N]<sup>-</sup> anions with a 37.58 Å side length chosen to reproduce pure RTIL density. In a first try, Zn<sup>2+</sup> was represented with Merz and Li<sup>18</sup> LJ parameters already employed for simulations with the non-polarizable model (**Chapter 4**). In this case, the vdW interaction between Zn<sup>2+</sup> and the RTIL acts only via LJ potential, but the ionic liquid is polarized by the RTIL-RTIL interaction and by the net charge of the metal ion. An NVT run was carried out by equilibrating the system at 700 K and then cooling back at 300 K. The Velocity-Verlet algorithm<sup>19</sup> was employed to propagate the equations of motion with a time step of 1 fs, while temperature was kept constant with the Nosé-Hoover thermostat.<sup>20,21</sup> A cut-off of 10 Å was used for long-range non-bonded interactions, with Ewald summation<sup>22</sup> employed for the electrostatic part. As a result, this interaction potential gave rise to a coordination very different to that found experimentally. In particular, some [Tf<sub>2</sub>N]<sup>-</sup> anions were found to coordinate the metal with two oxygen atoms coming from the same -SO<sub>2</sub> moiety and also fluorine coordination was observed.

Given the poor results provided by literature LJ parameters for this case, a different strategy was tried to describe the Zn-RTIL interaction. In particular, an *ab initio* fitting of the Zn-RTIL interaction potential was carried out. To this purpose, a classical MD simulation with non-polarizable CL&P was carried out on a smaller box of 1 Zn<sup>2+</sup>, 14 [C<sub>4</sub>mim]<sup>+</sup> and 16 [Tf<sub>2</sub>N]<sup>-</sup> anions. From the result of this simulation, 20 configurations were collected and on each of them a wave-function optimization was carried out with the plane-wave DFT package CPMD.<sup>23</sup> The BLYP functional<sup>24,25</sup> was employed along with Norm-Conserving Martin-Troullier pseudo potentials<sup>26</sup> for all the atoms with a 80 Ry cutoff for plane waves. Grimme's empirical corrections for dispersion were also taken into account.<sup>27</sup> Forces acting on Zn<sup>2+</sup> were then collected and a force-matching fitting procedure was carried out. To this purpose, a screening of Zn<sup>2+</sup> LJ parameters was performed by varying  $\sigma$  from 1.5 to 4 Å and  $\epsilon$  from 0.001 to 1 kJ mol<sup>-1</sup>. For each couple of parameters, the agreement between DFT-calculated forces acting on Zn<sup>2+</sup> and those calculated with the MD code including polarizability for the RTIL was calculated by a mean-square relative error  $\chi^2$ . The obtained map is reported in **Fig. B.1**.

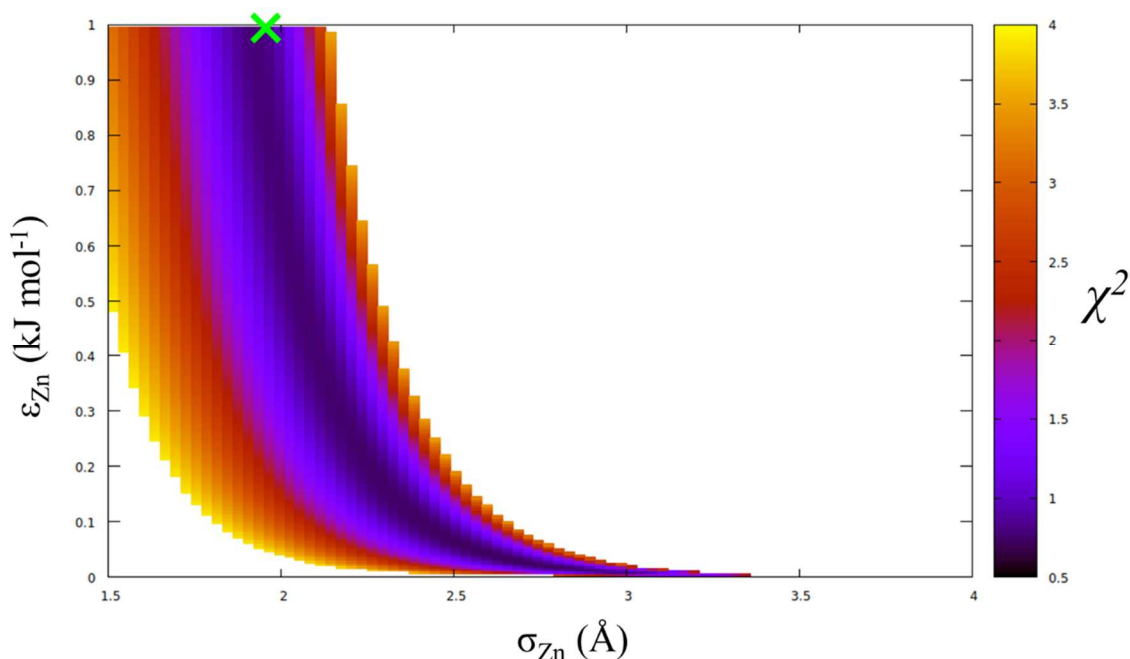


**Figure B.1.** Mean-square relative error  $\chi^2$  calculated between the atomic forces acting on  $\text{Zn}^{2+}$  at DFT level and in the polarizable MD simulation at dependence of  $\text{Zn}^{2+}$  LJ parameters. The position of the chosen set is indicated by the green cross.

The plot shows that the minimum value ( $\sim 0.5$ ) of  $\chi^2$  is obtained for different equivalent couples of LJ parameters. Therefore,  $\sigma = 1.92 \text{ \AA}$  and  $\epsilon = 1.0 \text{ kJ mol}^{-1}$  were arbitrary chosen among these values. An NVT run was then performed by representing  $\text{Zn}^{2+}$  with this LJ set in the polarizable RTIL. The system was equilibrated at 700 K for 5 ns and then cooled back and simulated at 300 K for 1 ns. Structural data of the metal first solvation shell were obtained from the Zn-O( $\text{Tf}_2\text{N}$ ) and Zn-N( $\text{Tf}_2\text{N}$ )  $g(r)$ 's shown in **Fig. B.2**. The results are reported in **Tab. B.1**. Surprisingly, also in this case the coordination resulted to be unusual. As can be observed, the Zn-O  $g(r)$  shows a first intense peak at  $2.07 \text{ \AA}$  from the metal ion integrating 4.0 oxygens, but the Zn-N distribution also shows a peak at  $2.05 \text{ \AA}$  integrating 2.0 atoms. Therefore, nitrogen coordination was observed. Taking into account that pure oxygen coordination has been reported experimentally by means of XAS data,<sup>17</sup> also this strategy was discarded.

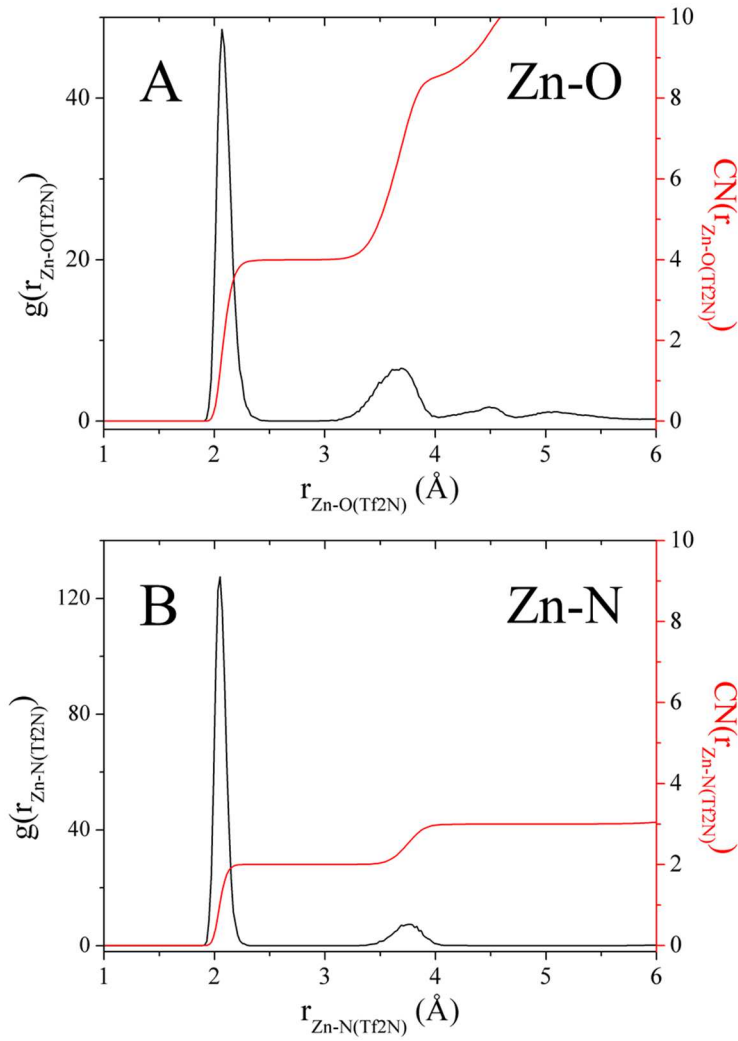


**Figure B.2.** Zn-O(Tf<sub>2</sub>N) and Zn-N(Tf<sub>2</sub>N) pairs  $g(r)$ 's obtained for Zn<sup>2+</sup> in [C<sub>2</sub>mim][Tf<sub>2</sub>N] by representing the RTIL with CL&P polarizable force field and the metal ion with LJ parameters from the *ab initio* fitting procedure.

As a last try, parameters for Zn<sup>2+</sup> were taken from a recent work by Borodin *et al.*,<sup>28</sup> where the authors carried out polarizable MD simulations in RTILs of some alkali and transition metal ions, including Zn<sup>2+</sup>. In this work, the authors employed the following interaction potential for the repulsion and dispersion energy terms:

$$V_{vdW} = \sum_{i,j} A_{ij} e^{-B_{ij} r_{ij}} - \frac{C_{ij}}{r_{ij}^6} + D \left( \frac{12}{B_{ij} r_{ij}} \right)^{12} \quad (\text{B.6})$$

In our case, the third term of **Eq. B.6** was set to zero for the Zn-RTIL interaction, providing essentially a Buckingham potential (**Eq. 3.13** of **Chapter 3**). Successively, different NVT runs were carried out

by manually varying the B parameter to match the experimental bond distance between  $\text{Zn}^{2+}$  and  $[\text{Tf}_2\text{N}]^-$  coordinating oxygen atoms.<sup>17</sup> A good match was found after increasing  $B_{ij}$  of 2.5% for each pair interaction. An NVT run was then performed with this potential by equilibrating the system at 700 K for 10 ns, while data collection was performed for 5 ns at 300 K. In **Tab. B.1** the obtained coordination for the Zn-O and Zn-N pairs is reported, while the comparison of the  $g(r)$ 's is shown in **Fig. B.3**. As can be observed, a definite Zn-O first peak integrating 6.0 oxygen atoms is obtained at 2.07 Å. The average bond distance is therefore in good agreement with the experimental of 2.06 Å as found from XAS data.<sup>17</sup> The Zn-N  $g(r)$  also shows one intense peak, this time centered at 4.31 Å. Therefore, N is set in the second coordination shell and no nitrogen coordination is observed in this case. The integration number is 6.0, providing a total number of six  $[\text{Tf}_2\text{N}]^-$  anions coordinating the metal and therefore the  $[\text{Zn}(\text{Tf}_2\text{N})_6]^{4-}$  species in agreement with experimental data.<sup>17</sup>

**Table B.1.** MD results of first solvation sphere structure for  $\text{Zn}^{2+}$  in  $[\text{C}_2\text{mim}][\text{Tf}_2\text{N}]$  obtained by representing the RTIL with CL&P polarizable force field<sup>5</sup> and the Zn-RTIL interaction with parameters from the *ab initio* fitting procedure (LJ potential) and from those adapted from Borodin *et al.*<sup>28</sup> (Buckingham potential).

Zn-RTIL potential	$r_{\text{Zn-O}}$ (Å) <sup>*</sup>	$\text{CN}_{\text{O}}$ <sup>†</sup>	$r_{\text{Zn-N}}$ (Å) <sup>*</sup>	$\text{CN}_{\text{N}}$ <sup>†</sup>
<i>Ab initio</i> fit	2.07	4.0	2.05	2.0
Borodin adapted	2.07	6.0	4.31	6.0

<sup>\*</sup>Average bond distance between the  $\text{Zn}^{2+}$  ion and the oxygen or nitrogen atoms of first solvation shell  $[\text{Tf}_2\text{N}]^-$  anions;

<sup>†</sup> $\text{Zn-O}(\text{Tf}_2\text{N})$  and  $\text{Zn-N}(\text{Tf}_2\text{N})$  first  $g(r)$  peak integration numbers.

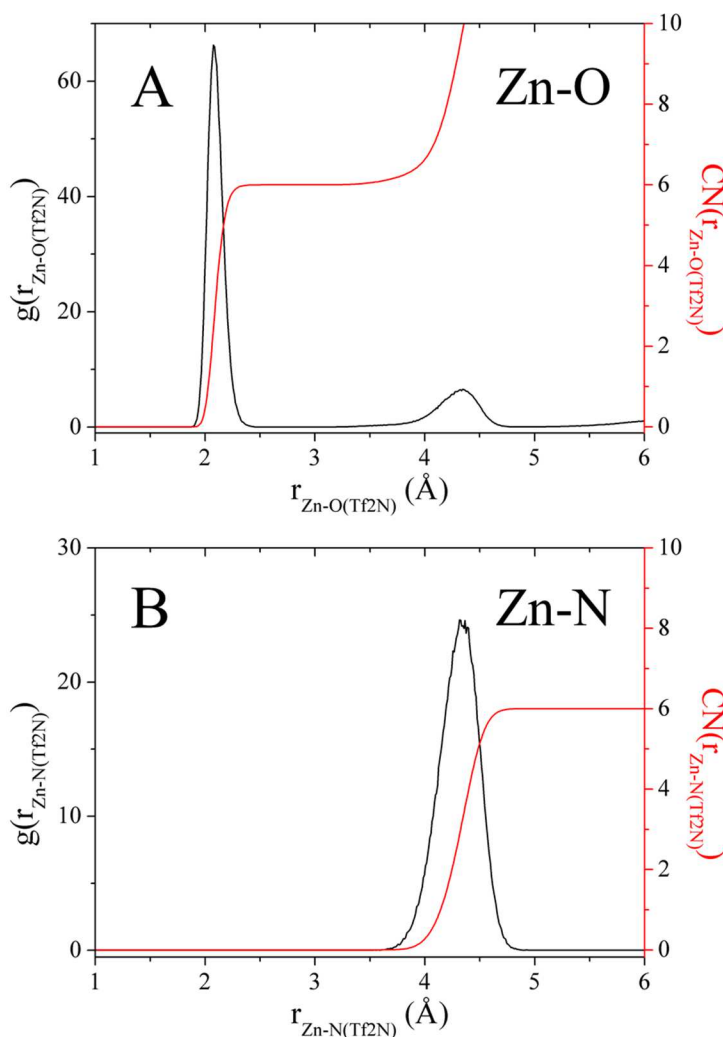


**Figure B.3.** Zn-O(Tf<sub>2</sub>N) and Zn-N(Tf<sub>2</sub>N) pairs  $g(r)$ 's obtained for Zn<sup>2+</sup> in [C<sub>2</sub>mim][Tf<sub>2</sub>N] by representing the RTIL with CL&P polarizable force field<sup>5</sup> and the metal ion with parameters adapted from Borodin *et al.*<sup>28</sup>

### B.3 Conclusions

Classical MD simulations of Zn<sup>2+</sup> in [C<sub>2</sub>mim][Tf<sub>2</sub>N] employing a polarizable force field for the ionic liquid were carried out. The results showed that with the additional degree of freedom of explicit polarization, literature LJ sets parametrized for simulations of the same metal ion in water are not transferable any more, differently to what was found for non-polarizable calculations of the same system (**Chapter 4**). Indeed, an *ad hoc* refinement of the Zn-RTIL interaction potential was necessary to reproduce the experimental coordination of the metal ion in this solvent.

# Bibliography

- 1 M. Salanne, Simulations of room temperature ionic liquids: from polarizable to coarse-grained force fields, *Phys. Chem. Chem. Phys.*, 2015, **17**, 14270–14279.
- 2 F. Dommert, K. Wendler, R. Berger, L. Delle Site and C. Holm, Force fields for studying the structure and dynamics of ionic liquids: A critical review of recent developments, *ChemPhysChem*, 2012, **13**, 1625–1637.
- 3 C. Schröder, T. Sonnleitner, R. Buchner and O. Steinhauser, The influence of polarizability on the dielectric spectrum of the ionic liquid 1-ethyl-3-methylimidazolium triflate, *Phys. Chem. Chem. Phys.*, 2011, **13**, 12240–12248.
- 4 J. N. Canongia Lopes and A. A. H. Pádua, CL&P: A generic and systematic force field for ionic liquids modeling, *Theor. Chem. Acc.*, 2012, **131**, 1–11.
- 5 A. A. H. Pádua, Resolving dispersion and induction components for polarisable molecular simulations of ionic liquids, *J. Chem. Phys.*, 2017, **146**, 204501.
- 6 C. Schröder, Comparing reduced partial charge models with polarizable simulations of ionic liquids, *Phys. Chem. Chem. Phys.*, 2012, **14**, 3089–3102.
- 7 J. Schmidt, C. Krekeler, F. Dommert, Y. Zhao, R. Berger, L. D. Site and C. Holm, Ionic Charge Reduction and Atomic Partial Charges from First-Principles Calculations of 1,3-Dimethylimidazolium Chloride, *J. Phys. Chem. B*, 2010, **114**, 6150–6155.
- 8 P. A. Hunt, B. Kirchner and T. Welton, Characterising the Electronic Structure of Ionic Liquids: An Examination of the 1-Butyl-3-Methylimidazolium Chloride Ion Pair, *Chem. – A Eur. J.*, 2006, **12**, 6762–6775.
- 9 F. Dommert, J. Schmidt, C. Krekeler, Y. Y. Zhao, R. Berger, L. D. Site and C. Holm, Towards multiscale modeling of ionic liquids: From electronic structure to bulk properties, *J. Mol. Liq.*, 2010, **152**, 2–8.
- 10 K. Cui, A. Yethiraj and J. R. Schmidt, Influence of Charge Scaling on the Solvation Properties of Ionic Liquid Solutions, *J. Phys. Chem. B*, 2019, **XXXX**, XXX–XXX.
- 11 M. Salanne, L. J. A. Siqueira, A. P. Seitsonen, P. A. Madden and B. Kirchner, From molten salts to room temperature ionic liquids: Simulation studies on chloroaluminate systems, *Faraday Discuss.*, 2012, **154**, 171–188.
- 12 K. T. Tang and J. P. Toennies, An improved simple model for the van der Waals potential based on universal damping functions for the dispersion coefficients, *J. Chem. Phys.*, 1984,

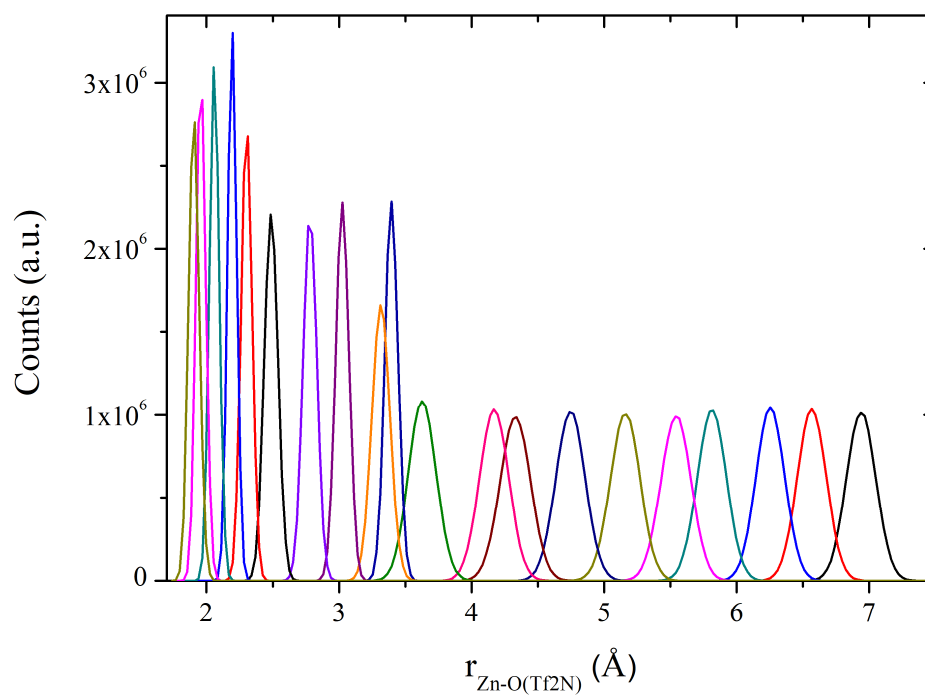
- 80**, 3726–3741.
- 13 O. Borodin, Polarizable force field development and molecular dynamics simulations of ionic liquids, *J. Phys. Chem. B*, 2009, **113**, 11463–11478.
  - 14 B. T. Thole, Molecular polarizabilities calculated with a modified dipole interaction, *Chem. Phys.*, 1981, **59**, 341–350.
  - 15 J. G. McDaniel, C. Y. Son and A. Yethiraj, Ab Initio Force Fields for Organic Anions: Properties of [BMIM][TFSI], [BMIM][FSI], and [BMIM][OTf] Ionic Liquids, *J. Phys. Chem. B*, 2018, **122**, 4101–4114.
  - 16 J. G. McDaniel, E. Choi, C. Y. Son, J. R. Schmidt and A. Yethiraj, Ab Initio Force Fields for Imidazolium-Based Ionic Liquids, *J. Phys. Chem. B*, 2016, **120**, 7024–7036.
  - 17 F. Sessa, V. Migliorati, A. Serva, A. Lapi, G. Aquilanti, G. Mancini and P. D’Angelo, On the coordination of Zn<sup>2+</sup> ion in Tf<sub>2</sub>N<sup>-</sup> based ionic liquids: structural and dynamic properties depending on the nature of the organic cation, *Phys. Chem. Chem. Phys.*, 2018, **20**, 2662–2675.
  - 18 P. Li, B. P. Roberts, D. K. Chakravorty and K. M. Merz, Rational design of particle mesh ewald compatible lennard-jones parameters for +2 metal cations in explicit solvent, *J. Chem. Theory Comput.*, 2013, **9**, 2733–2748.
  - 19 W. C. Swope, H. C. Andersen, P. H. Berens and K. R. Wilson, A computer simulation method for the calculation of equilibrium constants for the formation of physical clusters of molecules: Application to small water clusters, *J. Chem. Phys.*, 1982, **76**, 637–649.
  - 20 S. Nosé, A molecular dynamics method for simulations in the canonical ensemble, *Mol. Phys.*, 1984, **52**, 255–268.
  - 21 W. G. Hoover, Canonical dynamics: Equilibrium phase-space distributions, *Phys. Rev. A*, 1985, **31**, 1695–1697.
  - 22 P. P. Ewald, Die Berechnung optischer und elektrostatischer Gitterpotentiale, *Ann. Phys.*, 1921, **369**, 253–287.
  - 23 R. Car and M. Parrinello, Unified Approach for Molecular Dynamics and Density-Functional Theory, *Phys. Rev. Lett.*, 1985, **55**, 2471–2474.
  - 24 A. D. Becke, Density-functional exchange-energy approximation with correct asymptotic behavior, *Phys. Rev. A*, 1988, **38**, 3098–3100.
  - 25 C. Lee, W. Yang and R. G. Parr, Development of the Colle-Salvetti correlation-energy formula into a functional of the electron density, *Phys. Rev. B*, 1988, **37**, 785–789.
  - 26 N. Troullier and J. L. Martins, Efficient pseudopotentials for plane-wave calculations, *Phys. Rev. B*, 1991, **43**, 1993–2006.

- 27 S. Grimme, Semiempirical GGA-type density functional constructed with a long-range dispersion correction, *J. Comput. Chem.*, 2006, **27**, 1787–1799.
- 28 O. Borodin, G. A. Giffin, A. Moretti, J. B. Haskins, J. W. Lawson, W. A. Henderson and S. Passerini, Insights into the Structure and Transport of the Lithium, Sodium, Magnesium, and Zinc Bis(trifluoromethanesulfonyl)imide Salts in Ionic Liquids, *J. Phys. Chem. C*, 2018, **122**, 20108–20121.

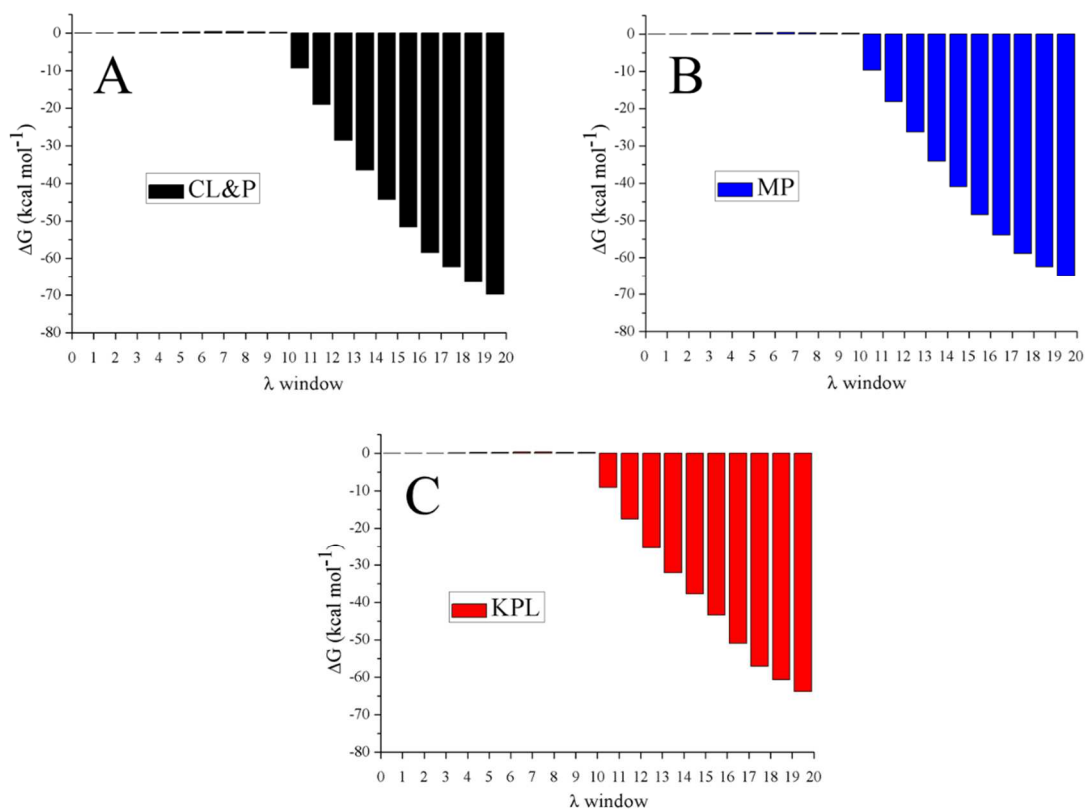


# Appendix C

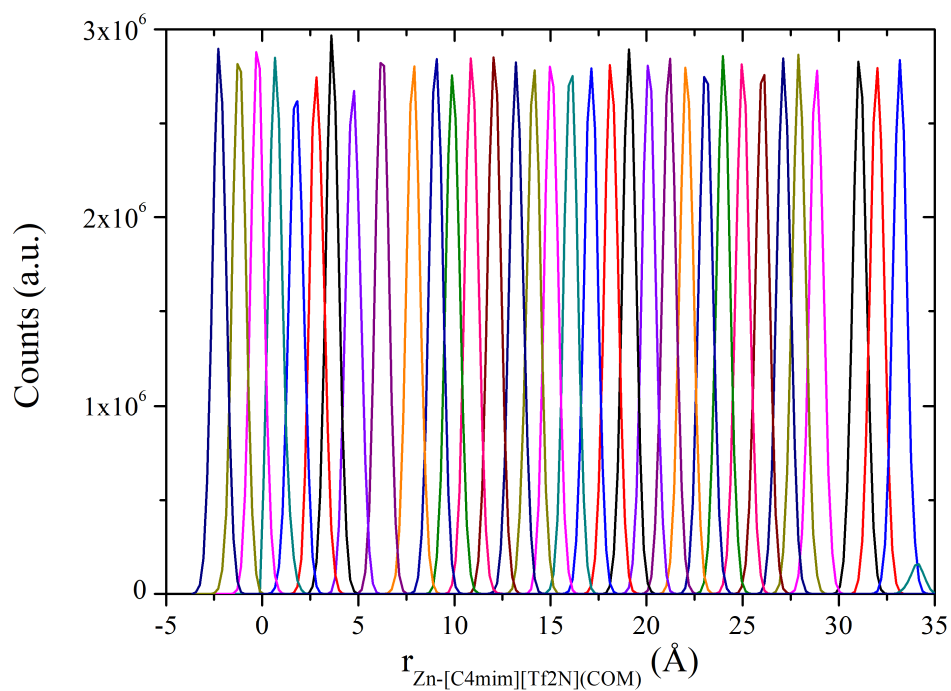
## Materials for Chapter 4: “Zn<sup>2+</sup> ion in Tf<sub>2</sub>N- and BF<sub>4</sub>-based imidazolium RTILs”.



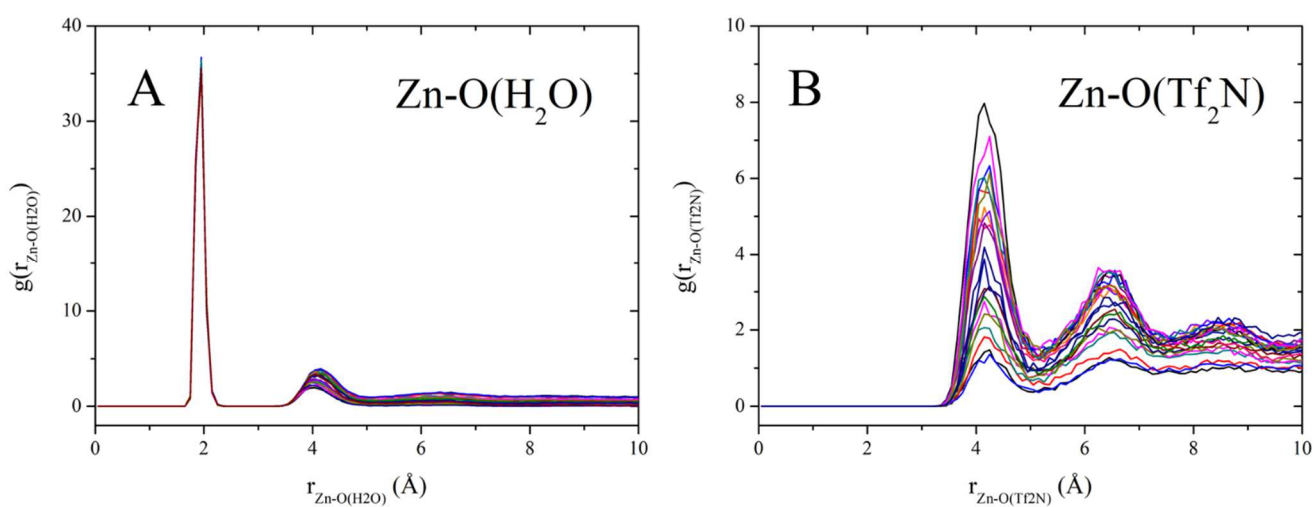
**Figure C.1.** Histograms of the configurations within the umbrella sampling windows for the addition of a [Tf<sub>2</sub>N]<sup>-</sup> anion to the [Zn(Tf<sub>2</sub>N)<sub>5</sub>]<sup>3-</sup> unit.



**Figure C.2.** Gromacs BAR module output showing the relative free energy differences calculated between neighboring  $\lambda$  windows for Zn<sup>2+</sup> represented with Merz LJ parameters in [C<sub>4</sub>mim][Tf<sub>2</sub>N] with A) CL&P; B) KLP and C) MP force fields.

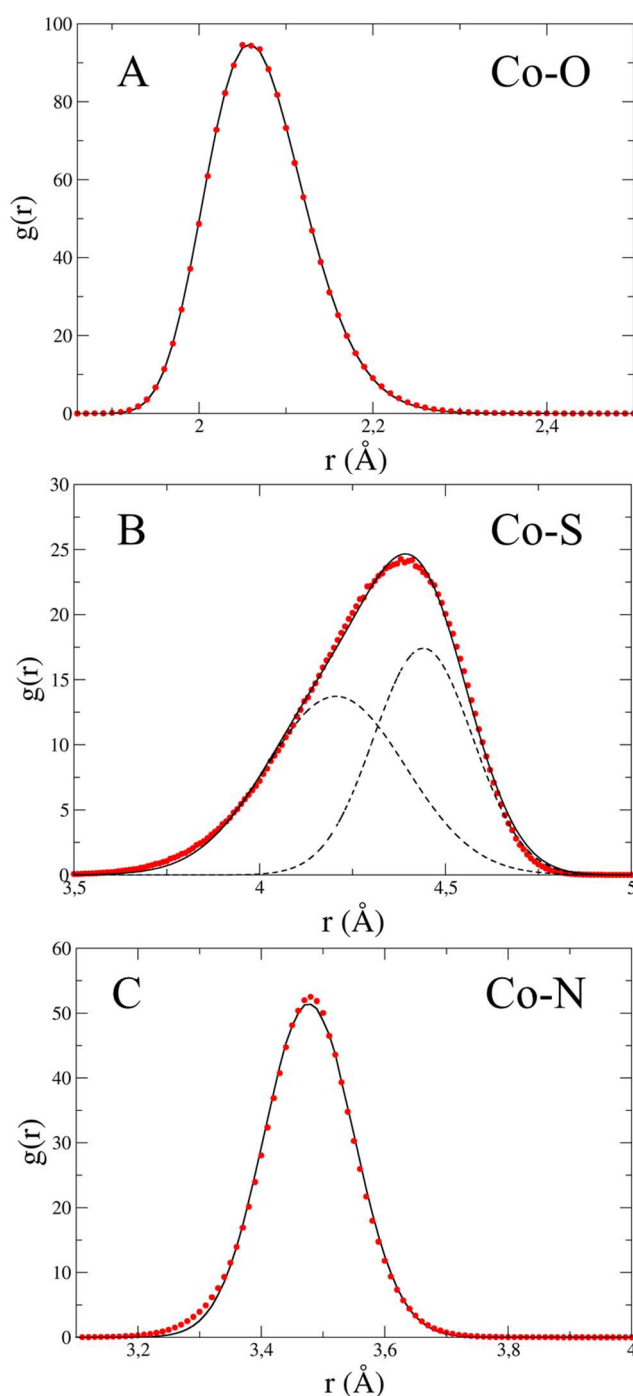


**Figure C.3.** Histograms of the configurations within the umbrella sampling windows for the transfer of  $\text{Zn}^{2+}$  from water to  $[\text{C4mim}][\text{Tf}_2\text{N}]$  in the biphasic system.

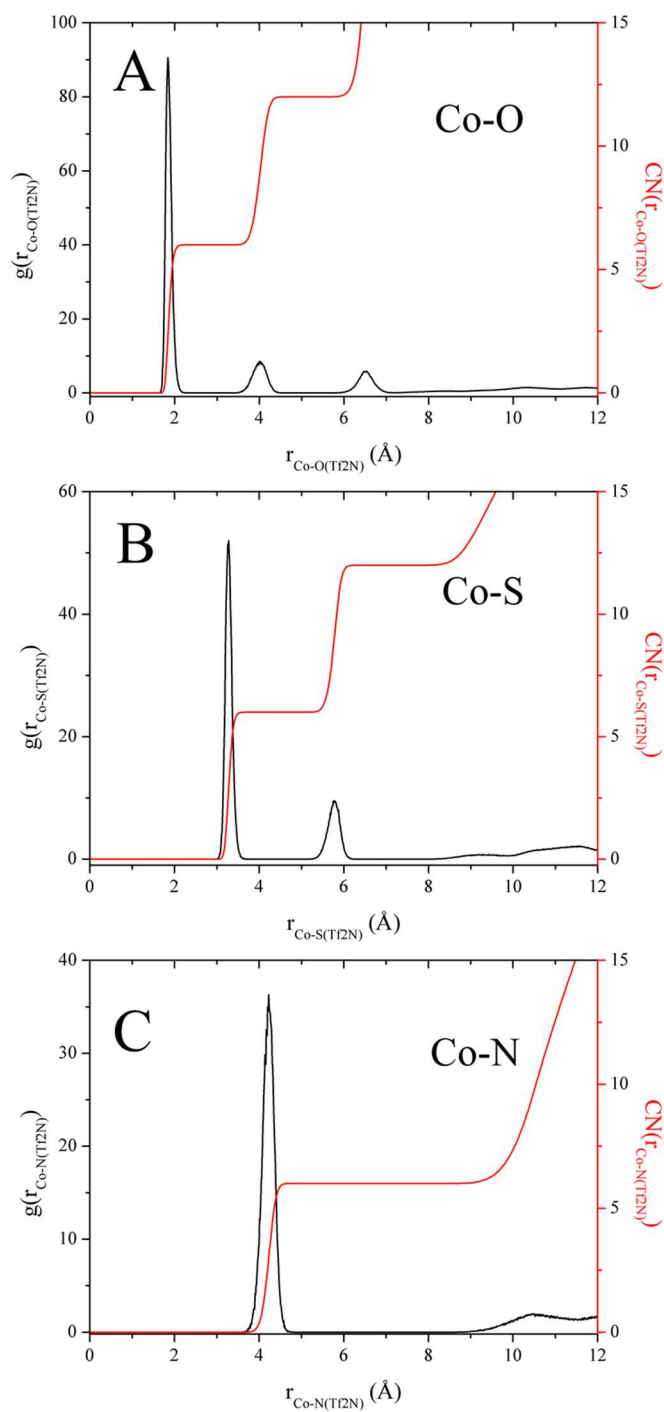


**Figure C.4.** A)  $\text{Zn-O}(\text{H}_2\text{O})$  and B)  $\text{Zn-O}(\text{Tf}_2\text{N})$  pairs  $g(r)$  along the reaction coordinate between the interphase (from top) to the ionic liquid bulk (to bottom).

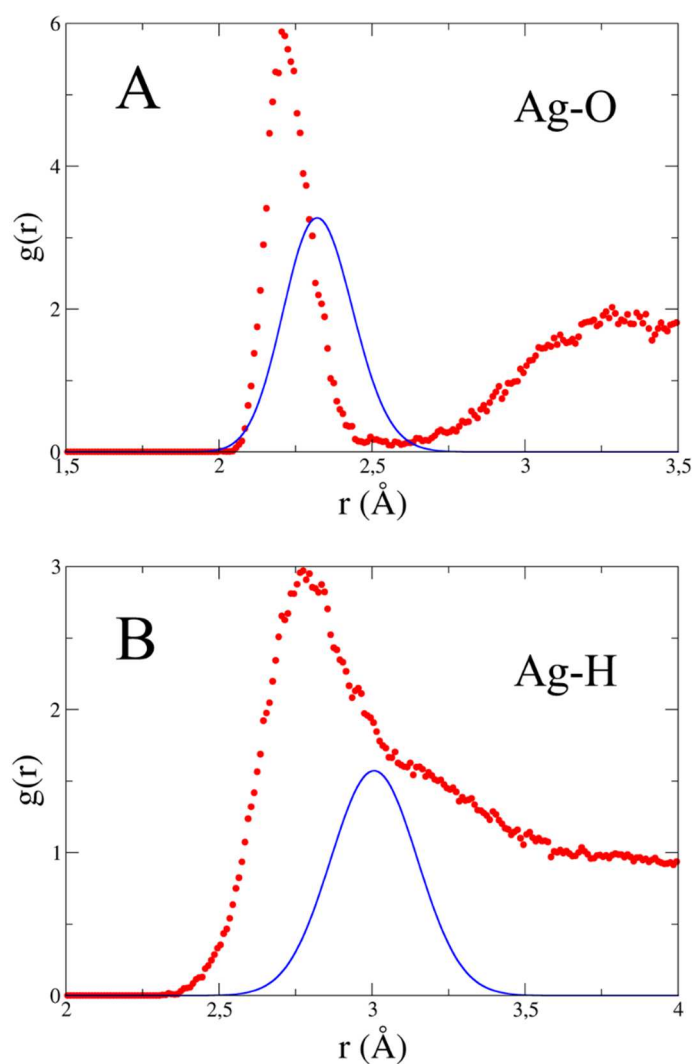
## Materials for Chapter 5: “Co<sup>2+</sup> ion in [C4mim][Tf<sub>2</sub>N]”.



**Figure C.5.** A) Co-O, B) Co-S and C) Co-N  $g(r)$ 's obtained from the MD simulations of Co(Tf<sub>2</sub>N)<sub>2</sub> in [C<sub>4</sub>mim][Tf<sub>2</sub>N] for the structural part (red dotted lines) as compared with the  $\Gamma$ -like functions obtained from the fitting procedure (solid black lines). In case of the Co-N distribution, also the two partial curves employed for the fit are showed (fragmented black lines).



**Figure C.6.** Radial distribution functions  $g(r)$ 's for the A) Co-O, B) Co-S and C) Co-N pairs calculated from the MD simulation of the Co(Tf<sub>2</sub>N)<sub>2</sub> solution in [C<sub>4</sub>mim][Tf<sub>2</sub>N] for the thermodynamic part.

**Materials for Chapter 6: “Ag<sup>+</sup> ion between water and RTILs”.**

**Figure C.7.** Comparison between A) Ag-O and B) Ag-H  $g(r)$ 's obtained from the CPMD simulation of Ag<sup>+</sup> in water (red dots) and from the fitting of the Ag K-edge EXAFS spectrum in aqueous solution (blue lines). In the latter case, the peaks are the resulting  $\Gamma$ -like functions for the Ag-O and Ag-H distributions that provided the best fit of the spectrum.

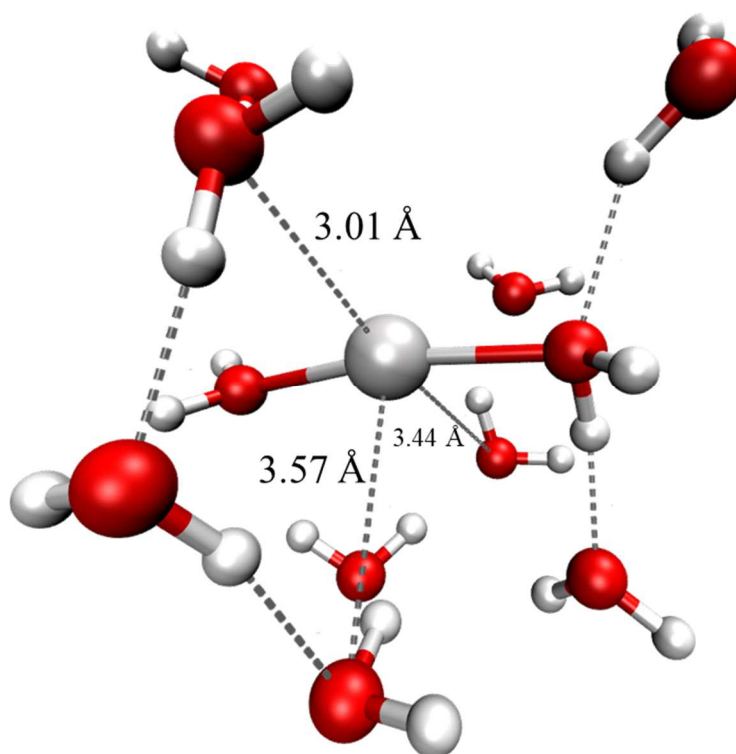


**Figure C.8.** Representative snapshot from the CPMD simulations of  $\text{Ag}^+$  in water showing the two coordinating water molecules in addition to selected outer-sphere waters. In particular, two water molecules connected with the first area in **Fig. 6.5 A (Chapter 6)** are present at distances of 3.01 Å, 3.44 Å and 3.57 Å from the silver atom. In addition, outer-sphere waters interacting with first-shell molecules by means of H-bonds are shown. (Balls and stricks:  $\text{Ag}^+$  and water, dashed lines: interaction between  $\text{Ag}^+$  and outer-sphere waters as well as H-bonds between water molecules). Non-isometric view is shown for sake of clarity.



## General conclusions and perspectives

A study about metal ions solvation in RTILs has been carried out from a structural and thermodynamic point of view. The results allowed to obtain useful data with the aim of helping improving new technological applications involving metals and this class of potentially sustainable solvents. In particular:

- $\text{Zn}^{2+}$  resulted to be more favorably solvated in water than in  $\text{Tf}_2\text{N}$ -based RTILs, as shown by positive  $\Delta G_{\text{trans}}$ . This is in agreement with the low solvation capabilities of the  $[\text{Tf}_2\text{N}]^-$  anion, as already argued in literature. XAS data analysis also confirmed this outline, showing that  $\text{Zn}^{2+}$  is coordinated only by water when it is present in the RTIL. However, the reasons at the origin of this picture were still unclear. In this work, it has been stressed that the  $\text{Zn}$ - $\text{Tf}_2\text{N}$  interaction is favorable from an enthalpic point of view (at least with respect to water), but an unfavorable entropic contribution is also present when the metal passes from an aqueous solution to the RTIL. In other words, bringing six  $[\text{Tf}_2\text{N}]^-$  anions from the solution bulk to the first coordination sphere and forming the  $[\text{Zn}(\text{Tf}_2\text{N})_6]^{4-}$  species means a great loss of disorder, therefore energy must be spent. This is in agreement also with data about complexation thermodynamics of metal ions in  $\text{Tf}_2\text{N}$ -based RTILs (see **Sec. 1.3.4 of Chapter 1**), where the substitution of this ligand with others of various nature is often favorable because of the positive entropic contribution followed by the release of  $[\text{Tf}_2\text{N}]^-$  from the first coordination sphere of the metal. According the results from this project, “neat”  $\text{Tf}_2\text{N}$ -based RTILs could difficultly be employed as extracting phase for this metal ion. Differently, the addition of extracting agents able to complex  $\text{Zn}^{2+}$  in the aqueous solution could make its distribution to the RTIL phase more favorable. As a future perspective, it would be interesting to study the complexation of the metal ion in RTILs with ligands of various nature, starting for example from the simple cases of  $\text{Cl}^-$  and  $\text{NO}_3^-$ .

A different situation is displayed for  $\text{Zn}^{2+}$  in  $[\text{C}_4\text{mim}][\text{BF}_4]$ , where a favorable  $\Delta G_{\text{trans}}$  from water was obtained. This result is in agreement with experimental data and with the picture of the higher solvating capabilities of the  $[\text{BF}_4]^-$  anion with respect to  $[\text{Tf}_2\text{N}]^-$ . The favorable transfer free energy seems to arise by a still negative  $\Delta H_{\text{trans}}$ , but in this case the entropic contribution is not unfavorable enough to prevent the process. The reason could be traced in the more rigid structure of  $[\text{BF}_4]^-$  with respect to  $[\text{Tf}_2\text{N}]^-$ , that is traduced in a smaller loss of

entropy suffered by the anion upon complexation. This direct comparison is allowed also because the same number of anions with respect to the Tf<sub>2</sub>N-case is found to coordinate the metal according to MD simulation, providing the [Zn(BF<sub>4</sub>)<sub>6</sub>]<sup>4-</sup> species. As a future perspective, XAS data collected on this sample could help in validate this structure.

- The picture obtained about Co<sup>2+</sup> in [C<sub>4</sub>mim][Tf<sub>2</sub>N] is not much different from that of Zn<sup>2+</sup> in the same RTIL. Also for cobalt, a favorable contribution to the transfer from water is given by  $\Delta H_{\text{trans}}$ , while transfer entropy opposes to the process. In addition, from UV-Vis data a blue-shift was observed by passing from [Tf<sub>2</sub>N]<sup>-</sup> to water coordination. This means that water is a stronger ligand for cobalt than the bis(trifluoromethylsulfonyl)imide, as also confirmed by DFT calculations. This result was in principle unexpected, because the negative  $\Delta H_{\text{trans}}(\text{water} \rightarrow [\text{C}_4\text{mim}][\text{Tf}_2\text{N}])$  obtained both for cobalt and zinc was at a first try interpreted by supposing that the “pure” metal-ligand interaction was stronger for [Tf<sub>2</sub>N]<sup>-</sup> with respect to water. However, UV-Vis results suggested that the negative transfer enthalpy must be provoked by effects that are not coming from the first coordination sphere. Therefore, the different reorganization of the outer-sphere solvent between the aqueous solution and the RTIL could have a crucial role in this case.

XAS data collected on the Co(Tf<sub>2</sub>N)<sub>2</sub> solid as well as on a Co(Tf<sub>2</sub>N)<sub>2</sub> solution in [C<sub>4</sub>mim][Tf<sub>2</sub>N] have shown that the RTIL is able to dissolve the metal salt giving rise to a different coordination with respect to the solid state. This result confirmed that the employment of powerful techniques like XAS is essential for the determination of the coordination in solution. EXAFS data analysis was also compared with structural results from the MD simulation. When we talk about metal ions coordination, we are often trained at thinking in terms of coordination numbers and bond distances. However, this study also showed how a slightly more complex description is required to achieve a fulfill picture about metal ions coordination in liquid disordered systems. In this case, MD was able to reproduce the same kind of coordination of the experimental, *i.e.* the [Co(Tf<sub>2</sub>N)<sub>6</sub>]<sup>4+</sup> cluster. However, the comparison between Co-RTIL  $g(r)$ 's as modelled with  $\Gamma$ -like functions also showed that coordination coming from MD and from EXAFS fitting were different in some other features. In particular, dynamical properties of [Tf<sub>2</sub>N]<sup>-</sup> coordination towards Co<sup>2+</sup> were not correctly reproduced, providing a too rigid interaction that was traduced in underestimated Debye-Waller factors. This is a known drawback of the LJ potential and of its simple, although fast and very commonly employed, formulation.

- XAS data fitting about  $\text{Ag}^+$  in water provided a picture of this metal ion as linearly coordinated in aqueous solution. This evidence suggested that the generally accepted model of  $\text{Ag}^+$  as tetrahedrally-coordinated in water is questionable. However, the employment of a LJ potential for the  $\text{Ag-H}_2\text{O}$  interaction in classical MD showed some limits in reproducing the experimental evidence. Also more complex, but still spherical potentials, could not allow to obtain a good compromise between CN and experimental bond distance.

The transfer of  $\text{Ag}^+$  from an aqueous solution to  $[\text{C}_4\text{mim}][\text{Tf}_2\text{N}]$  and  $[\text{C}_4\text{mim}][\text{BF}_4]$  resulted to be favorable. This seemed to arise from negative  $\Delta H_{\text{trans}}$ , while  $\Delta S_{\text{trans}}$  is not unfavorable enough to prevent the process. A favorable transfer towards  $[\text{C}_4\text{mim}][\text{BF}_4]$  has been found also for  $\text{Zn}^{2+}$ , but the interesting result is that the transfer of  $\text{Ag}^+$  is favorable also towards  $[\text{C}_4\text{mim}][\text{Tf}_2\text{N}]$ . This could arise from the different CN shown by  $\text{Ag}^+$  in the RTIL, forming the  $[\text{Ag}(\text{Tf}_2\text{N})_4]^{3-}$  or  $[\text{Ag}(\text{Tf}_2\text{N})_5]^{4-}$  species at dependence of the employed potential. The different coordination could be at the origin of the less unfavorable  $\Delta S_{\text{trans}}$ . In other words, bringing four or five  $[\text{Tf}_2\text{N}]^-$  anions from the solution bulk and ordering them in the first solvation sphere of  $\text{Ag}^+$  costs less energy with respect to the zinc case, where six anions are found to coordinate. However, care must be taken because of a possible change in the CN by passing from the aqueous solution (where  $\text{Ag}^+$  resulted to be linear) to the RTIL phase. Nevertheless, these results are encouraging for the employment of ionic liquids in the separation of this metal ion from aqueous solutions. XAS measures collected on  $\text{Ag}^+$  solutions in the studied RTILs would help in validating the structural results obtained by means of MD.

- A reasoning about the introduction of many-body polarizability in classical MD simulations of RTILs must be traced. As has been demonstrated through all this project, a description of metal ions coordination and thermodynamic solvation properties in good agreement with experimental data can be obtained by MD with the employment of interaction potentials that were not parametrized for the specific case. This was not a trivial result, as RTILs force fields are usually refined to represent some solvent bulk properties. Therefore, this ability in reproducing solvation features arising from punctual interactions with a metal ion was not taken for granted. However, non-polarizable force fields interacting with metal ions *via* LJ potential also showed some drawbacks. For this reason, a compromise between structural and thermodynamic description has often to be taken into account. The purpose underneath the employment of RTILs polarizable force fields in this project has been the supposition that the addition of this additional degree of freedom could help in reproducing structural and thermodynamic solvation properties altogether. A description of  $\text{Zn}^{2+}$  coordination in

[C<sub>2</sub>mim][Tf<sub>2</sub>N] in agreement with the experimental has been obtain with this kind of potential. As a future perspective, the metal ion  $\Delta G_{\text{solv}}$  in the RTIL could be calculated with a thermodynamic integration method.

It has to be underlined that a drawback of polarizable force fields is that an increase in the computational effort of ~5 times has been observed with respect to non-polarizable simulations. This was an expected result, but can be detrimental in particular for RTILs, since these are known to be slow-dynamics solvents that often require long equilibration times.



# Acknowledgements

First of all, I want to thank my supervisor prof. Andrea Melchior and my co-supervisor prof. Marilena Tolazzi, without whom this project would have not been possible. I would like to thank them especially for the productive scientific discussion and constant support. I am also thankful to the people of the “Thermodynamics and Modelling” group, past and present, who have all made a contribution to my achievements: Dr. Daniele Veclani, Dr. Georgina Faura Muñoz, Martina Sanadar and our beloved problem-solver Pierluigi Polese. I would also like to thank collaborators that contributed to this project: prof. Paola D’Angelo from Sapienza Università di Roma; prof. Mathieu Salanne and Dr. Alessandra Serva from the PHENIX group of Sorbonne Université where I had the possibility to spend a research period of two months.

Last but not least I would like to thank all the people in my life who are not related to the chemistry world, like my family, for being a constant reference during this three years path.

# List of publications and communications

## Publications from this project

M. Busato, P. D'Angelo and A. Melchior, Solvation of  $Zn^{2+}$  ion in 1-alkyl-3-methylimidazolium bis(trifluoromethylsulfonyl)imide ionic liquids: a molecular dynamics and X-Ray absorption study, *Phys. Chem. Chem. Phys.*, 2019, **21**, 6958–6969

M. Busato, P. D'Angelo, A. Lapi, M. Tolazzi and A. Melchior, Solvation of  $Co^{2+}$  ion in 1-butyl-3-methylimidazolium bis(trifluoromethylsulfonyl)imide ionic liquid: a molecular dynamics and X-ray absorption study, *J. Mol. Liq.*, 2019, *in peer reviewing*

## Publications from other projects

J.I. Lachowicz, V.M. Nurchi, G. Crisponi, I. Cappai, R. Cappai, M. Busato, A. Melchior, M. Tolazzi, M. Peana, E. Garribba, M.A. Zoroddu, P. Coni, G. Pichiri, J. Aaseth, Para-Aminosalicylic acid in the treatment of manganese toxicity. Complexation of  $Mn^{2+}$  with 4-amino-2-hydroxybenzoic acid and its N-acetylated metabolite, *New J. Chem.*, 2018, **42**, 8035–8049

P.L. Zanonato, A. Melchior, M. Busato, P. Di Bernardo, M. Tolazzi, Silver(I) complexes with long-chain diamines in non-aqueous solvents, *J. Therm. Anal. Calorim.* (2019). doi:10.1007/s10973-019-08725-4

P. L. Zanonato, P. Di Bernardo, A. Melchior, M. Busato, M. Tolazzi, Lanthanides(III) Complex Formation with Triamines in DMSO: the Effect of Ligand Cyclization, *Inorg. Chim. Acta*, 2019, *in peer reviewing*

## **Presentations**

**12 – 13 June 2017**

VII Workshop Nazionale AICInG – Politecnico di Milano, Milan, Italy

Oral presentation: M. Busato, M. Tolazzi and A. Melchior

**Structural and Thermodynamics Properties of Transition Metal Ions in Room Temperature Ionic Liquids**

**11 – 13 September 2017**

Faraday discussion: “Ionic liquids: from fundamental properties to practical applications” – Murray Edwards Colledge, Cambridge, UK

Poster and flash presentation: M. Busato, M. Tolazzi and A. Melchior

**Structural and Thermodynamics Properties of Transition Metal Ions in Room Temperature Ionic Liquids**

**9 November 2018**

Società Chimica Italiana: “I giovani e la chimica in FVG” – Università degli Studi di Udine, Udine, Italy

Oral presentation: M. Busato, P. D’Angelo, M. Tolazzi and A. Melchior,

**Structural and Thermodynamic features of the Zn(II) ion in Room Temperature Ionic Liquids**

**12 November 2018**

ALBA Synchrotron Light Source, Belaterra, Barcelona, Spain

Seminar: M. Busato

**A combined approach between molecular dynamics (MD) simulations and X-ray absorption spectroscopy (XAS) for the study of metal ions in water and ionic liquids**

**15 – 20 September 2019**

Quantum ESPRESSO Summer School: “Advanced Materials and Molecular Modelling” – Jožef Stefan Institute, Ljubljana, Slovenia

Poster and flash presentation: M. Busato, A. Colella, G. Mancini, M. Peluso, D. Veclani, A. Melchior, M. Tolazzi, I. Persson, P. D’Angelo

**Evidence for a linear coordination of Ag<sup>+</sup> in water: a X-ray absorption spectroscopy, classical and *ab initio* Molecular Dynamics study**

**27 – 29 June 2019**

VIII Workshop Nazionale AICIng – Lipari, Italy

Oral presentation: M. Busato, P. D'Angelo, M. Tolazzi and A. Melchior

**Structural and Thermodynamic Properties of the Zn<sup>2+</sup> and Co<sup>2+</sup> Ions in Room Temperature Ionic Liquids**

**7 – 12 October 2018**

27<sup>th</sup> EuCheMS Conference on Molten Salts and Ionic Liquids – Lisbon, Portugal

Oral presentation: M. Busato, P. D'Angelo, M. Tolazzi and A. Melchior

**Structural and Thermodynamics Properties of Transition Metal Ions in Room Temperature Ionic Liquids**

**17 – 19 December 2018**

XL National Congress on Calorimetry Thermal Analysis and Applied Thermodynamics – Pisa, Italy

Poster: P.L. Zanonato, P. Di Bernardo, A. Melchior, M. Tolazzi, M. Busato

**Thermodynamics of Complex formation of Silver(I) with Long Chain Diamine Ligands in Non-aqueous Solvents**



Su ciò di cui non si può parlare, si deve tacere.

L. Wittgenstein, *Tractatus Logico-Philosophicus*

